



Stability Enhanced Perovskite Thin Films for Solar Energy Applications

A thesis submitted to The University of Manchester for the degree of

Doctor of Philosophy (PhD)

in the Faculty of Science and Engineering

2023

Fahad Aljuaid

Department of Materials, School of Natural Sciences

The University of Manchester

Supervisors

- Dr Andrew Thomas
- Dr David Lewis

Table of Contents

List of Figures	5
List of Tables	11
List of Abbreviations	12
Abstract	14
Declaration	15
Copyright Statements	16
Acknowledgements	17
Publications and Conferences	18
Chapter 1: Introduction	20
Chapter 2: Literature review	
2.1. Perovskite Solar Cells	25
2.1.1. Perovskite Material	26
2.1.2. Problems of PSCs	30
2.1.2.1. Stability	30
2.1.2.2. Toxicity	33
2.1.3. Review of the main strategies used in the studies of improving perovskite materials.	34
2.1.3.1. Multiple-Cation Perovskites	34
2.1.3.2. Passivation Strategy	37
2.1.3.3. The Encapsulation Strategy	39
2.1.3.4. Template strategy	40
2.2. Interfacial charge dynamics	45
2.3. Electron Transport Layers (ETL) in PSCs	48
2.3.1. Electron Transport Layer Requirements	48
2.3.2. Electron Transport Materials	48
2.3.3. Modifying the TiO ₂ Based Electron Transport Layer	49
2.3.3.1. Controlling the Morphology of the TiO ₂ ETL	50
2.3.3.2. Doping of the TiO ₂ ETL	51
2.3.3.3. Modifying the TiO ₂ surface	51
Chapter 3: Theory and techniques	
3.1. Background Theory of photovoltaic devices	57
3.1.1. Band Structure of semiconductors.	57
3.1.1.1. Fermi energy	58
3.1.1.2. Metals, Insulators and Semiconductors	58
3.1.2. Photovoltaic effect	60
3.1.2.1. Optical absorption in semiconductors	61
3.1.2.2. Charge separation	62
3.1.2.3. Shockley-Quesser	64
3.1.2.4. Performance of solar cells	67
3.2. Perovskite solar cells (PSCs)	70
3.2.1. PSCs Construction	70
3.2.2. Architectures of perovskite solar cells	71
3.2.3. Principle of Operation of Perovskite Solar Cells	72

3.3. Materials	73
3.3.1. Perovskite	73
3.3.2. Peptide Gels	74
3.3.3. Titanium dioxide (TiO ₂)	79
3.4. Techniques	82
3.4.1. X-ray Photoelectron spectroscopy (XPS)	82
3.4.2. Ultraviolet-visible (UV-vis) spectrophotometry	84
3.4.3. Scanning Electron Microscope (SEM)	86
2.3.4. Photoluminescence spectroscopy	86
2.3.5. Time-resolved photoluminescence spectroscopy (TRPL)	88
2.3.6. X-ray diffraction (XRD)	89
2.3.7. Photovoltaic characterization	91

Chapter 4: Investigation of using FEFKFEFK peptide gel as a template in the fabrication of methylammonium lead iodide perovskite.

4.1. INTRODUCTION	94
4.2. EXPERIMENTAL SECTION	96
4.2.1. Materials	96
4.2.2. Preparation of MAPI-peptide thin films:	96
4.2.3. Manufacture of perovskite solar cells	97
4.2.4. Instrumentation	98
4.3. RESULTS AND DISCUSSION	98
4.3.1. Effect of peptide on MAPI properties	101
4.3.1.1. The crystal size of MAPI	101
4.3.1.2. Optoelectronic properties of MAPI	103
4.3.2. Effect of peptide on the morphology of MAPI	110
4.3.3. Effect on the stability of MAPI	111
4.3.4. Effect of peptide gel on efficiency of solar cells	116
4.4. CONCLUSION	119

Chapter 5: Investigation of using FEFKFEFKK peptide gel as a template in the fabrication of methylammonium lead iodide perovskite.

5.1. INTRODUCTION	121
5.2. EXPERIMENTAL SECTION	122
5.2.1. Materials	122
5.2.2. Preparation of MAPI-peptide thin films:	122
5.2.3. Instrumentation	122
5.3. RESULTS AND DISCUSSION	123
5.3.1. Effect of peptide on MAPI properties	125
5.3.1.1. The crystal size of MAPI	125
5.3.1.2. Optoelectronic properties of MAPI	127
5.3.2. Increasing the stability of MAPI	134
5.4. CONCLUSION	141

Chapter 6: Treatment of titanium dioxide by 4-Fluoroaniline (4-FA)

6.1. INTRODUCTION	143
6.2. EXPERIMENTAL SECTION	146
6.2.1. Materials	146
6.2.2. Preparation of TiO₂ thin films	146
6.2.3. Treatment of TiO₂ thin films by 4-Fluoroaniline	146
6.2.3.1. Method 1: Treatment of TiO₂ thin films by immersing them in 4-fluoroaniline solution	146
6.2.3.2. Method 2: Treatment of TiO₂ thin films with 4-fluoroaniline vapour.	147
6.2.4. Instrumentation	147
6.3. RESULTS AND DISCUSSION	148
6.3.1. XPS results	148
6.3.1.1. Treatment of TiO₂ thin films by immersing in 4-FA.	151
6.3.1.1.1. Using the cleaning by IPA (Isopropyl alcohol) to remove excess 4-FA.	151
6.3.1.1.2. Heating to remove the excess 4-FA	158
6.3.1.2. Treatment of TiO₂ thin films by using the evaporation of 4-fluoroaniline solution without direct contact between them.	164
6.3.2. The UV-vis transmittance spectra	167
6.4. CONCLUSIONS	168

Chapter 7: Conclusions and Future work

7.1. CONCLUSIONS	170
7.2. SUGGESTIONS FUTURE WORK	171
REFERENCES	172

List of Figures

Fig (1.1)	Best research-cell efficiencies chart for different photovoltaic technologies from 1975 to 2022	23
Fig (2-1)	Schematic illustration for typical perovskite solar cells.	25
Fig (2-2)	The energy payback time of PV modules. P-1 is PSC-based on TiO ₂ , P-2 is PSC-based on ZnO. EPBT is the annual ratio of consumption to generation.	26
Fig (2-3)	Crystal structure of perovskite ABX ₃	27
Fig (2-4)	Illustration Map (r _A - r _X) for theoretically stable halide perovskites based on B-site cations Pb, Sn, and Ba	28
Fig (2-5)	A comparison of absorption coefficients of halide perovskites with those of silicon and most thin films solar cells	29
Fig (2-6)	Schematic energy level diagram of different perovskites based on different chemical compositions	29
Fig (2-7)	Illustration of the suggested layer-by-layer decomposition of perovskite during 85 °C annealing	32
Fig (2-8)	Optoelectronic and Thermoelectric Applications of (A) Lead-Based Perovskite Materials and (b) Low-Toxicity Perovskite Materials	34
Fig (2-9)	X-ray diffraction patterns of FA _x MA _(1-x) PbI ₃ thin films with different concentrations of FA, showing a decrease in 2θ (110 plane)	35
Fig (2-10)	Scheme for (a) pure FAPI (non-stabilised hexagonal structure- δ phase) and FA/MA-based FAPI structural phase transitions (stabilised trigonal structure- α phase) (b) Optimised structure model of MA-stabilized FAPI	36
Fig (2-11))	Scheme for structural complexity of organic-inorganic hybrid perovskites and the related improvements in stability	37
Fig (2-12)	Schematic diagram showing various types of defects in organic lead halide perovskite that could act as traps assisted non-radiative recombination or cause perovskite decomposition	38
Fig (2-13)	Schematic of patterning of perovskite thin films by different templates	41
Fig (2.-14)	The absorption (Black) and PL (Red) spectra of templated MAPI in PAMs with different diameters pores	43
Fig (2-15)	Schematic Illustration for steps of loading MAPbI ₂ X into MOF pores	43
Fig (2-16)	PL spectra of templated MAPbI ₂ X thin film with their references ((a) X= Cl, (b) X = Br, and (c) X = I	44
Fig (2-17)	Schematic for the dynamic of charge carriers in PSCs, where 1,2 and 3 are the pathways of the injection of charge carriers to charge-carrier transport layers to generate the photocurrent (desirable). From 4 to 8 are the photoelectrons recombination pathways(undesirable). 9, I and II are the pathways of electrons' trapping by defects, whether photoelectrons or from perovskite (undesirable).	46
Fig (2-18)	Energy level diagram of the materials used as ETL	48

Fig (2-19):	Schematic for interfacial monolayer modifiers based on organic compounds with two-functional-group	52
Fig (2-20)	The relationship between the ratio C to Ti (C/Ti) and contact angle	54
Fig (3-1)	The allowed bands of energies due to the splitting of energy states (n=1,2 and 3)	57
Fig (3-2)	The function of Fermi probability versus energy for different temperatures	58
Fig (3-3)	Valence and conduction bands in insulator, semiconductor, and conductor.	59
Fig (3-4)	Position of the Fermi level in intrinsic, <i>n</i> -type and <i>p</i> -type semiconductors. n_D is the position of the donor level in an <i>n</i> -doped semiconductor and n_A the position of the acceptor level in a <i>p</i> -doped semiconductor.	60
Fig (3-5)	Direct band gap semiconductor <i>e.g.</i> perovskite vs indirect band gap semiconductor <i>e.g.</i> Si	62
Fig (3-6)	The mechanism of charge separation in a <i>p-i-n</i> junction solar cell	63
Fig (3-7)	The loss mechanisms in single-junction solar cells with different E_g .	64
Fig (3-8)	Incident solid angle and the emission solid angle	65
Fig (3-9)	The balance detailed balance limit of the conversion efficiency of single-junction solar cell	67
Fig (3-10)	Equivalent circuit diagram of a solar cell contacted to the external load resistance (R_L)	67
Fig (3-11)	J-V characteristics of a solar cell showing the open circuit voltage V_{OC} , short circuit current J_{SC} and the maximum power point P_m	69
Fig (3-12)	Diagram illustrates the structure of four common types of perovskite solar cells: (a) mesoscopic <i>n-i-p</i> , (b) planar <i>n-i-p</i> , (c) planar <i>p-i-n</i> , and (d) mesoscopic <i>p-i-n</i>	71
Fig (3-13)	Schematic illustration of the operation principles of PSC, the numbers in the diagram indicate the edges of VB and CB for each layer	73
Fig (3-14)	A general chemical structure of an amino acid	74
Fig (3-15)	Peptide bond formation	76
Fig (3-16)	(a) Peptide backbone, C_α is a carbon atom bonded to the N-terminal (NH_3) and C-terminal ($-COOH$) of the peptide with rotation angles; ϕ and ψ , respectively., (b) Peptide secondary structures including hydrogen bonds: Parallel β -sheet and Anti-parallel β -sheet [82], (c) α helix structure	76
Fig (3-17)	Crystalline structures of titanium dioxide (a) anatase, (b) rutile, (c) brookite	79
Fig (3-18)	(A) Pure lattice, (B) interstitial defect, (C) O-vacancy, (D) Ti-vacancy, (E) Replacing O with a foreign atom, and (F) Replacing Ti with a foreign atom	80
Fig (3-19)	Schematic of the main components of a photoelectron spectrometer	82
Fig (3-20)	Working Principle of UV-vis spectrophotometry.	84
Fig (3-21)	Tauc plot from UV-Vis of $MAPbI_3$	85

Fig (3-22)	The major components of an SEM	86
Fig (3-23)	Schematic diagram of a fluorescence spectrometer.	87
Fig (3-24)	Schematic representation of photoluminescence (PL) spectra principle.	88
Fig (3-25)	Schematics of the time-resolved photoluminescence (TRPL)	89
Fig (3-26)	Diffraction of X-rays from the planes in a crystal (9). $a_1 = a_2 = d \sin \theta$	90
Fig (3-27)	(a) Solar simulator, (b) an electrometer (Keithley), (c) a square metal mask, (d) an NREL-certified reference silicon cell.	91
Fig (4-1)	Chemical structures of F8 peptide presented in a schematic antiparallel β -sheet conformation	95
Fig (4-2)	Schematic representation of the self-assembly and gelation pathway of β -sheet forming peptides	95
Fig (4-3)	FTIR spectra obtained for FEFKFEFK peptide dissolved in MAPI precursor solution. The strong absorption band at 1625 cm^{-1} and a weaker one at 1696 cm^{-1} indicates the formation of β -sheets in agreement with the work of Saiani et al	99
Fig (4-4)	Measured XRD pattern for prepared samples (Pure MAPI and MAPI-peptide) and calculated PXRD of MAPI	100
Fig (4-5)	XRD for MAPI and MAPI peptide mixture (different concentrations of peptide) thin films.	102
Fig (4-6)	Absorbance spectrum of MAPI thin film and MAPI peptide mixture thin films (different concentration).	103
Fig (4-7)	Photoluminescence spectra of MAPI thin film and MAPI peptide composite thin films at different concentrations	105
Fig (4-8)	Photoluminescence spectrum of MAPI thin film and MAPI peptide mixture thin films (different concentration).	106
Fig (4-9)	The relationship between the concentration of peptide and PL intensity.	106
Fig (4-10)	PL blinking mechanism and trap-assisted non-radiative recombination	106
Fig (4-11)	N 1s core spectra from pure MAPI and MAPI-peptide	107
Fig (4-12)	The TCSPC decay curves for Pure MAPI, Mix10 and Mix 40. The red line is the fitting decay data with a two-exponential decay function.	108
Fig (4-13)	The TCSPC decay curves for Pure MAPI and Mix 40. The red line is the fitting decay data with a mono-exponential decay function.	109
Fig (4-14)	SEM images for MAPI and MAPI peptide mixture (different concentrations of peptide) thin films.	110
Fig (4-15)	Photographs of MAPI film with and without peptide during exposure to water vapor over three weeks.	111
Fig (4-16)	XRD pattern of MAPI film (a) and MAPI peptide mixture (40 mg/ml) film (b) (fresh and after 82 hours exposure for water vapour).	112
Fig (4-17)	The XPS spectra of (a) Pb 4f, (b) I 3d and N 1s core levels from pure MAPI thin film at different temperatures (RT, 100 and 150 °C)	113

Fig (4-18)	The XPS spectra of (a) Pb4f, (b) I 3d and N 1s core level from MAPI-Peptide thin film at different temperatures (RT, 100 and 150 °C)	114
Fig (4-19)	(a) The ratio of metallic Pb in Pure MAPI and MAPI-Peptide thin films at different temperatures (RT, 100 and 150 C), (b) the relative ratio of I to Pb in Pure MAPI and MAPI-Peptide thin films at different temperatures (RT, 100 and 150 °C)	115
Fig (4-20):	Schematic illustration for perovskite solar cells fabricated.	116
Fig (4-21):	<i>J-V</i> curve of PSCs based on pure MAPI and MAPI-peptide.	116
Fig (4-22)	<i>J-V</i> curve of PSCs based on pure MAPI and MAPI-peptide with different concentrations (10, 20 and 40 mg/ mL).	117
Fig (4-23)	Measurements of PSC devices' efficiency that based on pure MAPI and MAPI-peptide for different periods during two weeks. The devices are kept in a 35% humidity environment.	118
Fig (5-1)	Chemical structures of peptide F9	121
Fig (5-2)	The FTIR spectrum of the FEFKFEKK peptide that is dissolved in the MAPI precursor solution.	123
Fig (5-3)	Measured XRD pattern for prepared samples (Pure MAPI and MAPI-peptide) and calculated PXRD of MAPI.	124
Fig (5-4)	XRD for MAPI and MAPI peptide mixture (different concentrations of peptide) thin films.	125
Fig (5-5)	Absorbance spectrum of MAPI thin film and MAPI peptide mixture thin films (different concentration).	128
Fig (5-6)	Photoluminescence spectrum of MAPI thin film and MAPI peptide mixture thin films (different concentration).	129
Fig (5-7)	The relationship between the concentration of peptide and PL intensity.	129
Fig (5-8)	N 1s core-level spectra from pure MAPI and MAPI-FEFKFEFKK	130
Fig (5-9)	The TCSPC decay curves for Pure MAPI, MixN0 and MixN40. The red line is the fitting decay data with a two-exponential decay function.	132
Fig (5-10)	The TCSPC decay curves for Pure MAPI and MixN40. The red line is the fitting decay data with a mono-exponential decay function.	132
Fig (5-11)	A: XRD for fresh pure MAPI and F9-MAPI thin films, B: Photographs of MAPI film with and without peptide during exposure to water vapour over 19 days, C: XRD for pure MAPI and F9-MAPI thin films after exposure to water vapour for 19 days.	136
Fig (5-12)	SEM images for MAPI and MAPI-F9 (concentration 40 mg/ml)	137
Fig (5-13)	The XPS spectra of (a) Pb4f, (b) I 3d and N 1s core level from pure MAPI thin film at different temperatures (RT, 100 and 150 °C)	138
Fig (5-14)	The XPS spectra of (a) Pb4f, (b) I 3d and N 1s core level from MAPI-FEFKFEFKK thin film at different temperatures (RT, 100 and 150 °C)	139

Fig (5-15)	(a) The ratio of metallic Pb in pure MAPI and MAPI-F9 thin films at different temperatures (RT, 100 and 150 C), (b) the relative ratio of I to Pb in Pure MAPI and MAPI-F9 thin films at different temperatures (RT, 100 and 150 °C)	139
Fig (5-16)	The ratio of metallic Pb in F8-MAPI and F9-MAPI thin films at different temperatures (RT, 100 and 150° C)	140
Fig (6-1)	Energy level diagram of the materials used as ETL, where Zero refers to the energy level of the vacuum, and the upper and lower numbers refer to the relative position of the conduction and valence bands, respectively, for each material	143
Fig (6-2)	4-Fluoroaniline molecule	145
Fig (6-3)	XPS survey spectra of fresh untreated TiO ₂	148
Fig (6-4)	C 1s spectrum from fresh untreated TiO ₂	149
Fig (6-5)	O 1s spectrum from fresh untreated TiO ₂	149
Fig (6-6)	Ti 2p (a), O 1s (b) and C 1s(c) spectra from untreated TiO ₂ – fresh, aged 35 days and aged 50 days.	150
Fig (6-7):	Relative atomic concentrations of C1s (a) and O1s (b) for Untreated TiO ₂ -Fresh, Aged 35 days and 50.	151
Fig (6-8)	(a) and (b): F 1s and N 1s spectra, respectively, from fresh treated samples; once, twice and four times, (c): Relative atomic concentrations of F1s from fresh treated TiO ₂ ; Once, Twice and Four times.	152
Fig (6-9)	C 1s spectra from fresh untreated -TiO ₂ and treated samples; once, twice and four times.	154
Fig (6-10)	Relative atomic concentrations of C 1s from fresh treated TiO ₂ ; Once, Twice and Four times.	155
Fig (6-11)	O 1s spectra from fresh untreated -TiO ₂ and treated samples; once, twice and four times.	156
Fig (6-12)	Relative atomic concentrations of O 1s from fresh treated TiO ₂ ; Once, Twice and Four times	157
Fig (6-13)	Relative atomic concentrations of C1s from fresh and aged untreated and treated TiO ₂ ; Once, Twice and Four times.	157
Fig (6-14)	Relative atomic concentrations of F1s from fresh and aged untreated and treated TiO ₂ ; Once, Twice and Four times. (Left for F-Ti and right for F-C)	158
Fig (6-15)	F 1s spectra from fresh treated and heated samples; (a) samples heated at 120 and 150 for 15 min (b) samples heated at 150 and 180 for 11 min.	159
Fig (6-16)	Relative atomic concentrations of F1s from fresh unheated and heated samples at different temperatures for different times.	160
Fig (6-17)	C 1s spectra from untreated samples and treated by heating; (a) samples heated at 120 and 150 for 15 min (b) samples heated at 150 and 180 for 11 min.	161
Fig (6-18)	Relative atomic concentrations of C1s from fresh samples; untreated sample, unheated and heated treated samples (different temperatures)	162

Fig (6-19)	Relative atomic concentrations of O1s from fresh samples; untreated sample, unheated and heated treated samples (different temperatures)	162
Fig (6-20)	Relative atomic concentrations of C1s from fresh and aged untreated and treated TiO ₂ ; different temperatures and heating times.	163
Fig (6-21)	Relative atomic concentrations of F1s from fresh and aged untreated and treated TiO ₂ ; different temperatures and heating times.	163
Fig (6-22)	F 1s spectra from fresh treated samples treated by exposing them to 4FA for one hour (M1) and four hours (M4).	164
Fig (6-23)	Relative atomic concentrations of F1s from fresh treated by immersing and cleaning by IPA (one time C) and exposing them to 4FA for one hour (M1) and four hours (M4).	164
Fig (6-24):	Relative atomic concentrations of C1s (a) and O1s (b) from fresh samples; untreated sample, treated by immersing and cleaning by IPA (one time C) and exposing them to 4FA for one hour (M1) and four hours (M4).	165
Fig (6-25)	Relative atomic concentrations of C1s from fresh and aged untreated and treated TiO ₂ by exposing it to 4FA for one hour (M1)	166
Fig (6-26)	Relative atomic concentrations of F1s from fresh and aged untreated and treated TiO ₂ by exposing it to 4FA for one hour (M1)	166
Fig (6-27):	The UV–vis transmittance spectra of untreated TiO ₂ and treated samples; (a) by immersing and cleaning (b) by exposing them to 4FA (c) by immersing and heating.	167

List of Tables

Table (3.1)	Amino acids and their properties.	78
Table 3.2	The seven crystal systems and fourteen Bravais lattices	88
Table (4-1)	The average size of crystals of un-templated and templated MAPI by mixing different concentrations of peptide.	101
Table (4-2)	Table (4-2): The experimental and theoretical bandgap of un-templated and templated MAPI by mixing different peptide concentrations.	104
Table (4-3)	The atomic ratios at the surface of the MAPI and MAPI-Peptide samples	107
Table (4-4):	Photoluminescent lifetimes for pure MAPI, Mix10 and Mix 40	109
Table (4-5):	The atomic ratios of <i>N 1s</i> to <i>Pb 4f</i> at the surface of the MAPI-Peptide sample	115
Table (4-6)	Photovoltaic parameters of PSCs based on pure MAPI and MAPI-peptide	117
Table (5-1)	The average size of crystals of un-templated and templated MAPI by mixing different concentrations of peptide.	125
Table (5-2):	The bandgap of un-templated and templated MAPI by mixing different peptide concentrations.	127
Table (5-3)	Photoluminescent lifetimes for pure MAPI, MixN20 and MixN40	132
Table (5-4)	Comparison of the effect of F8 and F9 on the properties (particle size, bandgap, PL intensity and lifetime PL) of fabricated MAPI.	133
Table (5-5)	The atomic ratios of <i>N 1s</i> to <i>Pb 4f</i> at the surface of the F8- MAPI and F9-MAPI samples	140
Table (6-1)	Types of samples treated based on temperature and heating time	147
Table (6-2):	The atomic ratio of F 1s, C 1s and N 1s to Ti at the surface of fresh treated and heated samples at 150 °C and 180 °C for 10 min.	160

List of abbreviations

Abbreviation	Expansion
4-FA	4-Fluoroaniline
AAO	Anodic aluminum oxide
ACN	Acetonitrile
AVT	Average visible transmittance
CB	Conduction band
CGC	Critical gelation concentration
CHA	Concentric hemispherical analyser
CVD	Chemical vapor deposition
DIO	Disordered inverse opal
DMF	N, N-dimethylformamide
DMSO	dimethyl sulfoxide
DSSC	Dye-sensitized solar cell
E_F	Fermi energy
E_g	Bandgap energy
EPBT	the annual ratio of consumption to generation
ETL	electron transport layer
F8	FEFKFEFK peptide
F9	FEFKFEFKK peptide
FA	Formamidinium
FAPbI ₃	Formamidinium lead iodide perovskite
FF	Fill factor
FTO	Fluorine doped tin oxide
GB	Grain boundary
GQDs	Graphene quantum dots
HAXPES	hard XPS
HFC	hydrofluorocarbons
HKUST-1	(Cu ₃ (BTC), BTC= 1,3,5-benzene tricarboxylate)
HOIP	Hybrid organic-inorganic perovskites
HOMO	Highest occupied molecular orbital
HTL	Hole transport layer
HTM	Hole transporting material
IPA	propan-2-ol, isopropyl alcohol
ITO	Indium-doped tin oxide
LD	Carrier diffusion length
Li-TFSI	Bis(trifluoromethane)sulfonimide lithium salt
LUMO	Lowest unoccupied molecular orbital
MA	Methylammonium
MACE	Metal-assisted chemical etching
MAI	Methylammonium iodide
MAPbI ₃	Methylammonium lead iodide perovskite, CH ₃ NH ₃ PbI ₃
MG	Microgels
MOF	Metal-organic framework
MS	Mesoporous silica
NAP-XPS	near ambient pressure X-ray photoelectron spectroscopy

NCs	Nanocrystals
NERL	National Renewable Energy Laboratory
NWs	Nanowires
PAMs	Porous alumina membranes
PbI ₂	Lead iodide
PCE	Power conversion efficiency
PDI	Perylene diimide derivative
PDMS	polydimethylsiloxane
PL	Photoluminescence
PNVF–NVEE	Poly(N-vinyl-formamide-co-2-(N-vinylformamido) ethyl ether)
PS	Polystyrene
PSCs	Perovskite solar cells
PVP	Poly (4-vinylpyridine
QD	Quantum dot
QWs	Quantum wires
SAPs	Self-assembling peptides
SEM	Scanning Electron Microscopy
Spiro-OMeTAD	2,2,7,7-tetrakis(N,N-p-dimethoxyphenylamino)- 9,90-spirobifluorene
TBP	4-tert-butyl pyridine
TCO	Transparent conductive oxide
TCSPC	Time-correlated, single-photon counting
TFE	Thin-film encapsulation
TiO ₂	Titanium dioxide
TRPL	Time-resolved photoluminescence lifetime
UHV	ultrahigh vacuum
UV	Ultraviolet
VB	Valence band
Vis	visible
V _{oc}	Open circuit voltage
XPS	X-ray Photoelectron spectroscopy
XRD	X-ray diffraction

Abstract

Organic-inorganic hybrid perovskites have gained significant attention due to their promising optical and electrical properties, particularly in photovoltaic solar cells. However, their stability under ambient conditions remains a considerable challenge. Numerous research articles have focused on various strategies to address this issue, including using mixed cations to enhance stability and modify optoelectronic properties. Encapsulation techniques have also been employed to protect perovskite solar cells from degradation caused by environmental factors. Another practical approach is the use of templates, which achieve both size control and enhanced stability since they contribute to the control of the size and shape of nanomaterials during synthesis by templating them inside the pores of materials. Various porous materials, such as mesoporous silica, microgels, polystyrene, metal-organic frameworks, and anodised aluminium oxide, can be utilised as templates for this purpose. Peptide gels can also be used as templates due to their ability to self-assemble and functionalise materials and act as a medium in the synthesis and construction of nanostructures. It is possible, then, that their network structures could be used to govern the growth of the perovskite, controlling the shape and size of the grains and also passivating defects in the perovskites. This study focused on the use of two peptide gels, specifically FEFKFEFK (F8) and FEFKFEFKK (F9), as templates for fabricating methylammonium lead iodide (MAPI) perovskite nanomaterials. Two chapters of the study explored the effects of these peptides on the size, optoelectronic properties, and stability of the fabricated MAPI perovskite-peptide “composites”. The results indicated that both F8 and F9 peptides contribute to control in the particle size of MAPI, leading to changes in its optoelectronic properties. The stability of the templated MAPI perovskite was also improved. The effect of templating increased with higher peptide concentrations, which resulted in increased fibre density and decreased network mesh size, ultimately influencing the properties of the fabricated MAPI. Notably, F9 exhibited higher solubility in the MAPI precursor, allowing for the addition of larger amounts, which further decreased the size of MAPI particles and led to a greater blue shift in photoluminescence (PL) spectra. Regarding solar cells, an optimal amount of F8 peptide was determined, and was found to improve the efficiency and stability of devices based on templated MAPI. However, exceeding this optimal amount resulted in a decrease in photocurrent, possibly due to the formation of an insulating layer that affected the transport of charge carriers to the transport layers.

In addition to peptide templating, the study also investigated the use of 4-fluoroaniline (4-FA) as a treatment agent to fluorinate TiO_2 surfaces and prevent or reduce carbon contamination. The results demonstrated that the fluorinated samples' surfaces exhibited increased resistance to adsorbing carbon species compared to the reference sample over the same period. However, the treatment efficiency decreased with prolonged exposure time, accompanied by fluorine loss from the surfaces, which requires further investigation.

Declaration

I declare that no portion of the work referred to in the thesis has been submitted in support of an application for another degree or qualification of this or any other university or other institute of learning.

Fahad Aljuaid



19 May 2023

Copyright Statements

1. The author of this thesis (including any appendices and/or schedules to this thesis) owns certain copyright or related rights in it (the “Copyright”) and he has given The University of Manchester certain rights to use such copyright, including for administrative purposes.
2. Copies of this thesis, either in full or in extracts and whether in hard or electronic copy, may be made only in accordance with the Copyright, Designs and Patents Act 1988 (as amended) and regulations issued under it or, where appropriate, in accordance with licensing agreements which the University has entered into. This page must form part of any such copies made.
3. The ownership of certain copyright, patents, designs, trademarks and other intellectual property (the “Intellectual Property”) and any reproductions of copyright works in the thesis, for example graphs and tables (“Reproductions”), which may be described in this thesis, may not be owned by the author and may be owned by third parties. Such Intellectual Property and Reproductions cannot and must not be made available for use without the prior written permission of the owner(s) of the relevant Intellectual Property and/or Reproductions.
4. Further information on the conditions under which disclosure, publication and commercialisation of this thesis, the Copyright and any Intellectual Property and/or Reproductions described in it may take place is available in the University IP Policy (see <http://documents.manchester.ac.uk/display.aspx?DocID=487>), in any relevant Thesis restriction declarations deposited in the University Library, The University Library’s regulations see (<http://www.manchester.ac.uk/library/aboutus/regulations>) and in The University’s Guidance for the Presentation of Thesis.

Fahad Aljuaid



19 May 2023

Acknowledgements

I would like to express my profound gratitude to my exceptional supervisor, Dr. Andrew Thomas, whose unwavering support has been invaluable throughout my PhD journey. His guidance and mentorship have played a pivotal role in shaping the success of my research. I am truly grateful for the outstanding guidance provided by Dr. Thomas, creating an environment conducive to my research endeavours. His patience, unwavering encouragement, and vast knowledge have been instrumental in my growth as a researcher and writer. I consider myself fortunate to have such an esteemed reference who has consistently provided invaluable insights and expertise. I also do not miss to express my heartfelt gratitude to my co-supervisor, Dr David Lewis, for their invaluable guidance, support, and expertise throughout my research journey.

Also, I take this opportunity to express my sincere thanks to Dr Ben Spencer for his help with the XPS measurements and Dr Janet Jacobs for her help and training me on the required types of equipment. Also, I am grateful to express my appreciation to my colleagues, with whom I have had the privilege of collaborating throughout my years of study. I would like to extend my thanks to Dr. Suresh Maniyarasu, Thomas Flavell, Dawei Zhao, and Kejian Hou for their valuable contributions in terms of sharing expertise, ideas, and experiences, and providing experimental support. Our collaborative efforts have been crucial in overcoming the challenges we encountered during our experiments. Furthermore, I am grateful for the strong bond of friendship we have developed, supporting each other not only in our scientific endeavours but also in our daily lives.

I would like to extend my sincere appreciation and gratitude to King Khalid University for awarding me the scholarship that has supported my academic journey. The financial assistance provided by the university has alleviated the financial burden and allowed me to fully dedicate myself to my studies and research. I am deeply grateful for the opportunity to pursue higher education and for the trust and confidence that King Khalid University has placed in me. This scholarship has not only enabled me to pursue my academic goals but has also enriched my overall learning experience. I am thankful for the resources, facilities, and educational environment that the university has provided, which have been instrumental in my intellectual and personal development. I am proud to be associated with King Khalid University, and I am honoured to have been a recipient of their scholarship program.

Finally, I would like to express my deepest gratitude to my family, especially my wife and children, for their standing by my side, unwavering support and endless patience throughout my academic journey. Their understanding, encouragement, and sacrifices have been the foundation of my success. Thank you from the bottom of my heart for being there for me every step of the way. I am grateful for the love and inspiration you bring into my life.

Publications and Conferences

Publications

Dawei Zhao, Tom A. Flavell, **Fahad Aljuaid**, Stephen Edmondson, Ben F. Spencer, Alex S. Walton, Andrew G. Thomas, and Wendy R. Flavell, **Elucidating the Mechanism of Self-Healing in Hydrogel-Lead Halide Perovskite Composites for Use in Photovoltaic Devices**, ACS applied materials & interfaces. <https://doi.org/10.1021/acsami.3c03359>.

Conferences

Fahad Aljuaid, Thomas Flavell, Alberto Saiani, Ben Spencer and Andrew Thomas, Investigation of using a peptide gel as a template in the fabrication of methylammonium lead iodide perovskite, Interdisciplinary Surface Science Conference (ISSC-23) (Poster), during April 19-21/2021.

Fahad Aljuaid: General introduction about templates, PGR Conference 2019 (Oral presentation)

Fahad Aljuaid: Investigation of using a peptide gel as a template in the fabrication of methylammonium lead iodide perovskite, PGR Conference 2021 (Poster)

Chapter 1

Introduction

1.1 Introduction

World energy consumption is still increasing, due to the continued rapid increase in world population and the development of industries that depend on energy. The main energy source used presently are derived from fossil fuel. This source has many problems, such as the fact that it is limited, and that it pollutes the environment because carbon dioxide, the final product of burned fossil fuel, is known to influence the Earth's climate significantly [1]. Because of this, the development of naturally available renewable energy is urgently required. Solar energy is one of the best options among these renewable energy sources, for several reasons: it is the most plentiful source, is available at low cost, and does not have any direct harmful impact on the ecosystem. The most prominent method for exploiting solar energy is photovoltaic technology, which depends in its principles on the photovoltaic effect, discovered in the 19th century by Becquerel [2]. Photovoltaic technology and the materials used have been developed continuously to improve the efficiency of conversion of sunlight to electrical energy and reduce costs. Based on the different principles of operation, device architecture and materials, solar cells can be grouped into 3 different generations:

First generation solar cells are the well-established silicon-based, photovoltaic cells that have traditionally, and still do, dominate the solar cells market. They are dominant due to their high efficiency which is typically close to 20%, but have a relatively high energy-payback time [3] and they suffer from their high manufacturing costs, although these are reducing significantly year on year [4].

Second generation cells, are known as thin-film solar cells, and are cheaper than first generation cells but have until recently had lower efficiencies, although some CIGS cells have been reported with lab efficiencies of ~ 23 %, which is comparable to polycrystalline Si solar cells [5]. The great advantage of second generation, thin-film solar cells, along with low cost[6], is that they can be coated onto flexible substrates. Thin-film technology has spurred lightweight, aesthetically pleasing solar innovations such as solar shingles and solar panels that can be rolled out onto a roof or other surface. These solar cells are operational and their efficiency could be around 20% but they are still facing difficulties in large-scale production due to the availability of the materials used, and toxicity of the heavy metals such as Cd which is used in them [3].

Third-generation solar cells are the cutting edge of solar technology. Still in the research phase, they have moved well beyond silicon-based cells. Generally, third-generation cells include solar cells that do not need the p-n junction found in traditional semiconductor, silicon-based

cells. This generation contains a wide range of potential solar innovations, including quantum dot solar cells, dye-sensitized solar cells, and multi-junction solar cells, as well as perovskite solar cells. The latter have shown remarkable improvements in efficiency as seen in the National Renewable Energy Laboratory (NREL) chart (Figure 1.1) that shows the highest confirmed conversion efficiencies for research cells for different photovoltaic technologies. It is clear that the cells based on organic lead halide perovskite solar harvesting materials have shown a remarkable rise in efficiency since their discovery in 2009, but their widespread commercialisation is hampered because their stability is poor [3].

The work in this thesis will focus on perovskite-based solar cells, with the aim of improving their efficiency and stability. This will involve a studying the effect of adding two different peptide gels to the perovskite, to determine whether the gels can control the particle size of the perovskite. In addition, we will look to determine the effects on the optoelectronic properties of these peptide/perovskite devices. Peptides are of interest since as biomolecules they could easily be produced by genetically modified organisms, which means that there is no need for synthesis of polymers from fossil fuel sources. In addition, the thesis will investigate the effect of fluoridation of the TiO₂ electron transport layer using a simple technique, on the adsorption of atmospheric hydrocarbons, which may affect charge transport at the perovskite-TiO₂ interface.

This thesis consists of 7 chapters organized as follows:

Chapter 1 is the introduction which presents the research background and the aim and structure of this thesis.

Chapter 2 is the literature review that is divided into two main parts:

Part 1: Overview of Perovskite solar cells (PSCs), including the attractive properties of perovskite materials and their problems, history and state of the art of PSCs and, finally, the main strategies used in the studies of improving perovskite materials.

Part 2: Overview of the electron transport layer, including the electron transport layer requirements, suitable materials and modifying the TiO₂-Based Electron transport layer by controlling the morphology, doping method and surface modification.

Chapter 3 covers the theory and techniques and contains the background theory of energy band structure and photovoltaic effect and the PSC's construction and architectures and,

principle of operation photovoltaic cells. It also gives an overview of the background theory of the materials and characterisation techniques used in the experiment work.

Chapters 4, 5 and 6 are the main contribution of this thesis, and each one contains an Introduction, experimental section, results and discussion and conclusion. These chapters cover the following topics:

Chapter 4: Investigation of using FEFKFEFK peptide gel as a template in fabricating methylammonium lead iodide perovskite.

Chapter 5: Investigation of using FEFKFEFKK peptide gel as a template in the fabrication of methylammonium lead iodide perovskite.

Chapter 6: Treatment of titanium dioxide by 4-Fluoroaniline (4-FA)

Finally, **Chapter 7** is the conclusion and future works.

Chapter 2

Literature review

2.1. Perovskite Solar Cells

Perovskite solar cells (PSCs) are solar cells based on using perovskite as the absorber material responsible for light absorption in the solar spectrum. This layer position is between the electron transport layer (ETL) and the hole transport layer (HTL) to extract charge carriers from perovskite after its excitation and transport them to the external circuit through the front and back electrodes for solar cells. Fig (2-1) shows the main components of typical perovskite solar cells that will be detailed in Chapter 3, Section (3.2.1).

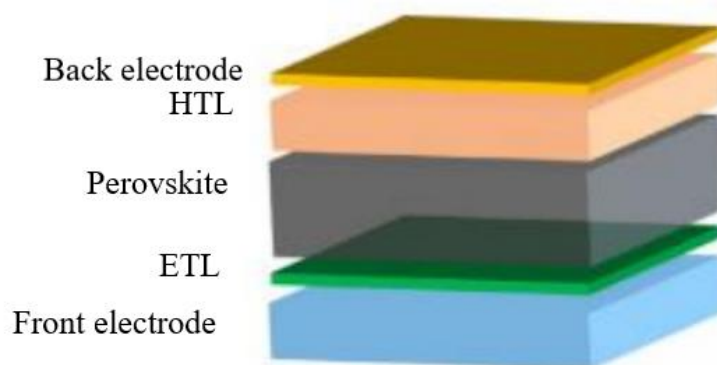


Fig (2-1): Schematic illustration for typical perovskite solar cells.

PSCs first appeared in 2009, when Miyasaka and co-workers used $\text{CH}_3\text{NH}_3\text{PbBr}_3$ and $\text{CH}_3\text{NH}_3\text{PbI}_3$ perovskites as alternative sensitizers for dye in the dye-sensitized solar cell (DSSC) that employed TiO_2 as an electron transport layer and an organic electrolyte solution containing lithium halide and a halogen as the hole transport layer. These cells achieved an efficiency of 3.13 and 3.28%, respectively [13]. In 2011, Park *et al.* improved the efficiency of these cells to 6.54% by optimizing the TiO_2 thickness and the precursor concentration of perovskite [14]. However, the cells were found to be unstable due to the dissolution and degradation of the perovskite in the liquid electrolyte, resulting in the replacement of a liquid electrolyte with a solid hole transporting material (HTM) in PSCs.

In 2012, Park, Grätzel and co-workers reported a solid-state perovskite solar cell in which they used 2,2,7,7-tetrakis(N,N-p-dimethoxyphenylamino)-9,9,0-spirobifluorene (spiro-OMeTAD) as the HTM, to give another improvement in the efficiency (9.7%) and stability (500 h) of the cell [15].

Since then, there has been an explosion in research activities focusing on PSCs, aiming to improve their performance and treatment of their problems with various strategies, including

compositional engineering, interface engineering and modification of the optoelectronic properties. As a result, PSCs have developed rapidly, and their efficiency has reached 25.7% in just 13 years [5]. In addition to this rapid development in the efficiency of PSCs, the preparation methods for the halide perovskites used in photovoltaic devices are simple and low-cost, and the raw materials are earth-abundant. PSCs have a short energy payback time: much shorter than others, as shown in Fig (2-2).

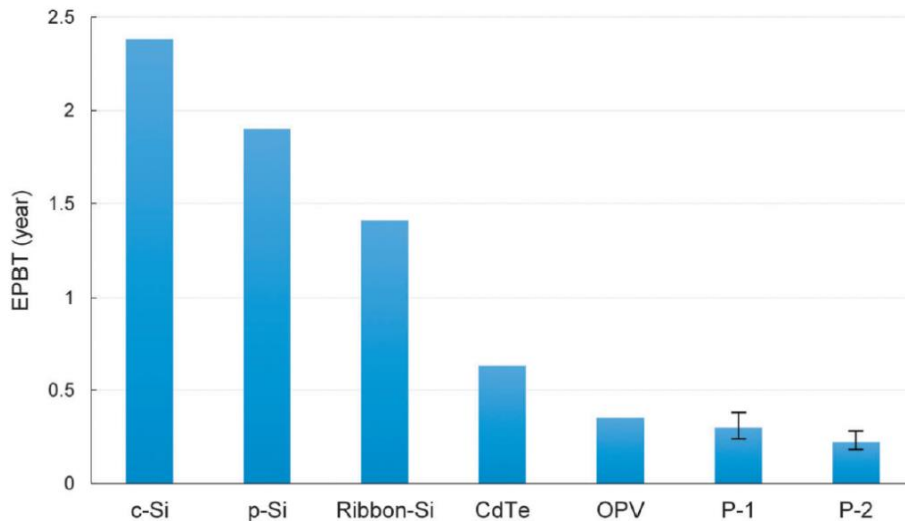


Fig (2-2): The energy payback time of PV modules. P-1 is PSC-based on TiO_2 , P-2 is PSC-based on ZnO . EPBT is the annual ratio of consumption to generation [3].

2.1.1. Perovskite Material

Organic-lead halide perovskites have attracted the attention of researchers since it was widely recognized in 2009 that they could be applied as an absorber layer in solar cells. The name perovskite originates from CaTiO_3 form that takes on a crystal structure containing corner-sharing TiO_6 octahedra in three dimensions, with Ca occupying the cuboctahedral cavity in each unit cell as shown in Fig (2-3). The general formula for CaTiO_3 would be ABX_3 where Ca is the A cation, Ti is the B cation and O is the anion. Varying the A, B and X ions allows many materials with the ABX_3 formula to be synthesised. They can also be obtained in several ways while maintaining the charge (q) balance ($q_A + q_B + 3q_X = 0$), in line with the formula ABX_3 . Therefore, they can be found as metal oxide perovskites, halide perovskites, oxy-nitride perovskites, oxy-halide perovskites or hybrid halide perovskites.

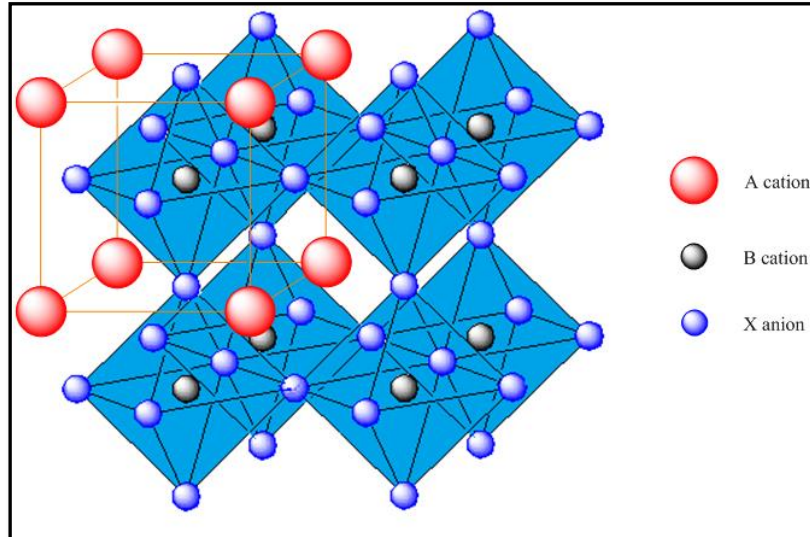


Fig (2-3): Crystal structure of perovskite ABX_3 [3]

Evaluating the perovskite formation and stability depends on the tolerance factor (t) and the octahedral factor. This tolerance factor (t) was proposed by Goldschmidt (1927) [7] and is given by the equation (2.1):

$$t = \frac{(r_A + r_X)}{\sqrt{2}(r_B + r_X)} \quad (2.1)$$

Where r_A , r_B and r_X are the ionic radii of the A , B and X ions, respectively. Generally, the value of the tolerance factor for the stability of perovskite structure is in the range of $0.81 < t < 1.11$ [8].

The octahedral factor (μ) is defined as the ratio of the radii of the small cation B to the anion X for octahedral BX_6 [7], it is given by:

$$\mu = \frac{r_B}{r_X} . \quad (2.2)$$

Where r_B and r_X are the ionic radii of the B and X atoms. The value of the octahedral factor (μ) for the stability of the halide perovskites ranges between 0.44 and 0.9.

From these factors, the ion combinations that generate stable halide perovskites can be selected from among several theoretically possible configurations [9] as shown in Fig (2-4).

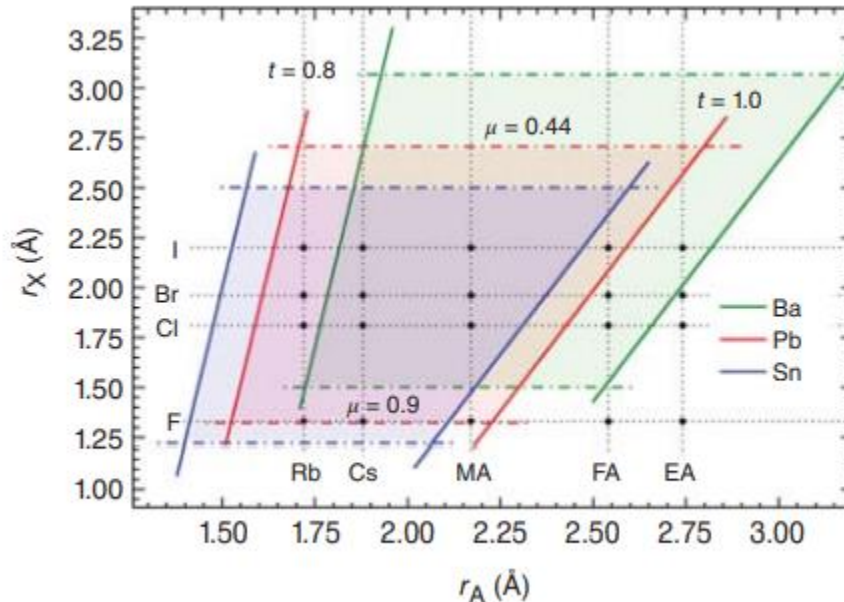


Fig (2-4): Illustration Map ($r_A - r_X$) for theoretically stable halide perovskites based on B-site cations Pb, Sn, and Ba. [9]

However, it's important to exercise caution when using a geometric approach to predict solid-state structures in hybrid halide perovskites due to several underlying assumptions that need to be questioned. Firstly, the organic cations are non-spherical, which makes it challenging to define the ionic radius for the A site using equation (2.1). Secondly, the low-temperature syntheses used to produce hybrid perovskites can result in the kinetic trapping of less thermodynamically stable structures. Thirdly, the lower electronegativity and greater chemical softness of heavier halides, particularly the iodide anion, compared to oxides and fluorides, means that the assumption that ions are unpolarizable hard spheres is less valid [10].

Perovskite materials have many properties that have attracted researchers to study their use in several electronic applications. These include the simple manufacturing processes and optoelectronic properties such as a high absorption coefficient, tuneable optical band gap and long charge carrier diffusion length (LD).

The absorption coefficient is an optical constant that indicates the capacity of the material to absorb light. Halide perovskites have very high absorption coefficients in the visible spectrum, as shown in Fig (2-5), making them an excellent candidate for use as absorber layers in solar cells [11].

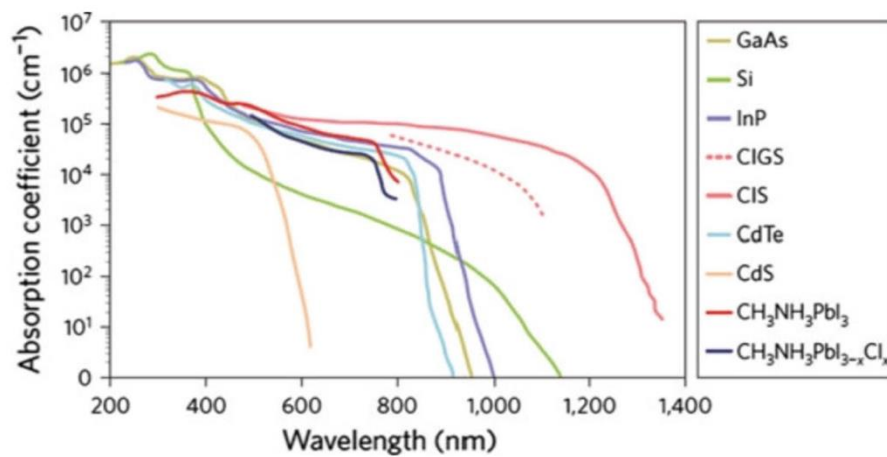


Fig (2-5): A comparison of absorption coefficients of halide perovskites with those of silicon and most thin films solar cells [11].

The tunability of the optical bandgap of perovskite materials via compositional engineering is another property of halide perovskites which makes them of interest in optoelectronic applications. Changing the elements that correspond to the A, B, and X site ions leads to a

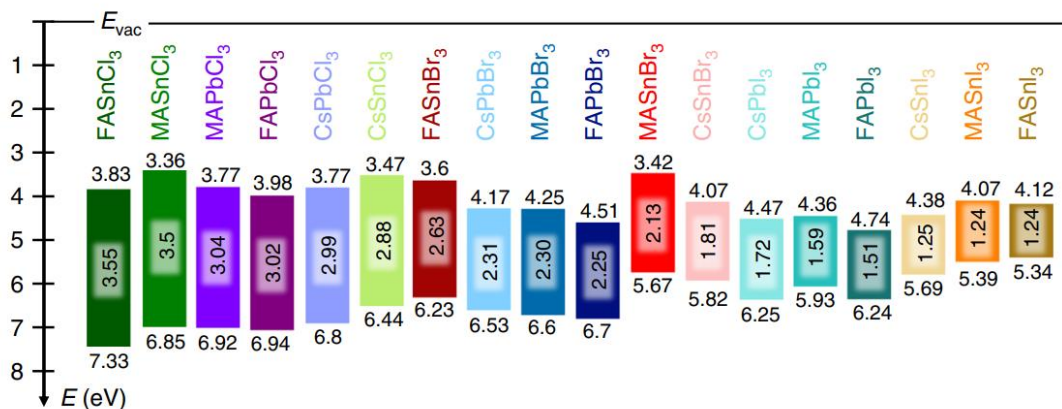


Fig (2-6): Schematic energy level diagram of different perovskites based on different chemical compositions [12]. The coloured blocks represent the bandgap and the numbers at the top and bottom of the blocks are the conduction band and valence band energies relative to the vacuum level, respectively.

corresponding change in the band gap of perovskites over a range from 1.24 to 3.55 eV, as shown in Fig (2-6). This wide range of bandgaps for perovskite materials has made them appropriate for a wide variety of applications [12].

The carrier diffusion length (LD) is a crucial parameter for materials used in solar cells. LD determines the path length that the charge carriers can travel before recombining; based on this, a suitable film thickness is selected, which should be shorter than LD. Halide perovskites demonstrate a considerable diffusion length, ranging from around 100 nm for pure iodide-based perovskite to 1100 nm for mixed halide perovskite. Due to this long carrier diffusion length, and the high absorption coefficient they are promising to use in solar cells as absorber layers using relatively thick layers, leading to higher absorption and, thus, higher currents [11].

Along with the above advantages, perovskite films have high electron mobility: as high as ~60–100 cm² V⁻¹ s⁻¹ [11], which means the use of perovskite in photovoltaic applications to obtain low-cost and high-efficiency solar cells has great potential.

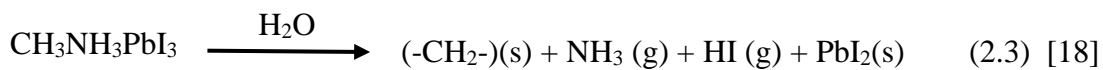
2.1.2. Problems of PSCs

2.1.2.1. Stability

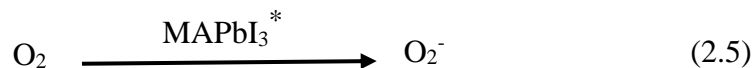
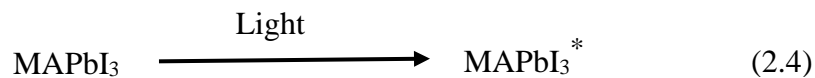
Solar modules, typically installed on the rooftops of buildings, must be resistant to moisture, heat, and light for an extended period. Despite the high efficiency of PSCs, their stability is one of the biggest challenges that prevents their practical application. The main reason for this issue is that perovskite materials are chemically vulnerable to water, superoxide molecules, and high-intensity visible light and UV light, resulting in degradation of perovskite and then damage to devices based on them. The following paragraphs will summarise the critical factors that affect perovskite stability.

The degradation of perovskite in humid environments is a challenging issue due to the hydrophilic nature of amine salts. Tenuta *et al.* reported that the high solubility in water of methylammonium iodide (MAI) contributes to its decomposition. It has been found that MAPI completely degrades after 18h when exposed to air at 35 °C at a humidity of 60% [16]. According to Aurelien *et al.*, the decomposition mechanism is that hydration of MAPI converts it to the monohydrate (CH₃NH₃PbI₃·H₂O) and dihydrate perovskite (CH₃NH₃)₄PbI₆·2H₂O phases. These reactions are reversible, so that MAPI perovskite can “self-heal” if exposed to a dry atmosphere subsequently, but continuous exposure to water vapour results in the

irreversible decomposition of perovskite into PbI_2 and other gaseous chemicals [17] as shown in equation (2.3). Ke *et al.* confirmed this irreversible process in MAPI using near ambient pressure X-ray photoelectron spectroscopy (NAP-XPS). MAPI films were exposed to 9 mbar of water vapour, and it was observed that only PbI_2 and hydrocarbon species survived, while the surface nitrogen was completely lost [18]. According to F. Tian *et al.*, grain boundary (GB) defects facilitate water diffusion along the GB as well as from the GB to the bulk of the MAPI grain, which leads to its degradation. Consequently, increasing the grain size and improving the crystallinity of MAPI are successful methods for improving the stability of perovskites in humid settings [19].

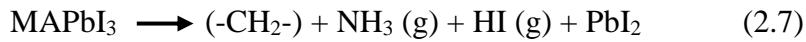


Oxygen is also a degradation factor for perovskite materials in the presence of light or heat. Haque *et al.* reported that exposure of the MAPI thin film to light and oxygen for 48 hours causes a significant blue shift in the absorption onset from 780 nm to 520 nm and a dramatic change in colour from dark brown to yellow. These observations appeared consistent with the breakdown of the perovskite crystal and the subsequent presence of PbI_2 in the final degraded films. The reaction mechanism suggested from these results is that molecular oxygen diffuses into the bulk MAPI through iodine vacancies that can be generated rapidly upon photoexcitation of MAPI. Once oxygen molecules are adsorbed, they act as electron traps, resulting in charged superoxide, which can react with the organic cation and deprotonate it [20]. The mechanism of this degradation is shown in the following equations (2.4), (2.5), and (2.6) [20]:



The thermal stability of solar cells over the long term is essential to meet industry standards, but the stability of perovskite films is still a problem. Some studies reported that heating MAPI at temperatures of 120 -140 °C in vacuum or dry air forms PbI_2 within 30 min, indicating

sublimation of the organic and halide components, although the temperatures are below the sublimation temperatures of organic and halide species[21]. Conings *et al.* reported that heating the MAPI films at 85 °C resulted in the formation of PbI₂ within 24 hours[22]. The proposed mechanism of decomposition is shown in the equation (2.7) [23]:



According to Qiny Bao *et al.*, this thermal deterioration could develop successively, layer by layer, from the film surface into the bulk (Fig (2-7)), because the surface of the solution-processed perovskite film is less stable due to electronic defects created from under-coordinated lead and iodide ions [23].

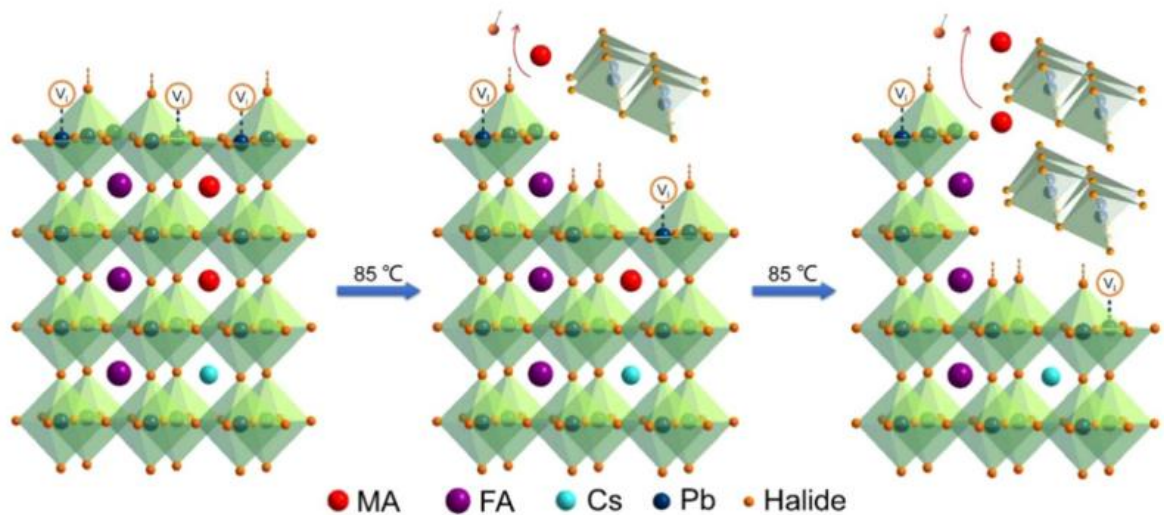


Fig (2-7): Illustration of the suggested layer-by-layer decomposition of perovskite during 85 °C annealing [23].

In addition, because of the significant differences in the thermal expansion coefficient of the components of PSCs, and phase changes within the operating condition (54 °C from tetragonal to cubic for MAPbI₃), day-to-night temperature cycling can induce mechanical stress in the perovskite module, which can result in long-term damage [24].

Also, light illumination plays a key role in hybrid perovskite degradation. It has a crucial role in creating defects and vacancies that permits oxygen to diffuse into bulk perovskite, which results in its degradation, as mentioned above. The internal charge creation and relocation caused by light result in random local charge currents limited only by defects, charge traps, and

grain boundaries in the perovskite film. The random ion movement leads to the development of CH_3NH_2 and HI degradation products and can then be eliminated at all exposed surfaces, including the top surface and grain boundary surfaces. On the other hand, applying an electric field transversely can contribute to directing ion migration through the perovskite film that results in self-doping to form p–n junctions and changing the chemical composition.

UV light is a common extrinsic degradation factor for perovskite solar systems. Perovskite device structures often employ metal oxides as electron transport layers (ETL). TiO_2 is commonly used and has high efficiency in this function. However, TiO_2 acts as a photocatalyst to oxidise organic materials. Therefore, exposure of perovskite to UV light in the presence of TiO_2 leads to degradation due to the oxidation of iodide ions, which then causes degradation of methylamine. So, modifying TiO_2 or using other alternative less photoactive materials, such as Al_2O_3 or SnO_2 , have been studied and introduced as solutions to this issue [25].

In general, the stability of perovskites and increasing their resistance to these factors are the focus of the attention of researchers as there are many studies with various strategies to solve this issue.

2.1.2.2. Toxicity

Despite Pb- based perovskite's attractive applications in optoelectronic devices, the toxicity of Pb^{2+} may cause environmental issues during production, use, and disposal, which is regarded as another obstacle to their practical application. This has led to researchers to try to replace Pb with other environmentally friendly, less toxic elements, such as Ge^{2+} , Sn^{2+} , Bi^{3+} and Sb^{3+} . These elements have an outer-shell s-orbital (similar to Pb^{2+}), which is crucial to the photovoltaic properties of perovskite materials [26]. However, to date, there are some restrictions for the application of lead-free perovskite due to the undesirable properties of these elements, such as the easy oxidation of Sn^{2+} to Sn^{4+} . Fig (2-8) shows Pb-based and Pb-free perovskite materials for applications as optoelectronic and thermoelectric applications. For this, the studies in this field aim to improve their performance and treatment of their problems with various strategies, including additive engineering, mixed perovskite and double perovskites [26].

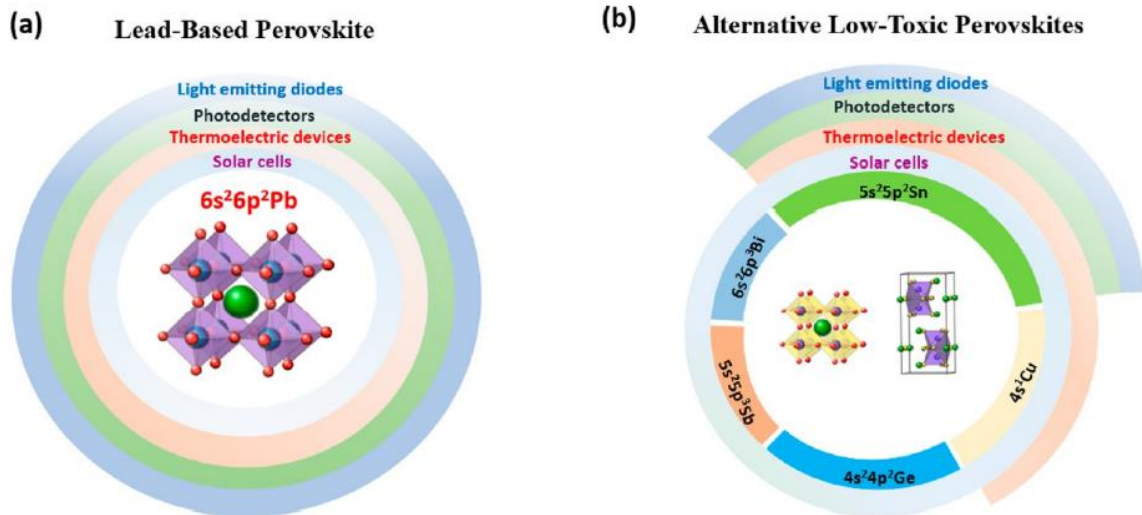


Fig (2-8): Optoelectronic and Thermoelectric Applications of (a) Lead-Based Perovskite Materials and (b) Low-Toxicity Perovskite Materials [26].

2.1.3. Review of the main strategies used in the studies of improving perovskite materials

This section will review the research that studied perovskite, aiming to improve its performance as an absorber layer in PSCs and increase its stability. The review will be divided based on the strategies used.

2.1.3.1. Multiple-Cation Perovskites

Goldschmidt's tolerance factor predicts the production of an intrinsically stable perovskite structure, permitting the flexibility of components in the ABX_3 framework if $0.9 \leq t \leq 1$ is met. The chemical processing of multiple-cation perovskites is a crucial method for overcoming phase instability and thermal instability. The A-site represents a template for perovskite, where its structure depends on the A-cation shape, size, and charge distribution. The deliberate alloying of several cations at the A-site of the ABX_3 perovskite could increase the stability of the typically sensitive $MAPbI_3$ perovskite towards phase transition and moisture [27].

Pellet *et al.* investigated the mixing of formamidinium (FA) and methylammonium (MA) cations in 3D hybrid perovskites to broaden the absorption spectrum and reduce the band gap. Combining A-site cation mixing with successive deposition, yielded phase-pure double-cation black perovskite [28]. Zhang *et al.* reported that increasing the amount of FA^+ into $MAPbI_3$

increased PL lifetimes due to improved crystallinity, which leads to a decrease in trap states and an increase in carrier-diffusion length. They noted that the positions of XRD peaks of perovskite moved to lower 2θ values as the FA^+ concentration increased (Fig (2-9)), indicating the transition of the crystal lattice to a cubic or quasi-cubic crystal phase. On the other hand, adding a small amount of MA enhanced the stability of FAPbI_3 [29]. According to Binek *et al.*, the incorporation of 15% of MA cations is adequate to stabilise the trigonal structure (α phase) of FAPbI_3 at low temperatures (Fig (2-10a)). They attributed this behaviour to the dipole moment of MA, which strengthens the hydrogen bonding to the inorganic Pb–I cage. In addition, as a result of enhanced Coulomb interactions between the high dipole moment and Pb–I octahedra, improved stability is achieved (Fig (2.-10b)) [30].

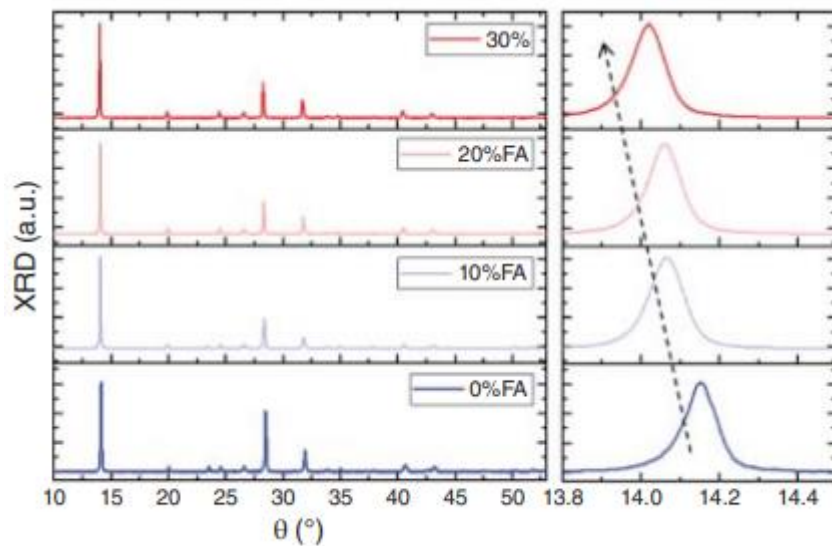


Fig (2-9): X-ray diffraction patterns of $\text{FA}_x\text{MA}_{(1-x)}\text{PbI}_3$ thin films with different concentrations of FA, showing a decrease in 2θ (110 plane) [29].

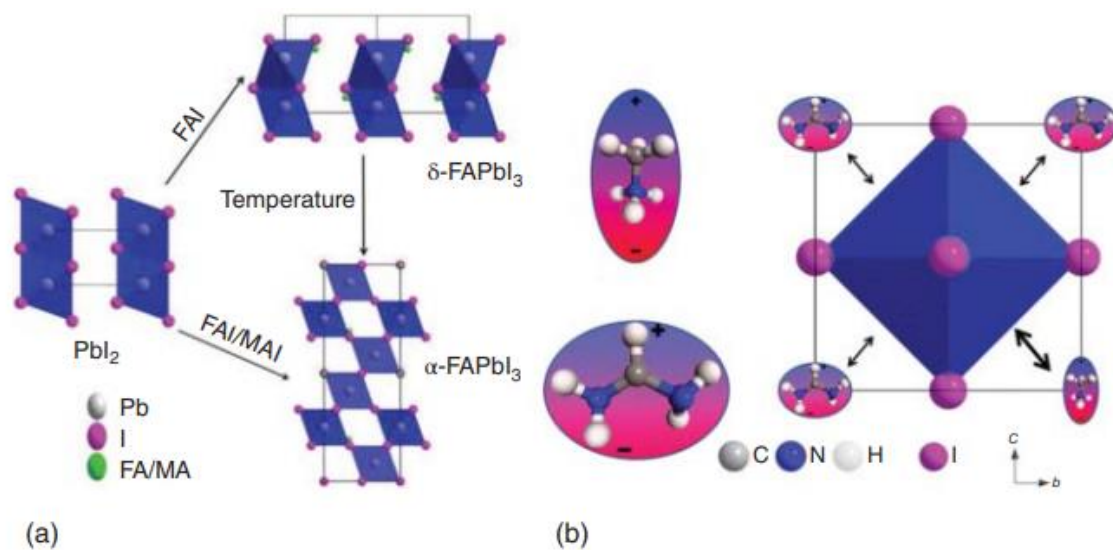


Fig (2-10): Scheme for (a) pure FAPI (non-stabilised hexagonal structure- δ phase) and FA/MA-based FAPI structural phase transitions (stabilised trigonal structure- α phase) (b) Optimised structure model of MA-stabilized FAPI [30].

A-site cation engineering allows the incorporation of further cations within the range of the Goldschmidt tolerance factor that could help solve perovskite problems. This has led to attempts to stabilize MAPbI_3 and FAPbI_3 by incorporating inorganic alternatives such as caesium (Cs) and rubidium (Rb), which gave positive results. Niu and co-workers found the performance and thermal stability of an unencapsulated device based on $\text{Cs}_x\text{MA}_{1-x}\text{PbI}_3$ ($x=0.9$) improved compared to MAPI [31]. Park *et al.* found incorporating a small amount of Rubidium (Rb) (0.05) into FAPbI_3 increased PL lifetime, resulting in an enhancement of PCE from 13.56% (FAPbI_3) to 17.16% [32].

Saliba *et al.* studied the inclusion of Cs^+ in FA/MA perovskite. They found increase in the stability of the black cubic phase at room temperature without any impurities of the photoinactive phase of FAPbI_3 . The smaller radius of Cs^+ (1.81 \AA) contributed to reducing the influential tolerance factor and achieved a cubic or pseudo-cubic perovskite structure [33]. In general, there are numerous studies carried out in this field that confirm the effectiveness of this strategy. Their results are summarised in the schematic in Fig (2-11), which depicts the configurational complexity achievable in multiple-cation perovskites, which has resulted in enhanced performance [27].

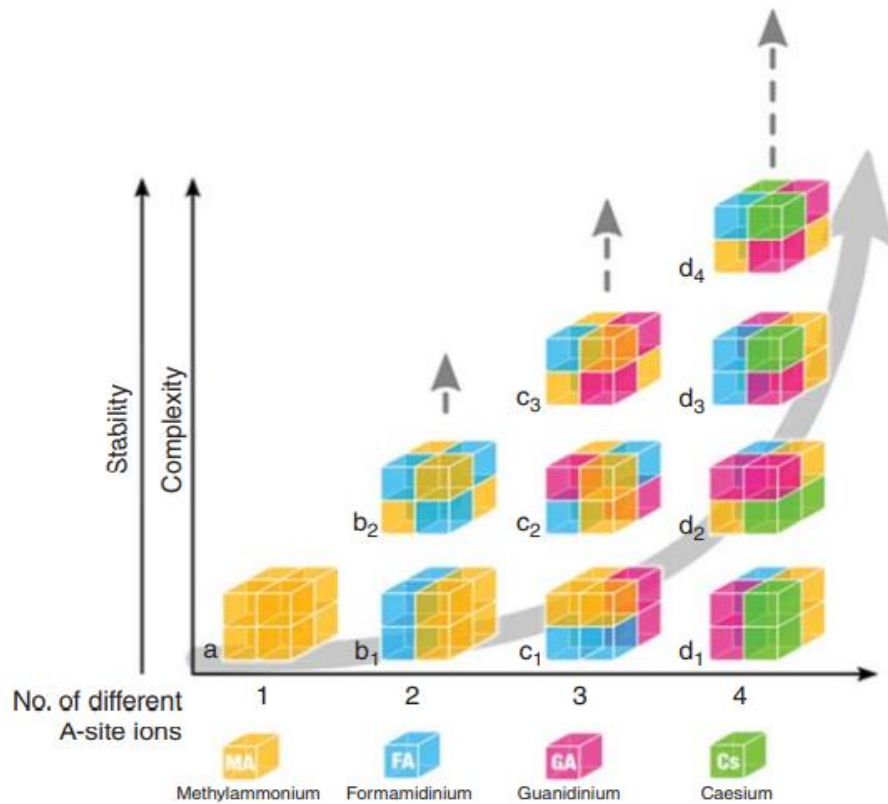


Fig (2-11): Scheme for structural complexity of organic-inorganic hybrid perovskites and the related improvements in stability [27].

2.1.3.2. Passivation Strategy

Perovskite passivation is a research technique that aims to enhance PSCs performance by suppressing the intrinsic and extrinsic defects of perovskite. The schematic in Fig (2-12) summarises the different types of these defects. The effects of defects extend from limiting solar cell efficiency to contributing to perovskite decomposition, making their passivation important [27].

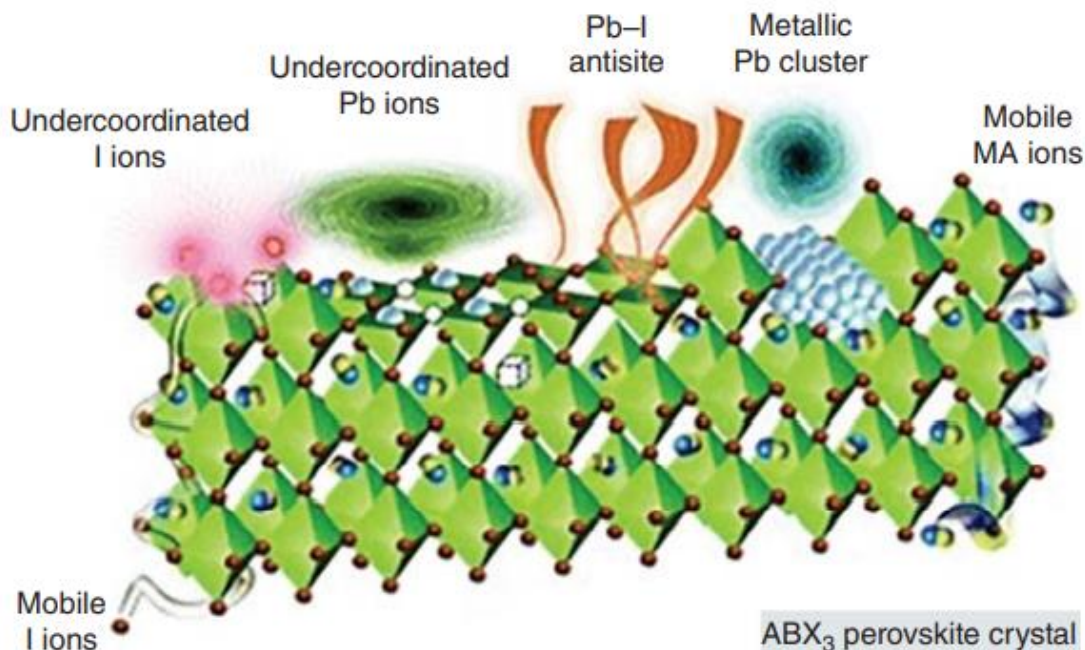


Fig (2-12): Schematic diagram showing various types of defects in organic lead halide perovskite that could act as traps assisted non-radiative recombination or cause perovskite decomposition. [27].

Passivation can target the bulk perovskite or its surface depending on the methods of processing applied. Bulk passivation is achieved by including suitable materials directly into the perovskite, whether by adding them together in the precursor solution or the anti-solvent that is dropped during thin film deposition. This leads to incorporating the passivating agents within the perovskite layer [27]. Niu *et al.* introduced semiconducting molecules via Lewis acid or base functional groups ((PCBM, ITIC, DTS and DR3T) into MAPI through an antisolvent drip approach. They found that the devices based on passivated MAPI exhibit drastically improved thermal stability and high efficiency as a result of passivating of defects at grain boundaries within the bulk film [34].

Passivation of the perovskite surface can be carried out as a post-treatment, after the deposition of perovskite films. It effectively improves the performance of PSCs by suppressing the surface defects, which could lead to electron-hole recombination at the interfaces [27]. Wang *et al.* reported that the antisite defects generated from Pb on the perovskite surface are more noticeable. These can be successfully passivated using molecules containing N—H and C=O groups [35]. Chaudhary *et al.* deposited a thin layer of hydrophobic polymer (poly (4-vinylpyridine) (PVP)) over MAPI film by spin coating and then heating at 70 °C for 20 min.

They found that the pyridine Lewis base side chains of PVP passivated the under-coordinated Pb which act as surface-trap states, reducing the non-radiative recombination, which increases photoluminescence (PL) intensity. It was also found that the efficiency and stability of devices based on MAPI/PVP improved compared to the control sample [36].

In general, numerous studies using passivation techniques have been studied, using a wide-range of materials as passivating agents, including organic acids, amines, organosulfur, graphene, metal oxides, metal halides, organic halides, zwitterions, quantum dots and polymers. The results of these studies show the beneficial effect of passivation in controlling crystal growth, passivating grain boundaries, and suppressing various traps that lead to improved stability and performance of perovskite solar cells [27]. One of the motivations in this work in using peptide gels is that they too contain amines, but as biomolecules they can be produced sustainably from genetically modified organisms.

2.1.3.3. The Encapsulation Strategy

The encapsulation of PSCs has been employed to avoid the leakage of lead and prevent the degradation of the device due to environmental factors such as moisture, oxygen, and heat. The stability of PSCs has been improved effectively upon encapsulation, where the encapsulated devices maintained over 80% of the initial power conversion efficiency (PCE) under different tests, including damp heat (85 °C / 85 % RH), 200 times temperature cycling test (40 °C to 85 °C) and 1000 hours maximum power point output test [37].

The encapsulation used to improve PSC stability can be divided into external and internal encapsulation. External encapsulation is the prevalent method to address the problem of oxygen and moisture infiltration. It can be achieved using UV-curable adhesive or glass–glass vacuum laminated encapsulation[37]. Dong *et al.* showed that the encapsulation of devices with UV-curable polymers improved the device stability, leading to the retention of 85% of their original PCE under continuous illumination at 85 °C and 65% RH for 144 hours. Bush *et al.* found that devices encapsulated by the vacuum laminated encapsulation method have a high photostability and thermal cycling stability [38].

Internal encapsulation is used to address the intrinsic instability issues in PSCs, such as thermal degradation, ion migration and hygroscopicity. Techniques for internal encapsulation include surface encapsulation, interface encapsulation, grain boundary encapsulation, and hydrophobic thin films, all of which further improve the stability concerning moisture and oxygen, photostability, and thermal stability [37]. Lee *et al.* studied the encapsulation of devices with

the thin-film encapsulation (TFE) system composed of a multilayer stack of organic/inorganic layers. They used a pair of Al_2O_3 inorganic and pV3D3 organic layers and found the encapsulated devices maintained 97% of their initial efficiency after exposure to 50 °C and 50 % RH for 300 hours [39]. Liu *et al.* reported that encapsulation of perovskite ($\text{FA}_{0.85}\text{Cs}_{0.15}\text{PbI}_3$) grain boundaries by amorphous silica slowed down the transition from α -phase to δ -phase and thus improved the thermodynamic stability of these materials [40]. Lin *et al.* reported that the reaction of n-butylamine (BA) with the surface of 3D perovskites leads to the construction of 2D perovskite $(\text{BA})_2\text{PbI}_4$ layers at the grain boundary or on the surface of MAPI could improve the thermodynamic stability [41].

Suitable encapsulation materials are selected based on their protection of PSCs against environmental factors and to meet the requirements for different operation conditions. To achieve that, the parameters that can be considered for encapsulation materials are hydrophobicity, UV resistance, chemical inertness, degree of crosslinking, dielectric breakdown and transition rate with regards to temperature, oxygen and water vapour [37].

In general, the encapsulation strategy is a promising research field to find new materials and technologies that satisfy the protection requirements of PSCs that make them reliable and stable.

2.1.3.4. Template strategy

Synthesis using a nanostructured template is one of the best ways to get high levels of synthetic control, which typically results in nanomaterials with well-defined sizes, shapes and structures due to the influence of the templates. The template method could be served by any material with nanostructured characteristics, natural (nano minerals, biological molecules, etc.) or synthesised materials (surface active agents, porous materials and nanoparticles, etc.) [42].

Based on the properties of these materials, the templates can be divided into soft and hard templates. The soft template is thought to lead to the aggregation of nanoparticles, forming specific structures with certain shapes and sizes by intermolecular or intramolecular interaction forces such as hydrogen bonding, chemical bonding and static electricity. Surfactants, biopolymers and polymers are good examples of soft templates. The hard template is a stiff substance whose stable structure directly controls the templated particles' size and morphology due to restricting them inside template pores. There is a wide range of hard templates such as porous anodic aluminum oxide (AAO), porous membrane and plastic foam[43].

Template techniques offer an opportunity to synthesise perovskite nanomaterials with well-controlled size, shape and stability. The formation of patterned perovskites using rigid or flexible templates has also been studied [44]. Wang *et al.* put three silicon moulds, flat, nanopillar and nanograting, into spin-coated perovskite thin films, resulting in fabrication of highly crystalline patterned structures as shown in Fig (2-13) [45]. Following their work, similar techniques were used to manufacture metasurfaces using different surface-modifying agents, such as polydimethylsiloxane (PDMS) and anodised aluminium oxide (AAO) [44].

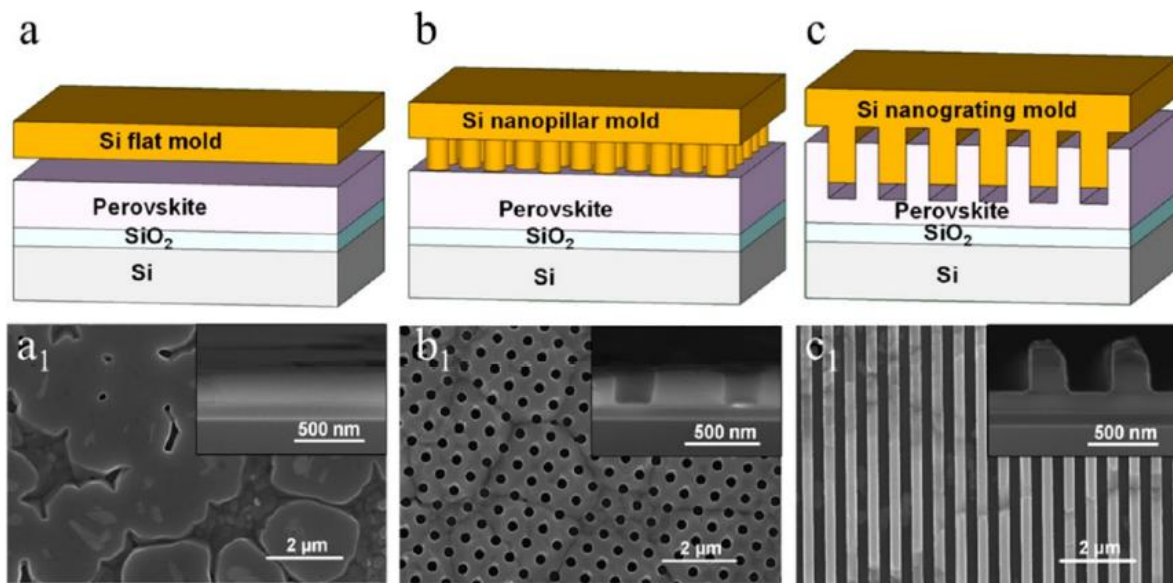


Fig (2-13): Schematic of patterning of perovskite thin films by different templates [44]

For the formation of perovskite nanocrystals (NCs)/microcrystals, a variety of templates can be used. The template type employed determines the resulting crystal dimensions, size, shape, and morphology and could improve their stability [46]. In this aspect, the template-based synthesis method is advantageous, as the desired size and shape of the NCs can be achieved by employing suitable templates. There are various porous materials that can serve as templates for these purposes, such as mesoporous silica (MS), metal-organic framework (MOF), polystyrene (PS) and anodized aluminium oxide (AAO) [46].

MS has attracted considerable interest as a template due to its desirable features, which include a high surface area, a large pore volume, and the capacity to modify its surface. Malgras *et al.* used KIT-6 MS with various pores sizes (5.1 nm- 11.9 nm) as templates for synthesising MAPbX_3 ($X=\text{Br}, \text{I}$). They found that the resulting perovskite particles had dimensions similar to the pore sizes of the templates. Also, they observed a gradual blue shift in the PL when the

pore size was reduced from 11.9 nm to 5.1 nm, which could be attributed to the quantum confinement effect [47]. Ghosh et al. reported that the porous Si nanowires (NWs) could be served as nucleation sites for the growth of QD perovskite. They studied the synthesis of MAPI by spin coating of its precursor solution on MS NWs' surface prepared on Si wafers using the metal-assisted chemical etching (MACE) method at room temperature. Their findings indicated the growth of crystalline perovskite highly with an average particle size between 20 and 35 nm. High-intensity, blue shifted PL was observed in the smaller particles and attributed to the quantum confinement effect [48]. According to Hu et al., MS templates are also suitable for double perovskite, where they used three MS templates, KIT-6, SBA-15 and MCM-41, for the growth of $\text{Cs}_2\text{AgBiBr}_6$ NCs with various band gaps of the NCs depending on pore sizes of the template used [49]. Regarding the stability of perovskite, Yu *et al.* introduced a route that protected perovskite against water beside the formation of QD, where they found dual mesoporous superhydrophobic silica with gold nanocore can be served as template assistance for this purpose because they have hydrophobic functional groups and rough structures [50].

AAO templates are used to prepare 1D perovskite NWs due to their advantageous characteristics, including highly ordered pore structures, adjustable pore shape, and a sizable surface area [46]. Tavakoli *et al.* reported that $\text{MAPbI}_3/\text{MASnI}_3$ NWs grown utilising the AAO template exhibited improved stability and controllability in their diameter and height [51]. Zhang *et al.* used porous alumina membranes (PAMs) with various diameters pores (from 5.7 to 200 nm) as templates to synthesise MAPI. They found a gradual shift in the absorption edge and the photoluminescence (PL) spectra of the array of as-prepared MAPbI_3 quantum wires (QWs) with a change in the pore diameter of the PAMs as shown in Fig (2-14), indicating an increase in the bandgap caused by the quantum confinement effect. Moreover, the higher PL quantum yield is observed for the smaller diameter QWs, attributing to increased radiative recombination and the high surface-to-volume ratio. Also, they found improvement in the stability of MAPI QWs due to templating them inside PAMs, resulting in their encapsulation of them [52].

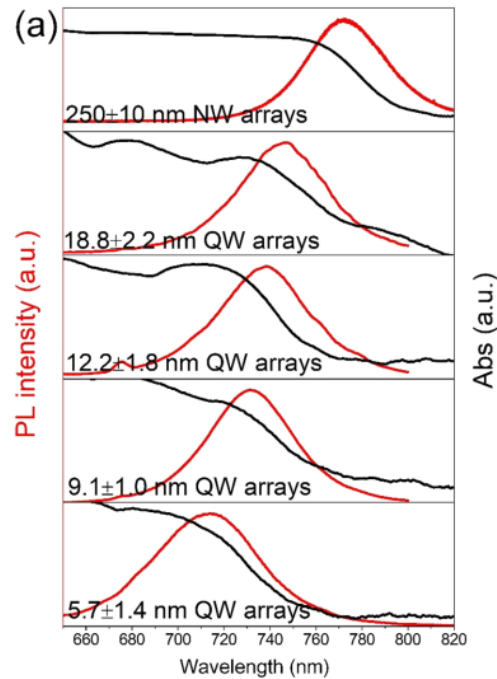


Fig (2-14): The absorption (Black) and PL (Red) spectra of templated MAPI in PAMs with different diameters pores. [52]

MOFs are crystalline porous organic-inorganic hybrid materials with a remarkably high interior surface area. They have a variety of distinctive qualities, such as structural variety, controllable pore diameters, and adaptable functions [46]. Rambabu *et al.* synthesised MAPbBr₃ QD using MOF MA-M (HCOO)₃ (M = Mn and Co). The blue shift in PL spectra for the templated

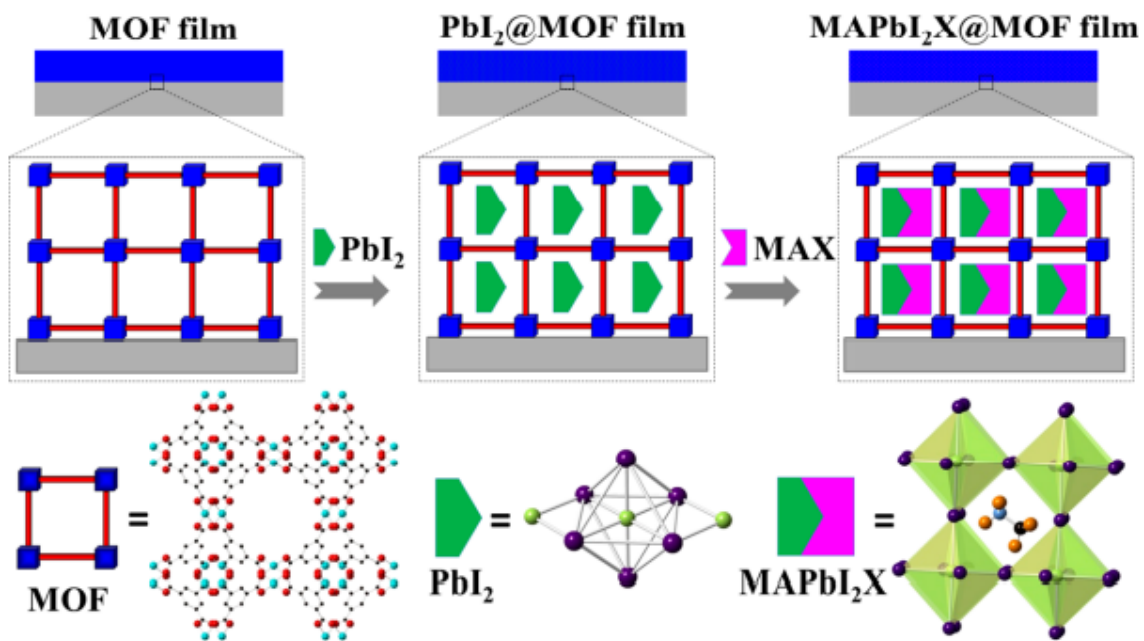


Fig (2-15): Schematic Illustration for steps of loading MAPbI₂X into MOF pores [53].

samples compared to bulk perovskite is evidence of the quantum confinement effect and formation of MAPbBr₃ QD by this approach. Also, the stability of MAPbBr₃ QD@MA-Mn(HCOO)₃ was improved [53]. Z Chen *et al.* used MOF HKUST-1 (Cu₃(BTC), BTC= 1,3,5-benzene tricarboxylate) to fabricate MAPbI₂X (X = Cl, Br, and I) perovskite QD. They loaded the perovskite into the MOF in two steps as shown in Fig (2-15); immersing the HKUST-1 thin film in PbI₂ solution to load PbI₂ first and then adding an ethanolic solution of CH₃NH₃X (MAX, X = Cl, Br, and I) on PbI₂@HKUST-1. Their findings reveal a blue shift in the PL for loaded MAPbI₃ and MAPbI₂Br as shown in Fig (2-16), attributed to a quantum confinement effect that resulted in the formation of perovskite QDs in the pores of the MOF HKUST-1 template. Also, they found that the templated MAPI QD is highly stable compared to the bulk one [54].

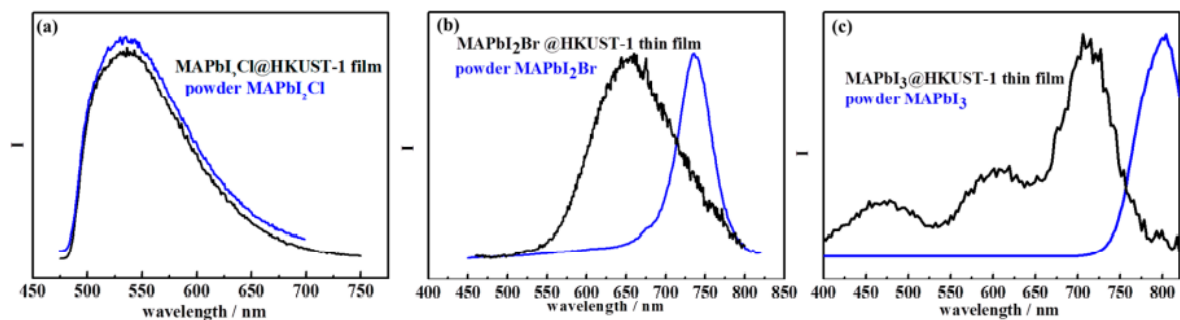


Fig (2-16): PL spectra of templated MAPbI₂X thin film with their references ((a) X= Cl, (b) X = Br, and (c) X = I [53]

Other porous materials can be used as templates, including polymer networks, hydrogels, biomolecules and assemblies [54]. Utilising these materials for synthesising perovskite is considered a promising field of research especially in the case of polymers which can be designed to prevent moisture ingress or improve charge transport between the perovskite grains. C Dokkhan *et al.* investigated the role of microgels (MG) in controlling perovskite's morphology and optoelectronic properties. They used poly(N-vinyl-formamide-co-2-(N-vinylformamido) ethyl ether) (PNVF-NVEE) as MG template to synthesise of MAPbI₃-xCl_x perovskite. They found that MGs cause micropatterning of perovskite to form disordered inverse opal (DIO) morphology that could contribute to an increase in light absorption and PL intensity of the perovskite, thus improving the efficiency of devices based on perovskite/MG compared to an MG-free device [55]. Also, MGs could be used as permanent 2D array

nanopore formers within the perovskite layer. O. Alkudhari *et al.* used poly(N-isopropyl acrylamide) (PNP) MG to form 2D array nanopores during perovskite deposition and provide other valuable roles like shunt-blocking and passivation that increase the PL intensity and time-resolved photoluminescence lifetime (TRPL) as well as power conversion efficiency (PCE) and average visible transmittance (AVT) of devices based on perovskite/MG [56].

2.1.4. Interfacial charge dynamics

The performance and stability of PSCs are significantly influenced by charge dynamics at the interface between the perovskite layer and charge-carrier transport layer (ETL and HTL), including injection, recombination, and trapping. Fig (2-17) summarises the various pathways for charge carriers after the perovskite is excited by absorbing light. The desirable pathways (1, 2 and 3) represent the injection of charge carriers to charge-carrier transport layers, thus transporting photocurrent to the external circuit. Other pathways are undesirable and can impair device performance. These paths are represented by the recombination of photoelectrons (from 4 to 8) or trapping at defect states at interfaces (9). Exciting the ETL with sunlight can also create defect states in the valence band of the ETL. These defects can create other undesirable pathways (I and II in Fig (2-17) leading to the trapping of electrons at interfaces or from perovskite, leading to photoactivated decomposition of the perovskite and therefore reducing device stability [57]. Therefore, the nature of the interfaces between the layers of the PSC device plays a vital role in determining their performance and operational lifetime.

The structural characteristics of perovskite thin films, such as crystal quality, pinhole density, grain size and number of grain boundaries, determine the PSC's performance. In order to achieve the desired perovskite materials chemistry, grain size, and microstructure, various modifications have been investigated, including: utilising different deposition techniques, solvent treatment, and introduction of additives to improve control of crystal morphology and quality, surface roughness, and coverage [9].

In 2014, Jeon *et al.* reported that adding toluene while depositing the MAPI precursor (prepared with a mixture of solvents (γ -butyrolactone and DMSO) by spin coating leads to highly uniform and dense perovskite layers, enabling manufacture of improved devices with efficiencies of up to 16.2% [58]. Since then, several antisolvents have been investigated for this purpose, such as chlorobenzene, diethyl ether and ethyl acetate. The best results are obtained when ethyl acetate is used as an antisolvent. Chemical vapor deposition (CVD) has also been employed to deposit

perovskite thin films and has given good results competing with counterparts prepared by the solution-process method[9].

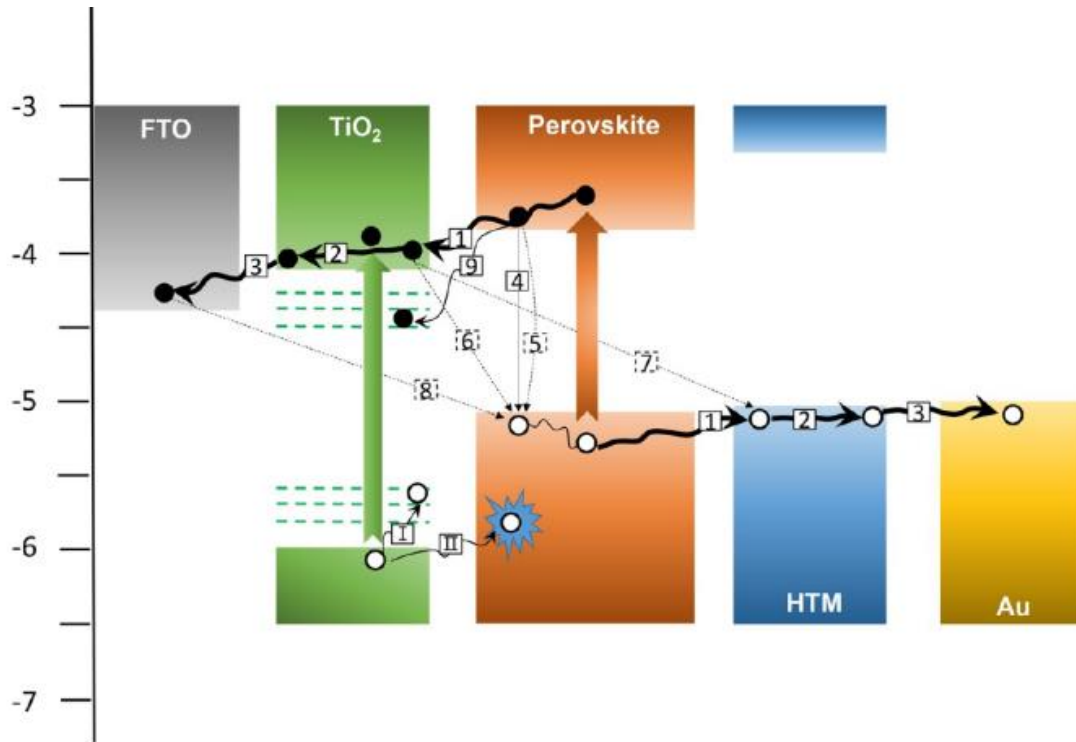


Fig (2-17): Schematic for the dynamic of charge carriers in PSCs, where 1,2 and 3 are the pathways of the injection of charge carriers to charge-carrier transport layers to generate the photocurrent (desirable). From 4 to 8 are the photoelectrons recombination pathways(undesirable). 9, I and II are the pathways of electrons' trapping by defects, whether photoelectrons or from perovskite (undesirable) [57].

It has been established that grain boundaries play a negative function in the stability of perovskite and that increasing the perovskite grain size is advantageous both for stability and performance of the cells. Larger grains increase carrier mobility, as the carriers will undergo fewer intergranular crossing events, and reduce the overall surface area of grain boundaries, which are frequently observed to result in more defect concentrations [9]. As mentioned previously, the grain boundaries are also widely believed to be key sites for degradation to occur since they allow diffusion of water and oxygen [19]. In 2018, Garnett *et al.* found that crystallinity at the grain boundaries and the amorphous interface between them may significantly influence PL lifetime and intensity. They attributed this to the passivation of grain boundaries or getting of native defects, an effective means to reduce the concentration of impurities and defects in the crystal lattice [59][60]. In general, the passivation and

encapsulation strategies as well as improving stability, can also lead to improved performance in PSCs by passivating defects that affect the charge carrier dynamics.

2.2. Electron Transport Layers (ETL) in PSCs

2.2.1. Electron Transport Layer Requirements

The electron transport layer (ETL) in a perovskite solar cell is positioned between the perovskite absorber layer and the cathode electrode to facilitate the extraction of photoelectrons from the perovskite. To achieve this purpose, the ETL should satisfy specific requirements regarding electronic properties, morphology, and defect states. The most fundamental characteristic of an ETL is its optical transparency. The ETL should have a large band gap to allow the passing of maximum intensity of visible light to the light absorber layer [9]. In addition, a suitable energy level alignment between the ETL layer and the perovskite layer is essential in selecting ETL materials. This means the lowest unoccupied molecular orbital (LUMO) or conduction band minimum (CB) of the ETL should align well with the CB of the perovskite, facilitating extraction and transport of photoelectrons to the cathode electrode. At the same time, the highest occupied molecular orbital (HOMO) or valence band (VB) of the ETL should be lower than the VB of perovskite, blocking the transport of photo-generated holes to the ETL. Another essential requirement for the electronic properties of the ETL is electron mobility, which should be higher than those of the perovskite to ensure effective transport of the photoelectrons and avoid charge recombination [9].

In addition, the morphology and structure of the ETL thin film may considerably impact the device performance and stability. A compact layer devoid of pinholes and defects enhances the contact between the perovskite layer and the ETL, reducing leakage and interfacial charge recombination and thus improving device efficiency. Also, the hydrophobicity of materials used as an ETL could be a helpful feature in preventing moisture from penetrating the perovskite active layer and shortening the device's lifetime [9].

2.2.2. Electron Transport Materials

Many organic and inorganic materials satisfy the requirements of an ETL for PSCs and are used to fabricate PSCs devices. Fig (2-18) shows the energy levels of some materials used as ETLs.

Metal oxide materials are excellent candidates as ETL materials in PSCs due to their n-type character and work functions. In addition, the energy levels (as shown in Fig (2.16)) are suitable for facilitating extraction and transportation of photoelectrons and blocking the movement of photoholes. These oxides often have high electron mobilities, good stability and low fabrication

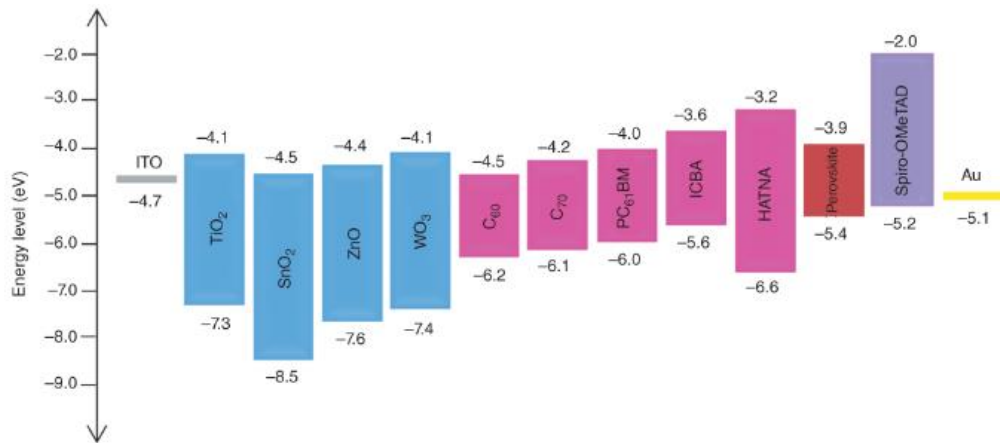


Fig (2-18): Energy level diagram of the materials used as ETL [9].

costs [9]. TiO₂, SnO₂ and ZnO which have been the most commonly used ETL materials for PSC applications produce high-efficiency PSCs with PCEs of 24%, 20.9% and 21.1 %, respectively [61]. Studies employing other metal oxides as the ETL in PSCs, such as barium stannate (BaSnO₃), strontium stannate (SrSnO₃), zirconium stannate (ZrSnO₄) and niobium pentoxide (Nb₂O₅) have resulted in PSCs with efficiencies of 21.2%, 19%, 16.76% and 20.2% respectively [61].

Organic materials, both fullerene and non-fullerene, have also been employed in PSCs as ETL. Fullerenes and their derivatives, such as C₆₀, C₇₀ and PC₆₁BM ([6,6]-phenyl-C₆₁-butyric acid methyl ester), are commonly used as ETLs in inverted PSCs due to properties such as the relatively high electron mobility, low fabrication temperature and energy level alignment that match the requirements of ETLs as mentioned above. It has been reported that the efficiency of PSCs based on fullerene-organic ETLs is over 20% [9]. A non-fullerene small organic molecule such as a perylene diimide derivative (PDI) demonstrated promising performance as an n-type organic material in the PSC [9]. Zhang *et al.* reported that PSCs based on amino-substituted PDI (N-PDI) as the ETL achieved an efficiency of 17.66 % [62]. Therefore, they are promising alternatives for ETLs, especially since some of these materials are thermally stable and hydrophobic, features that would be helpful for PSCs.

2.2.3. Modifying the TiO₂ Based Electron Transport Layer

TiO₂ is a typical n-type semiconductor with a wide bandgap of 3.0–3.2 eV. It is chemically and thermally stable and accessible to fabrication easily and at a low cost. As a result of these properties and the excellent band alignment with respect to the perovskites, TiO₂ thin films have been widely used as the ETL in PSCs. Devices based on TiO₂ have also achieved a high

efficiency. Despite the excellent device performance, TiO₂ thin films have several significant drawbacks, including relatively high processing temperature, intrinsic low bulk electron mobility and high photocatalytic activity, which can affect the stability of perovskite materials and, thus the long-term stability of devices. Consequently, extensive studies with various strategies have focused on understanding TiO₂ and modifying its properties to improve its performance in PSCs [57].

2.2.3.1. Controlling the Morphology of the TiO₂ ETL

The morphology of the TiO₂ ETL is directly related to the efficient transport of electrons through interfaces from the perovskite layer to the anode electrode. An efficient ETL in a PSC should have complete contact with the perovskite absorber layer and the anode electrode, full coverage for the collector electrode and rapid electron transit. This can be achieved by compact TiO₂ thin films (10-100 nm) without pinholes and cracks. Various deposition methods, such as spin coating, spray pyrolysis, magnetron sputtering, and atomic layer deposition, have been investigated to optimise the quality of the TiO₂ films. The results of these investigations show that magnetron sputtering and atomic layer deposition are excellent methods for high-quality compact TiO₂ thin films where the PSCs based on them achieved high efficiency compared to those prepared by spin coating and spray pyrolysis [57]. On the other hand, sputtering and ALD processes tend to be higher cost than spin coating and spray pyrolysis and are less amenable to roll-to-roll processing.

Porous TiO₂ films can be added above the compact layer and also significantly contribute to the performance enhancement of mesostructured devices. Porous TiO₂ increases the contact area surface between the perovskite and TiO₂, collecting photoelectrons from the perovskite absorber and delivering them to the TiO₂ compact layer. The injection of electrons into TiO₂ happens within around 300 ps, much shorter than the lifetime of photoelectrons (within microseconds), thereby reducing their recombination with photoholes and improving the efficiency of PSCs [57]. The shape and size of TiO₂ nanoparticles also influence the contact surface area between perovskite inside porous TiO₂. Sung *et al* used layers of TiO₂ nanoparticles of different sizes (30, 40, 50, and 65 nm) as a scaffold layer in mesostructured PSCs. They found the diameter of the resultant pores to be 24, 34, 45, and 56 nm with surface-specific areas of 57, 40, 34, and 28 m² g⁻¹. The best efficiency was obtained with 50 nm spherical TiO₂ nanocrystals due to a balance between better pore filling by the perovskite and

the increase in its contact area with the TiO₂ [63]. In addition, vertically aligned TiO₂ nanorod/nanowire arrays have also been used in PSCs and studied to determine the effects of tuning the thickness, length and density. The findings indicated that the efficiency of PSCs based on TiO₂ nanorods/nanowires could be improved by optimising these factors [57].

2.2.3.2. Doping of the TiO₂ ETL

Doping TiO₂ by other elements to chemically modify the intrinsic properties of TiO₂ is a standard method and has been widely investigated. Adding different dopants to TiO₂ will change optoelectronic properties, including band gap, energy level alignment, charge carrier density and mobility, and trap state densities and distributions. These changes could affect the function as an ETL in PSCs. *e.g.* improvement of conductivity and the photoelectron injection processes could be achieved by doping TiO₂ with higher positive valent dopants, such as Nb⁺⁵, where the extra electrons contribute to a positive shift of the conduction band of TiO₂ [57]. Numerous studies have investigated dopants to employ them in improving the properties of the TiO₂ ETL and overcoming their drawbacks, improving PSCs efficiency.

2.2.3.3. Modifying the TiO₂ surface

At the perovskite/TiO₂ interface, two essential charge carrier dynamics occur concurrently; transfer and recombination. Accelerating the transfer of the charge carriers and suppressing their recombination is desired for efficient PSCs. The TiO₂ and perovskite surfaces have trap states, due to defects, that increase the recombination rate, impede charge extraction and transfer of charge carriers, and therefore reducing the performance of PSCs [57]. Therefore, modifying the TiO₂ surface could adjust the dynamics of charge carriers at the perovskite/TiO₂ interface.

One of the most crucial surface modification techniques is passivation of surface trap states of the TiO₂ ETL and/or perovskite absorber. This can be achieved by inserting a monolayer of suitable materials between TiO₂ and perovskite layers for the passivation of surface traps in either of them. Snaith *et al.* inserted a C₆₀-substituted benzoic acid self-assembled monolayer (C₆₀SAM) between compact TiO₂ and perovskite to passivate interface trap states and reduce the barrier of the interfacial electron transfer. They found the efficiency of modified devices improved to 17.3%. This could be attributed to the fact that the oxygen of the benzoic acid

group grafted onto the fullerene passivates the surface trap states of the TiO₂. Meanwhile, the exposure of the C₆₀ fullerene molecule to perovskite simultaneously passivates perovskite trap states. Both of these processes reduce trapping and recombination of charge carriers and improve efficiency[64].

Bifunctional-group grafted small organic compounds such as self-assembled 4-aminobenzoic acid (PABA) (4-NH₂-Ph-COOH) have been used as interfacial monolayer modifiers and have been shown to contribute to improving the efficiencies of PSCs. Here the carboxylic group is thought to passivate the trap states by chemically bonding to TiO₂, while the ammonium group acts as an active site for perovskite growth as shown in Fig (2-19) [65].

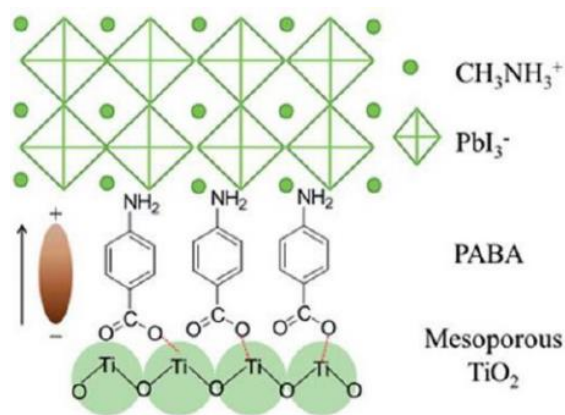


Fig (2-19): Schematic for interfacial monolayer modifiers based on organic compounds with two-functional-group [65]

The intermediate layer between TiO₂ and perovskite can also be a thin layer of an appropriate organic or inorganic material which functions as a bridge to facilitate the transfer of electrons from TiO₂ to perovskite. Many studies use this strategy and deposited a thin layer of materials such as graphene quantum dots (GQDs) [66], or lithium-neutralized graphene oxide (GO-Li) [67] that contribute to improving the performance of PSCs.

On the other hand, one of the restrictions that could affect the TiO₂ function in its application is hydrocarboncarbon contamination of the TiO₂ thin film surface. Exposure of a TiO₂ surface to atmosphere leads to spontaneous formation a monolayer of organic hydrocarbon compounds, in particular, small carboxylic acids, as reported by Baljlka *et al.* [68] and bicarbonate, as mentioned by Song *et al* [69]. It is expected that this monolayer may block unsaturated Ti sites at ambient temperature and will have a profound effect on chemical reactions occurring on TiO₂ surfaces [69]. It is also known that this so-called adventitious

hydrocarbon layer results in a hydrophobic surface, which may impede the efficient growth of the perovskite [65]. In addition, this carbon contamination could affect the efficient transfer of charge between the perovskite and the ETL. Several studies have focused on this so-called adventitious carbon overlayer and its influences. Baljlka *et al.* found that TiO₂ surfaces in ambient environments shift from hydrophilic into hydrophobic in the dark. They attributed this phenomenon to carbon contamination by the spontaneous formation of mixed formate/ acetate monolayers on the TiO₂ surface due to adsorption of these species from the ambient air [68]. In the presence of UV radiation these overlayers could be photocatalytically degraded resulting again in the hydrophilic surface. The same result was obtained by Yahn *et al.* when they studied the “Influence of Carbon Contamination on the Contact Angle Relaxation” of 1 μ L droplets (pure deionized water, 99.9%) on three types of TiO₂ films (anatase, mixed-phase anatase + rutile and amorphous TiO₂) over 60 days as an indicator of hydrophobicity. Their findings indicate a relationship between carbon contamination and contact angle relaxation, as shown in Fig (2-20), which means the carbon contamination contributed to increasing the hydrophobicity of thin films. This relationship depends on the surface energy of the TiO₂ film, which changes with the type of TiO₂ [70]. Regarding the electrical effects of carbon impurities, according to Wu *et al.* [71]. and Sun *et al.* [72], carbon contamination acts as a defect in semiconductors and negatively affects the electrical performance of electronic devices. Also, Cha *et al.* studied the influence of carbon contamination on the electrochemical characteristics of fuel cells. They found that C contamination formed internal short circuits, which resulted in decreased open circuit voltages [73].

Therefore, significant efforts have focused on developing possible approaches to remove the unwanted surface adsorbents or hinder adsorption by modifying or passivating surfaces with thin layers of molecules that block active sites; to avoid their negative effects on metal oxides' properties and, therefore, functions. Among the adsorbed atoms used for treating the TiO₂ surface is fluorine (F), which gives effective results, yielding the lowest value of surface energy, which has led to its use as a shape-control agent and thus a reactivity-control agent in TiO₂ nanocrystal growth. Also, F promotes the growth of anatase TiO₂ single crystals along the [010] and [100] axes when added to TiO₂ growth solutions [74][75]. Hines *et al.* [75] investigated using XeF₂ as a fluorination agent to passivate the TiO₂ surface and study the effect on its resistance to carbon contamination when exposed to air and immersed in boiling H₂O. They found that the fluorinated surface was notably free of adventitious carbon species

even after exposure to air and immersion in boiling water for ten minutes. This is attributed to blocking the under saturated Ti-sites by bonding between Ti and F.

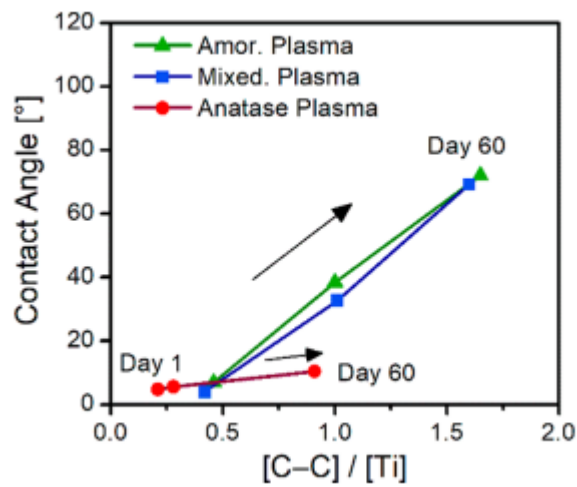


Fig (2-20): The relationship between the ratio C to Ti (C/Ti) and contact angle [70].

In summary, the above review identifies two of the important layers in perovskite solar cells: the perovskite layer as an absorber layer and TiO₂ as an electron transport layer. The main challenges of the perovskite layer are the degradation of perovskite materials when exposed to environmental factors such as moisture, oxygen and light, as well as the toxicity of some elements used in common perovskite materials. Moreover, perovskite materials deposited by solution processes have electronic defects that can affect the dynamics of charge carriers. Numerous studies with various strategies have investigated perovskite materials, aiming to overcome the challenges of stability and improved power conversion efficiency by improving their properties by controlling the shape, size and structures. The main strategies used are multiple cation perovskite, passivation, encapsulation and templates, all contributing to improvements in the stability and performances of PSCs. A templating technique offers an opportunity to synthesise perovskite nanomaterials with well-controllable size, shape and stability.

Regarding TiO₂, many studies with different strategies have focused on TiO₂ to enhance its function in the extraction and transfer of photoelectrons. These studies aim to control the morphology, doping and modification of the surface of the TiO₂ layer. The modification of the surface aims to passivate trap states at the perovskite-TiO₂ interface to enhance the desired charge carrier dynamics. On the other hand, exposure of TiO₂ thin film surfaces to air leads to

spontaneous formation of a monolayer of organic carbon compounds such as carboxylic acids and bicarbonate. Several studies found that carbon contamination can affect the properties of TiO_2 and thus could impair charge injection from the perovskite to TiO_2 . Therefore, studies have focused on developing possible approaches to remove the unwanted surface adsorbents or hinder adsorption by modifying or passivating surfaces with thin layers of molecules that block active sites to avoid adverse effects, or promote charge injection. Among the species studied for treating the TiO_2 surface is fluorine (F), which gives effective results where it yields low values of surface energy. The F-layer is thought to block the undercoordinated Ti sites, increasing the resistance of TiO_2 thin film surface to carbon contamination.

In this thesis the effect of peptide gels in improving the stability of perovskite by protecting them from water will be investigated along with a study of whether the gels can be used to template the perovskite, and confine the size of the particles that are grown. This may allow us to tune the optoelectronic properties, in particular, the absorption and emission wavelengths of the perovskite. In the final chapter the effect of treating a compact TiO_2 layer surface with fluorine to reduce the surface hydrocarbon contamination will be studied in order to understand the effect on efficiency of cells treated in this way.

Chapter 3

Theory and techniques

3.1 Theory of photovoltaic devices

3.1.1 Band Structure of semiconductors.

Energy bands are formed from a splitting of electron states formed by an overlap of electronic orbitals of atoms in a crystal. This overlap usually occurs between adjacent atoms via outer orbitals (involving valence electrons) rather than the inner electrons. The degree of overlap depends on the inter-atomic distance as shown in Fig (3-1). The electrons will occupy only discrete energy states called the allowed states, which are separated by forbidden energy bands. Within the bands energy differences are extremely small, thus, the bands can be considered as an almost continuous energy distribution through allowed states [76].

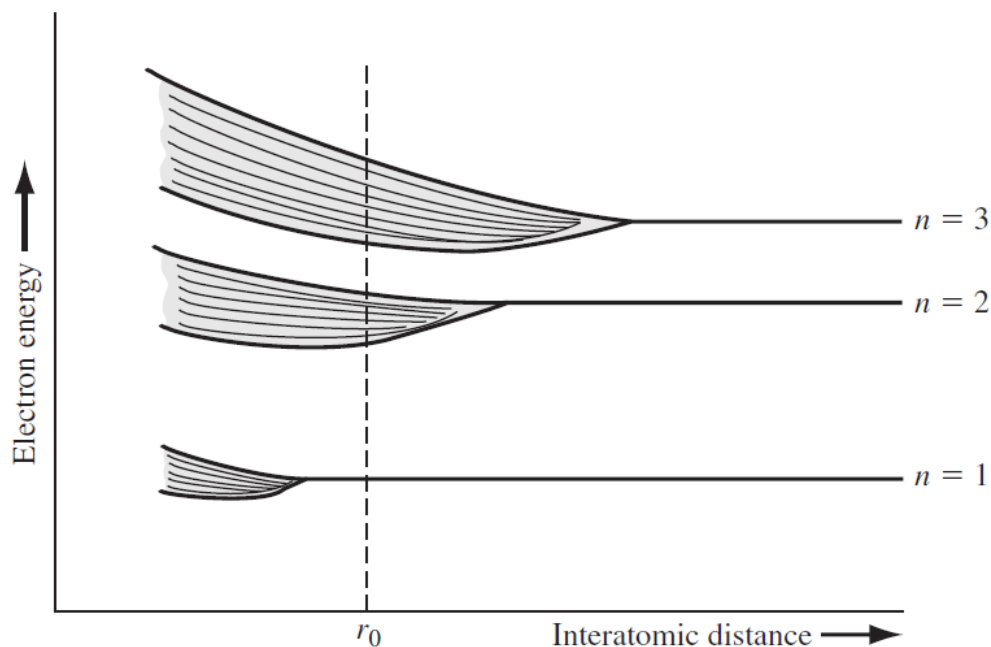


Fig (3-1): The allowed bands of energies due to the splitting of energy states ($n = 1, 2$ and 3) [76].

In all atomic orbitals, the electrons are placed into the empty states which have the lowest energy first, according to the Pauli Exclusion Principle. The outer bands can be divided to lower energy states that are full at $T = 0$ K (the valence band) and higher energy states that are empty at $T = 0$ K (the conduction band). The width of the forbidden energy band that separates the top of the valence band (the uppermost occupied band in a semiconductor) and the bottom of the conduction band (the lowest energy unoccupied band in a semiconductor) is known as the bandgap energy (E_g) of the crystal [76], [77].

3.1.1.1 Fermi energy

The ratio of the number of particles $N(E)$ to the density of quantum states $g(E)$ can be obtained by a distribution function called the Fermi–Dirac distribution ($f_F(E)$) which is defined as

$$\frac{N(E)}{g(E)} = f_F(E) = \frac{1}{1 + e^{\frac{(E-E_F)}{KT}}} \quad (3.1)$$

where k is Boltzmann constant, T is temperature and E_F is Fermi energy. The Fermi energy can be defined as an energy level where the probability of electron states being filled below it is 1.0 and above it, the probability is zero at $T = 0$ K. However, at $T > 0$, the probability of electron states being occupied at this level is 50% [76] as shown in Fig (3-2).

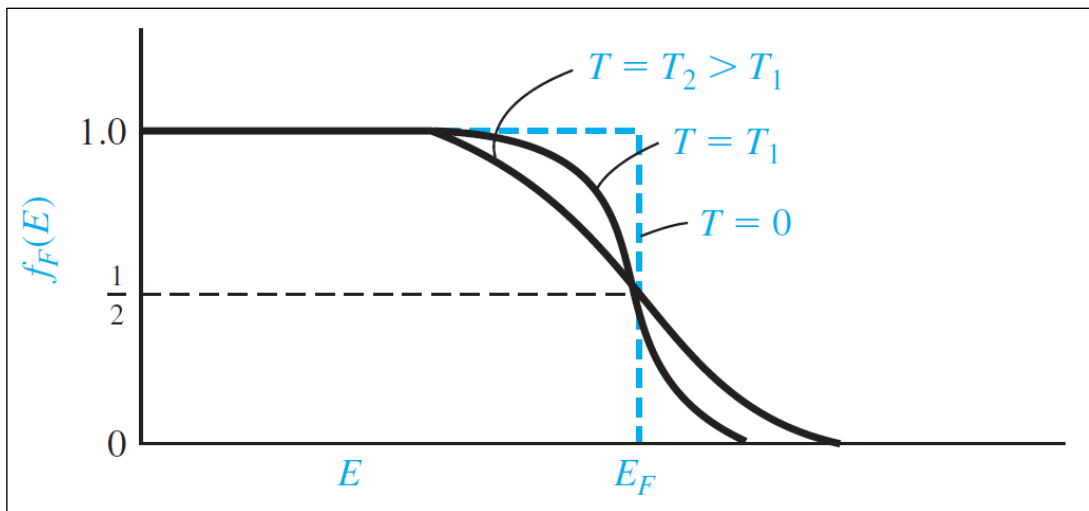


Fig (3-2): The function of Fermi probability versus energy for different temperatures [76].

3.1.1.2 Metals, Insulators and Semiconductors

Every material has its own band structure, arising from the electron configuration of the constituent atoms and the crystal structure, which determine the properties of electrical conductivity. The conductivity then depends heavily on the size of the bandgap. According to the bandgap, materials can be divided into insulators, semiconductors, and conductors (as shown in the simplified energy-band diagram in Fig (3-3)).

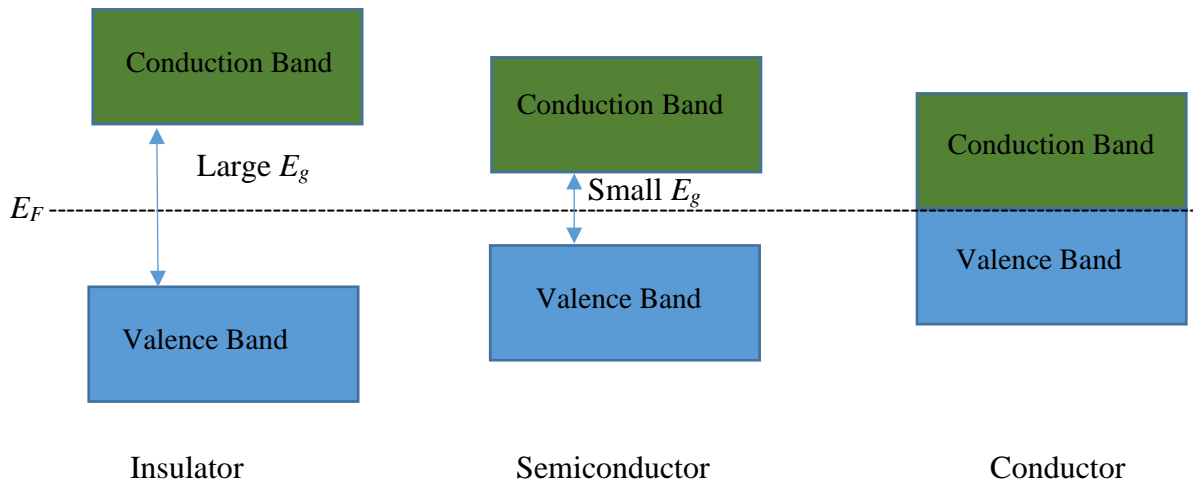


Fig (3-3): Valence and conduction bands in insulator, semiconductor, and conductor.

For insulators, the band-gap energy is in the range of 3.5 eV to 6 eV or more, which makes it challenging to promote electrons across the band-gap. Semiconductors, on the other hand, have a small band gap that allows electrons to be promoted across the gap by thermal or optical energy. In the case of the conductor, or metal, the conduction band and valence band effectively overlap so that there is no band gap. Therefore, a small electric field is enough to promote the electrons from the valence band into the higher energy conduction band [76].

In semiconductors, the Fermi level lies in the band gap, but its absolute position can be affected by the type of the majority charge carriers. The Fermi level in intrinsic semiconductors (undoped) lies in the middle of the band gap (Fig (3-4)) due to the distribution of charge carriers in the valence band and the conduction band. When an electron is excited from the valence band to the conduction band this leaves behind a hole in the valence band. When the intrinsic semiconductor is doped with a donor element, it forms an n -type semiconductor that has a concentration of electrons higher than that of the holes. Due to the fact that the majority carriers are electrons in n -type semiconductors, the probability of finding an electron near the conduction band edge is increased; therefore, the Fermi level is closer to the conduction band (Fig (3-4)). In contrast, a p -type semiconductor is formed by doping an intrinsic semiconductor by acceptor impurities, resulting in the concentration of holes becoming higher than the electrons. This leads to a decrease in the probability of finding an electron near the conduction band edge, therefore, the Fermi level is closer to the valence band (Fig (3-4)).

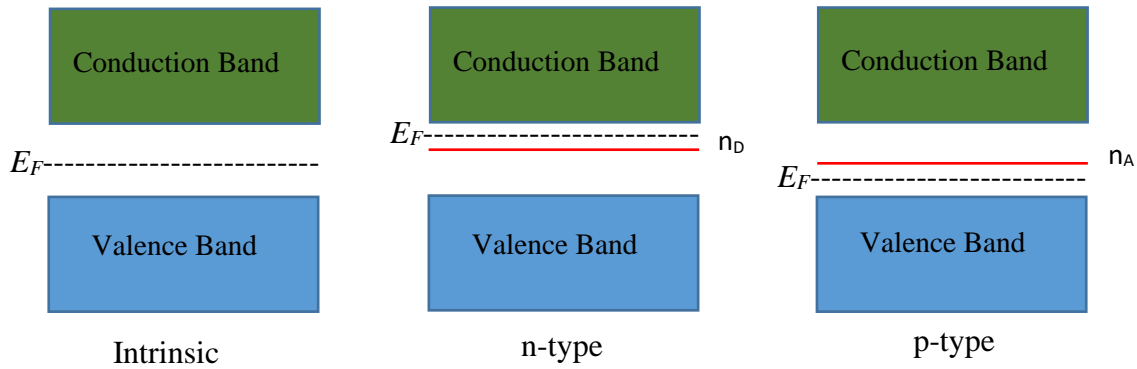


Fig (3-4): Position of the Fermi level in intrinsic, n -type and p -type semiconductors. n_D is the position of the donor level in an n -doped semiconductor and n_A the position of the acceptor level in a p -doped semiconductor.

3.1.2 The Photovoltaic effect

A solar cell is an electrical device that converts light directly, in one step, to electricity, based on the photovoltaic effect. Light has energy, which depends on its frequency. When light with sufficient energy to excite electrons is absorbed, electrons are excited from the valence band (VB) to a higher energy level (conduction band (CB)) where they are free to move, leaving behind the holes in the valence band. In a solar or photovoltaic cell, before relaxing back, the generated charge carriers are pulled away into an external circuit due to a potential difference that forms as a result of the internal electric field induced by ionised impurities on either side of the junction region. The efficiency of a photovoltaic device depends on the selected light absorber materials and the manner in which they are coupled to the external circuit.

3.1.2.1 Optical absorption in semiconductors

Optical absorption of light by a semiconductor depends on the band gap and absorption coefficient. The semiconductor absorbs the photons with energy equal to or higher than their band gap, which excites the electrons which transit from the valence band to the conduction band. The probability of the transition process of an electron differs depending on the type of semiconductor, in particular whether it has direct or indirect band-gap as shown in Fig (3-5)

For a direct band-gap semiconductor, the maximum of valence band and the minimum of conduction band both occur at the same \mathbf{k} -value, i.e. they have the same value of crystal momentum, which is a function of the crystal lattice. The transition of the electron, in this case, can take place with no change in crystal momentum (Fig (3.5 a)) which increases the rate of absorption and the absorption coefficient α just depends on the difference between the photon energy and the band gap (eq 3.2)[78].

$$\alpha \propto (h\nu - E_g)^{\frac{1}{2}} \quad (3.2)$$

In materials with an indirect band gap, the valence band maximum and the conduction band minimum do not occur at the same k value. Therefore, additional small energy, or more specifically a change in momentum, is required to make up the k difference. This can be provided by a lattice vibration or phonon. Due to energy conservation, the absorption starts below the band gap at the energy $E_g - \hbar\omega_{ph}$ (Fig (3.5 b)) but with lower probability than for the direct transition. The absorption coefficients in these indirect band gap materials depend on the photon energy, the band gap and phonon energy (eq 3.3) and their values are smaller than those for the direct band gap materials[78].

$$\alpha \propto (h\nu - E_g - \hbar\omega_{ph})^2 \quad (3.3)$$

Si, for example, has an indirect bandgap, which is why it has a much lower absorption coefficient than the perovskite materials discussed in Chapter 2.

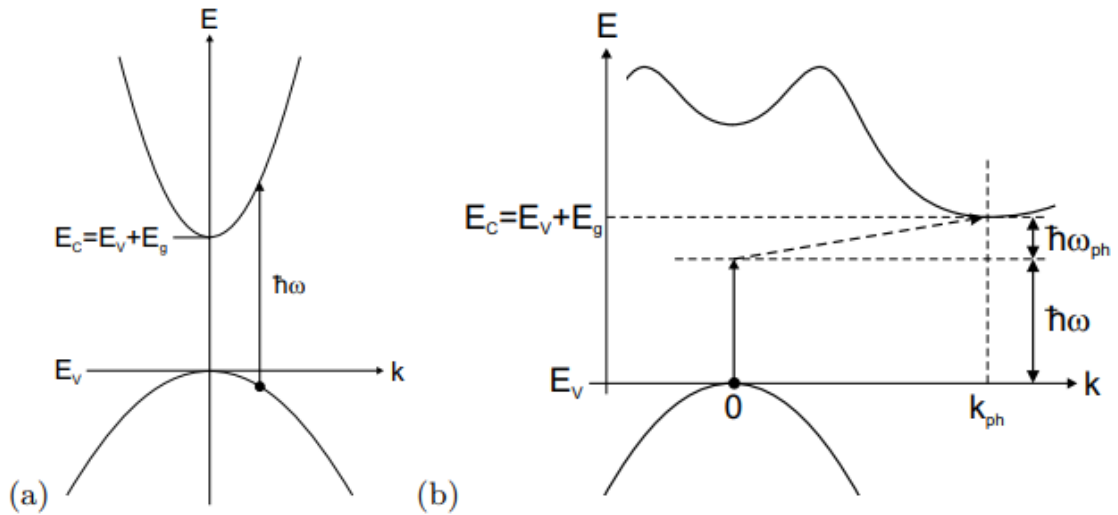


Fig (3-5): Direct band gap semiconductor *e.g.* perovskite vs indirect band gap semiconductor *e.g.* Si [78].

3.1.2.2 Charge separation

Charge separation in photovoltaics depends on how the absorbed material is coupled to the external circuit. An *p-n* solar cell consists of two main regions; an *n*-doped region and a *p*-doped region. The *n*-type material contains excess electrons due to doping with donor elements, while *p*-type is doped by acceptor elements, resulting in positively charged holes that are free to move in the lattice. When the *n*-type and *p*-type materials are introduced on both sides of each other, electrons diffuse from the *n*-type to the *p*-type. In contrast, the holes diffuse in the opposite direction. Eventually, the migration and recombination of mobile charges give rise to a region depleted of mobile carriers, with ionized impurities forming an electric field. This electric field pulls the photoelectrons excited by absorbing light into the *n*-type material, and likewise the photogenerated holes into the *p*-type material (Fig (3.6)) thus, a photocurrent is generated by the cell [79].

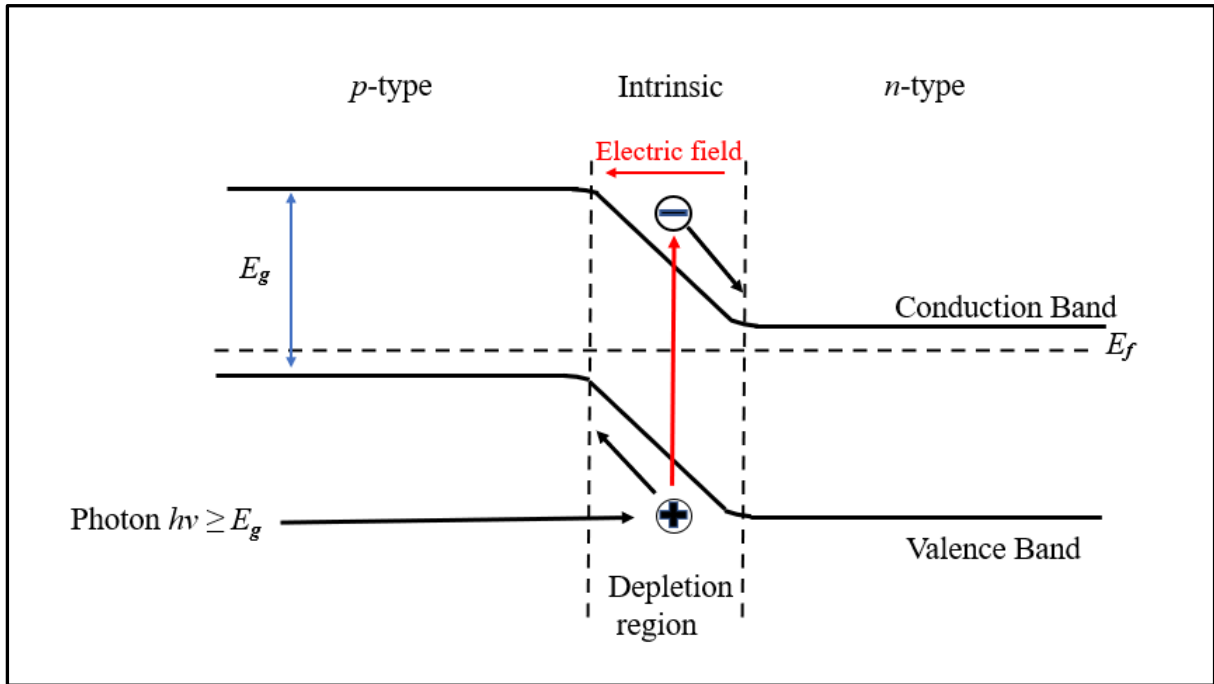


Fig (3-6): The mechanism of charge separation in a *p-i-n* junction solar cell

3.1.2.3 Shockley–Queisser limit.

The Shockley–Queisser limit is the maximum conversion efficiency of a single junction solar cell that takes into account all inevitable losses resulting from applying a number of restrictions on the solar cell. These inevitable losses can be summarised in the loss mechanisms [80] as follows and shown in Fig (3-7). Each of these losses is described below.

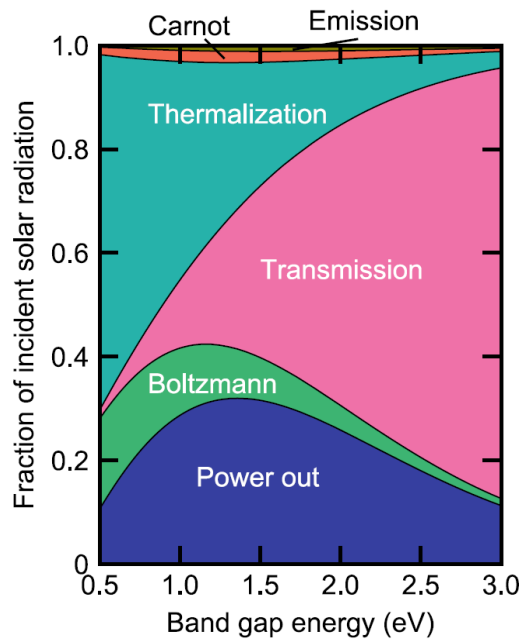


Fig (3-7): The loss mechanisms in single-junction solar cells with different E_g [80].

3.1.2.3.1 Transmission losses

Photons with energy less than the band-gap cannot be absorbed by the solar cell so the transmission losses can be obtained from equation (3.4). These losses lead to a reduction in the output current.

$$P_{below} = \int_0^{\nu_g} G(\nu, T) \times h\nu d\nu, \quad (3.4)$$

where, $G(\nu, T)$ is the electromagnetic radiation emitted from the light source *e.g.* the sun, ν is the frequency of the photon and ν_g is the frequency of a photon that equals the band gap energy.

3.1.2.3.2 Thermalization losses

Thermalization losses occur when the photons that have energy higher than the band-gap energy are absorbed but the excess energy above E_g is converted to heat, so can be considered to be wasted energy in electricity generation. This heat also has negative effects on the performance of the solar cell. These losses can be found by equation (3.5) which leads to a decrease in output voltage.

$$P_{thermalization} = \int_{v_g}^{\infty} G(v, T) \times hv dv - \int_{v_g}^{\infty} G(v, T) \times hv_g dv . \quad (3.5)$$

3.1.2.3.3 Carnot loss

The Carnot loss represents a voltage loss which occurs when the solar cell's temperature increases according to the relation:

$$P_{Carnot} = I(V_{max}) \frac{E_g}{e} \left(\frac{T_c}{T_s} \right) . \quad (3.5)$$

Here, V_{max} is a voltage of the maximum output power obtained, T_c is solar cell's temperature, and T_s is temperature of sun.

3.1.2.3.4 Boltzmann loss

The Boltzmann loss represents a voltage loss that occurs due to the reason that solid angle of the light emitted from the solar cell is larger than the angle of sunlight incident on the solar cell as shown in Fig (3-8). It can be obtained from:

$$P_{Boltzman} = I(V_{max}) \frac{kT_c}{e} \ln \frac{2\pi}{\pi f_{\omega}} \quad (3.6)$$

Where f_{ω} is the geometrical factor ($f_{\omega} \equiv 2.18 \times 10^{-5}$)

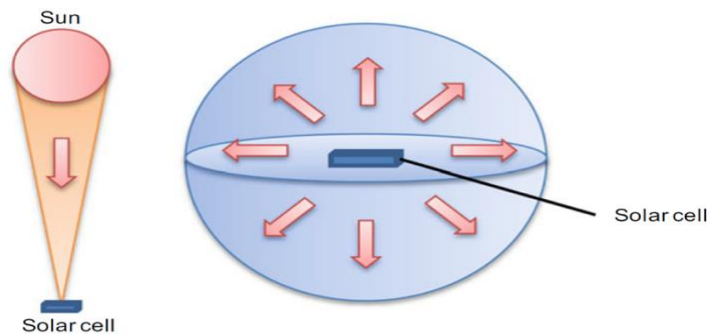


Fig (3-8): Incident solid angle and the emission solid angle [80].

3.1.2.3.5 Radiative recombination

Radiative recombination contributes to energy losses by losing the energy of each carrier involved in the recombination, which is equal to the band-gap energy of the material used. These losses in photocurrent can be obtained from [80]:

$$P_{emission} = \frac{E_g}{e} \times eF_c(V_{max}) \quad (3.7)$$

Where F_c is the radiative recombination rate and eF_c represents the current losses.

Due to the losses described above, and within the framework of the detailed balance theory, the conversion efficiency of a solar cell with a single band-gap is therefore limited. This limit is called the detailed balance limit or Shockley–Queisser limit and was introduced by William Shockley and Hans-Joachim Queisser in 1961. Fig (3-9) shows the detailed balance limit of the conversion efficiency of single-junction solar cell as a function of bandgap for two air mass (AM) sources and demonstrates that the maximum limit is around 33%.

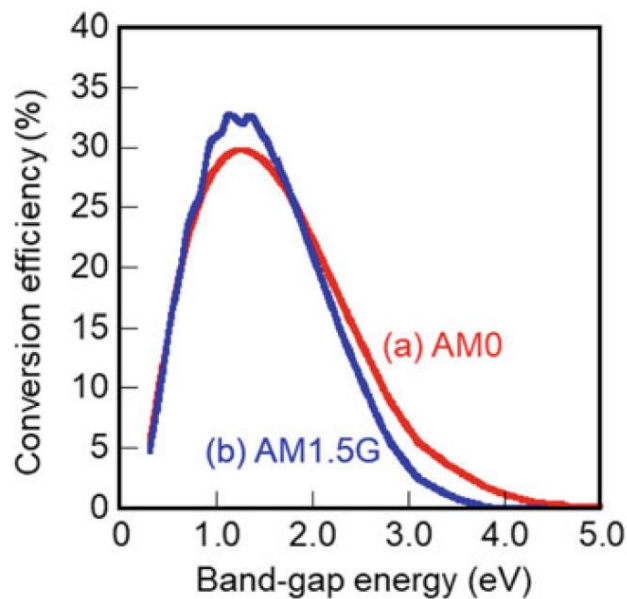


Fig (3-9): The detailed balance limit of the conversion efficiency of single-junction solar cell [80].

3.1.2.4 Performance of solar cells

Solar cells act as a diode in the dark, while under illumination, they provide a photovoltage and direct photocurrent, the values of which depend on the conversion efficiency of the solar cells. This efficiency depends on many parameters as illustrated below: Fig (3-10) shows a simplified equivalent circuit of a real solar cell. It consists of the diode (D) and the photocurrent (I_L) source in addition to two resistances, namely a series (R_s) and a shunt (R_{sh}) resistance. The shunt resistances are usually due to manufacturing defects and poor solar cell design. In contrast, series resistances are due to the contact resistance between the metal contact and the solar cell. The stray currents caused by R_{sh} and R_s resistances are marked I_{sh} and I_s , respectively [81]. Whereas I_d and V_d represent the voltage and current losses caused by the recombination.

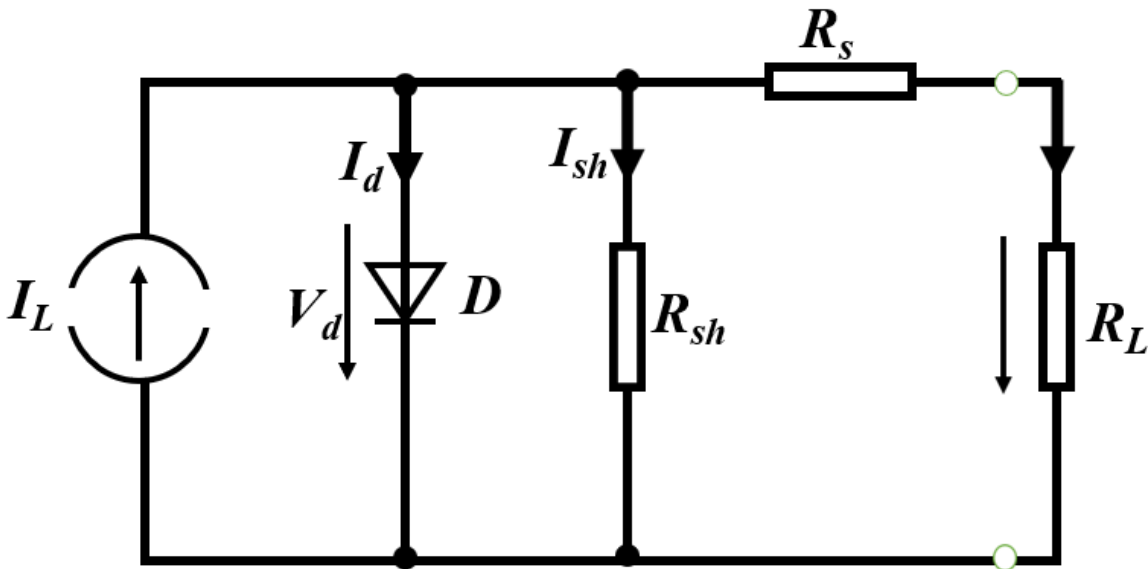


Fig (3-10): Equivalent circuit diagram of a solar cell contacted to the external load resistance (R_L) [81].

The current density of the output photocurrent (J) of a solar cell is given as:

$$J = J_{SC} - J_{dark} \quad (3.8)$$

Where J_{SC} is the short circuit photocurrent density, which depends on the probability of the generation of an excited electron for each photon absorbed *i.e.* the quantum efficiency $QE(E)$ of the cell, which depends on the wavelength (energy) of the photon.

Thus, J_{SC} is given by:

$$J_{SC} = q \int b_s(E)QE(E)dE \quad (3.9)$$

Where b_s is the incident spectral photon density and q is the electron charge.

J_{dark} is the current density in the absence of light and is given by the diode formula,

$$J_{dark} = J_0 \left(\exp \frac{qV}{mk_B T} - 1 \right) \quad (3.10)$$

Where, J_0 is the reverse current, m is a factor accounting for non-ideal diode behaviour k_B is Boltzmann constant and T is the temperature.

The range of operation of the solar cell is between $V=0$ and V_{oc} . The latter is the voltage obtained under open circuit conditions and is known as the open circuit voltage. Its value can be found from:

$$V_{oc} = \frac{kT}{q} \ln \left(\frac{J_{sc}}{J_0} + 1 \right). \quad (3.11)$$

From the above we can define the power density, P , of the solar cell as,

$$P = JV \quad (3.12)$$

Fig (3-11), shows a typical plot of the current density vs bias voltage, which provides a clear means for illustrating the maximum power point of the solar cell that occurs at voltage, V_m , with a corresponding current density, J_m , therefore the maximum power is given by,

$$P_m = V_m \times J_m \quad (3.13).$$

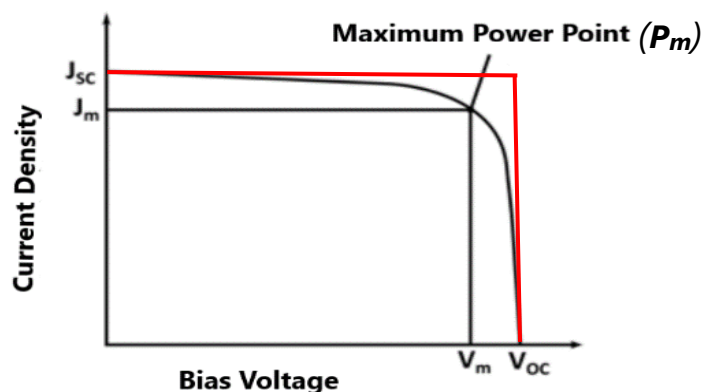


Fig (3-11): J - V characteristics of a solar cell showing the open circuit voltage V_{oc} , short circuit current J_{sc} and the maximum power point P_m , the red box is the rectangle obtained from the product of J_{sc} and V_{oc} , and the black box is the rectangle beneath the I - V curve (the product of J_m and V_m) [81].

Also shown are the positions of V_{oc} and J_{sc} . The maximum power provided by the cell and the product of V_{oc} and J_{sc} give rise to a useful measure of the performance of a photovoltaic cell known as the fill factor (FF), which is the ratio of the quasi-rectangle obtained from the product of J_{sc} and V_{oc} , shown by the red rectangle, and the rectangle beneath the curve (the product of J_m and V_m) [82] shown in Fig (3.11) *i.e.*,

$$FF = \frac{J_m V_m}{J_{sc} V_{oc}} \quad (3.14)$$

The power conversion efficiency, PCE, of a solar cell (η) is the ratio of the power density delivered at the maximum power point (P_m) to the power density of the incident light (P_{in})

$$\eta = \frac{P_m}{P_{in}} = \frac{J_m V_m}{P_{in}} \quad (3.15)$$

From equation (3.14), the efficiency can then be obtained directly from J_{sc} , V_{oc} and FF by

$$\eta = \frac{J_{sc} V_{oc} FF}{P_{in}} \quad (3.16)$$

3.2 Perovskite solar cells (PSCs)

3.2.1.1 Construction of PSCs.

Perovskite solar cells are solar cells based on the use of perovskite as the absorber material in their fabrication. The basic structure of PSCs can be divided into three main components:

- The electron transporting layer (ETL) plays a vital function in extracting and transporting photogenerated electrons. Many organic and inorganic materials, satisfy the requirements of the ETL for PSCs and are described in detail in section (2.2). Examples of *n*-type metal oxides such as tin oxide (SnO₂), titanium dioxide (TiO₂) and zinc oxide (ZnO) are commonly used in this layer with and control of their morphology can be used to improve the performance of the cell. Examples of the morphology include the compact and mesoporous structures the use of which depend on the architectures of perovskite solar cells, i.e. planar or mesoscopic, as shown in Fig (3.10).
- The active layer, or light-harvesting material, is responsible for the system's optical features; this layer light absorption in the solar spectrum. Perovskite materials play this role in a PSC. Most of the perovskite materials, including organic-inorganic perovskite, fully inorganic perovskites and lead-free perovskites, have been investigated for use as an absorber layer. These are discussed more fully in Chapter 2.
- The hole transport layer (HTL) is a mediator for positive charge (hole) transport from the excited perovskite to the counter electrode. Many materials have been applied in this layer, both organic, such as 2,2',7,7'-tetrakis(N,N-di-p-methoxyphenyl-amine)9,9'-spirobifluorene (spiro-OMeTAD) or inorganic such as Copper iodide (CuI).

The ETL and HTL are sandwiched between two electrodes. In a typical PSC (n-i-p structure), the front electrode is a transparent conductive oxide (TCO) that allows the light to pass through it and at the same time, collects electrons from ETL and passes them to the external circuit. Common materials used as the TCO are fluorine doped tin oxide (FTO) and indium-doped tin oxide (ITO). The back electrode is usually a metal electrode such as gold (Au) or silver (Ag). It collects the holes from the HTL and transfers them to the external circuit.

3.2.1.2 Architectures of perovskite solar cells

Assessing the overall performance of perovskite solar cells depends significantly on the device configuration. Perovskite solar cells are categorized as regular (n-i-p) and inverted (p-i-n) structures, depending on the type of transport material (electron/hole) present on the outermost part of the cell or encountered first by incident light. These two configurations can be further classified as either mesoscopic or planar structures, as shown in Fig (3-12)[83].

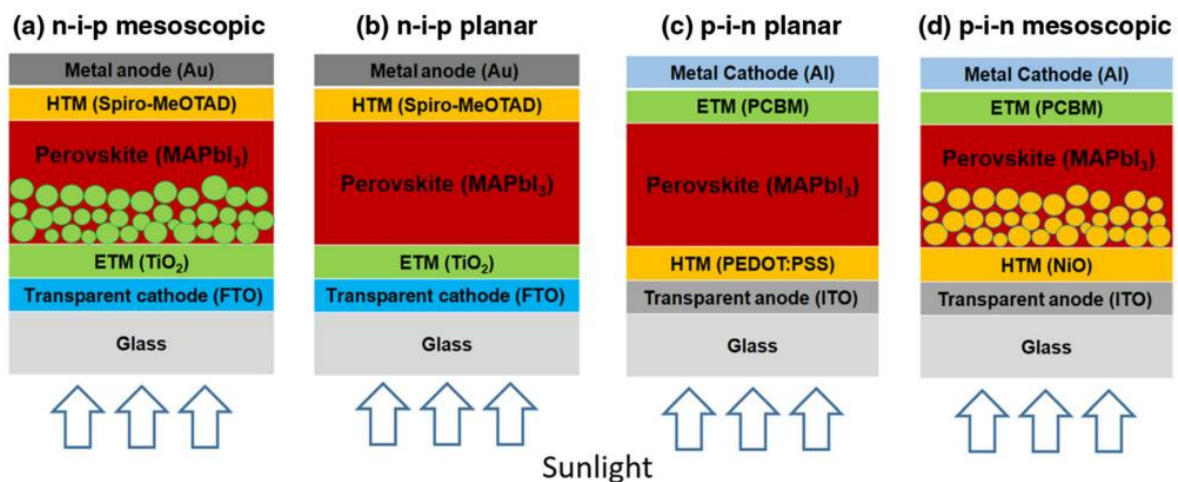


Fig (3-12): Diagram illustrates the structure of four common types of perovskite solar cells: (a) mesoscopic n-i-p, (b) planar n-i-p, (c) planar p-i-n, and (d) mesoscopic p-i-n [83].

3.2.1.2.1 Regular n-i-p structure

The mesoscopic structure is a classic perovskite solar cell architecture that has its roots in dye-sensitized solar cells. The structure consists of a transparent conducting oxide (TCO), ETL, a mesoporous metal oxide layer such as TiO₂ and Al₃O as a scaffold layer, a perovskite layer, HTL, and a metal electrode as shown in Fig (3-10 a). The mesoporous layer acts as a scaffold, improving the adhesion and filling of perovskite materials, resulting in a more continuous and homogenous perovskite film [83]. The use of mesoporous layers can be beneficial for solar cells that have light absorbers with short charge-diffusion lengths and tightly bound excitons because they can increase the interface surface area and enhance charge separation and extraction processes. However, this advantage may not be relevant for perovskite solar cells due to the long charge-diffusion length and relatively low exciton binding energy of perovskite materials. Additionally, excitons in most perovskite materials can easily be thermally dissociated at ambient temperatures [9].

The planar structure is an updated version of the mesoscopic design, where the perovskite layer is situated between the ETM and HTM without a mesoporous metal oxide layer, leading to a simpler structure overall as shown in Fig (3-10b). The interface between the different layers that make up the PSC, including the perovskite layer, the electron-transporting layer, the hole-transporting layer, and the electrodes, can be carefully controlled to achieve high efficiency without the mesoporous layer. In a planar n-i-p PSC with the same materials and approach, higher open-circuit voltage and short-circuit current density were observed compared to a mesoscopic PSC. However, the planar configuration exhibited more severe J - V hysteresis, which could be affected by the thickness and grain size of the buffer layer [83].

3.2.1.2.2 Inverted p-i-n structure

The p-i-n structure for PSCs was inspired by organic solar cells. In the planar perovskite architecture, the HTM layer is applied first on TCO, followed by the Perovskite layer, the ETM layer and the metal cathode, as shown in Fig (3-10c). Researchers discovered that perovskites could conduct holes themselves, leading to the development of the first planar hetero-junction PSC with an inverted design. This advancement opened up opportunities to explore selective layers made of both organic and inorganic materials. Oxide HTMs also allowed for the construction of mesoscopic p-i-n devices as shown in Fig (3-10d)[83].

3.2.1.3 Principle of Operation of Perovskite Solar Cells.

As mentioned above, perovskite is the active layer in PSCs. Therefore, upon absorption of photons, electrons are excited from the valence band to the conduction band and are then injected into the conduction band of the electron transport material (ETM), leading to perovskite ionization [84], shown schematically in Fig (3-13). The injected electrons are transported between the ETM particles and then extracted to the external load, where the work done is delivered as electrical energy. The hole transporting material (HTM) is used as an

electron mediator between the ETM and the back electrode. Therefore, the ionized perovskite is regenerated by receiving electrons from HTM.

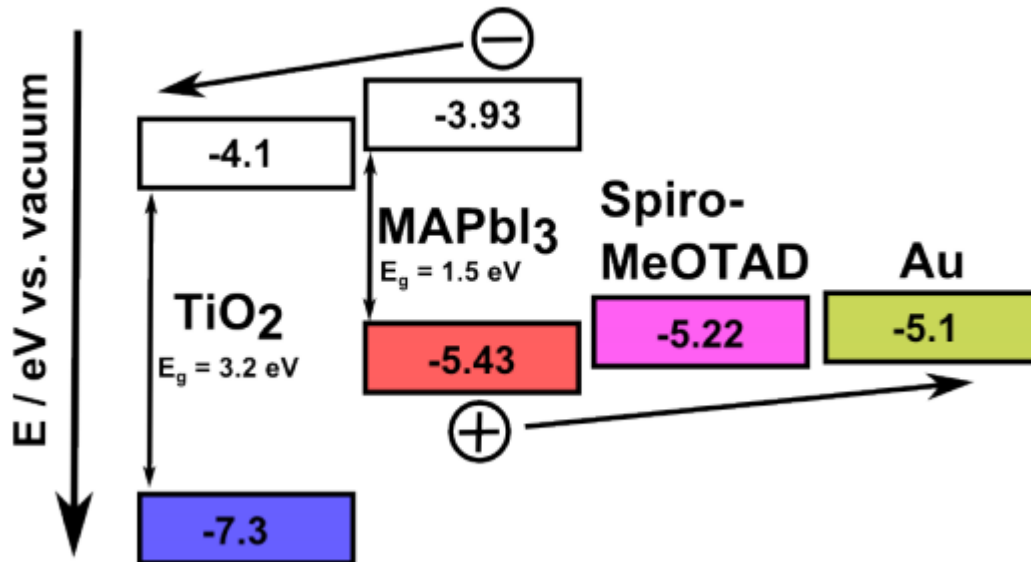


Fig (3-13): Schematic illustration of the operation principles of PSC, the numbers in the diagram indicate the edges of VB and CB for each layer [84].

3.3 Materials.

3.3.1 Perovskite

Hybrid organic-inorganic perovskites (HOIP) have many properties that make them suitable for applications such as solar cells, LEDs and other optoelectronic devices. As discussed in Chapter 2 the most prominent of these properties are ultrahigh photoluminescence quantum yield (PLQY) and low manufacturing costs, as well as their semiconductor properties, including high absorption coefficient, long carrier transport distance, and tuneable band gap. However, their stability is poor, which is a problem for application of devices based on these materials. Therefore, many studies have focused on them to improve their properties and stability as described in Chapter 2. Methylammonium lead iodide ($\text{CH}_3\text{NH}_3\text{PbI}_3$ (MAPI)) and formamidinium lead iodide ($\text{CH}(\text{NH}_2)_2\text{PbI}_3$, FAPI) are the main organic-inorganic halide perovskites that have been studied. In both of these perovskites, solution processing and spin coating have been used to prepare samples and a number of strategies have been applied to improve stability and efficiency of devices based on these materials (see Chapter 2).

3.3.2 Peptide Gels

Peptides are biological molecules that contain a chain of amino acid monomers linked by peptide bonds. The length, structure and chemistry of the peptide depends on the number of amino acids in the chain, and the side groups of the amino acids. A peptide can consist of 2 to 50 amino acids. Any chain of more than 50 amino acids is generally regarded as a protein. The chains of amino acids can form different types of peptide structures depending on the amino acids present in the chain and the chemical environment such as pH, salt concentration, temperature, and light [85]. Therefore, the peptides can be classified depending on the types of amino acids contained and the structures formed.

There are 20 natural amino acids whose general structures (Fig 3-14) are similar in that they all contain an amino group and a carboxylic acid group, but differ in the nature of the side chain group, R in Fig (3-14). This group identifies the type of each amino acid [86] [87], where the physical and chemical properties of an amino acid depend on it. Thus, the type and sequence of amino acids in the chain determine the properties of the peptide. The R-groups fall into different categories depending on basicity or acidity, aromaticity, hydrophobicity, charge and polarity, and it is these properties and the number of amino acids of particular R-groups which ultimately determine the structure and behaviour of a peptide and protein.

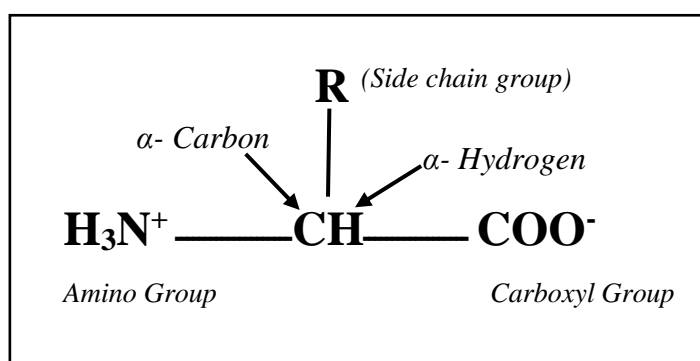


Fig (3-14): A general chemical structure of an amino acid

3.3.2.1 Structure of peptide

The structure of a peptide can be identified by the primary structure and secondary structure. The amino acid sequence gives the peptide's primary structure. Peptide bonds form when the amino group ($-\text{NH}_2$) of one amino acid molecule reacts with the carboxyl group ($-\text{COO}^-$) of another, with the elimination of H_2O as shown in Fig (3-15).

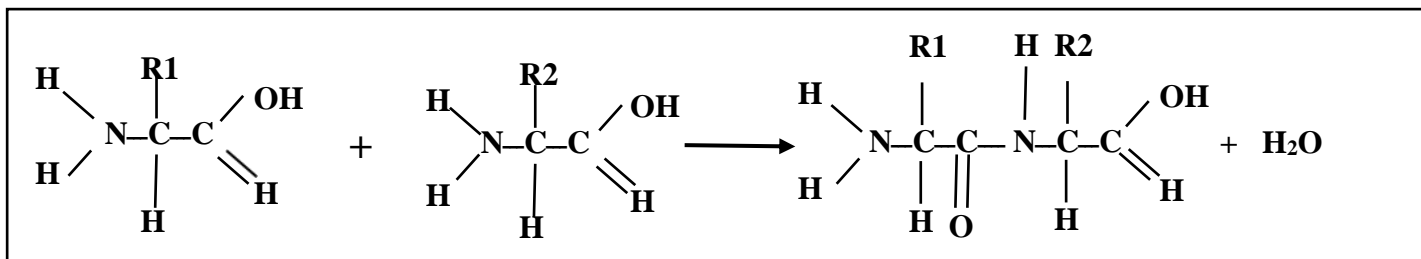


Fig (3-15): Peptide bond formation.

The secondary structure of the peptide describes how the amino acids in neighbouring peptide strands (or in long chains within a strand) interact with each other. These can consist of hydrogen bonds between the amine hydrogen and carboxylate oxygen, or chemical bonds such as sulphide bonds, for example. The secondary structure also defines bond angles of the amino acids that include the torsion angles ϕ and ψ along the peptide backbone as shown in Fig (3-15a). Typical secondary structures formed are:

β -sheet: a β -sheet is formed between two polypeptides that are linked by hydrogen bonds along their backbone. Each sheet consists of several peptides' strands (β -strands) that are joined by hydrogen bonds. β -strands linked could be in the same direction, thus form a parallel sheet or in opposite directions to form the antiparallel type [87] as shown in Fig (3-16b)

α helix: An alpha helix structure is formed spontaneously by linking spirally between the amide hydrogen and carbonyl oxygen of the amino acids by hydrogen bonds as shown in Fig (3-16c) [88]

3.3.2.2 Self-assembling peptides

Self-assembling peptides (SAPs) are peptides that are built by spontaneous associating of the molecules into ordered and well-defined structures. The self-assembled system is the result of non-covalent interactions that include hydrogen bonding, electrostatic interactions, and van der Waals forces. There are many factors that influence these interactions, and therefore define the structure and properties of SAPs. These factors can be summarised as follows:

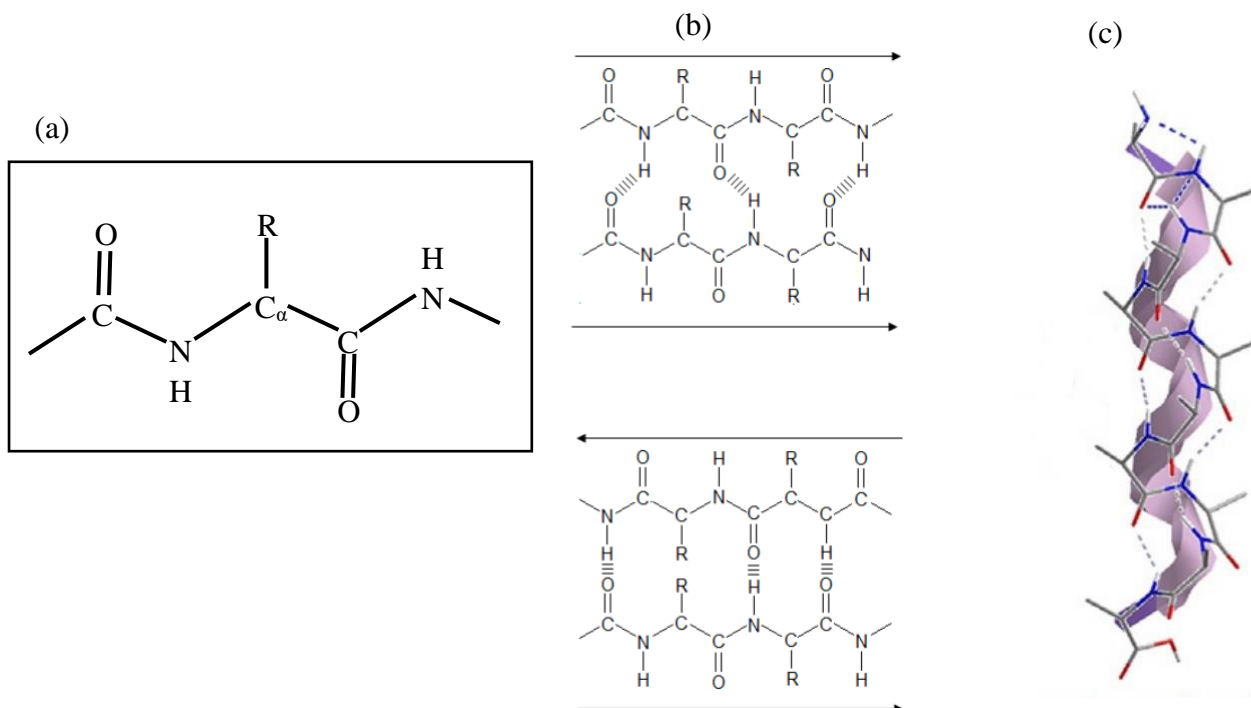


Fig (3-16): (a) Peptide backbone, C_{α} is a carbon atom bonded to the N-terminal (NH_3) and C-terminal ($-COOH$) of the peptide with rotation angles; φ and ψ , respectively., (b) Peptide secondary structures including hydrogen bonds: Parallel β -sheet and Anti-parallel β -sheet [87], (c) α helix structure [88].

3.3.2.2.1 Amino acids sequence and peptide length

Zhang *et al.* reported that altering the length of the peptides or changing the order of their amino acid sequence, affects the overall properties of the structure. This effect is attributed to a shift of electrostatic and hydrophobic interactions; hence the nature of the self-assembly of the peptides is modified. Gao *et al.* confirmed this argument by comparing peptides FEFEFKFK and FEFKFEFK, where the change in sequence of the amino acids resulted in a difference in their properties.

3.3.2.2.2 Concentration

The concentration of the peptides also affects the structure and properties of SAPs, where an increase in concentration of the peptide can result in a transition in the structure from fibrils to fibres and then to β sheets. At low concentration, peptides often form a random coil conformation. Also, the network mesh size of peptides decreases due to a rise in the density of the fibrils as the peptide concentration increases. Therefore, the structures and mesh size of SAPs can be controlled by adjusting their concentrations.

The gelatinous properties of a peptide appear at a peptide concentration higher than a specific level called critical gelation concentration (CGC). Saiani *et al.* reported that phenylalanine based peptides formed hydrogels when the concentration is higher than 8mg/ml [89].

3.3.2.2.3 pH

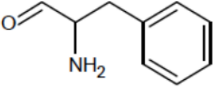
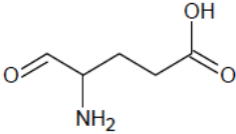
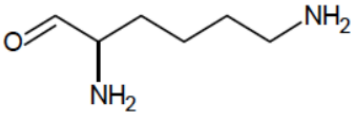
A change in pH affects the peptide structure due to inducing protonation or deprotonation of the amino and carboxyl groups, thus varying the static electric forces. This variation of forces, in turn, influences the molecular arrangement of the peptide [90]. It has been reported that MAXI peptide (n-VKVKVKVKVDPPTKVVKVKV-NH₂-c) is in a random coil conformation at pH 5.5, whereas when pH is adjusted to 9, its structure becomes a β -sheet [86].

3.3.2.2.4 The temperature

Temperature has an effect on the structure of SAPs. These effects include a denaturing of structure, triggering of assembly, or folding of the structure of the peptide depending on the type. The folding of the structure is attributed to the hydrophobic collapse due to dehydration of the nonpolar residues of an unfolded peptide by the increasing temperature [87]. It has been reported that the peptide MAX3 (VKVKVKTKVDPPTKVTKVKVNH₂) exists as an unfolded structure at 5°C, whereas at 80°C it forms a β -sheet [86].

The first part of this thesis will investigate the use of an octapeptide FEFKFEFK in the fabrication of MAPI perovskite. This is a self-assembled peptide that contains eight amino acid residues where F, E, and K refer to phenylalanine, glutamic, and lysine, respectively, as detailed in Table (3.1).

Table (3.1): Amino acids and their properties.

Amino Acid	Symbol	Structure	Properties
Phenylalanine	Phe, F		Neutral, Positively charged, hydrophobic
Glutamic	Glu, E		Acidic, Negatively charged
Lysine	Lys, K		Basic, Negatively charged, hydrophilic

FEFKFEFK peptide was found to self-assemble in solution to form a β -sheet structure. Its morphology is a relatively homogeneous dense network of the overlapped fibres with a mesh size from 15 to 30 nm and a fibre diameter of around 4nm [89].

The second part of this thesis will investigate using an octapeptide FEFKFEFKK to fabricate MAPI perovskite. This is a self-assembled peptide that contains nine of the previous amino acids. It is self-assembly in the solution to form extended fibrillar networks with a B-sheet structure. The width of network fibres was 3-4 nm, while fibre bundle sizes varied from ~5 to ~20 nm[91].

3.3.3 Titanium dioxide (TiO₂)

Titanium dioxide (TiO₂) is a semiconductor with a bandgap of 3.0 to 3.2 eV, corresponding to an absorption edge of light of around 387 nm – i.e. the near UV. There are at least 11 different crystalline forms of TiO₂ with crystal structures that are tetragonal, orthorhombic or monoclinic. Six phases are stable at low pressure, *i.e.* rutile, anatase, brookite, TiO₂(B), hollandite-like TiO₂(H) and ramsdellite-like TiO₂(R). whereas the columbite-like TiO₂(II), baddeleyite-like, TiO₂(OI), cotunnite-like TiO₂(OII), and fluorite-like cubic phases are usually formed at high-pressure in a laboratory under controlled pressure conditions. Rutile, anatase and brookite have primarily been studied for applications because they are naturally occurring titanium oxides and stable at atmospheric pressure. The structure of the three phases exists in different lattice configurations by stacking TiO₆ octahedrons in various ways as a basic unit, which is made up of a titanium atom surrounded by six oxygen atoms, as shown in Fig (3-17).[92][93].

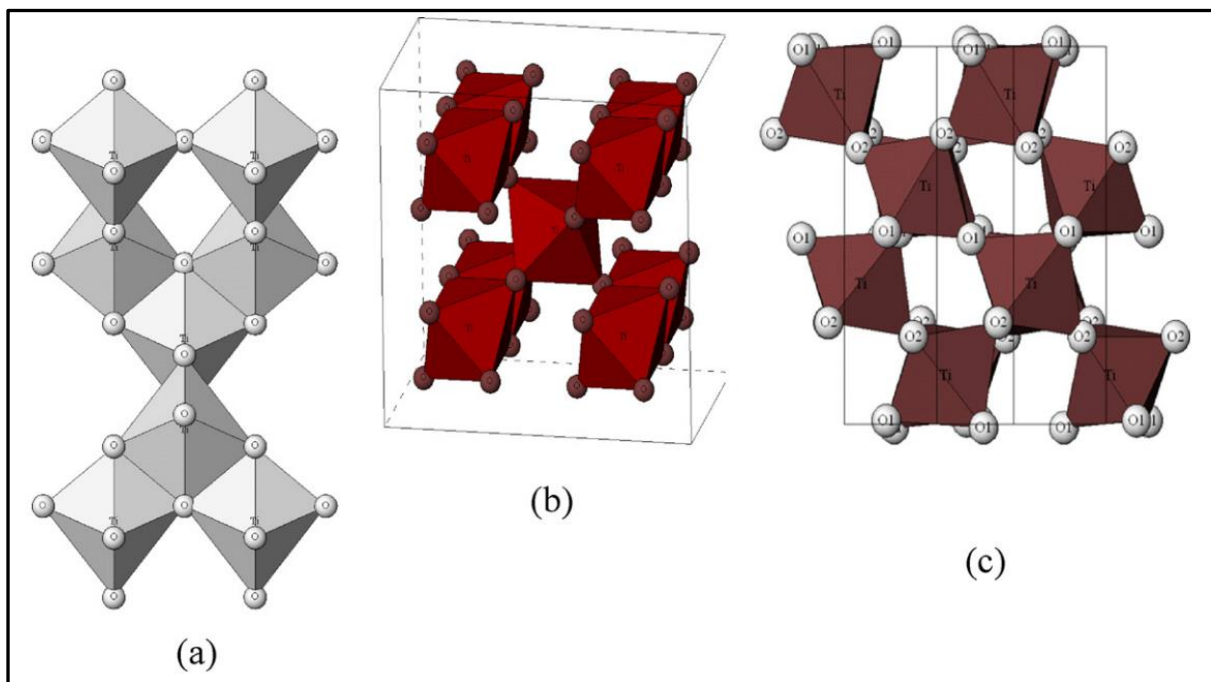


Fig (3-17): Crystalline structures of titanium dioxide (a) anatase, (b) rutile, (c) brookite [93].

TiO₂ has many properties, such as being a nontoxic, inexpensive material, with high chemical stability and various values of electrical conductivity attributed to the oxygen defects present

that depend on the chemical composition. This makes TiO₂ a good candidate for many applications, from a white pigment to photocatalytic and photovoltaic technology.

Defects in TiO₂ play a crucial role in nearly all applications, as they frequently dictate or affect its physicochemical properties. They can cause significant modifications that affect surface interactions in (photo)catalytic applications, influence mechanical characteristics, cause changes in electronic structure, and allow for the adjustment of the optical properties.

Defects in TiO₂ nanocrystals can arise from the inclusion of an extra atom that could be a foreign impurity, such as Ca, or a titanium or oxygen atom which is present not on a lattice site. These are called interstitial or Frenkel defects, as shown in Fig (3-18B). Ti interstitial defects are common and significantly impact surface reactions [92]. In contrast, missing oxygen (Fig (3-18C) or titanium (Fig (3-18D) atoms that typically occupy a lattice site, cause vacancy defects. O vacancies, common in reduced TiO₂ samples, are responsible for the n-type feature of TiO₂ due to the generation of two free electrons. In specific cases, loss of elemental oxygen from TiO₂ is possible under low oxygen pressure, resulting in the creation of oxygen vacancies and/or Ti interstitials. Releasing each oxygen molecule results in four electrons available that could cause creating Ti³⁺. Also, there are substitution defects that can be generated by replacing oxygen (Fig (3-18E) or titanium (Fig (3-18F) sites in the lattice TiO₂ with a foreign atom: positive ions such as P, S and Fe or negative ions like N, F and C are common substitution species in TiO₂[92].

Additionally, there are more defect types, such as dislocation defects and grain boundaries that form on the edge of crystals and at interfaces between crystals, grains, different phases or other materials.

Even though these defects could play a positive role in some applications, they could be a key to some drawbacks of TiO₂, such as forming carbon contamination on the TiO₂ surface, which could change some of its properties and affect its function as described in Section 2.2.3.3. Therefore, the passivation of these defects has been the target of several studies using different dopants and agents to reduce and prevent these negative effects. Here, we will investigate modifying thin films of TiO₂ using 4-fluoroaniline as a source for the fluorine.

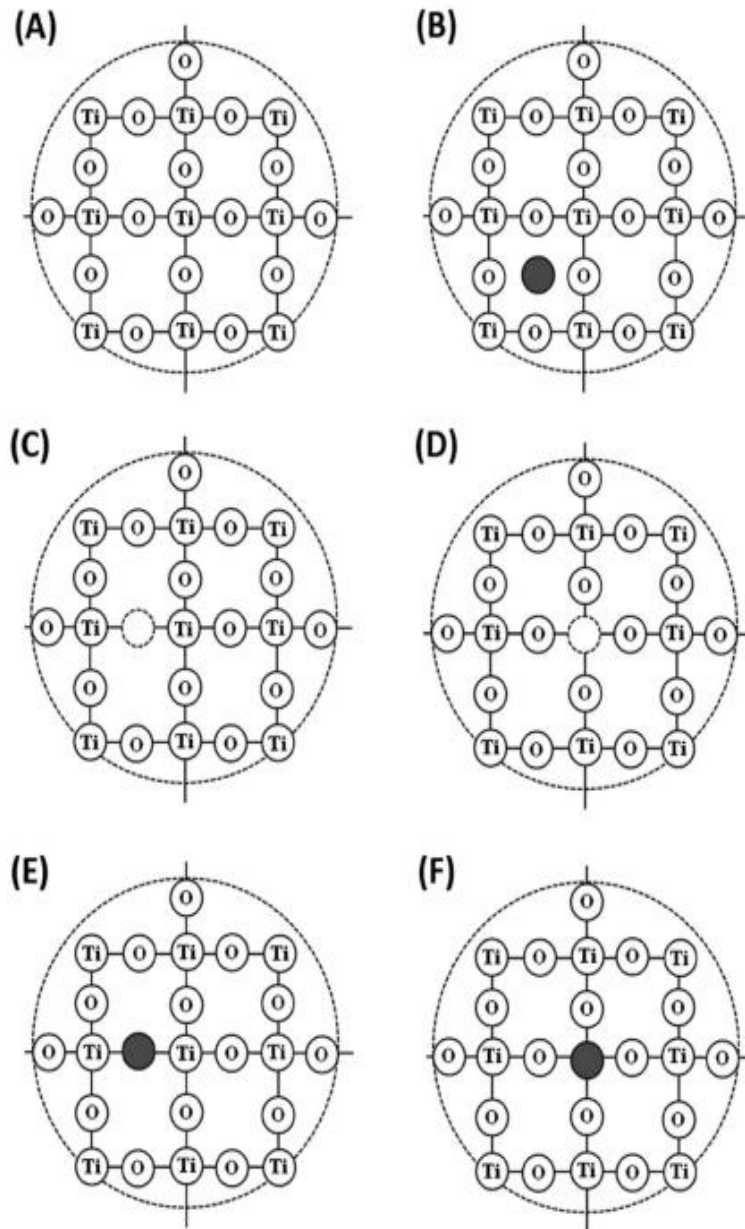


Fig (3-18): (A) Pure lattice, (B) interstitial defect, (C) O-vacancy, (D) Ti-vacancy, (E) Replacing O with a foreign atom, and (F) Replacing Ti with a foreign atom [92]

3.4 Techniques

3.4.1 X-ray Photoelectron spectroscopy (XPS)

X-ray photoelectron spectroscopy is the most widely used technique for all contemporary surface characterization methods [94]. It provides important information about surfaces, including quantitative and qualitative data for all elements present, except H and He. It can be used to determine the spatial chemistry of a surface on the μm scale, and understand the electronic structure of materials [92].

The physical principle of XPS depends on Einstein's interpretation of the photoelectric effect in 1905 [95]. Photoelectrons are emitted after a core-level electron absorbs a photon. The photoelectrons are emitted with a kinetic energy which depends on the energy of the exciting photon and the binding energy of the electron in the atom/ion, and it is the kinetic energy that is measured by XPS. Therefore, the electron binding energy can be calculated from the equation:

$$BE = h\nu - KE - \phi \quad (3.17)$$

where BE is the electron binding energy, $h\nu$ is the energy of the incident photon, KE is the kinetic energy of the photoelectron and ϕ is the work function and is the minimum energy needed to remove the electron from the highest occupied level of a metal into a vacuum [96]. Therefore, by measuring the binding energy, the elements on the surface sample can be identified. The key principle of XPS is that, due to scattering and transfer of energy during the scattering events, the electrons emitted from deeper into the sample lose kinetic energy. This means that only photoelectrons emitted from atoms close to the surface (1-10 nm) can escape into the vacuum and be measured without any loss of energy. The scattered electrons contribute to the measured background of the spectrum although they can also give rise to satellite features which can provide additional information about the material being studied.

To increase the sensitivity of XPS, ultrahigh vacuum (UHV) is necessary to avoid collisions between photoelectrons emitted and gas molecules, which allows most of the photoelectrons emitted to reach the analyser. The vacuum also prevents contamination of the sample surface by atmospheric gas molecules during the measurement time [97]. UHV can be achieved with a pumping system that removes gas from the measurement chamber until its air pressure reaches around 10^{-10} mbar [96]. Despite the importance of UHV, some problems may however arise during its application that may affect results. One issue is that some of the chemical species which form under high pressure, may desorb from the sample surface during

measurement, so freezing and measuring them under low temperatures ($T < 130$ K) is required to avoid this [98]. Also, there is a probability of the presence of differences in surface structure and chemistry in UHV in comparison to realistic conditions [97].

The main components of most modern XPS spectrometers are the monochromatic X-ray source and the electron energy analyzer, as shown schematically in Fig (3-19). The monochromatic X-rays source usually consist of an electron gun as a source of a beam of electrons and a coated anode as a target material. The beam of electrons generated by the electron gun can produce a tightly focused electron spot on the anode, creating a core hole through electron excitation. Filling this core hole by outer shell electrons leads to a well-defined X-ray beam emission. The X-rays are then focused onto the sample using a crystal grating, typically based on a Rowland circle [99].

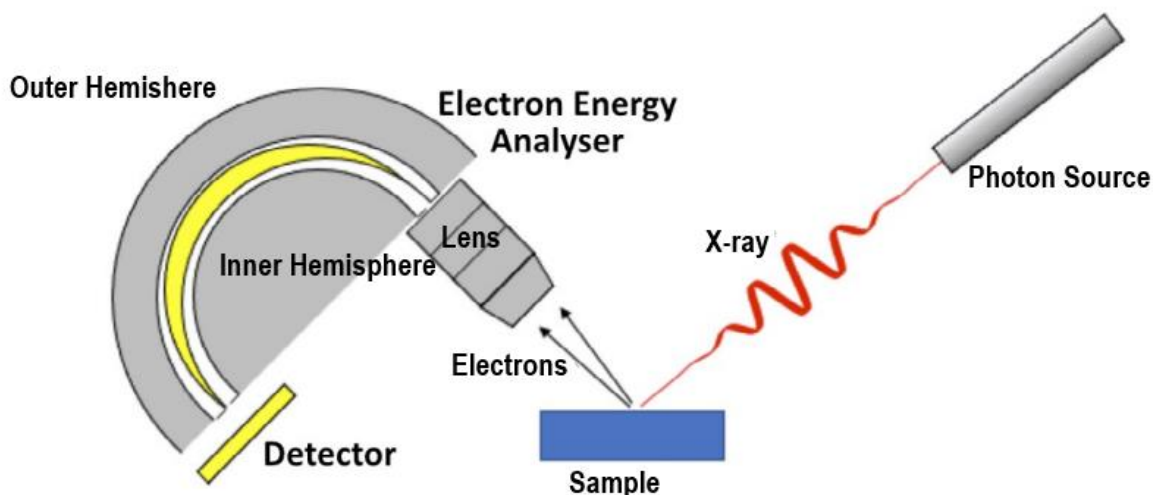


Fig (3-19): Schematic of the main components of a photoelectron spectrometer [99]

The electron energy analyser measures the photoelectrons emitted from the sample at each kinetic energy to generate an XPS spectrum. The electron energy analyser, usually used with modern XPS, is a concentric hemispherical analyser (CHA). The CHA comprises three distinct components: an electrostatic lens, inner and outer concentric hemispherical electrodes, and an electron detector, as shown in Fig (3-19). The potential difference between the two hemispheres governs the passage of electrons through the analyser's exit slit and onto the detector. A lens device retards or accelerates photoelectrons and focuses them on an entrance slit before these hemispheres. The instrumental energy resolution of measurements is usually governed by an

operator-controlled parameter called pass energy, which depends on the kinetic energy of photoelectrons passing through the hemispheres and the energy width of the X-ray source.

In this work, conventional XPS equipment at the PSI is used to analyse the surfaces of the thin films prepared.

3.4.2 Ultraviolet-visible (UV-vis) spectrophotometry

UV-vis spectrophotometer is an versatile tool to determine the transmittance, absorbance and reflectance spectrum of materials studied [100]. It can also allow the band gap of a material to be measured. A Perkin Elmer lambda 1050UV/Vis/NIR spectroscope was used to measure the absorption and transmittance of prepared samples from 250 to 850 nm. The spectrometer consists of a UV- visible light source, reference and measurement cuvette, and detector. Fig (3-20) shows the principle of operation, which depends on measurement of the intensity of light transmitted through the sample (I) and reference (I_0). From this, the absorbance (A) of the sample is given by

$$A = \log_{10}\left(\frac{I_0}{I}\right) \quad (3.18)$$

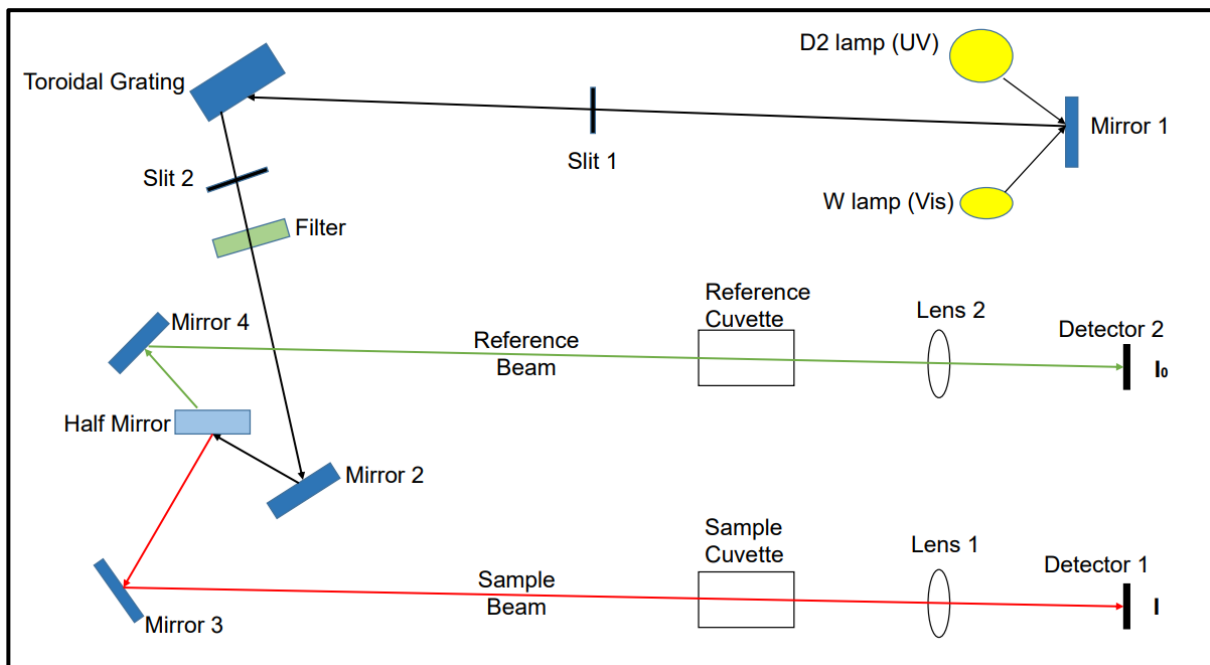


Fig (3-20): Working Principle of UV-vis spectrophotometry.

The absorption coefficient (α) can be found from the Beer–Lambert law:

$$I = I_0 e^{-\alpha d} \quad (3.19)$$

So, absorbance is related to the absorption coefficient by,

$$\alpha = \frac{2.303 A}{d} \quad (3.20)$$

The optical band gap and absorption coefficient can be related by:

$$\alpha = \left(\frac{k}{hv}\right)(hv - E_g)^\beta \quad (3.21)$$

where k is a constant, h is Planck's constant, and $\beta = \frac{1}{2}$ or 2 for a direct band-gap or indirect band-gap material, respectively. Because perovskite has a direct gap, Equation (3-21) becomes:

$$\alpha = \left(\frac{k}{hv}\right)(hv - E_g)^{\frac{1}{2}} \quad (3.22)$$

Which gives

$$(hv\alpha)^2 = C(hv - E_g) \quad (3.23)$$

Where C is constant. Therefore, the band gap can be estimated from the linear relationship between $(hv\alpha)^2$ and (hv) where E_g is calculated from the intersection of the linear region of the

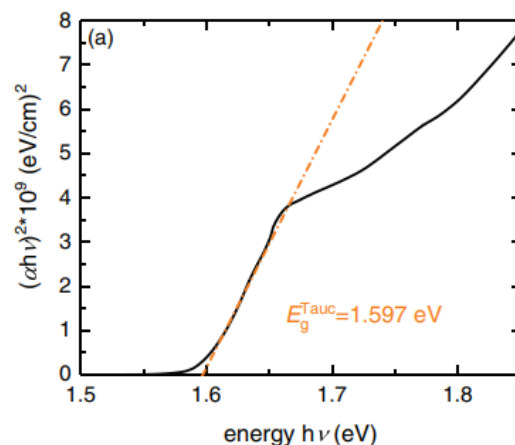


Fig (3-21): Tauc plot from UV-Vis of MAPbI₃ [101].

absorption curve with the x axis, as shown in Fig (3-21). This is an example Tauc plot from UV–Vis analysis of a MAPbI₃ [101].

3.4.3 Scanning Electron Microscopy (SEM)

An FEI Quanta 250 FEG-SEM was used to observe the surface morphology of the prepared samples. Scanning electron microscopy (SEM) is a technique for creating images on the micrometre or nanometre scale. It consists of an electron source, electromagnetic lens system and a detector as shown in Fig (3-22). The principle of SEM operation is based on a beam of electrons, generated from a tungsten filament or a field emission gun, and focused by a series of apertures and lenses. This beam hits the sample surface, emits electrons that will be collected by detectors, which are then used to create a magnified image of the specimen.

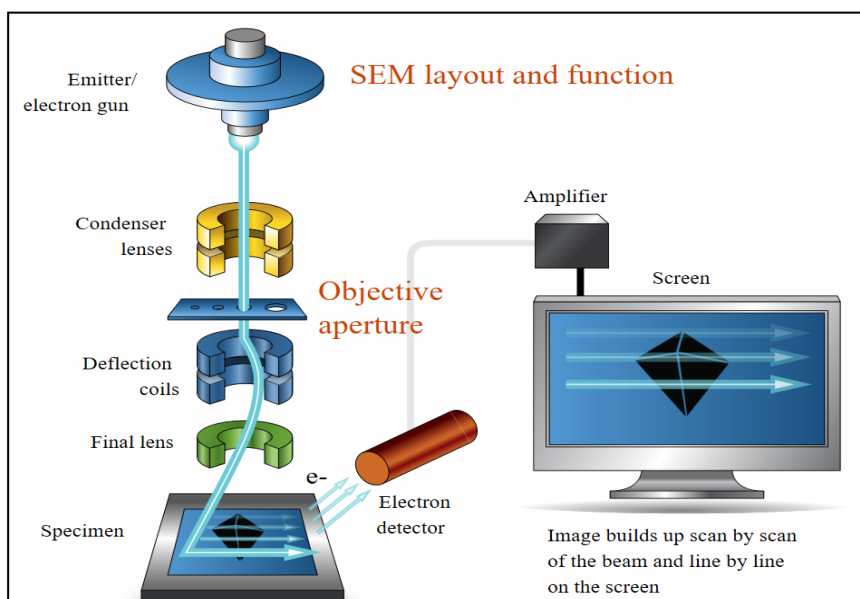


Fig (3-22) The major components of an SEM (<https://myscope.training>)

3.4.4 Photoluminescence spectroscopy

Photoluminescence (PL) spectroscopy is a technique to measure the optical properties of a sample, using electron-hole recombination. The schematic of the main components of a fluorescence spectrometer and the principle of operation is shown in Fig (3-23)[101]. The sample absorbs the energy of an incident photon, which causes the film to generate free carriers (electrons and holes). When the radiative recombination between the generated electrons and holes occurs, a photon is released (photoluminescence) and recorded by the detector as a PL spectrum as shown in Fig (3-24), with intensity and wavelength depending on the recombination conditions that occur. The efficiency of the photoluminescence process also depends on the quantum yield ϕ that can be measured from equation (3.24) [3].

$$\phi = \frac{\text{Number of photons emitted}}{\text{Number of photons absorbed}} \quad (3.24)$$

Here, photoluminescence (PL) spectra were measured using a Horiba Fluorolog Visible PL/PLE spectrometer. The PL measurements in this work were carried out using a $\lambda = 450$ nm excitation source and collecting light emitted at wavelengths between 500nm and 850nm.

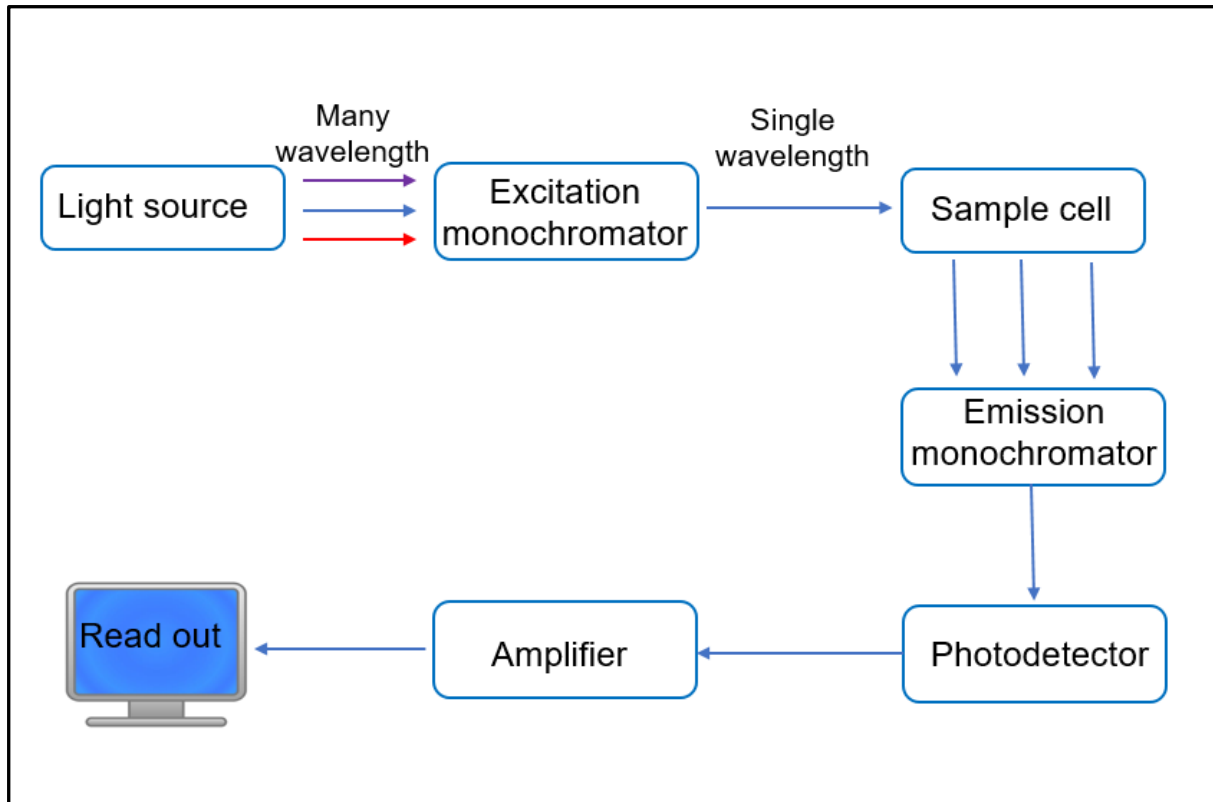


Fig (3.23): Schematic diagram of a fluorescence spectrometer.

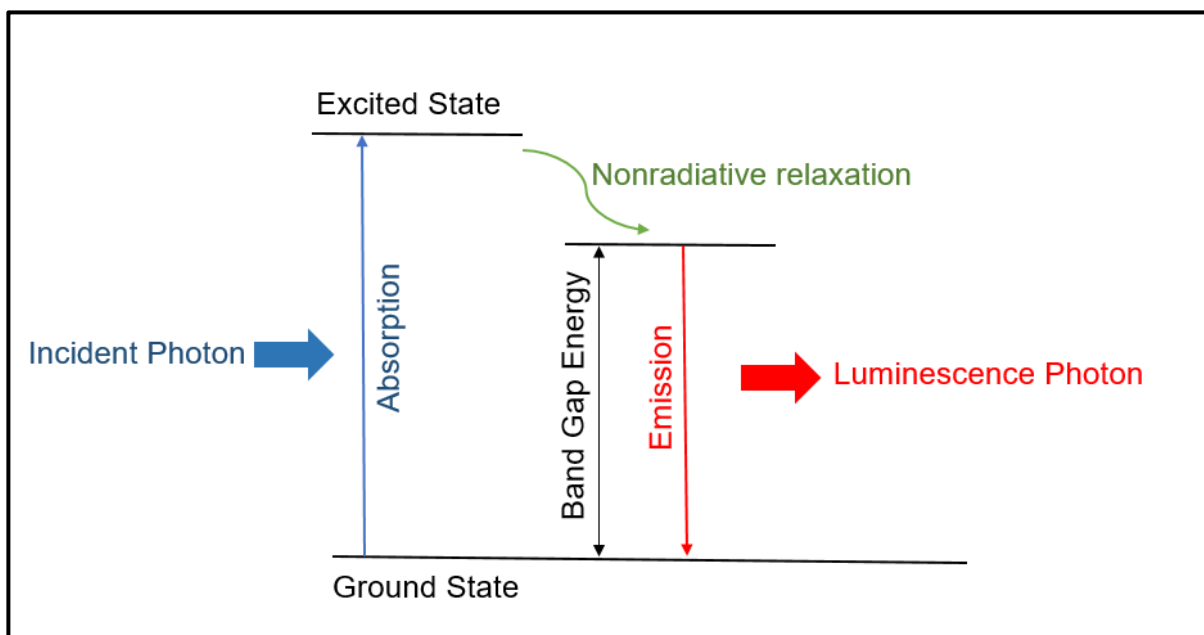


Fig (3-24): Schematic representation of photoluminescence (PL) spectra principle.

3.4.5 Time-resolved photoluminescence spectroscopy (TRPL)

Time-resolved photoluminescence (TRPL) is an extension of fluorescence/photoluminescence spectroscopy, in which the fluorescence signal of a sample is measured as a function of time after it has been excited by a pulsed laser. It is a direct method for measuring the fluorescence lifetime resulting from the radiative recombination of photogenerated charge carriers. Fig (3-25) shows the main components of a typical TRPL instrument. The core of the system is the time-correlated single-photon counting (TCSPC) system, which typically employs electronics to guide the laser pulse as the "start" signal, with the measured photons from the single-photon sensitive detectors acting as the "stop" signal. A histogram that displays the appearance of emissions with time following the excitation pulse is created by sorting the delay times. The measurement is performed numerous times to account for the statistical nature of the fluorescence emission [102]. Here, TCSPC is used to measure the PL lifetime decay using a $\lambda = 450$ nm excitation light source and collecting light emitted at a wavelength of 770 nm.

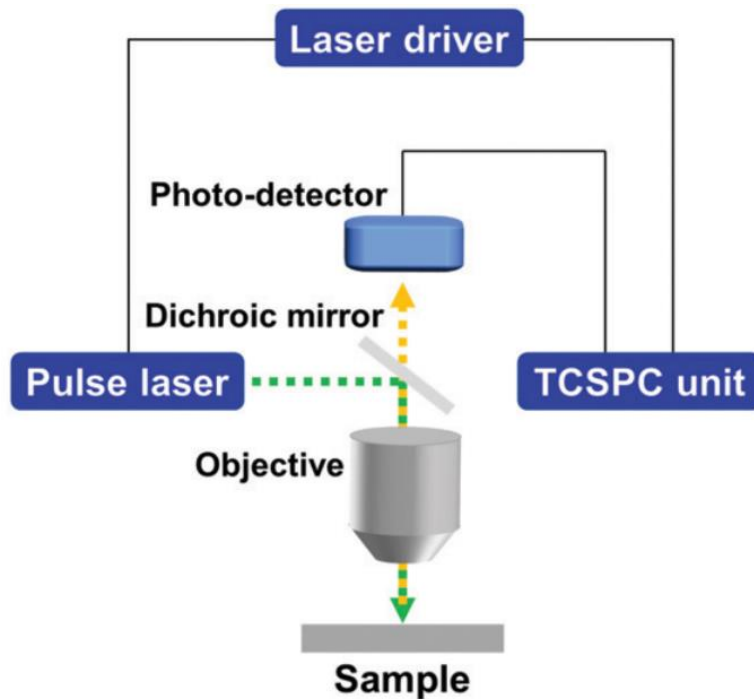


Fig (3-25): Schematics of the time-resolved photoluminescence (TRPL) [102]

3.4.6 X-ray diffraction (XRD)

X-ray diffraction is an analysis technique which utilises the diffraction of X-rays by crystal planes to form a diffraction pattern on a detector. The diffraction patterns are characteristic of a given material based on its crystal structure. The crystal lattice is governed by an arrangement of atoms that repeat three-dimensionally to make up the crystal structure. Each symmetrically unique group of atoms is represented as a single point called a lattice point. Lattice points are arranged into three-dimensional periodic arrays. These periodic arrays can be described by a unit cell, which is determined by connecting vectors extending between the lattice points along the three principal axes of the coordinate system. Unit cells differ by varying lengths of the three vectors (a , b , c) and the angles made between each other (α , β , γ). This results in seven distinct structures, called crystal systems, i.e. triclinic, monoclinic, orthorhombic, tetragonal, hexagonal, rhombohedral, and cubic as shown in Table 3.2. Also, these basic lattice types can vary by the position of the lattice points, i.e. they could be at corners only (*Primitive* (**P**)) or with additional lattice points in the middle of each cell (*Body-centered* (**I**)), a center of each face (*Face-centered* (**F**)) or at the base of the cell (*Base-centered* (**C**)). Based on the crystal system and the various types of unit cells allowed for each symmetry, there are only fourteen ways for periodically filling space called Bravais lattices [103] as illustrated in Table (3.2).

Table 3.2: The seven crystal systems and fourteen Bravais lattices

Crystal system	Axis system		Bravais lattice
Cubic	$a = b = c$	$\alpha = \beta = \gamma = 90^\circ$	P,I,F
Tetragonal	$a = b \neq c$	$\alpha = \beta = \gamma = 90^\circ$	P,I
Hexagonal	$a = b \neq c$	$\alpha = \beta = 90^\circ, \gamma = 120^\circ$	P
Trigonal	$a = b = c$	$\alpha = \beta = \gamma \neq 90^\circ$	P
Orthorhombic	$a \neq b \neq c$	$\alpha = \beta = \gamma = 90^\circ$	P,C,I,F
Monoclinic	$a \neq b \neq c$	$\alpha = \gamma = 90^\circ, \beta \neq 90^\circ$	P,C
Triclinic	$a \neq b \neq c$	$\alpha \neq \beta \neq \gamma \neq 90^\circ$	P

X-ray diffraction works on the principle of interference between the scattered waves by neighbouring lattice planes, where peaks arise in the directions in which constructive interference occurs. Constructive interference or diffraction is obtained when the scattered waves satisfy Bragg's Law, where the difference between the phase of waves scattered from adjacent lattice planes is an integer multiple of wavelengths. Fig (3-26) illustrates this situation for two lattice planes where $a_1 + a_2 = n \lambda$ [104]. Therefore, the Bragg equation that describes the condition for diffraction to occur is

$$n\lambda = 2d \sin \theta \quad (3.25) \quad [104]$$

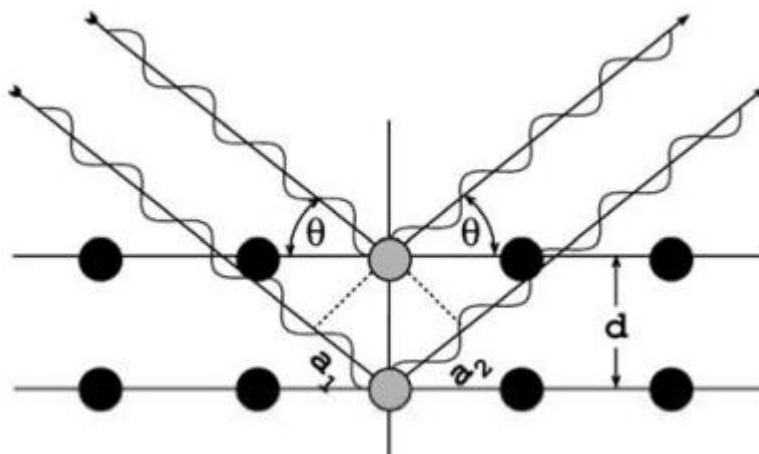


Fig (3-26): Diffraction of X-rays from the planes in a crystal (9). $a_1 = a_2 = d \sin \theta$. [104]

Where n is the order of diffraction, λ is the wavelength of X-ray, d is the lattice spacing, and θ is the angle between the lattice planes and the incident beam.

Therefore, the pattern of the resulting diffraction peaks characterises the crystal structure of the measured material. It can be defined by comparing the resulting diffraction pattern with literature or by use of the crystallographic database to identify the structure; thus, the material prepared can be determined.

Additionally, the crystallite size of the material can be determined by the observed broadening of peaks. In large crystals, the constructive interference, which occurs whenever a phase difference between scattered waves is not exactly λ , is cancelled by destructive interference with diffracted waves from deeper planes when the phase difference is around $\lambda/2$; hence sharp peaks are observed. In very small crystals, on the other hand, the absence of diffracted waves from deeper planes, which cancel the constructive interference from minor deviations from the ideal Bragg angle, produces intensity at lower and higher angles than the Bragg angle, thus broadening the peaks. The X-ray diffraction peaks broadening is related to the crystallite size via the Scherrer equation, which is

$$d = \frac{k\lambda}{\beta \cos \theta} \quad (3.26) \quad [105]$$

Where d is the crystallite size; λ is the wavelength of the X-ray; β is the full width at half maximum of the diffraction peak (FWHM); θ is a diffraction angle; and k is the Scherrer constant.

A Philips X'pert Pro XRD instrument was used to measure thin films prepared in this thesis.

3.4.7 Photovoltaic characterization

Fig (3-27) shows the system used to measure the photovoltaic characteristics of the prepared devices. It consists of a solar simulator (Solar-Light) which produces AM1.5 light (Fig (3-27a)). This is connected to an electrometer (Keithley, 2420 model) (Fig (3.27b)). The 2420 electrometer is connected to the prepared devices through a square metal mask (Fig (3-27c)), which defines an area of 0.024 cm^2 as the effective area under illumination. This system is connected to a computer to record and plot the I-V characteristics of the devices through *I-V* software. Before the measurement, an NREL-certified reference silicon cell (Fig (3-27d)) is used to calibrate the solar simulator.

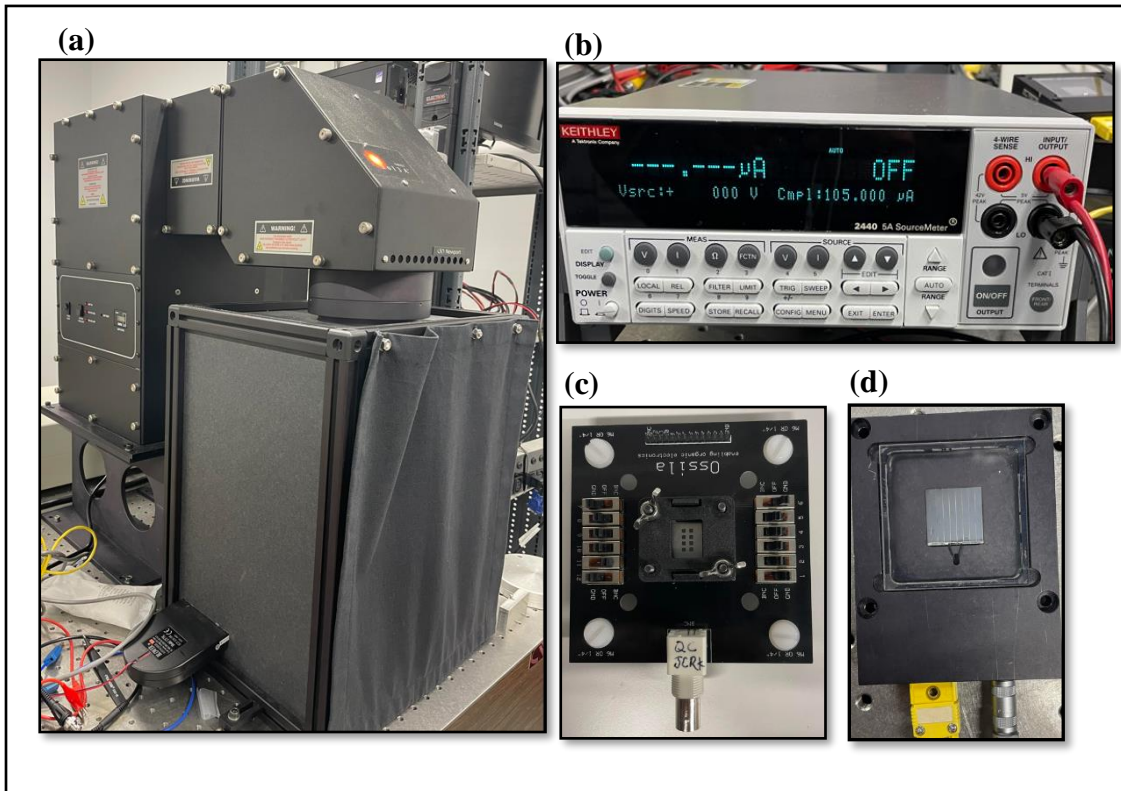


Fig (3-27): (a) Solar simulator, (b) source-meter (Keithley), (c) a square metal mask, (d) an NREL-certified reference silicon cell.

In this thesis the techniques and materials outlined above are used to characterise the optoelectronic properties of peptide-perovskite materials and to determine the efficiency of photovoltaic cells constructed from the peptide-perovskite composite. In addition, XPS and is used to determine the surface chemistry and stability of peptide-perovskite and the effect of F-doping TiO_2 to determine whether this can reduce the amount of hydrocarbon contamination on the surface. XRD is used to determine structure and stability of the peptide-perovskite composite materials as a function of humidity.

Chapter 4. The effect of a FEFKFEFK peptide gel as a template in the fabrication and stability of methylammonium lead iodide perovskite.

4.1 INTRODUCTION

Organic-inorganic hybrid perovskites have attracted the attention of researchers due to their optical and electrical properties as well as the high-efficiency of photovoltaic solar cells that use them as a light absorber layer. It has been found that the properties of perovskite can be controlled by controlling the size, shape, spatial arrangement and composition, factors that all depend on fabrication strategies [46]. One of the major problems with the application of these perovskites is their stability in ambient conditions. It is well known that these materials decompose when exposed to water vapour, heat and UV light [20] [16]. Numerous research articles have focused on perovskites with various strategies aiming to treat the problems of degradation. Mixing multiple cations to synthesise perovskite is a known strategy for overcoming phase, and thermal instability, where mixing of formamidinium (FA) and methylammonium (MA) cations in perovskites can lead to enhanced stability of perovskite as well as a change in optoelectronic properties such as broadening of the absorption spectrum, reduction of the band gap and increasing PL lifetimes[28][29][30]. Also, the encapsulation of PSCs has been employed, with an outer encapsulation that aims to prevent the degradation of the device due to environmental factors such as moisture, oxygen, and heat, or an internal encapsulation that could address intrinsic instability issues, such as thermal degradation, ion migration and hygroscopicity [37] [38]. The use of a template is considered to be an effective method to achieve both size control and enhanced stability, since it contributes to control of the size and shape of nanomaterials during synthesis, by templating them inside pores of materials[106]. The template method could be served by various porous materials for these purposes, such as mesoporous silica (MS), microgels (MGs)[55], polystyrene (PS), metal-organic framework (MOFs)[54] and anodized aluminium oxide (AAO) [106].

Peptide gels can also be used as templates due to their ability to self-assemble and to functionalise materials, as well as acting as a medium in the synthesis and construction of nanostructures [107]. It is possible then that their network structures could be used to govern the growth of the perovskite, controlling the shape and size of the grains and also passivating defects in the perovskites [65].

In this chapter, we investigate the use of an octapeptide, FEFKFEFK, in the fabrication of methylammonium lead iodide perovskite ($\text{CH}_3\text{NH}_3\text{PbI}_3$, MAPI) in order to determine whether

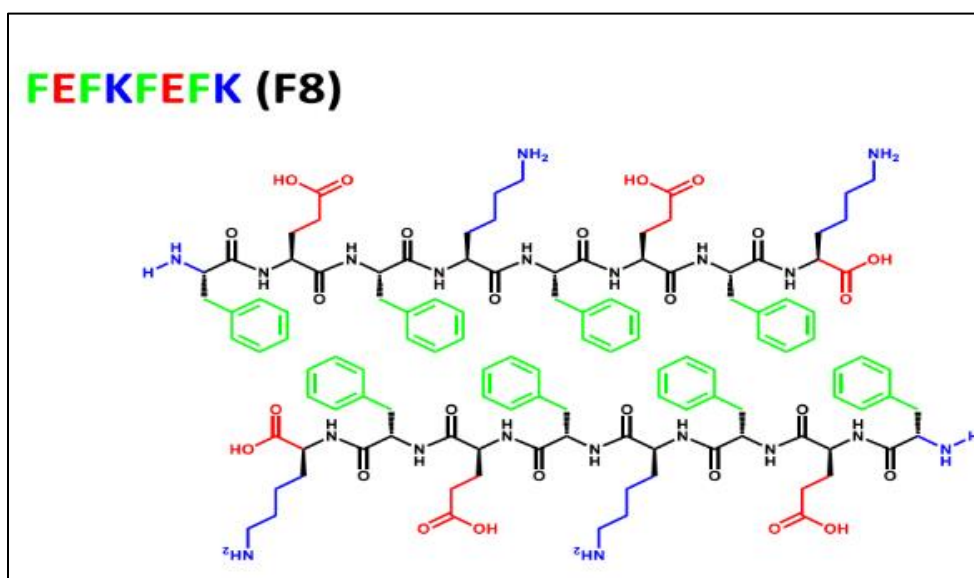


Fig (4-1): Chemical structures of F8 peptide presented in a schematic antiparallel β -sheet conformation [85].

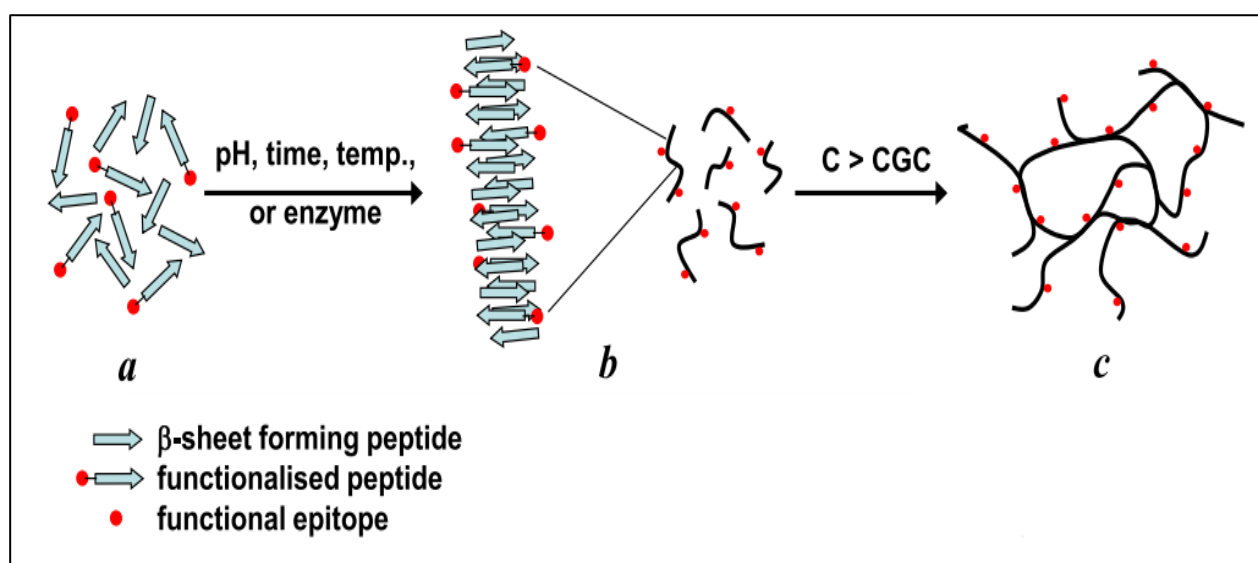


Fig (4-2): Schematic representation of the self-assembly and gelation pathway of β -sheet forming peptides, where a is the formation of the β -strand, b is the formation of the antiparallel β -sheet, and c is the formation of the “elemental” fibres of the network. [85].

these gels are able to control the particle size and improve the stability of the perovskite. The octapeptide FEFKFEFK is a self-assembled peptide that contains eight amino acid residues where F, E, and K refer to phenylalanine, glutamic acid, and lysine. This peptide is known to

self-assemble into antiparallel β -sheet-rich fibres (Figure (4-1)) and form transparent gels at concentrations higher than 8 mg/ ml, which is the critical gelation concentration (CGC). Synthesis and gel formation follows the path shown in Figure (4-2).[85]

4.2 EXPERIMENTAL SECTION

4.2.1 Materials:

The following materials were used in the synthesis of perovskite- peptide composite: lead iodide (99%, Sigma- Aldrich) and N, N-dimethylformamide (DMF) (99.8%, Sigma-Aldrich), methylammonium iodide (MAI) (98%, Ossila), indium tin oxide (ITO) substrates (Ossila), the peptide (FEFKFEFK) (BIOMATIK), titanium diisopropoxide bis (acetylacetonate) (Sigma-Aldrich), 1-butanol (Sigma-Aldrich), bis(trifluoromethane)sulfonimide lithium salt (Li-TFSI)(99.95%, Sigma-Aldrich), 4-tert-butyl pyridine (TBP)(98%, Sigma-Aldrich), acetonitrile, anhydrous,(99.8%, Sigma-Aldrich), chlorobenzene, anhydrous, 99.8%, Sigma-Aldrich) and 2,2',7,7'-tetrakis(N,N-di-p-methoxyphenylamine)-9,9'-spirobifluorene (Spiro-MeOTAD)(99 %, Ossila). TAPE, POLYIMIDE MASK, 12 mm, 33M; Tape Type: masking; tape backing material (PI).

4.2.2 Preparation of MAPI-peptide thin films.

The thin films studied were prepared by the following steps:

4.2.2.1 MAPI precursor solution

1.1 moles of lead iodide (PbI_2) were dissolved in N, N-dimethylformamide (DMF) as a solvent with stirring on a hotplate for one hour at 70 °C. Then, methylammonium iodide (MAI) was added to the lead iodide solution and stirred for 30 min at room temperature. The molar ratio of MAI to PbI_2 was kept at 1:1.

4.2.2.2 MAPI-peptide solutions

Different amounts of the peptide (40, 60, 80 and 100 mg/ml) were added to the prepared MAPI solution to obtain mixed solutions at different concentrations; marked Mix40, Mix60, Mix80 and Mix100, respectively.

4.2.2.3 Deposition of the thin films

Glass substrates covered by a thin film of indium-doped tin oxide (In-SnO_2 or ITO) were cleaned three times; in 3.0 vol% diluted Hellmanex III in DI water, then in pure DI water, then in ethanol or acetone or propane-2-ol (IPA) using ultrasonication for 10 mins (at least) in each

step. After being cleaned and dried, they were treated with UV-O₃ for 15 minutes before deposition of the perovskite films. After pre-heating the substrate, 100 μ l of the prepared solution was dropped onto the substrate and spin-coated at 4000 rpm for the 30s. Then, 200 μ l of ethyl acetate as an anti-solvent treatment was added after 10 sec running. Finally, the deposited substrates were heated on a hotplate at 100°C for 10min.

4.2.3 Manufacture of perovskite solar cells

To fabricate the devices, we used patterned ITO substrates, which were cleaned three times, as described above and then the following four layers were deposited:

4.2.3.1 Electron transport layer

A compact TiO₂ layer was deposited for this purpose. To achieve that:

- **Preparation of solution:** To deposit this layer, two concentrations of precursor solutions (0.1M and 0.3M) were prepared by adding 50 μ l and 150 μ l from titanium diisopropoxide bis(acetylacetonate) to 1 ml 1-butanol and stirring for 15 min.
- **Deposition of layer:** Before the deposition, half of the patterned ITO fingers are covered by P1 tape. 90 μ l of the 0.1 M solution was dropped onto the substrate, spin-coated at 2000 rpm for 30s and dried at 120 C on a hot-plate for 10 minutes. Then this step is repeated using the 0.3 M precursor solution as a second step. Finally, the deposited samples are annealed at 500 C for 30 min in a furnace.

4.2.3.2 Active layer

The active layer in PSCs is perovskite. Pure MAPI and the peptide-MAPI mixtures, of differing concentrations, were deposited on TiO₂, as mentioned in section 2.1.3.

4.2.3.3 Hole transporting layer (HTL)

Doped Spiro-MeOTAD was used for the hole transport layer. This was deposited on the perovskite layer after allowing it to cool down to room temperature. The doped Spiro-MeOTAD solution is prepared by mixing three solutions *i.e.*:

- Spiro-MeOTAD solution, prepared by dissolving 40 mg spiro-MeOTAD in 0.5 mL chlorobenzene.
- 10 μ l Li-TFSI solution, prepared by dissolving 520 mg Li-TFSI in 1mL acetonitrile (ACN) and stirring for 15 min.
- 15 μ l *tert*-butylpyridine (TBP).

Then, 90 μ l mixture was spin-coated at 2000 rpm for 30 s.

4.2.3.4 The Cathode

Finally, 100 nm of Au or Ag was deposited on HTL by thermal evaporating under a vacuum.

4.2.4 Instrumentation

X-ray diffraction (XRD) analysis was performed on a Bruker D8 Discover with a Cu-K α X-ray source with 2 wavelengths, 1.540598 Å and 1.544426 Å over the 2θ range of 7°–80° with a scanning rate of 5° min⁻¹. Photoluminescence (PL) spectra were measured using a Fluorolog Horiba Jobin Yvon spectrometer. The PL measurements were carried out using a $\lambda = 450$ nm excitation line and collecting light emitted at the wavelengths range between 500nm and 850nm. Time-resolved PL was measured for the prepared thin films using a time-correlated, single-photon counting (TCSPC). The samples were excited using picosecond pulsed diode-laser source at a wavelength, $\lambda = 450$ nm, and the detector was set to collect emitted photons at a wavelength of 770nm, as determined from the static PL measurements. Absorbance spectra were measured using a PerkinElmer Lambda 1050 with over the range between 250 to 850nm. The scanning electron microscope (SEM) was carried out using Quanta 250 FEG equipment to study the morphology of the samples' surface. XPS was performed to determine the surface chemistry of the sample. JV curves were used to determine the device PV potential, parameters, and conversion efficiency (η) based on templated MAPI.

4.3 RESULTS AND DISCUSSION

The FEFKFEFK peptide is self-assembled into antiparallel β -sheet-rich fibres when dissolved in water, as reported by A. Saiani *et al* [89], giving rise to a strong absorption band at 1625cm⁻¹ and a weak one at 1695 cm⁻¹. These same absorption bands can be seen in FTIR spectra when the peptide is dissolved in MAPI precursor solution, as shown in Figure (4-3). At the same time, XRD data suggest that the peptide does not prevent the fabrication of MAPI when mixing them.

Figure (4-4) shows the XRD pattern of MAPI and the MAPI peptide, confirming that the MAPI-peptide sample contains MAPI perovskite, matching the prepared pure MAPI sample, and MAPI calculated PXRD spectra. The calculated PXRD was obtained using Mercury software using CIF files (2107954) from the Crystallography Open Database[108]. Therefore, the proposed scenario is that MAPI crystallises inside the network mesh made of the peptide gel. The network mesh size and porosity decreases with an increase in peptide concentration

due to an increase in fibre density, as reported by Saiani et al.[89]. One might expect that this decrease in pore size may affect the MAPI crystal size and its optical and electrical properties as described previously. The results obtained during this investigation illustrate the apparent effects of mixing the peptide with MAPI that increase with an increase in peptide concentration. These effects can be summarised as outlined in sections from 4.3.1 to 4.3.4:

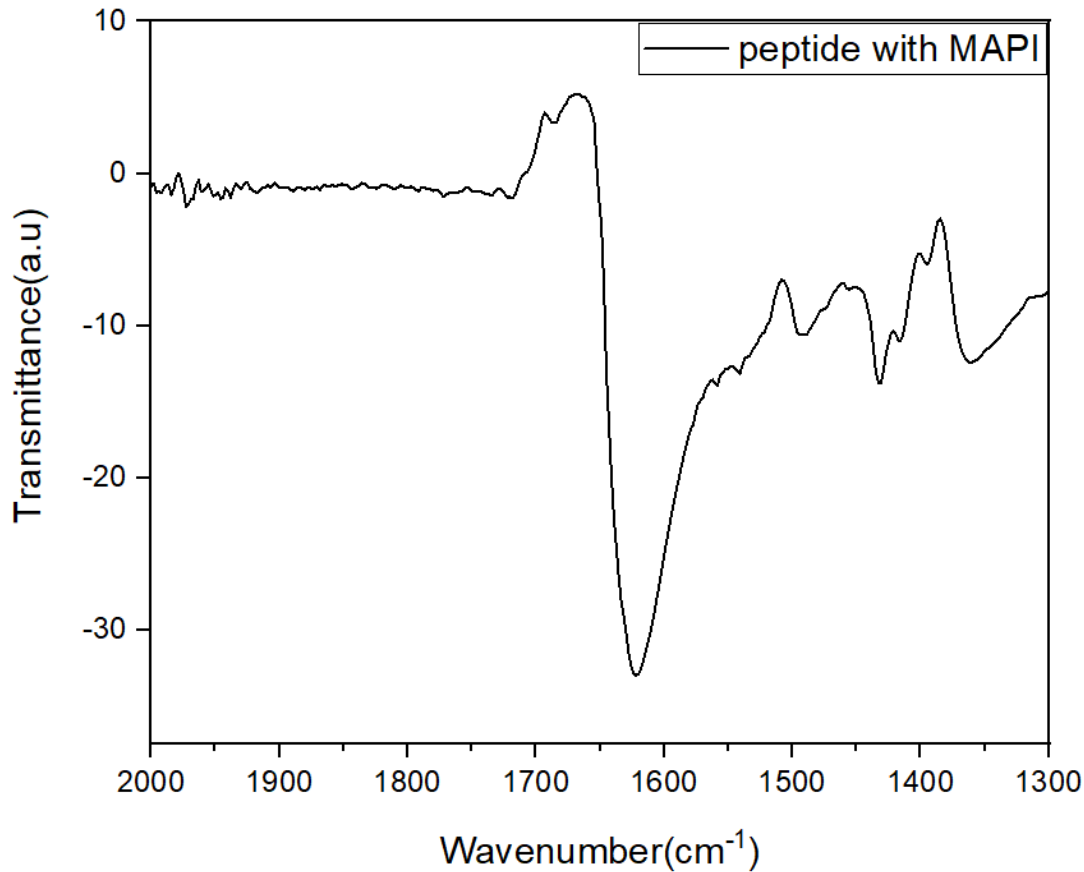


Fig (4-3): FTIR spectra obtained for FEFKFEFK peptide dissolved in MAPI precursor solution. The strong absorption band at 1625 cm^{-1} and a weaker one at 1696 cm^{-1} indicates the formation of β -sheets in agreement with the work of Saiani *et al* [84]

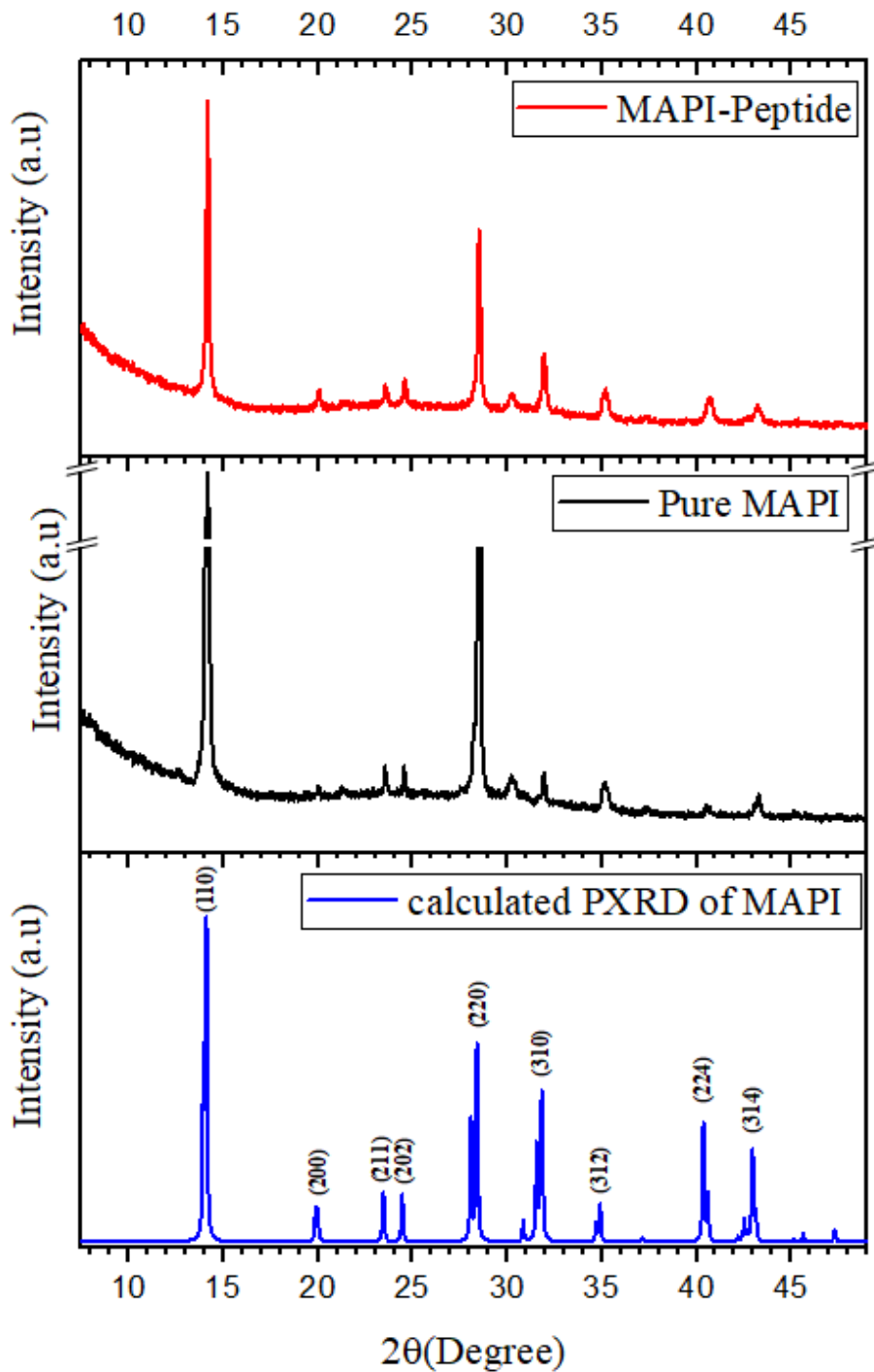


Fig (4-4): Measured XRD pattern for prepared samples (Pure MAPI and MAPI-peptide (Mix40)) and calculated PXR of MAPI.

4.3.1 Effect of peptide on MAPI properties

4.3.1.1 The crystal size of MAPI

Fig (4-5) shows the X-ray diffraction (XRD) of the prepared thin films; pure MAPI and MAPI-peptide thin films. From the XRD patterns, it is clear that the peptide affects the crystal size of the MAPI, as evidenced by an increase in the width of the XRD peaks. Table 1 illustrates the perovskite crystal size for pure and composite samples with different peptide concentrations, calculated using the Scherrer equation for the 14.2° reflection from the XRD patterns. There is a slight decrease in the size of the MAPI crystals when mixed with peptide compared to pure MAPI, which we attribute to the crystallisation of the MAPI particles inside the voids of the peptide gel network, which as mentioned above, have a size of 15-30 nm [89]. The decrease in average crystal size is linked to the increasing peptide concentration, and is attributed to a decrease in pore size of the peptide due to the rise in the density of fibres with increasing peptide concentration [89]. The fact that the observed crystallite size is larger than the approximate pore size of the peptide may lie in the formation of ‘free’ MAPI on the top of the peptide, thereby increasing the average particle size.

Table (4-1): The average size of crystals of un-templated and templated MAPI by mixing different concentrations of peptide.

Sample	Crystal size (nm)
MAPI	70 ± 7
Mix40	43 ± 8
Mix60	35 ± 4
Mix80	34 ± 1
Mix100	26 ± 4

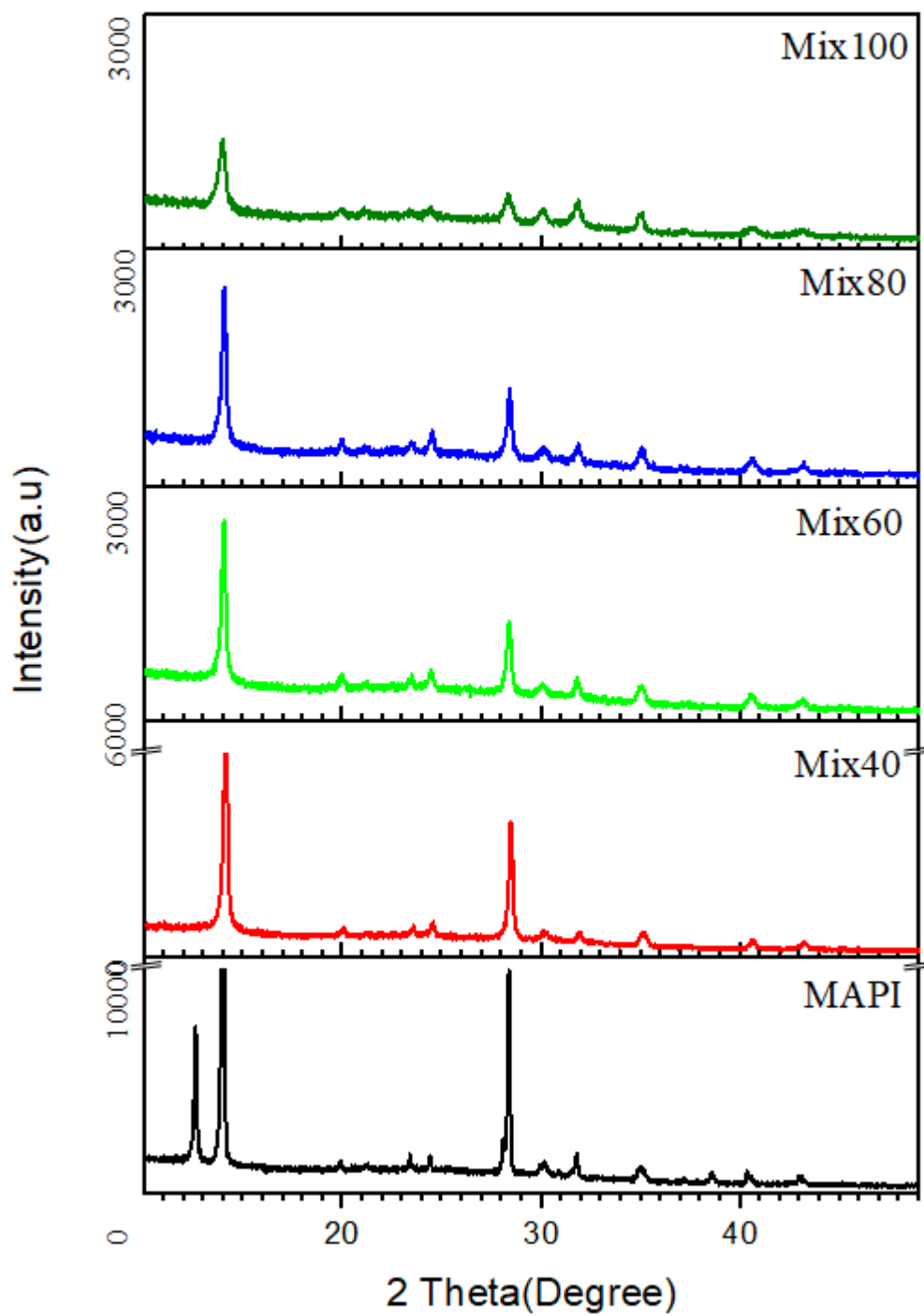


Fig (4-5): XRD for MAPI and MAPI peptide mixture (different concentrations of peptide) thin films.

4.3.1.2 Optoelectronic properties of MAPI

4.3.1.2.1 Absorbance spectra

To study the effect of the optoelectronic properties of MAPI, UV-Vis was carried out to measure the absorbance of prepared thin films. Fig (4-6) shows the absorbance spectra for pure MAPI and MAPI-peptide thin films with different concentrations. The spectra show a blue shift in the threshold edge of absorbance of peptide-MAPI thin films that increases with an increase in peptide concentration, attributed to an increasing bandgap that corresponds with the slight decrease in the size of the crystals mentioned above. Table (4-2) shows an increase in the bandgap of the templated MAPI that was determined using Tauc plots, which have been extracted from the absorbance spectra of thin films prepared.

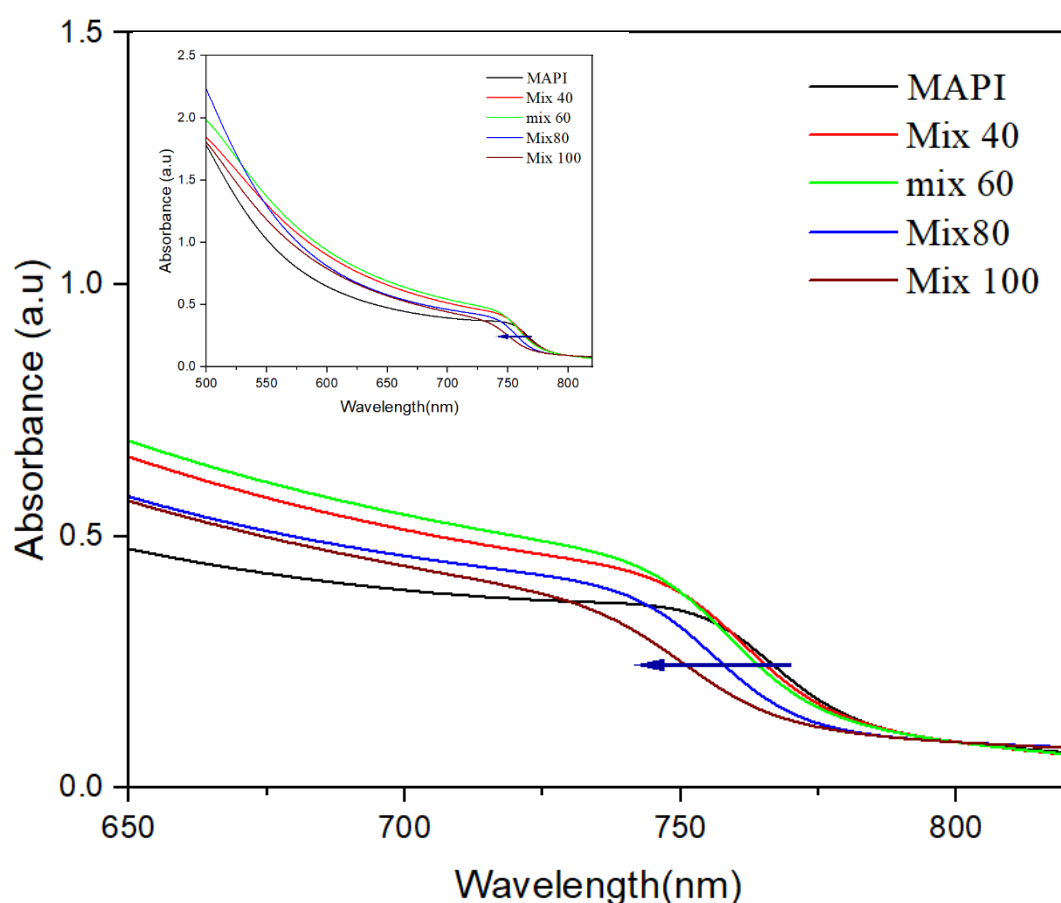


Fig (4-6): Absorbance spectrum of MAPI thin film and MAPI peptide mixture thin films (different concentration).

This increase in the bandgap of templated MAPI almost agrees with the change in calculated bandgap using the Burs equation (eq (4-1)), where table (4-2) shows the tiny increase in the calculated bandgap with a decrease in particles size for templated MAPI samples which roughly matches with the experimental values. This could be attributed to the quantum size effects on the MAPI-templated samples although their particles are large, where the quantum size effects could act in large physical sizes due to strong chemical bonding, as reported by Burs.[109].

The Burs equation used is:

$$E = E_g + \frac{h^2}{8R^2} \left[\frac{1}{m_e^*} + \frac{1}{m_h^*} \right] - \frac{1.8e^2}{4\pi\epsilon_0\epsilon_r R^2} \quad (4-1)[110]$$

Where E_g is the MAPI bandgap, h Plank constant, R is the radius of the particle, m_e^* and m_h^* are effective masses for electron and hole respectively in MAPI, ϵ_0 = permittivity of vacuum and ϵ_r = relative permittivity. Note that in applying the Burs equation it is assumed that the particles have a spherical shape.

Table (4-2): The experimental and theoretical bandgap of un-templated and templated MAPI by mixing different peptide concentrations.

Sample	The experimental Bandgap (eV)	The theoretical Bandgap (eV)
MAPI	1.58 ± 0.013	-
Mix40	1.59 ± 0.01	1.588 ± 0.003
Mix60	1.60 ± 0.012	1.591 ± 0.002
Mix80	1.61 ± 0.01	1.591 ± 0.001
Mix100	1.62 ± 0.01	1.6 ± 0.006

4.3.1.2.2 Photoluminescent emission spectra

To confirm the change in the bandgap of templated MAPI, PL was carried out on the samples by exciting them with a photon of wavelength, 450 nm as shown in Fig (4-7). The spectra show a blue shift in the photoluminescent emission that increases with an increase in the peptide

concentration reaching a minimum wavelength of 742 nm at a peptide concentration of 100 mg/ ml. This is consistent with the observed increase in bandgap and decrease in the crystal size of MAPI as a function of peptide concentration, as mentioned above.

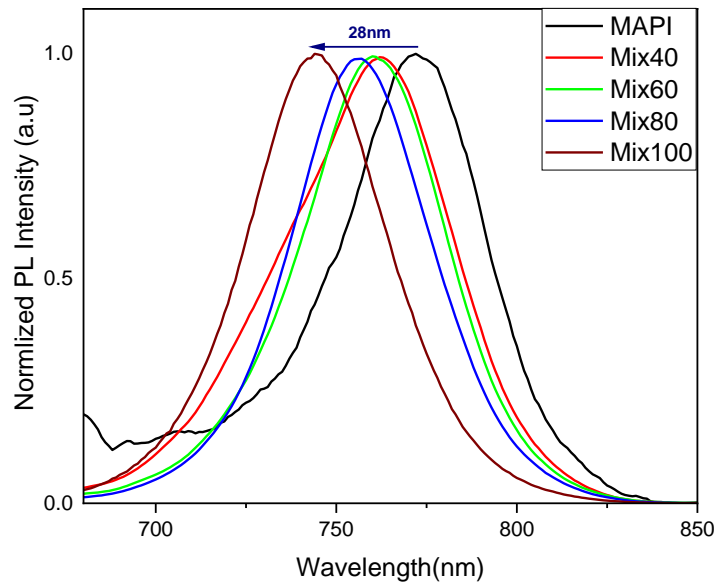


Fig (4-7): Photoluminescence spectra of MAPI thin film and MAPI peptide composite thin films at different concentrations.

Figure (4-8) shows the PL intensity of the pure MAPI-Peptide film, indicating that as the proportion of peptide concentration is increased, there is an increase in PL intensity as a logarithmic relationship as shown in Fig (4-9). This effect can be attributed to passivating defect sites in MAPI. Since MAPI is crystallised through a solution process, during the post-deposition thermal annealing process, iodide and methylammonium ions can be lost from the MAPI. Therefore, many positively charged under-coordinated lead ions may act as recombination-active defects in the material [111][112][113]. The presence of the amine group in the peptide may contribute to passivating these unintentional defects by coordinating bonding with the nitrogen atoms, resulting in charge neutralization and a consequential reduction in the number of electronic trap sites [113]. Alternatively the peptide gel may act to stop small molecules from leaving the perovskite surface and available to take part in self-healing of the perovskite, as has been observed for similar systems [114]. Therefore, the rate

of non-radiative recombination decreases, which increases the photoluminescence intensity and PL lifetime, as shown schematically in Fig (4-10).

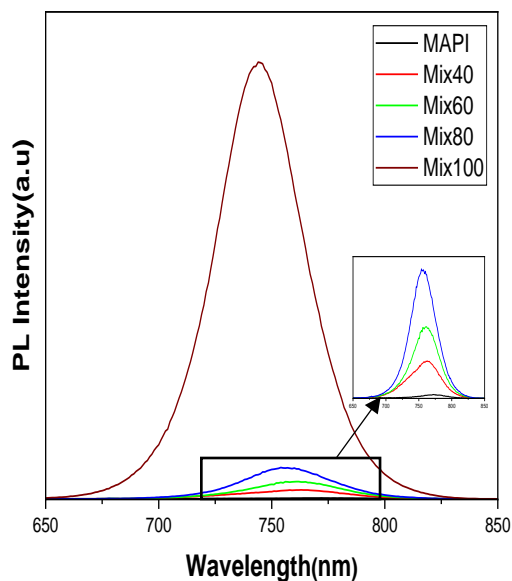


Fig (4-8): Photoluminescence spectrum of MAPI thin film and MAPI peptide mixture thin films (different concentration).

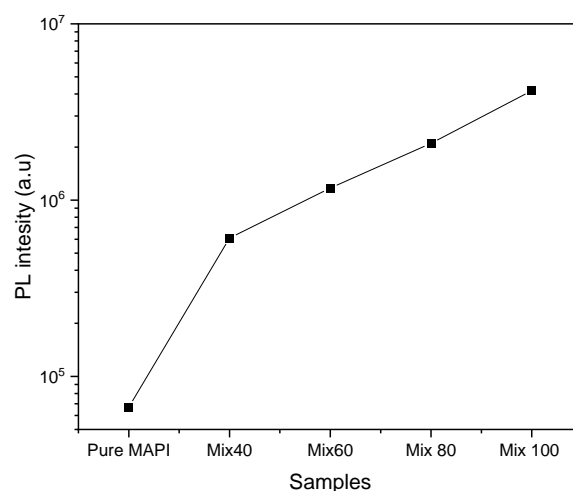


Fig (4-9): The relationship between the concentration of peptide and PL intensity.

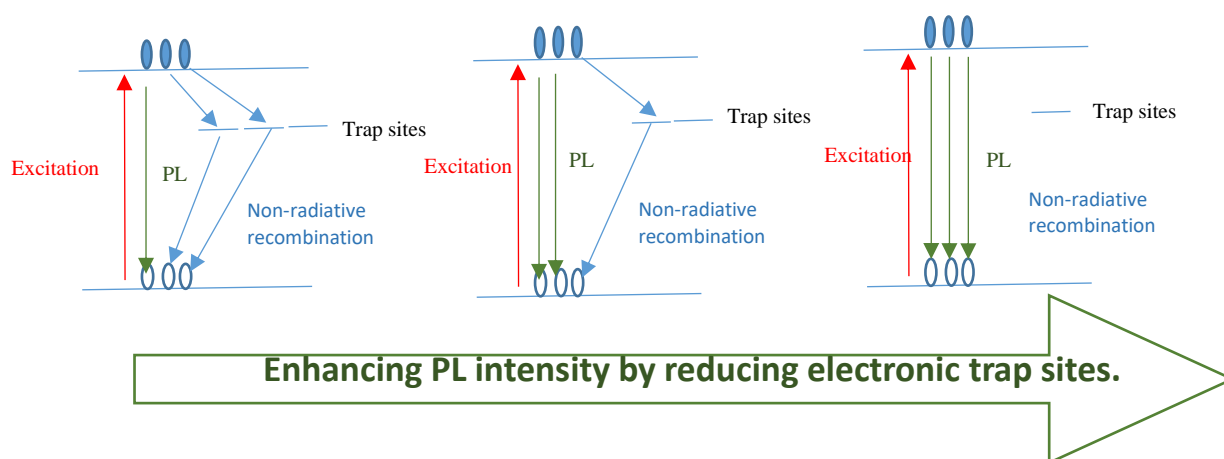


Fig (4-10): PL blinking mechanism and trap-assisted non-radiative recombination.

Table (4-3) shows the intensity ratio of I, Pb and N, calculated from the spectral peak area of XPS spectra of I 3d, Pb 4f and N 1s spectra normalised to the Kratos sensitivity factors. We find I/Pb and N/Pb ratios of around 2.5 and 0.7, respectively, for both pure MAPI and the mixture of MAPI and peptide. Note that for the MAPI/peptide material only the peak arising from MAPI was used in the calculation. By comparing the intensity ratio of I, Pb, and N to the chemical formula of MAPI ($\text{CH}_3\text{NH}_3\text{PbI}_3$), the I/Pb and N/Pb should be 3 and 1, indicating a reduction in N and I content at the surface, in agreement with published work for these materials [113]. This deficiency in N and I content may lead to under-coordinated lead ions which could act as recombination-active defects in the material as mentioned above. Fig (4-11) shows the N 1s spectrum in both samples. The MAPI-peptide spectrum has two peaks located at binding energies of 402.3 and 400.4 eV. The peak at a binding energy of 402.3 eV comes from the methylammonium group in MAPI [18] and is observed in both samples. The peak at a binding energy of 400.4 eV, on the other hand, appears only in the MAPI-peptide sample and could be attributed to the Pb-amide species [115] that resulted from a reaction of Pb^{+2} and amino acid. The inclusion of amide into MAPI films was associated with photoluminescence enhancements, consistent with the findings of amine passivating perovskite surfaces [115].

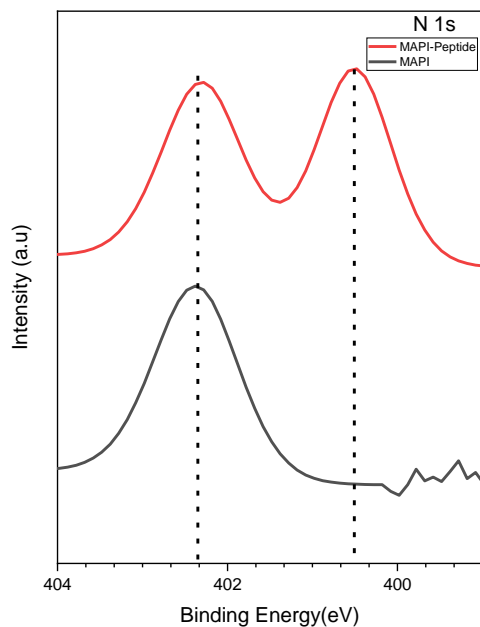


Fig (4-11): N 1s core spectra from pure MAPI and MAPI-peptide

Table (4-4): The atomic ratios at the surface of the MAPI and MAPI-Peptide samples

Sample	I/Pb	N/Pb
MAPI	2.47	0.78
MAPI-Peptide	2.48	0.73

4.3.1.2.3 Time-resolved PL decay.

Considering the substantial improvement in the PL intensity for a mixture of MAPI and peptide compared to pure MAPI, the photoluminescence lifetime should show an accompanying effect. Figure (4-12) shows PL decay for three samples and fitted line for; pure MAPI, Mix10 and Mix40. The fitted lines were obtained by fitting the decay data with a two-exponential decay function and then calculating the decay time (τ) from obtained parameters (A_1, τ_1, A_2 and τ_2) using the equation (4-1)[116]:

$$\tau = \frac{A_1\tau_1 + A_2\tau_2}{A_1 + A_2} \quad (4-1)$$

Where τ_1 and τ_2 are lifetime constants of fluorescence decays from short and long-lifetime components, and A_1 and A_2 are the corresponding initial amplitudes at zero time. Table (4-4) shows the calculated decay times for the measured samples. It can be seen that the MAPI-peptide thin films (Mix10 and Mix40) have longer PL lifetimes by a factor of 4 and 22 (respectively) than pure MAPI. On the other hand, when fitting the data with the single

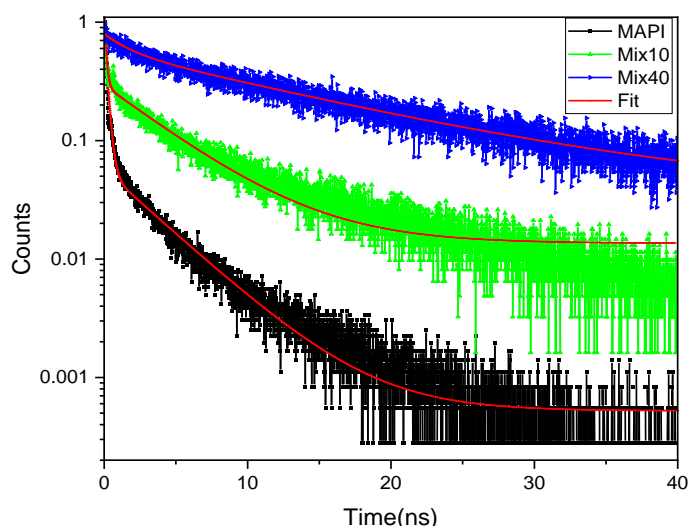


Fig (4-12): The TCSPC decay curves for Pure MAPI, Mix10 and Mix 40. The red line is the fitting decay data with a two-exponential decay function.

exponential decay function, as shown in Fig (4-13), it is clear that in pure MAPI, the PL decay curves cannot be explained by a mono-exponential model in contrast to the Mix40 that the PL where the lifetime appears to be mono-exponential indicating to there is a single rate-limiting

step in the luminescence process in Mix40. This could mean that the adding of the peptide to MAPI could minimize the non-radiative pathways [117] by passivating unintentional defects as mentioned above, which could lead to an enhancement of the PL lifetime with an increase peptide concentration that could be useful in solar cells which contribute to the extraction and transfer of charge carriers to transport layers before recombination.

Table (4-4): Photoluminescent lifetimes for pure MAPI, Mix10 and Mix 40

Sample	Decay time (ns)
MAPI	0.5 ± 0.01
Mix10	2 ± 0.02
Mix40	11 ± 0.2

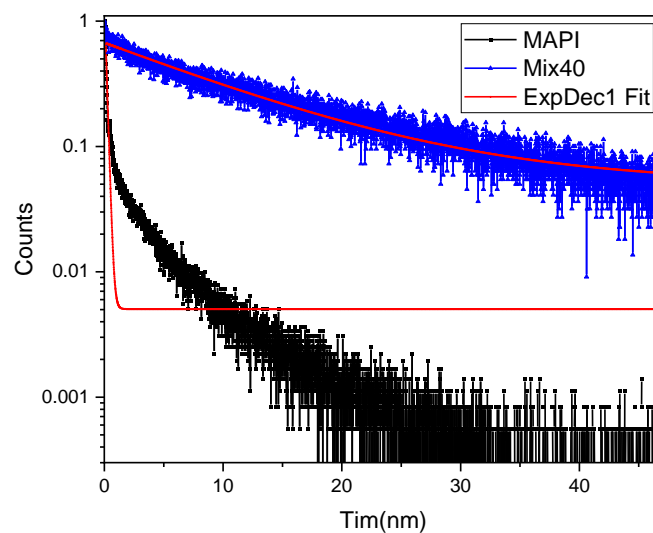


Fig (4-13): The TCSPC decay curves for Pure MAPI and Mix 40. The red line is the fitting decay data with a mono-exponential decay function.

4.3.2 Effect of peptide on the morphology of MAPI

SEM images of the films are shown in Figure (4-14) and show a fibrous-like structure in agreement with early work on these materials where only DMF as a solvent is used in the synthesis [118]. We avoided using the mixture of DMF and DMSO as the solvent, although it gives a controllable crystallisation and morphology of MAPI thin films [119] because the peptide completely dissolves in DMSO and loses the gel structure. SEM data do not conclusively allow us to determine whether the perovskite/peptide forms a layered structure or the perovskite is incorporated into the gel. It is clear that at higher peptide concentrations (above MIX40) the fibrous structure is lost.

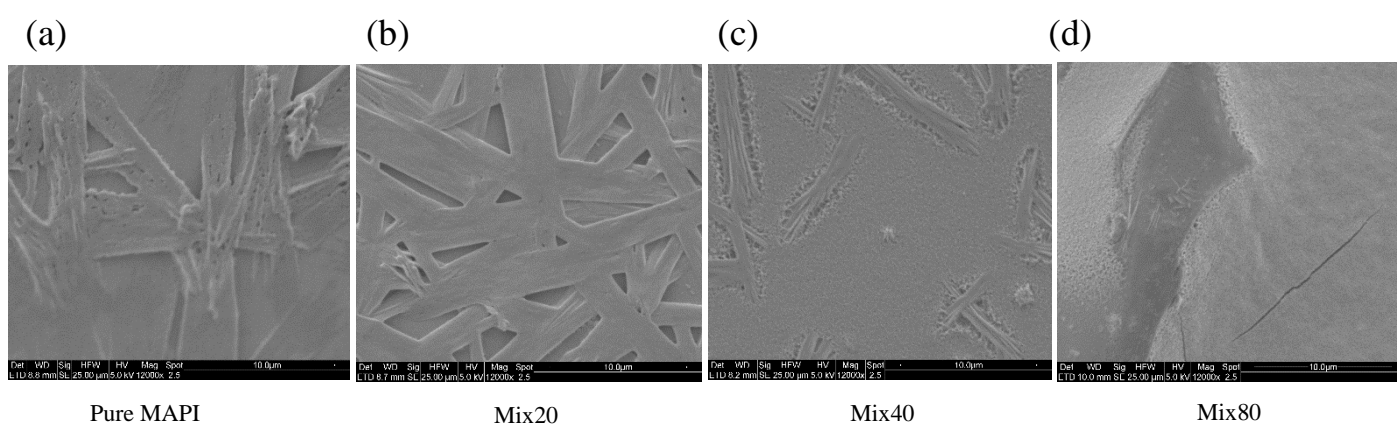


Fig (4-14): SEM images for pure MAPI (a) and MAPI peptide mixture (Mix20 (b), Mix40(c) and Mix80(c)) thin films.

4.3.3 Effect on the stability of MAPI

To investigate the effect of the peptide on the stability of MAPI perovskite, we examine the stability of fabricated thin films in two situations; following exposure to water vapour, and heating, as discussed below.

4.3.3.1 **Improvement of MAPI-peptide stability in a moist environment**

In order to examine the stability of the MAPI peptide mixture in a moist environment, a pure MAPI thin film and a MAPI-peptide composite thin film (40mg/ml) were kept in a container with water beneath the samples leading to exposure to water vapour for up to three weeks. As shown in photographs in Figure (4-15), the brown colour of the perovskite still appears in the peptide-MAPI thin film for up to 82 hours, whereas the pure MAPI film is completely degraded after only 60 hours water vapour exposure, which means the peptide appears to decrease the sensitivity of MAPI to water, increasing its stability. To confirm this result, X-ray diffraction (XRD) was carried out for the thin films after 82 hours, with the results shown in Figure (4-

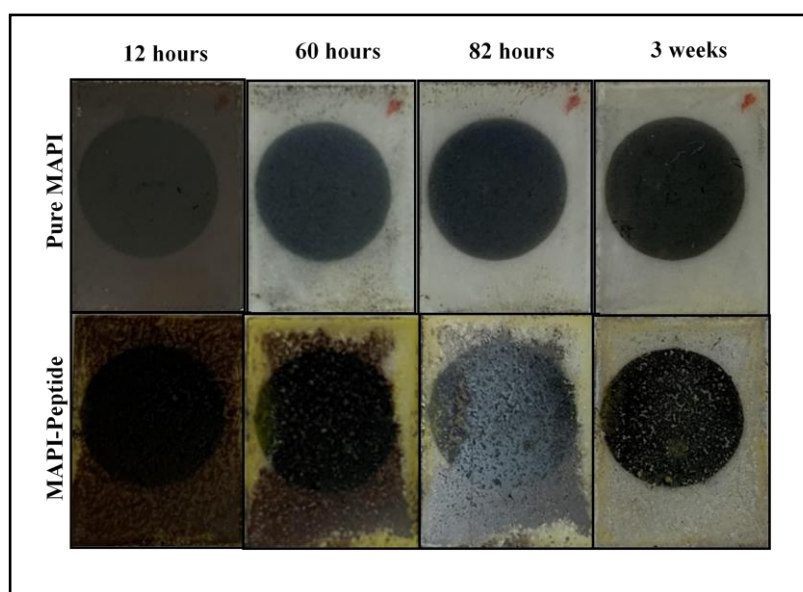


Fig (4-15): Photographs of MAPI film with and without peptide during exposure to water vapor over three weeks.

16). The XRD pattern of pure MAPI thin film (Fig (4-16 a)) shows that the main peaks of pure MAPI ($2\theta = 14.1^\circ, 28.5^\circ, 31.8^\circ, 40.6^\circ$ and 43.3°) have disappeared and been replaced by PbI_2 [119]. For the peptide-MAPI composite, however, MAPI peaks are still present in the XRD pattern although there is evidence of the formation of PbI_2 in this thin film (Fig (4-16 b)).

The observed differences could be attributed to the peptide preventing water vapour from reaching the MAPI because it seems that the MAPI is coated, as shown in SEM images (Fig (4-14)), whether simply lying beneath the peptide mesh or becoming incorporated into the gel.

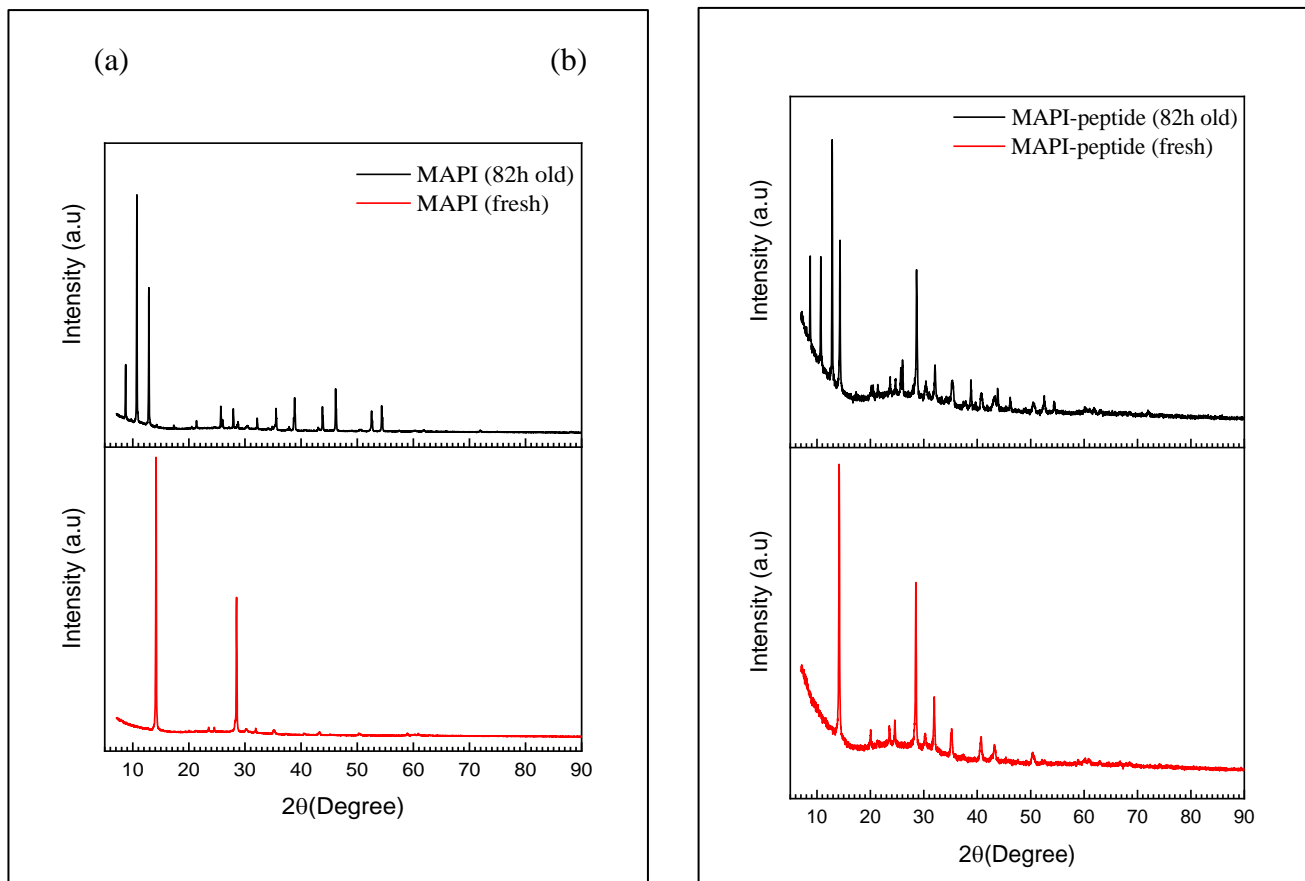


Fig (4-16): XRD pattern of MAPI film (a) and MAPI peptide mixture (40 mg/ ml) film (b) (fresh and after 82 hours exposure for water vapour).

4.3.3.2 Increase in MAPI-peptide stability against heating.

To investigate the effect of heating on the stability of MAPI with and without peptide, The pure MAPI and MAPI-peptide (40 mg/ml) thin films were tested using XPS. The samples were measured in XPS at three temperatures; room temperature (RT), 100 °C, and 150 °C. Fig (4-17) shows the XPS spectra of (a) Pb 4f, (b) I 3d and N 1s core level from pure MAPI thin film at different temperatures (RT, 100 and 150 °C). Pb 4f spectra show the presence of two prominent peaks at 138.4 eV and 143.2 eV that correspond to Pb 4f_{7/2} and Pb 4f_{5/2}, respectively, in the RT and 100 °C measurements. These peaks are in excellent agreement with literature reports for the Pb in MAPI perovskite with the presence of I 3d at 619.3 eV and N 1s at 402.4 eV that belong to MAPI perovskite [18]. In contrast, The result of the sample after heating at 150 °C reveals a shift of Pb 4f_{7/2} to higher binding energy 138.6 eV that can be attributed to the formation of PbI₂ and indicates degradation of MAPI as reported by Chun-Ren Ke *et al.* [18]. This shift matches with the disappearance of the N 1s peak and a shift in I 3d_{5/2}, indicating complete degradation of the MAPI film.

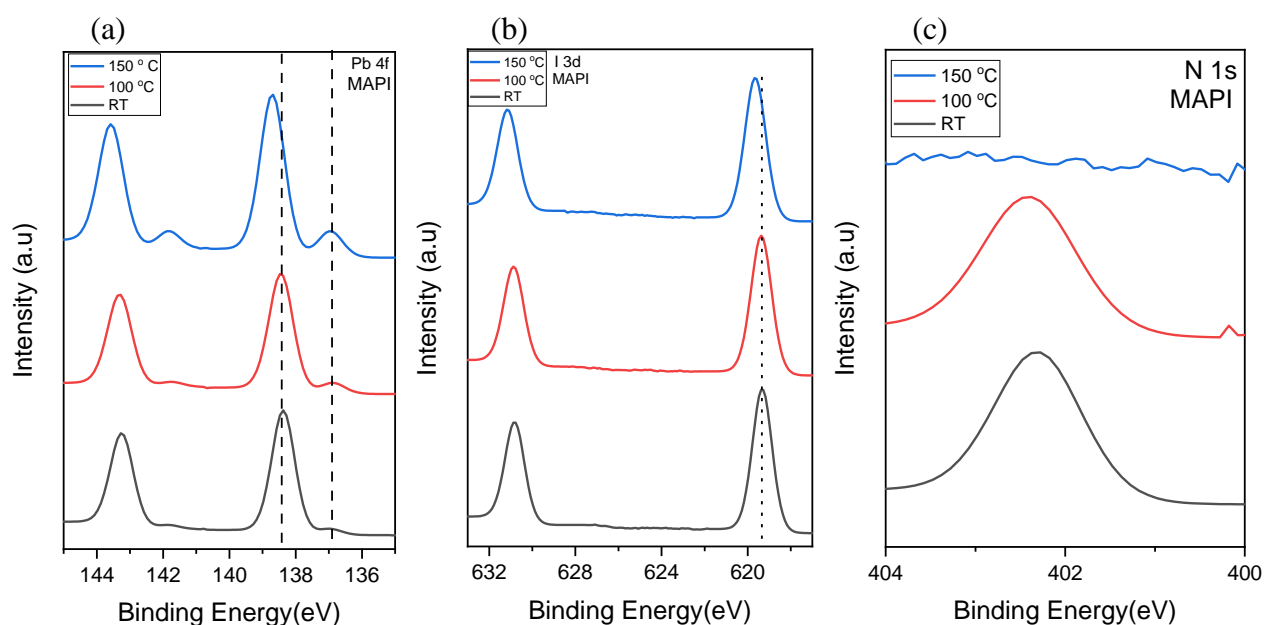


Fig (4-17): The XPS spectra of (a) Pb 4f, (b) I 3d and N 1s core levels from pure MAPI thin film at different temperatures (RT, 100 and 150 °C), The dashed lines show the resulting shifts in positions Pb 4f and I 3d and the difference obtained in the intensity of Pb metallic with increased heating temperatures.

Further evidence of the degradation is the growth of the peak in the Pb 4f_{7/2} spectrum at 136.9 eV which is attributed to metallic Pb. Although it is observed as a weak feature in the as-presented sample, in agreement with previous studies of MAPI using XPS [18], upon heating the intensity increases with heating, Fig (4-19 a) shows the intensity of the metallic lead, calculated by dividing the spectral peak area of metallic Pb by the relative sensitivity factor (R.S.F). This could be attributed to the degradation of MAPI with heating to PbI₂ and then further decomposition of PbI₂ to metallic Pb and I₂ (g) that also explains the decrease in the ratio of I to Pb in the sample heated at 150 C as shown in Fig(4-19 b).

In contrast, Fig(4-18) shows the XPS Pb 4f (a), I3d (b) and N 1s core-level spectra from the MAPI-Peptide thin film at different temperatures (RT, 100 and 150 °C). The Pb 4f and I 3d spectra of the sample at all three temperatures show MAPI peaks located at 138.4 eV and 619.3 eV, respectively, that correspond to Pb 4f_{7/2} and I 3d_{5/2}. No shift in binding energy is observed on heating which could indicate increased stability of MAPI-peptide. Interestingly the metallic Pb peak is not observed in the spectra obtained at RT and following heating to 100 °C. This can be clearly seen in the bar chart in Fig(4-19 a). At the same time, Fig (4-19 b) shows a decrease in the I to Pb ratio only for the sample heated to 150 °C but by a smaller amount than that seen for pure MAPI. This indicates that the peptide could contribute to increased stability of MAPI. The N 1s spectra sample at the three temperatures show two peaks at binding energies

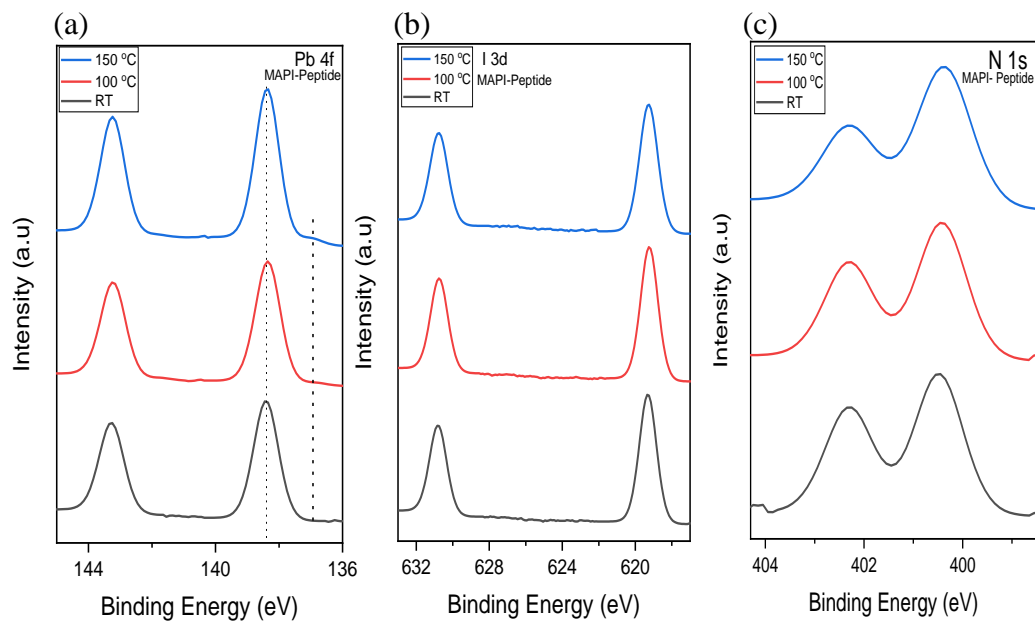


Fig (4-18): The XPS spectra of (a) Pb4f, (b) I 3d and N 1s core level from MAPI-Peptide thin film at different temperatures (RT, 100 and 150 °C)

of 402.3 eV and 400.5 eV that can be attributed to the organic cation of MAPI and nitrogen in the peptide chain, respectively. In the peptide the signal from the NH₂ is usually found at around 400 eV and a peak at ~402 eV is usually be assigned to NH₃⁺, i.e. the protonated amine [120]. Table (4-5) shows the ratio of *N 1s* to *Pb 4f* in the MAPI-peptide sample, which illustrates a

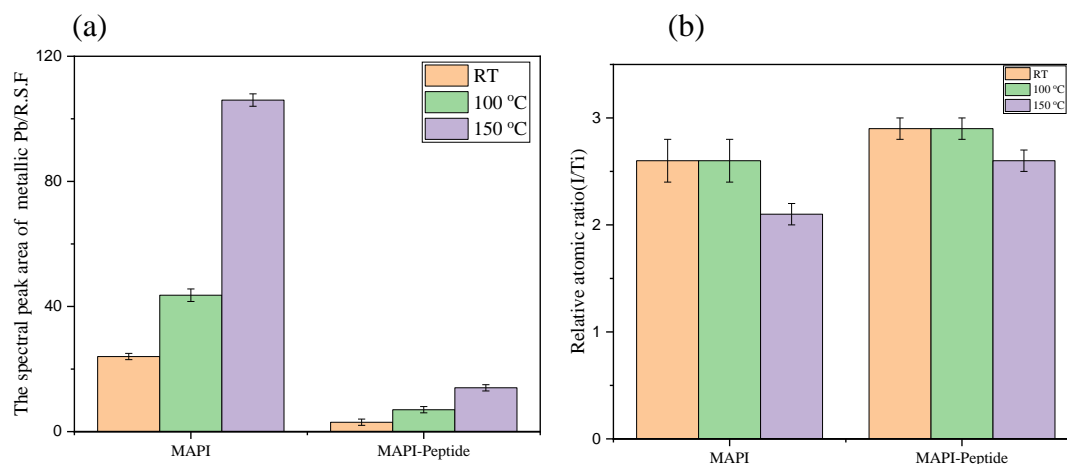


Fig (4-19): (a) The ratio of metallic Pb in Pure MAPI and MAPI-Peptide thin films at different temperatures (RT, 100 and 150 C), (b) the relative ratio of I to Pb in Pure MAPI and MAPI-Peptide thin films at different temperatures (RT, 100 and 150 °C)

reduction in the intensity of the higher binding energy component (402.3 eV) upon heating even to 150 °C. Although it is difficult to deconvolute the *N 1s* signal at 402.3 eV between the MAPI and that of the peptide resulting in it is difficult to determine whether the loss of N from MAPI or the peptide, the deficiency of the amount of *N 1s* is too small (just 0.3) compared to the pure MAPI, which completely disappeared. This small reduction in N amount, alongside the presence of Pb 4f and I 3d without any observed shift, could indicate the presence of MAPI, which means the contribution of the peptide to the increase of perovskite's stability against the heating, unlike the pure MAPI that degraded completely as discussed above.

Table (4-5): The atomic ratios of *N 1s* to *Pb 4f* at the surface of the MAPI-Peptide sample

		RT	100° C	150° C
Mix40	NH ₃ ⁺ (402.3eV)	1	0.9	0.7
	NH ₂ (400.5eV)	1.3	1.3	1.2

4.3.4 Effect of peptide gel on efficiency of solar cells

To study the effect of the peptide on the performance of perovskite solar cells (PSCs), pure MAPI and MAPI-peptide mixtures have been deposited as active layers in PSCs, as shown in Figure 4-20. Four perovskite solar cells were fabricated with one based on pure MAPI as a reference and three based on MAPI-peptide with different concentrations of peptide (10, 20 and 40 mg per ml MAPI precursor). The performance of each photovoltaic device was characterized by measuring its current-voltage (I - V) response under standard 1-sun illumination (1000 W/m^2 intensity with AM1.5G spectrum).

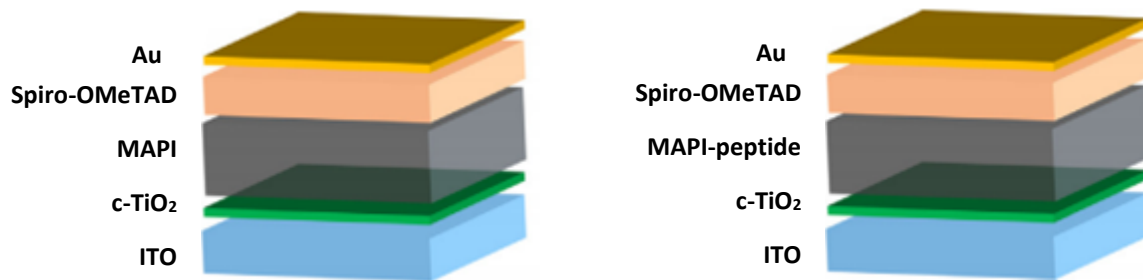


Fig (4-20): Schematic illustration for perovskite solar cells fabricated.

Figure (4-21) and Table (4-6) show the IV curve and main parameters for devices based on pure MAPI and a mixture of MAPI and peptide with concentration (10 mg peptide / 1 ml MAPI precursor). The finding indicates that the power conversion efficiency improves slightly for the device based on the mixture of peptide and MAPI, which achieved $15.2\% \pm 0.8$, compared to its

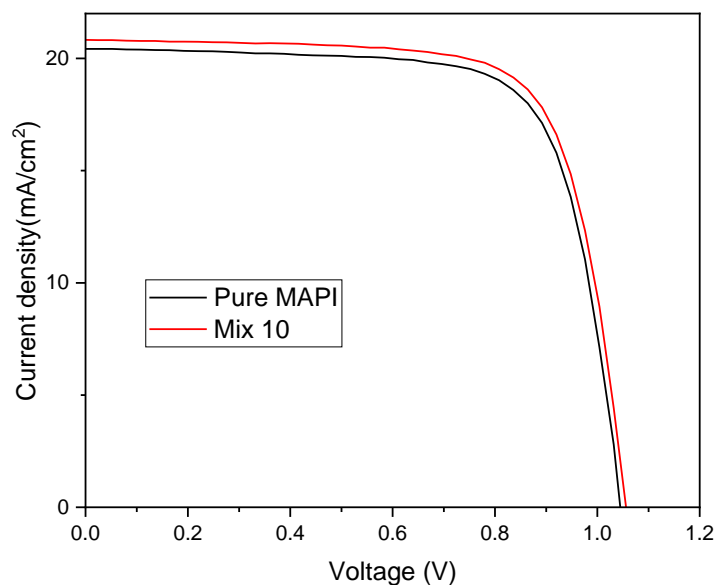


Fig (4-21): J - V curve of PSCs based on pure MAPI and MAPI-peptide

based on pure MAPI, which achieved $14.6\% \pm 1.1$. This improvement is due to an increase of V_{oc} , I_{sc} , and Fill factor (FF) of devices based on MAPI-peptide, as shown in Table (4-7). The increase of V_{oc} could be attributed to a low recombination rate due to the passivation of defects of MAPI by peptide, where reducing the recombination rate increases the charge carrier concentrations, moving the hole quasi-Fermi level closer to the highest occupied molecular orbital (HOMO) energy level of the hole transport layer (HTL), leading to an increased of V_{oc} . The increase of I_{sc} could be due to the increased lifetime of charge carriers generated in the

Table (4-6): Photovoltaic parameters of PSCs based on pure MAPI and MAPI-peptide

Sample		V_{oc} (V)	J_{sc} (mA/cm ²)	FF (%)	PCE (%)
Pure MAPI	Average of 8 cells	1.04±0.01	19.9±0.6	70.4±3.6	14.6±1.1
	The best one	1.04	20.43	72.7	15.6
Mix 10	Average of 8 cells	1.05±0.01	20.11±0.5	72.3±2.1	15.2±0.8
	The best one	1.06	20.83	73.1	16.09

MAPI-peptide composite film, as shown in Fig (4-13), that leads

to the extraction and transfer of charge carriers to transport layers before recombination. It the worth mentioning the initial attempts to study the effect of the peptide concentration on the performance of devices revealed that the higher peptide concentrations, such as 20 and 40 mg/ml, negatively affect the photocurrent, where it was found to decrease with an increase in the peptide concentration and, thus, the efficiency was reduced as shown in Fig (4-22). This could be because increasing the peptide concentration leads to the formation of a thick peptide

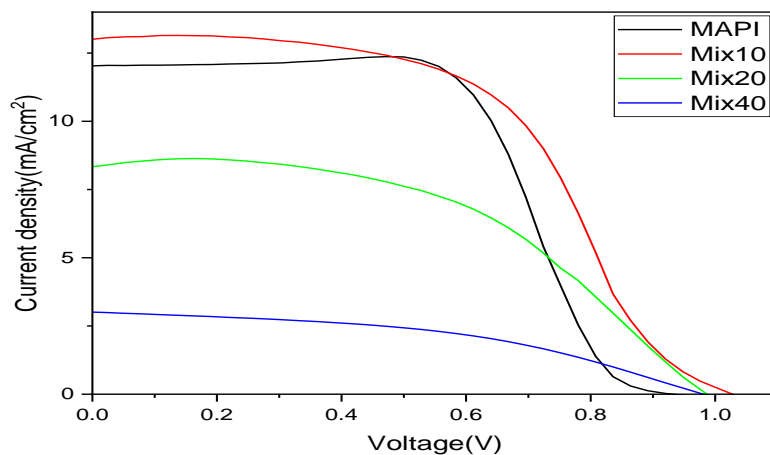


Fig (4-22): J-V curve of PSCs based on pure MAPI and MAPI-peptide with different concentrations (10, 20 and 40 mg/ mL).

layer above the MAPI, as shown in SEM images in Fig(4-15), which may negatively affect charge injection into the HTL.

To monitor the device stability and study the effect of the peptide on the stability, devices were kept at room temperature in a 35% relative humidity environment and continuously measured after different periods. Fig (4-23) shows the device efficiencies during these measurements. The MAPI-peptide device maintained 75% of the best efficiency after

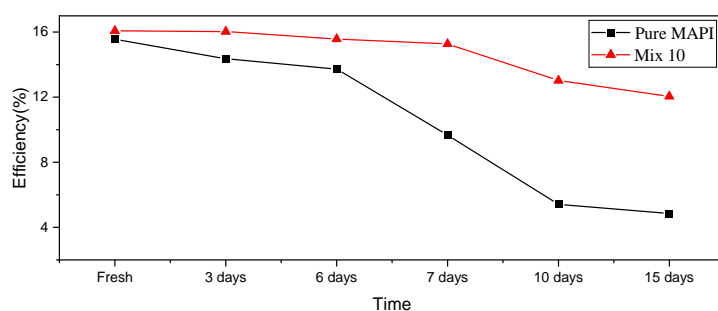


Fig (4-23): Measurements of PSC devices' efficiency that based on pure MAPI and MAPI-peptide for different periods during two weeks. The devices are kept in a 35% humidity environment.

ageing for two weeks, whereas the reference devices maintained only 32% during the same period and same conditions. This could be attributed to the improvement of perovskite stability by the peptide discussed above.

4.4 CONCLUSION

In this chapter, the fabrication of MAPI perovskite using FEFKFEFK peptide as a template was investigated to control particle size and optoelectronic properties and increase its stability through encapsulating MAPI crystals inside peptide a peptide gel. The samples were prepared and deposited using a solution process and spin-coating technique.

The optoelectronic properties of the films studied were characterised using photoluminescence (PL) spectra, absorbance spectra, and time-resolved PL. The morphology and structure of the films prepared were characterised using SEM and XRD, respectively. The surface chemistry of the samples was determined by performing XPS. The illuminated I/V-characterization technique was used to examine the PV potential and determine the PV parameters and conversion efficiency (η) of the devices based on templated MAPI.

The results indicate that there is a decrease in the crystal size of MAPI with an increase in the peptide concentration accompanied by a tiny increase of the bandgap of MAPI and a blue shift in PL emission. Also, the intensity of the PL is increased, which is attributed to passivation of electronic defects in the thin films. Time-resolved PL measurements also indicate that there is a single dominant rate determining step in the recombination suggesting that the peptide may reduce the effects of defects in the MAPI. These changes in optoelectronic properties contribute to an increase in the power conversion efficiency of devices based on the MAPI-peptide films. It was also found that the peptide led to an increased stability of MAPI thin films, which is reflected in the stability of devices based on a mixture of MAPI and peptide.

The increase in band gap, and decrease in average particle size observed on addition of the peptide to the MAPI precursor was found to increase with the peptide concentration until the solution precursor reached saturation at 100 mg of peptide per ml of MAPI precursor. At concentrations of more than 100 mg/ml the peptide did not dissolve and remained as sediment in the bottom of the solution. This led us to investigate another peptide that could be applied with higher solubility, which will be discussed in the next chapter.

Chapter 5: Investigation of using FEFKFEFKK peptide gel as a template in the fabrication of methylammonium lead iodide perovskite.

5.1 INTRODUCTION

The results of the previous chapter indicated that using the octapeptide FEFKFEFK led to effects on the morphology and properties of methylammonium lead iodide (MAPI), including a decrease in particle size and a change in optoelectrical properties. In addition it was found that the peptide led to an improvement in the stability of MAPI and on test solar cell devices that based the MAPI-peptide gel composite. These encouraging results led us to look to a second peptide gel, this time a nine amino acid peptide FEFKFEFKK which has slightly higher solubility than FEFKKEFK, and is slightly more basic due to the additional lysine residue.

The peptide FEFKFEFKK is a self-assembled peptide containing nine amino acid residues. F, E, and K refer to phenylalanine, glutamic acid, and lysine with chemical structure, as shown in Fig (5-1) [121]. According to Saiani et al.[91], Like F8, F9 is a self-assembling peptide that forms stable antiparallel β -sheet-rich fibres and hydrogels with a concentration above the critical gelation concentration (CGC) and its charge is +1 at pH 7 [121].

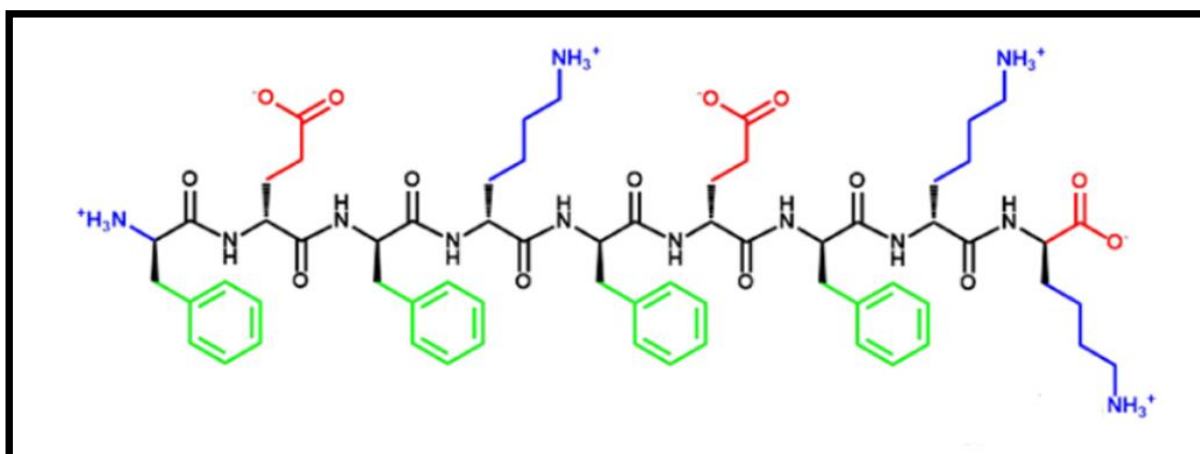


Fig (5-1): Chemical structures of peptide F9 [119]

5.2 EXPERIMENTAL SECTION

Materials: The following materials were used in the synthesis of perovskite-peptide composite: lead iodide (99%, Sigma- Aldrich) and N, N-dimethylformamide (DMF) (99.8%, Sigma-Aldrich), Methylammonium Iodide (MAI) (98%, Ossila) and ITO substrates (Ossila) the peptide (FEFKFEFKK) (BIOMATIK).

5.2.1 Preparation of MAPI-peptide thin films:

The thin films studied were prepared by the following steps:

5.2.1.1 **Preparing MAPI precursor solution**

The MAPI precursor solution was prepared by dissolving 1.1 moles of lead iodide (PbI_2) in N, N-Dimethylformamide (DMF) with stirring on the hotplate for one hour at 70 °C. It was then, cooled down to room temperature and 1.1 moles of MAI were added with stirring for 30 min.

5.2.1.2 **Preparation of MAPI-peptide solutions**

The mixture of MAPI and FEFKFEFKK peptide solutions with different concentrations were prepared by adding different amounts of peptide (40, 60, 80, 100, 120 and 160 mg) per ml of the prepared MAPI solution. These will be denoted MixN40, MixN60, MixN80, MixN100, MixN120 and MixN160, respectively hereafter.

5.2.1.3 **Deposition of the thin films**

ITO substrates were cleaned three times, using ultrasonic cleaning for 10 minutes (at least) each time in 3.0 vol% diluted Hellmanex III in DI water, pure DI water, and then ethanol, acetone, or IPA. They were cleaned, dried, and then subjected to a 15-minute UV-O₃ treatment before the deposition of the perovskite thin films. 100 μl of the prepared solution was poured onto the substrate after preheating it, and it was then spin-coated for 30s at a speed of 4000 rpm. After 10 seconds 200 μl of ethyl acetate was added as an anti-solvent treatment. The deposited thin films were heated on a hotplate for 10 minutes at 100°C.

5.2.2 Instrumentation

X-ray diffraction (XRD) analysis was carried out over the 2θ range of 7°–80° with a scanning rate of 5° min⁻¹. Photoluminescence (PL) spectra were performed utilising an excitation line of = 450 nm and gathering light emitted between 500nm and 850 nm. The time-resolved PL of the prepared thin coatings was measured using time-correlated, single-photon counting (TCSPC) with an excitation line of 450 nm and detection of the emitted photons at a wavelength of 770nm. The absorbance spectra were measured over the range of 250 to 850 nm. X-ray photoelectron spectroscopy was used to study the surface of the samples prepared.

5.3 RESULTS AND DISCUSSION.

According to A. Saiani *et al.*[121], the FEFKFEFKK peptide self-assembles into antiparallel -sheet-rich fibres when dissolved in water, producing a strong absorption band at 1625cm^{-1} and a faint one at 1695cm^{-1} . Figure (5-2) depicts these same absorption bands in FTIR spectra when the peptide is dissolved in MAPI precursor solution suggesting the peptide forms β -sheets. It also appears that this peptide again does not inhibit the production of MAPI when mixed with it. Figure (5-3) shows the XRD pattern from the MAPI-peptide perovskite, which confirms that the MAPI-peptide sample contains MAPI perovskite, as it matches the prepared pure MAPI sample and the MAPI-calculated PXRD spectra.

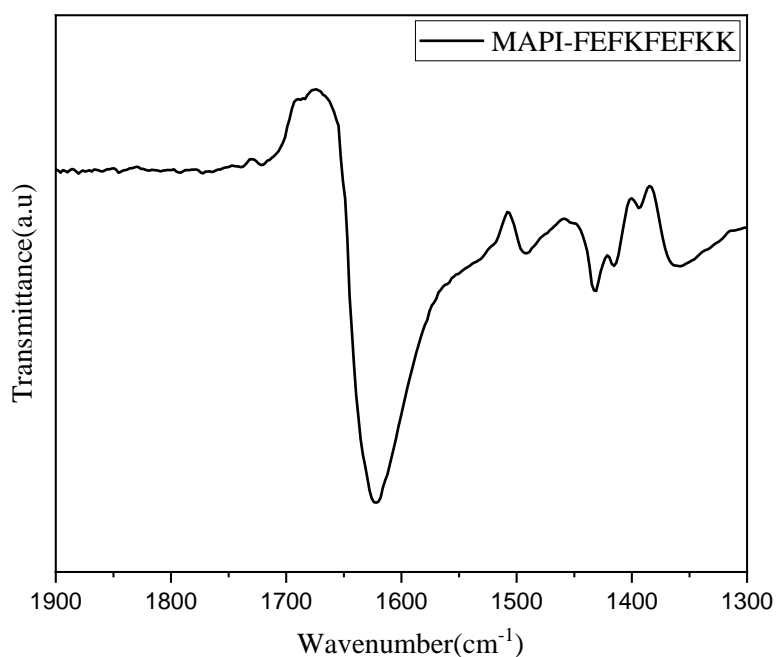


Fig (5-2): The FTIR spectrum of the FEFKFEKK peptide that is dissolved in the MAPI precursor solution.

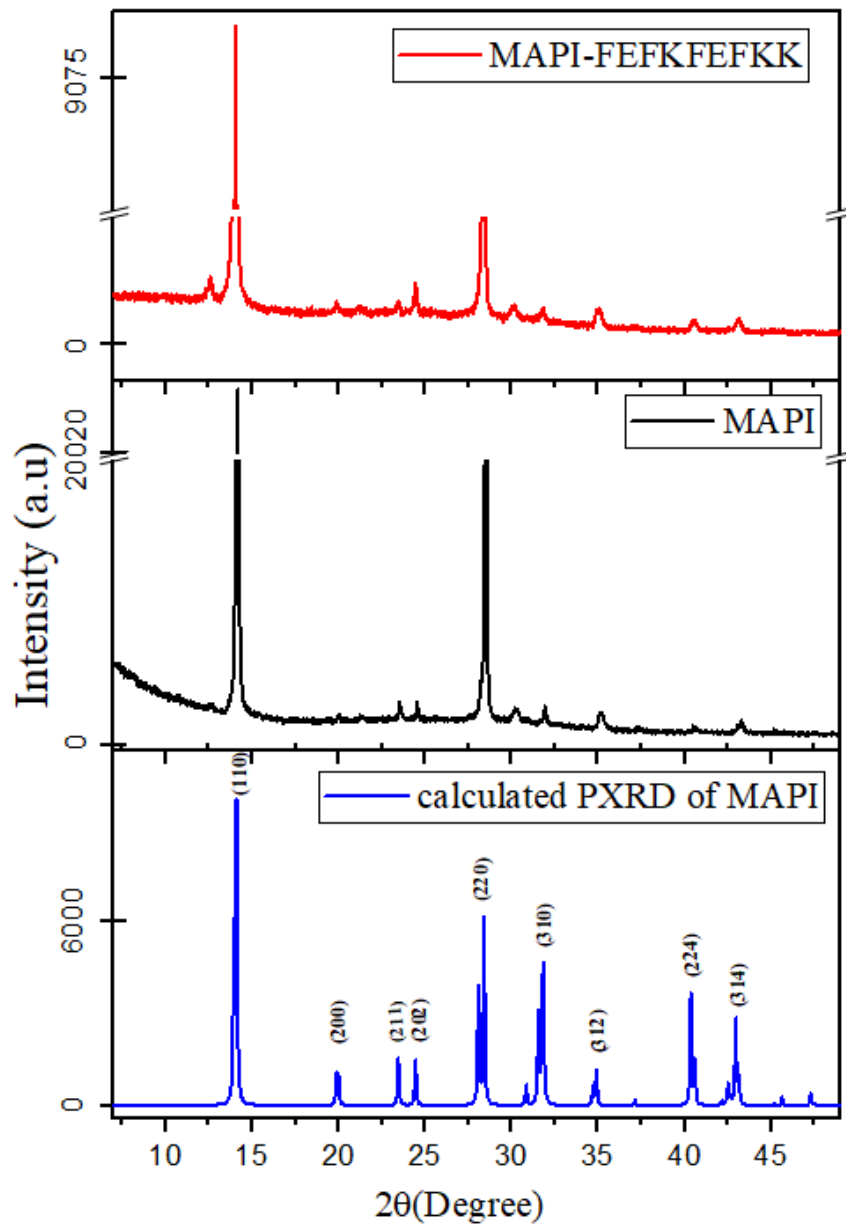


Fig (5-3): Measured XRD pattern for prepared samples (Pure MAPI and MAPI-peptide) and calculated PXR of MAPI.

According to Saiani et al. [14], the network mesh size and porosity diminish with increased peptide concentration due to the increased fibre density. As previously described, this decrease in pore size may influence the crystal size and optical and electrical properties of MAPI. The results of this investigation indicate that the effects of mixing the peptide with MAPI increase

as the peptide concentration increases. The following points may be used to summarise these effects:

5.3.1 Effect of peptide on MAPI properties

5.3.1.1 The crystal size of MAPI

X-ray diffraction (XRD) of the prepared MAPI and MAPI-peptide thin films is shown in Figure (5-4). It is evident from XRD patterns that the peptide influences the crystal size of MAPI, as evidenced by an increase in the width of the XRD peaks, that the peptide impacts the crystal size. Table (4-1) shows the perovskite crystal size for the pure MAPI and MAPI-FEFEKFEFKK composite samples, containing various concentrations of peptides, as determined from the Scherrer equation for the 14.2° reflection from the XRD patterns. We attribute the minor decrease in the size of the MAPI crystals when mixed with peptide to the crystallisation of the MAPI particles within the voids of the peptide gel network [89]. The decrease in average crystal size is associated with an increase in peptide concentration and is ascribed to a decrease in peptide pore size owing to an increase in fibre density with increasing peptide concentration[89]. The fact that to our knowledge, the mesh network size of this peptide (F9) is unknown, but we note that the average particle size with it is slightly larger than for the peptide consisting of 8 amino acids. It is not clear whether this is an effect of the size of the “voids” in the gel or some that there is more “free” perovskite in this gel.

Table (5-1): The average size of crystals of un-templated and templated MAPI by mixing different concentrations of peptide.

Sample	Crystal Size (nm)
MAPI	70 ± 7
MixN40	44 ± 6
MixN60	40 ± 2
MixN80	36 ± 1
MixN100	27 ± 3

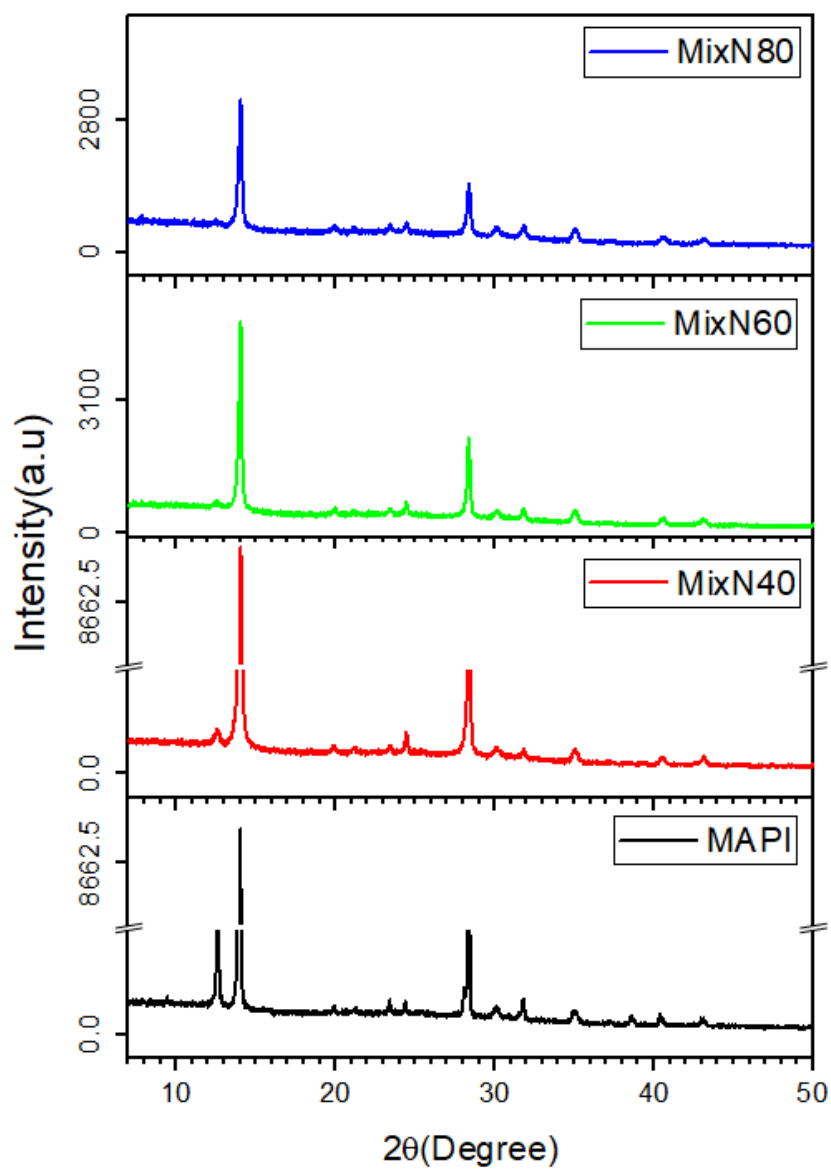


Fig (5-4): XRD for MAPI and MAPI peptide mixture (different concentrations of peptide) thin films.

5.3.1.2 The optoelectronic properties of MAPI

5.3.1.2.1 Absorbance spectra

To examine the effect on the optoelectronic properties of MAPI, the absorbance of prepared thin films of pure MAPI and the peptide-MAPI composite was measured using ultraviolet-visible (UV-vis) absorption spectroscopy. The absorbance spectra of unadulterated MAPI and MAPI-peptide thin films at different concentrations are shown in Fig (5-5). The spectra reveal a blue shift in the threshold edge of absorbance of peptide-MAPI thin films that increases with an increase in peptide concentration, attributable to a widening bandgap corresponding to the previously mentioned minor reduction in crystal size. Table (4-2) displays an increase in the bandgap of the templated MAPI as determined by Tauc plots derived from the absorbance spectra of prepared thin films. Again this is in agreement with the calculated bandgap and the observations for the eight amino acid peptide in the previous chapter.

Table (5-2): The bandgap of un-templated and templated MAPI by mixing different peptide concentrations.

Sample	Bandgap (eV)
MAPI	1.58 ±0.01
MixN60	1.59 ±0.01
MixN80	1.61 ±0.01
MixN100	1.62 ±0.01

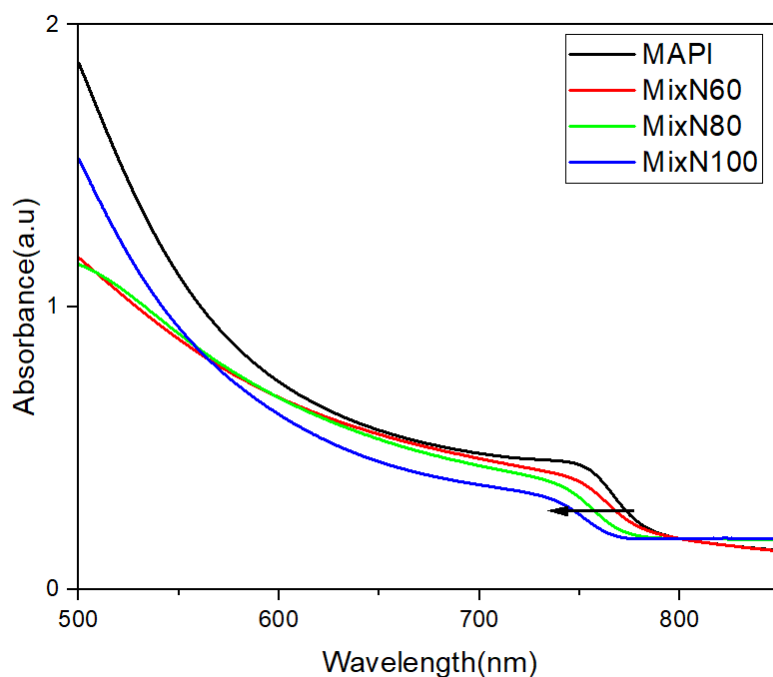


Fig (5-5): Absorbance spectrum of MAPI thin film and MAPI peptide mixture thin films (different concentration).

5.3.1.2.2 Photoluminescent emission spectra

To confirm the change in the bandgap of templated MAPI, PL was performed on samples by exciting them with a photon of 450 nm wavelength, as depicted in Figure (5-6). In agreement with the UV-vis spectroscopy the photoluminescent emission exhibits an increasing blue shift with increasing peptide concentration. Again this seems to indicate that the increased peptide concentration leads to an increase in fibre density in the peptide, resulting in a decrease in mesh size [89], and therefore, decreasing the particle size of the MAPI. At high concentration (100 and 120 mg/ml), the width of PL peaks increases, possibly due to the presence of more than one peak. Therefore, the broader peaks at high concentrations (100 and 120 mg/ml) could be an envelope for two peaks at around 700 and 750 nm, as shown in Fig (5-6). This could be attributed to a heterogeneous network with different mesh sizes that leads to fabrication of MAPI particles with different sizes and therefore bandgaps. This heterogeneous network could result from forming fibre bundles through lateral fibre association, as reported by Saiani *et al.* [122].

Figure (5-7) shows the relationship between the concentration of peptide and PL intensity of the MAPI-peptide film, indicating that as the concentration of peptides increases, so too does the PL intensity. This effect is attributable to the passivation of MAPI defect sites. Since MAPI is crystallised through a solution process, iodide and methylammonium ions can be lost during the post-deposition thermal annealing process. Consequently, numerous positively-charged, under-coordinated lead ions may function as recombination-active defects in the material[111][112]. By coordinating with the amine groups in the peptide and causing charge neutralisation, the amine group may help reduce the number of electronic trap sites and passivate these unintentional defects.

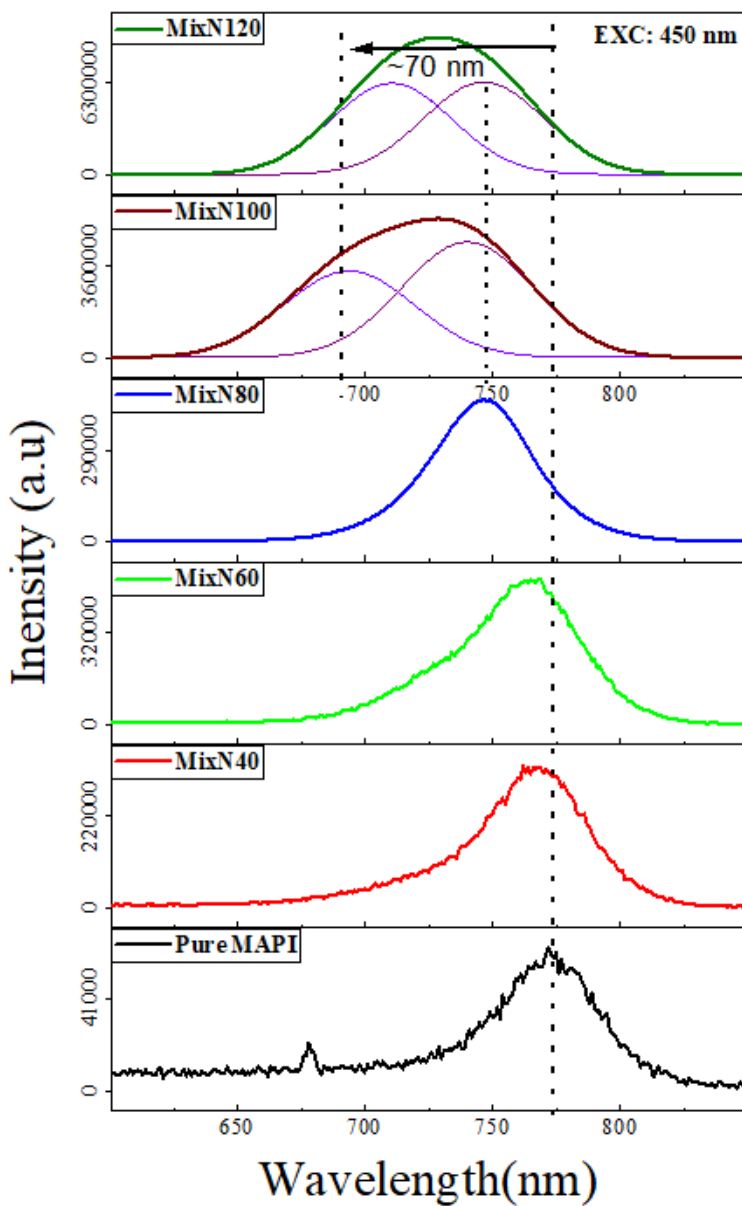


Fig (5-6): Photoluminescence spectrum of MAPI thin film and MAPI peptide mixture thin films (different concentration).

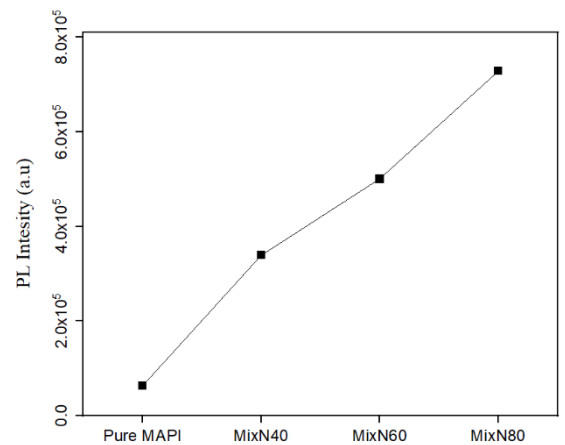


Fig (5-7): The relationship between the concentration of peptide and PL intensity.

The N 1s X-ray photoelectron spectra (XPS) for the pure MAPI and MAPI-peptide samples are depicted in Fig (5-8). Two peaks can be found in the MAPI-peptide spectrum at binding energies of 402.3 and 400.4 eV. Both samples have a peak at a binding energy of 402.3 eV, originating from the methylammonium group in MAPI [20]. On the other hand, the peak at a binding energy of 400.4 eV appears only in the MAPI-peptide sample and is therefore attributed to the NH/NH₂ amine groups in the FEFKFEFKK peptide that could contribute to the passivation of the electronic defects. As a result, as schematically depicted in the previous chapter in Figure (4-10), the rate of non-radiative recombination declines, increasing the photoluminescence intensity.

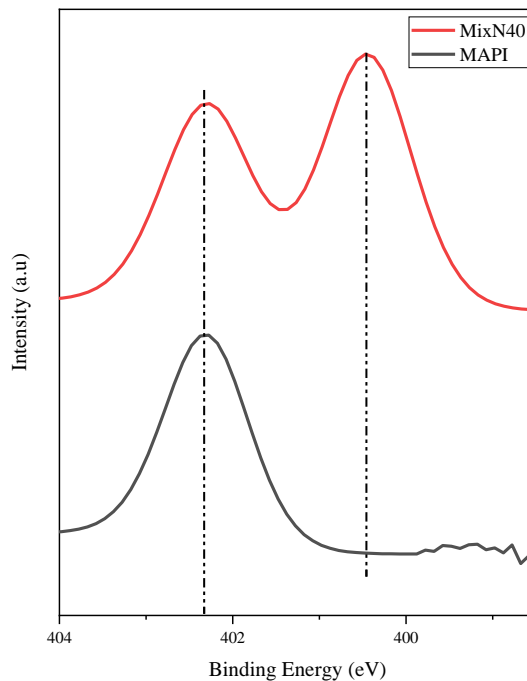


Fig (5-8): N 1s core-level spectra from pure MAPI and MAPI-FEFKFEFKK, the dashed lines show the positions of N 1s peaks in different chemical environments.

5.3.1.2.3 Time-resolved PL decay

Considering the considerable improvement in PL intensity between pure MAPI and a mixture of MAPI and peptide and the effect on lifetime observed for the eight amino acid peptide it is likely that the photoluminescence lifetime of this system will also be affected. Fig (5-9) shows the PL decay and the fitted line for unadulterated MAPI, MixN20, and MixN40. The fitted lines were obtained by fitting the decay data with a two-exponential decay function and then calculating the decay time (τ) using equation (4-1) with the obtained parameters (A_1, τ_1, A_2 and τ_2). Table (4-3) displays the decay time calculated for the measured samples. As observed, MAPI-FEFKFEFKK thin films (MixN20 and MixN40) have sixfold and tenfold longer PL lifetimes than unadulterated MAPI. This could be attributed to the fact that adding the peptide to MAPI could minimise non-radiative pathways by passivating unintentional defects, which in turn increases the PL lifetime at higher peptide concentrations. Fig(5-10) confirms minimising non-radiative pathways where it shows the fitting of PL decay of MixN40 thin film with mono-exponential indicating a single rate-limiting step in its luminescence process. In contrast, a mono-exponential model does not fit with the PL decay curve of pure MAPI due to the PL decay time containing two components; the fast decay time component that could be associated with the non-radiative recombination resulting from the recombination-active defects and slow decay time component that could correspond to radiative recombination. The same effect is observed when using the F8 peptide, but the increase in PL lifetime resulting from the use of the F8 is almost double that resulting from the F9, as we find this when comparing the PL lifetime of Mix40 (that is 11 ns) and MixN40 (that is 5ns) thin films.

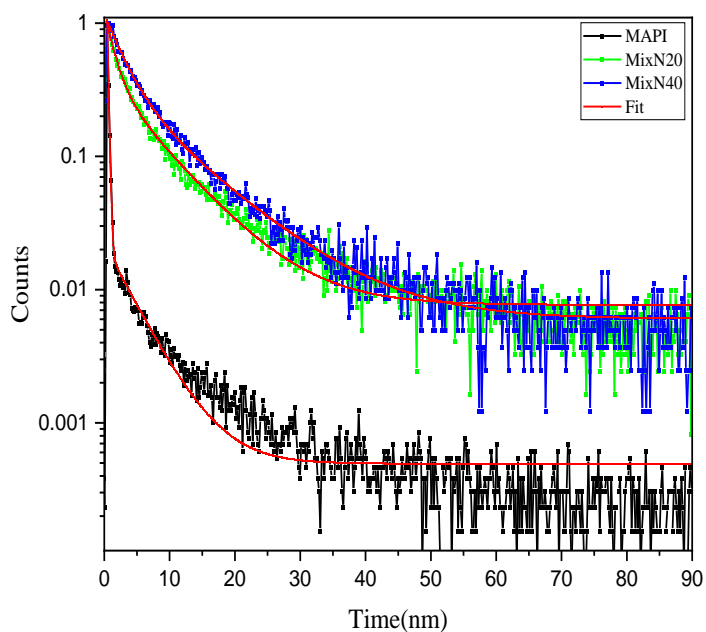


Fig (5-9): The TCSPC decay curves for Pure MAPI, MixN0 and MixN40. The red line is the fitting decay data with a two-exponential decay function.

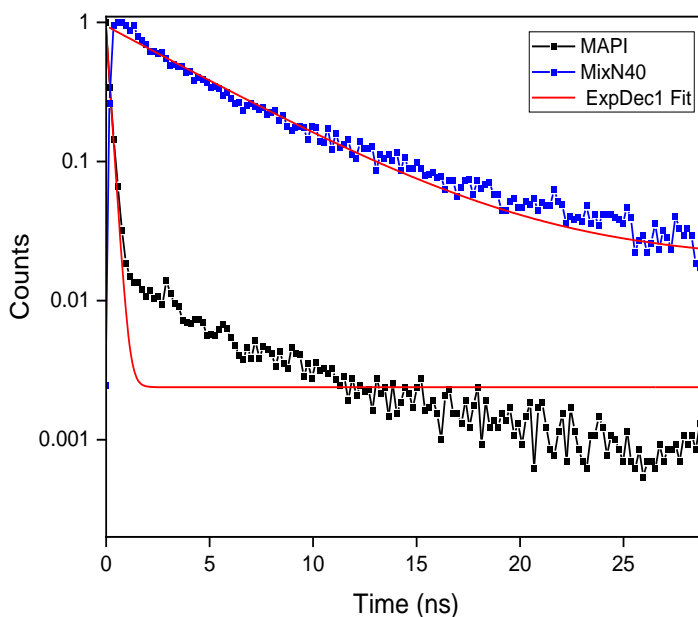


Fig (5-10): The TCSPC decay curves for Pure MAPI and MixN40. The red line is the fitting decay data with a mono-exponential decay function.

Table (5-3): Photoluminescent lifetimes for pure MAPI, MixN20 and MixN40

Sample	Decay time (ns)
MAPI	0.5 ± 0.01
MixN20	3.3 ± 0.01
MixN40	5 ± 0.01

By comparing the effect of F8 and F9 on the properties of fabricated MAPI, there is a notable convergence in the effects exerted by each of them on the properties of perovskite as a concept, but it is clear that some differences exist in the degree or scale of their influence on certain properties. The comparison in Table (5-4) presents data indicating no major differences in the particle size and average bandgaps of the MAPI thin films, which are fabricated using the same concentrations of F8 and F9. On the other hand, it was found that the PL intensity and lifetime PL of MAPI films templated with F8 was roughly double that of those fabricated using F9.

Table (5-4): Comparison of the effect of F8 and F9 on the properties (particle size, bandgap, PL intensity and lifetime PL) of fabricated MAPI.

Concentration of peptide	Particle size (nm)		Bandgap (eV)		PL Intensity (a.u)		Lifetime PL (ns)	
	F8	F9	F8	F9	F8	F9	F8	F9
0	70±7		1.58 ± 0.013		67×10 ³		0.5 ± 0.01	
40	43±8	44±7	1.59±0.01		61×10 ⁴	34×10 ⁴	11±0.02	5±0.01
60	35±4	40±6	1.6±0.012	1.59±0.01	117×10 ⁴	500×10 ⁴		
80	34±1	36±1	1.61±0.01	1.61±0.01	210×10 ⁴	73×10 ⁴		
100	26±4	27±3	1.62±0.01	1.62±0.01				

5.3.2 Increasing the stability of MAPI

In order to determine the effect of the peptide on the stability of MAPI perovskite, we investigated the stability of thin films under two conditions: exposure to water vapour and heating.

5.3.2.1 Improvement of MAPI-peptide stability in a moist environment

To investigate the stability of the MAPI peptide mixture in a humid environment (RH around 70%), a pure MAPI thin film and a MAPI-FEFKFEFKK composite thin film (40, 80, 120, and 160mg/ml) were placed in a container with water beneath the samples leading to exposure to water vapour for as long as 19 days. As shown in photographs in Figure (5-11 B), the brown colour of the perovskite still appears in the peptide-MAPI thin films for up to 19 days, whereas the pure MAPI film is wholly degraded after only three days of water vapour exposure, which means the peptide F9 appears to decrease the sensitivity of MAPI to water, increasing its stability. To confirm this result, X-ray diffraction (XRD) was carried out for the freshly prepared thin films and after exposure to water vapour for 19 days. Fig (5-11) A shows the prominent peak of MAPI perovskite at $2\theta = 14.1^\circ$ in the XRD pattern of in both the MAPI and the MAPI-peptide composite samples when fresh, confirming the presence of MAPI crystals in the prepared thin films. In contrast, (Figure 5-11C) shows XRD patterns for the samples, for a 2θ range of 5° – 20° , after exposure to water vapour for 19 days. The prominent peak of pure MAPI ($2\theta = 14.1^\circ$), which corresponds to the (110) crystal plane of MAPI, has reduced, and other peaks have appeared due to the presence of PbI_2 ($2\theta = 12.6^\circ$) [119] and MAI ($2\theta = 10.1^\circ$) [123], indicating it has thoroughly degraded. The FEFKFEFKK-MAPI composite thin films, however, still contain a clear MAPI in the XRD pattern, although there is some evidence of the formation of PbI_2 and MAI in FEFKFEFKK-MAPI thin films that decreases at high peptide concentrations. The observed differences could be attributed to the peptide F9 preventing water vapour from reaching the MAPI, if the MAPI is formed inside the mesh network of the gel or beneath the peptide layer. This latter structure, i.e. with a layer of peptide above the perovskite may explain the loss of the fibrous structure in the peptide -MAPI thin films in the SEM images of samples prepared as shown in Fig(5-12). Alternatively, it is possible that the addition of the peptide to the perovskite improves the crystallinity of the material by controlling the growth, as has been observed when other polymer additives have been mixed with the perovskite precursors [124]. On the other hand, this improvement of perovskite

stability may be self-healing of the perovskite, as has been seen for similar systems [114], where the peptide gel may work to prevent small molecules from leaving the perovskite surface and becoming available to participate in the resynthesis of the perovskite.

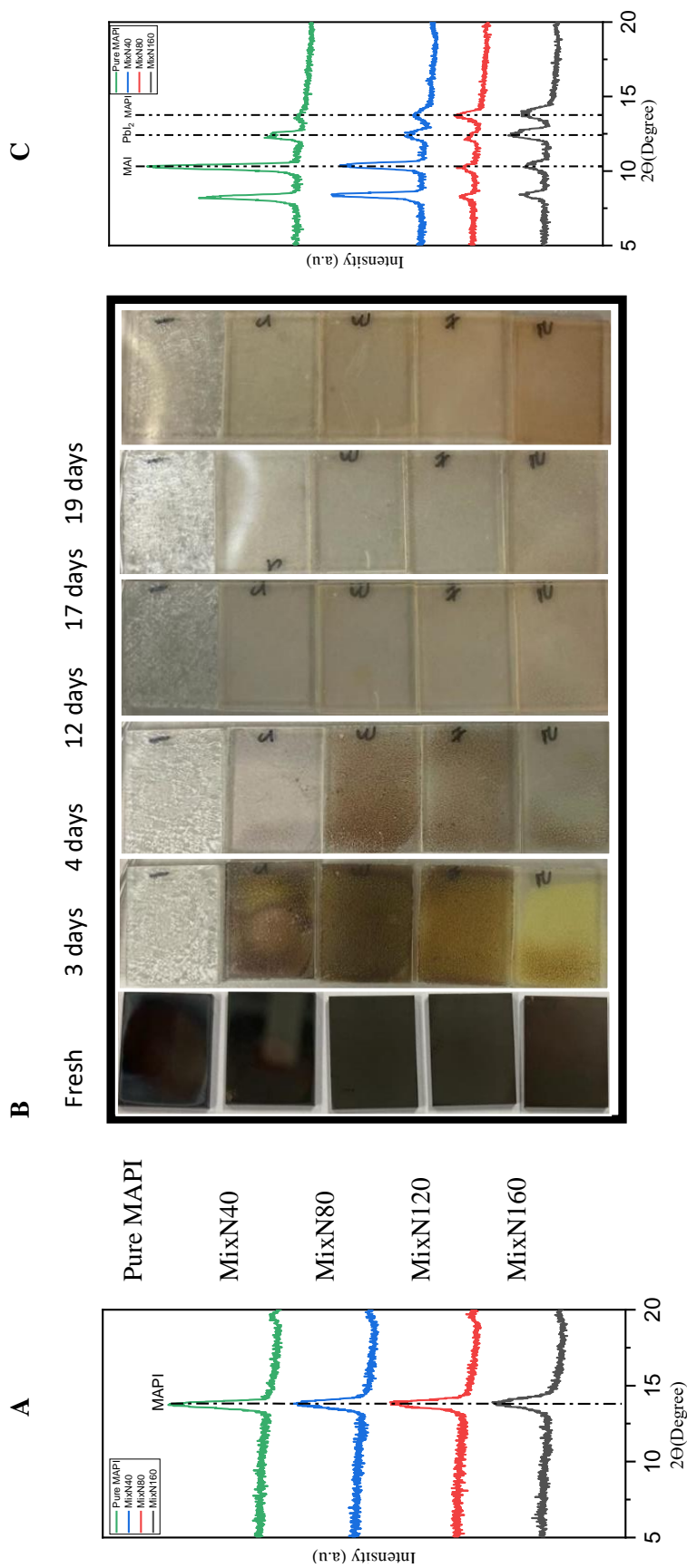
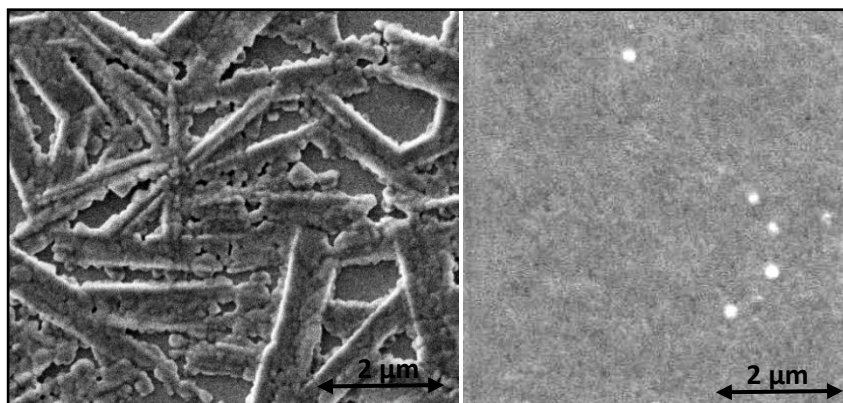


Fig (5-11) : A: XRD for fresh pure MAPI and F9-MAPI thin films, B: Photographs of MAPI film with and without peptide during exposure to water vapour over 19 days, C: XRD for pure MAPI and F9-MAPI thin films after exposure to water vapour for 19 days.



Pure MAPI

MixN40

Fig (5-12): SEM images for MAPI and MAPI-F9 (concentration 40 mg/ml)

5.3.2.2 Increase in MAPI-peptide stability against heating

XPS was employed to study the stability of pure MAPI and MAPI-F9 (40 mg/ml) thin films upon heating. Photoelectron spectra were measured from the thin films at room temperature (RT), 100 °C, and 150 °C. The XPS spectra of Pb 4f, I 3d, and N 1s core level from the pure MAPI thin film are shown in Fig (5-13) a, b and c, respectively. As discussed in the previous chapter, the results indicated degradation of MAPI with heating, especially when the temperature was increased above 150 °C, where the results indicate the disappearance of N from the sample and a shift in the binding energies of the Pb 4f and I 3d core levels to higher energy. This is clear evidence of degradation of MAPI [18]. In addition, the results showed the presence of a weak peak for a metallic Pb, in the pure MAPI sample, as discussed in the previous chapter [18], the intensity of which increases with heating, as confirmed by the plot of elemental ratios shown in Fig (5-15 a). Upon heating to 150 °C, the increase in the metallic lead is accompanied by a decrease in the I to Pb ratio, as shown in Fig (5-15 b), indicating the degradation of MAPI with heating to PbI_2 and then further decomposition of PbI_2 to metallic Pb and I (g) [20].

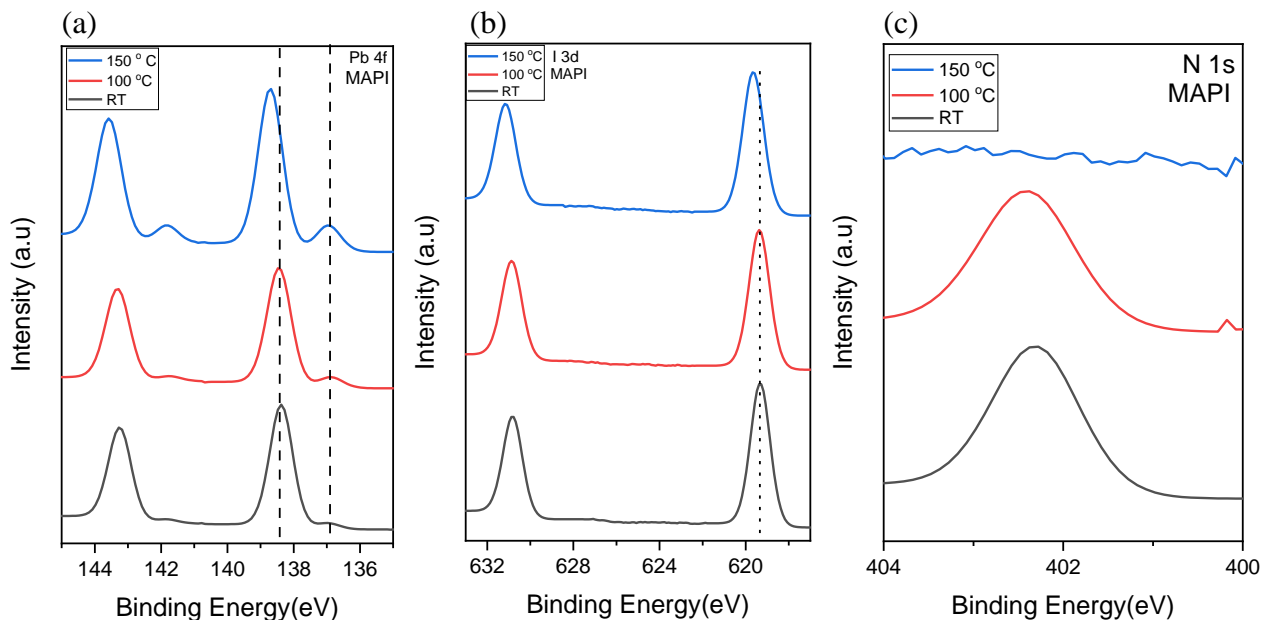


Fig (5-13): The XPS spectra of (a) Pb4f, (b) I 3d and (c) N 1s core level from pure MAPI thin film at different temperatures (RT, 100 and 150 °C)

Fig (5-14), shows XPS spectra of the core levels for the main elements of MAPI perovskite: Pb 4f (a), I3d (b), and N 1s from a MAPI-FEFKFEFKK thin film at different temperatures (RT, 100 and 150 °C). At all three temperatures, the Pb 4f_{7/2} and I 3d_{5/2} peak binding energies are consistent with the presence of MAPI, with binding energies of 138.4 eV and 619.3 eV. The metallic Pb peak is relatively weak at all three temperatures, compared to the pure MAPI sample, as shown by the element ratio plotted in Fig (5-15 a). The I 3d peak (5-15 b) demonstrates a decrease in the ratio of I to Pb for the sample heated at 150 °C but at a much lower rate than that seen for the pure MAPI film. This suggests that the F9 peptide may contribute to the enhanced stability of MAPI. The N 1s spectrum for the F9-MAPI composite film has two clear components at 402.3 eV and 400.5 eV binding energies that can be attributed to the organic cation of MAPI, with some contribution from protonated amine NH₃⁺ [120], and the amine environments comprising the peptide chain, respectively. This seems to indicate that some MAPI-related nitrogen remains, even after heating to 150 °C in vacuum. Although F9 has additional lysine compared to F8, the ratio of N in F9-MAPI in both chemical environments is almost the same as those in F8-MAPI, especially at room temperature and with heating at 100 C but with heating at 150 C, it had decreased in F9-MAPI by higher rate compared F8-MAPI as shown in the table (5-5). This, alongside an increase in metallic Pb in F9-MAPI thin film with the heating temperature rise by a higher rate compared to F8-MAPI, as shown in Fig (5-16), could indicate that F8 is better than F9 in improving the MAPI stability.

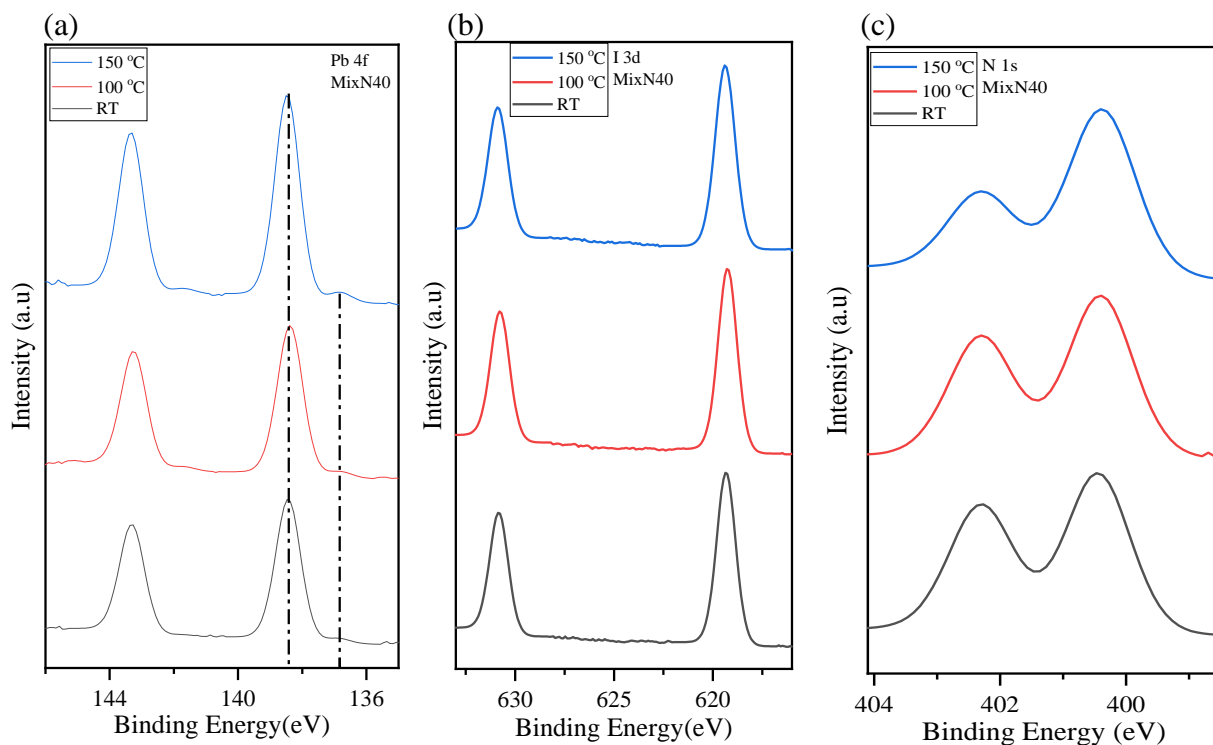


Fig (5-14): The XPS spectra of (a) Pb4f, (b) I 3d and N 1s core level from MAPI-FEFKFEFKK thin film at different temperatures (RT, 100 and 150 °C)

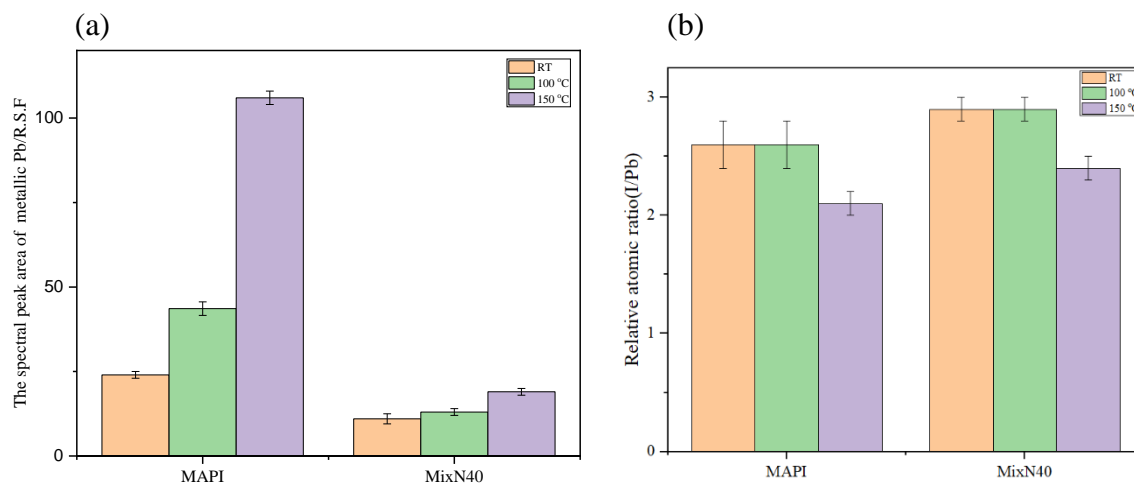


Fig (5-15): (a) The ratio of metallic Pb in pure MAPI and MAPI-F9 thin films at different temperatures (RT, 100 and 150 C), (b) the relative ratio of I to Pb in Pure MAPI and MAPI-F9 thin films at different temperatures (RT, 100 and 150 °C)

Table (5-5): The atomic ratios of *N 1s* to *Pb 4f* at the surface of the F8- MAPI and F9-MAPI samples

		RT	100° C	150° C
F8-MAPI	NH ₃ ⁺ (402.3eV)	1.01	0.89	0.7
	NH ₂ (400.5eV)	1.34	1.29	1.2
	NH ₃ ⁺ / NH ₂	0.75	0.69	0.54
F9-MAPI	NH ₃ ⁺ (402.3eV)	1.06	0.94	0.47
	NH ₂ (400.5eV)	1.34	1.27	1.02
	NH ₃ ⁺ / NH ₂	0.78	0.74	0.45

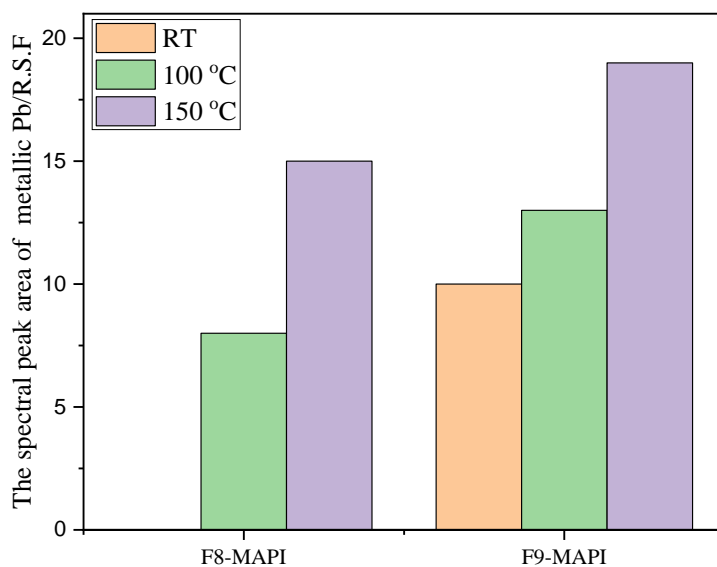


Fig (5-16): The ratio of metallic Pb in F8-MAPI and F9-MAPI thin films at different temperatures (RT, 100 and 150° C)

5.4 Conclusion

Using the FEFKFEFKK peptide as a template, the fabrication of MAPI perovskite was examined in this chapter in order to control its particles size and optoelectronic properties as well as improve its stability by encapsulating MAPI crystals inside peptide mesh. A solution process and a spin-coating approach were used to prepare and deposit the samples.

Utilizing photoluminescence (PL), absorbance, and time-resolved PL spectra, the optoelectronic characteristics of the films prepared were characterised. Utilizing SEM and XRD, respectively, the thin films' morphology and structure were described. XPS was used to identify the samples' surface chemistry.

The findings show a reduction in the MAPI crystal size with a rise in peptide concentration, accompanied by a slight increase in the MAPI bandgap and a blue shift in PL emission. The high concentration (100 and 120 mg/ml), the width of PL peaks increased, which could indicate to presence of particles of different sizes due to a heterogeneous network with different mesh sizes. Also, due to passivated electronic defects in thin layers, the intensity and time-resolved PL are enhanced. On another side, the observed effect is increased stability of templated MAPI thin films against moisture and heating compared to pure MAPI.

By comparison of this peptide (F9) with F8 investigated in the previous chapter, we find that there is a remarkable similarity in many of the effects that each of them affected the properties of perovskite as a concept, but the observed thing there is some of the difference in the magnitude of the effect. For example, the effect of the F8 peptide is better in increasing the PL lifetime of perovskite, where it increased the PL lifetime by around double that resulting from the F9. Also, F8 prevented an increased ratio of Pb metallic with heating by rate more than F9, which means it improved the MAPI stability more than F9. In contrast, the effect of F9 on the PL of MAPI was more than F8, where the high concentrations of F9 gave broader peaks that could be attributed to the presence of two peaks resulting from different particle sizes. The presence of a peak at around 700 nm could indicate to fabrication of particles smaller than those resulting from using F8, which could be attributed to the higher solubility of F9 compared to F8. In general, further study is needed to give clear interpreters about some reasons for these effects and the different effects of them.

**Chapter 6: Treatment of titanium dioxide by
4-Fluoroaniline (4-FA)**

6.1 INTRODUCTION

One of the main components of perovskite solar cells is the electron transport layer (ETL) which extracts and transports photoelectrons from the active layer to the external circuit. To fulfil this role, it should satisfy several requirements related to morphology, defect states, and optoelectronic properties, such as transparency, electron mobility and suitable energy level alignment with the perovskite layer. Metal oxide materials such as SnO₂ and TiO₂ are excellent candidates for use as electron transport materials in PSCs due to their n-type character, work functions, and conduction bands, which all match with those of many well-known hybrid perovskite materials. These advantageous properties arise due to the efficient hole-blocking barrier that results from their wide bandgap and deep-lying valence bands, compared to those for perovskites, as shown in Fig (6-1). In addition, these oxides often have high electron mobilities, stability and low fabrication costs [9].

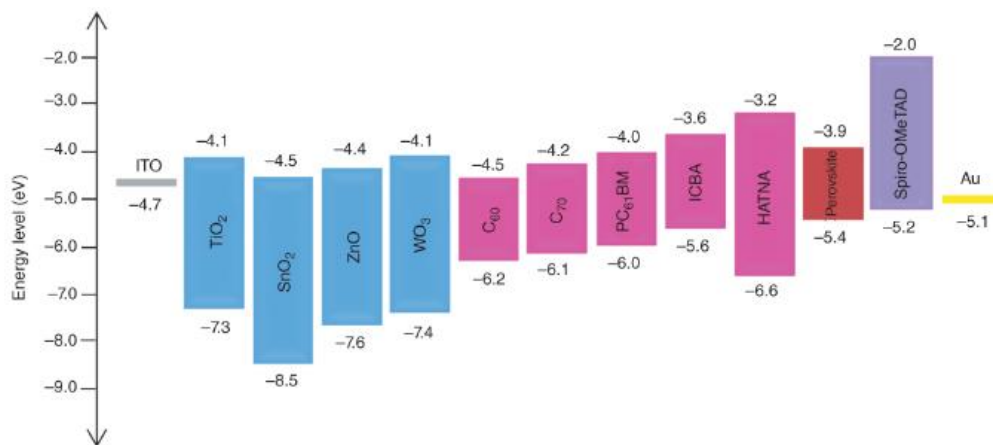


Fig (6-1): Energy level diagram of the materials used as ETL, where Zero refers to the energy level of the vacuum, and the upper and lower numbers refer to the relative position of the conduction and valence bands, respectively, for each material. [9].

TiO₂ thin films are commonly used as the ETL as a consequence of its early application in dye-sensitized solar cells (DSSCs) in the 1990s. They have been employed in PSCs since 2009, due to their ability to provide a thick and mesoscopic layer. TiO₂ can exist in three polymorphs: anatase, brookite, and rutile with a relatively large bandgap of 3.0 -3.4 eV as described in Chapter 3 section (3.3.3) [9]. This has led to intense research activity in order to improve and overcome some of the factors that limit the practical application and also that can negatively affect the performance of PSCs [125].

Among these potentially undesirable factors is the well-known hydrocarbon contamination layer that forms on the surface of any material, when exposed to air. This overlayer of organic carbon compounds spontaneously forms on the surface, and recent work has shown that on TiO₂ the primary components are small carboxylic acids, such as formic and acetic acid, and bicarbonates [126][69]. In dye-based PV cells where TiO₂ is used as the n-type material, there is some evidence that weakly bound organics such as catechols can be displaced by the dyes [127], the latter being bound via carboxylic acids to TiO₂ surfaces [128]. The displacement of organic acids from the surface of titania by other dyes is less well understood.

The effect of the adventitious C overlayer on the charge injection process is not known, although it is known that TiO₂ exposed to UV light/ozone is capable of degrading organic adsorbates [129]. It is widely believed that blocking of unsaturated Ti sites at ambient temperature could affect chemical reactions occurring on TiO₂ surfaces[69]. It has also been reported that TiO₂ surfaces in ambient environments shift from hydrophilic into hydrophobic in the dark, which can be attributed to the hydrocarbon contamination on TiO₂ thin film surface due to exposing TiO₂ to air [126][70]. Again, the effect of the hydrophobicity on the deposition of the organo-lead halide perovskites, which are often delivered from polar aprotic solvents such as DMSO and DMF, has not been studied. Finally, carbon impurities could act as defect sites or recombination centres in semiconductors and, therefore, negatively affect the performance of electronic devices, including charge transfer as mentioned above [130][72][73].

Therefore, to prevent these detrimental effects on the properties and, consequently, the functions of TiO₂, several studies have focused on developing potential methods to remove the unwanted surface adsorbents or hinder adsorption by modifying or passivating surfaces with thin layers of molecules that block active sites. Fluorine (F), has been investigated to treat the TiO₂ surface and was shown to have beneficial effects where it had the lowest surface energy, which led to its employment as a shape-control agent and hence a reactivity-control agent in TiO₂ nanocrystal development [74]. F has also been shown to promote growth of the (001) surface of the anatase form of TiO₂ [131], which is thought to be more photoactive than the (101) surface which is the most energetically stable crystal face of anatase. Hines *et al.* used XeF₂ to treat the TiO₂ surface and found the treated surface had an increased resistance to carbon contamination when exposed to air. This was attributed to blocking undersaturated Ti sites by binding to the F-layer. There are, however, two issues with using the XeF₂ method described by Hines *et al.*: Firstly, XeF₂ is highly reactive with water and must therefore be used

under controlled atmosphere conditions, which makes it costly. Secondly, the XeF₂ treatment lead to an increase in the roughness of the fluorinated surface compared to the initial atomically flat TiO₂, indicating the occurrence of a relatively isotropic etching reaction at many sites on the surface [75]. Because of this, there is a need for less reactive fluorinating agents to produce an atomically smooth fluorinated surface.

Previous work investigating the adsorption of 3-Fluoroaniline (3-FA) on a single crystal anatase TiO₂ surface in ultra-high vacuum, showed that UV-induced dissociation of 3-FA results in surface bound F, which may offer a simpler method to fluorinate and therefore passivate the TiO₂ surface, with regards to hydrocarbon adsorption [132]. In this chapter, therefore, we investigate the use of 4-FA) as a fluorination agent under ambient conditions to treat TiO₂ surfaces to prevent or reduce carbon contamination. 4-Fluoroaniline is an aromatic liquid. It contains a fluorine atom and an amino group, as shown in Fig (6-3)[133][134]. According to Sangchakr *et al*, hydrofluorocarbons (HFC) can be decomposed by longer wavelength UV radiation ($200 < \lambda < 390\text{nm}$) in the presence of TiO₂ particles [135]; fluoride ions are one of the degradation products [132] that could achieve the purpose of the treatment by bonding to Ti and forming a blocking layer prevent of adsorption adventitious carbon species [132].

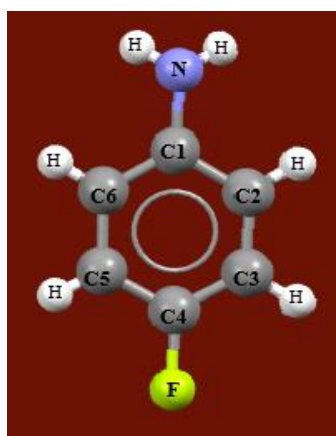


Fig (6-2): 4-Fluoroaniline molecule

6.2 EXPERIMENTAL SECTION

6.2.1 Materials:

The following materials were used in the synthesis of the TiO₂ thin films and their fluorination: titanium diisopropoxide bis (acetylacetonate) (Sigma-Aldrich), 1-butanol (Sigma-Aldrich), 4-fluoroaniline (Sigma-Aldrich) and ITO substrates (Ossila). All materials were used without further purification.

6.2.2 Preparation of TiO₂ thin films:

The thin films studied were prepared as described below:

6.2.2.1 Preparation of TiO₂ precursor solutions:

TiO₂ precursor solutions were prepared by mixing titanium diisopropoxide bis (acetylacetonate) and 1-butanol at two different ratios: *i.e.* 50 µl/mL and 150 µl/mL to obtain two concentrations, 0.1M and 0.3M. Then, they were stirred for 15 min at room temperature.

6.2.2.2 Deposition of the thin films

The cleaned ITO substrates were treated with UV-O₃ treatment for 15 minutes and placed on the rotating disk of the spin-coater. 100 µl of 0.1M precursor solution was put on the substrate and spin-coated at 2000 rpm for 30s with ACL 15/1680 and dried on a hotplate at 120 °C for 10 min. The same step was repeated to deposit a second layer using the 0.3M concentration. Then, the thin films deposited were annealed at 500°C for 30 minutes in a furnace and allowed to cool to room temperature naturally.

6.2.3 Treatment of TiO₂ thin films by 4-Fluoroaniline

6.2.3.1 Method 1: Treatment of TiO₂ thin films by immersing them in 4-fluoroaniline solution

TiO₂ films were placed in an ozone cleaner for 15 minutes. The samples were immersed in the 4-fluoroaniline (4-FA) solution and left for 10 minutes. These samples were then subjected to one of two procedures:

- rinsing in propan-2-ol (isopropyl alcohol, IPA) followed by exposure to UV-O₃ cleaning system after drying, or
- heating on a hot plate to remove excess 4-FA and then cleaning in the UV-O₃ system them as outlined below.

For the IPA rinsed samples the immersion/rinsing/drying steps were repeated several times for some samples in order to study the effect of repeating the treatment on F-uptake. The samples prepared were marked with the number of treatment cycles *i.e.* one, two or four cycles.

The samples treated by heating were dried and then heated to different temperatures, *i.e.* 120, 150, and 180 °C, and times, as detailed in table (6-1). Both sample treatments were then exposed to UV-O₃ 15 minutes in order to dissociate the 4FA [132]. The effect of heating at different temperatures and times was examined to determine the optimum heating time and temperature for treatment.

Table (6-1): Types of samples treated based on temperature and heating time.

Sample	Temperature	Time
1	120 °C	15 minutes
2	150 °C	15 minutes
3	150 °C	10 minutes
4	180 °C	10 minutes

6.2.3.2 Method 2: Treatment of TiO₂ thin films with 4-fluoroaniline vapour.

In a second approach to fluorinate the surface TiO₂ films were placed in UV-O₃ cleaner for 15 minutes to remove any adsorbed hydrocarbon. Under low vacuum ($\sim 1 \times 10^{-2}$ mbar), the samples and 0.2 ml of 4-fluoroaniline solution were put into a vessel without direct contact. Then, the samples were left for either 1 or 4 hours to allow the 4-fluoroaniline molecules to evaporate and adsorb to the surface of thin films. Samples were then transferred to the UV-O₃ cleaning system for 15 minutes, in order to decompose the 4-FA.

6.2.4 Instrumentation

X-ray photoelectron spectroscopy (XPS) was performed using a Kratos Axis Ultra XPS instrument to study the surface chemistry of the samples after exposure to 4-FA and determine the ratio of fluorine and carbon species absorbed on Ti to measure the treatment efficiency. Transmittance spectra were measured using a PerkinElmer Lambda 1050 with a scanning range between 250 to 850 nm.

6.3 RESULTS AND DISCUSSION

6.3.1 XPS results

The presence of carbon contamination on the metal oxide surfaces could be confirmed clearly in the XPS results. Fig (6-3) shows the survey spectrum from a TiO₂ thin film prepared without treatment, which displays the C 1s peaks, confirming the presence of adventitious hydrocarbon. We note that a portion of this carbon could result from the synthesis of the TiO₂ films from the titanium diisopropoxide bis(acetylacetonate) (C₁₆H₃₂O₆Ti) precursor [136] as well as from any adsorbed atmospheric hydrocarbon species. These peaks reveal different chemical states of carbon due to the presence of different carbon environments, where the lowest binding-energy peak (284.7eV) is attributed to the aliphatic carbon C-C/C-H and the higher binding energy peaks (286.7 and 288.9 eV) to C-OH/C-O-C and O-C=O [137] as shown in Fig (6-4). Also, Fig (6-5) shows the O 1s spectra from the fresh untreated sample. It is fitted with two peaks at binding energies of 530.3eV and 532.3 eV attributed to O-Ti in TiO₂ and O-C in the organic adventitious hydrocarbon on the surface [69], [138], respectively. It is therefore helpful to investigate the effect of the treatment on the presence of oxygen associated with the organic adventitious hydrocarbon, particularly since, as mentioned above, on TiO₂ the primary components of the adventitious carbon are thought to be small organic acids.

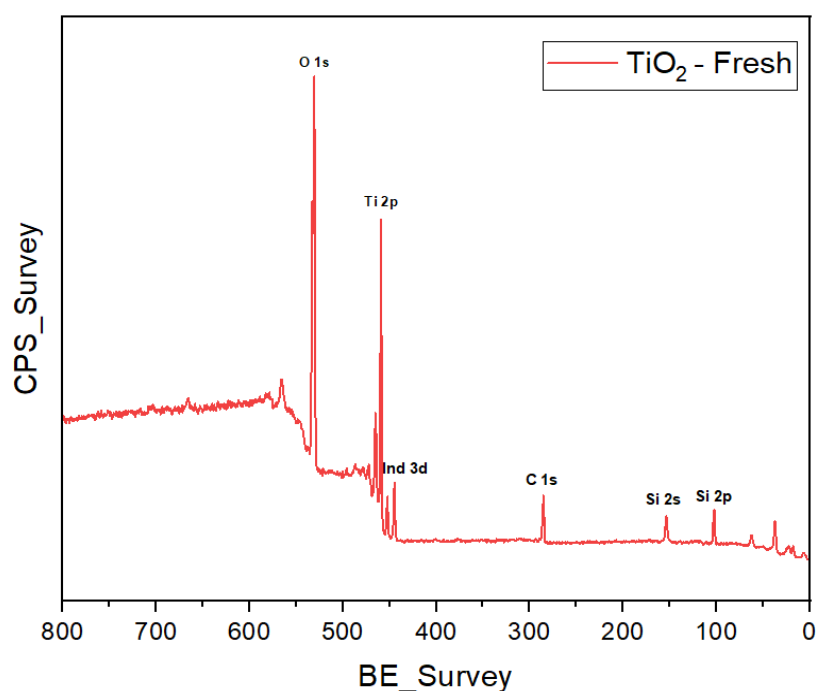


Fig (6-3): XPS survey spectra of fresh untreated TiO₂.

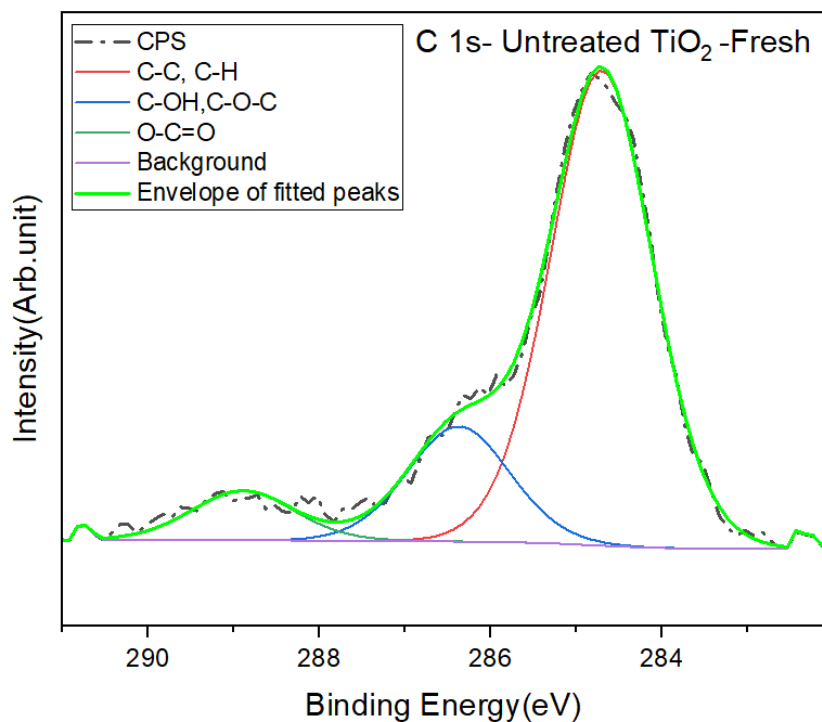


Fig (6-4): C 1s spectrum from fresh untreated TiO₂

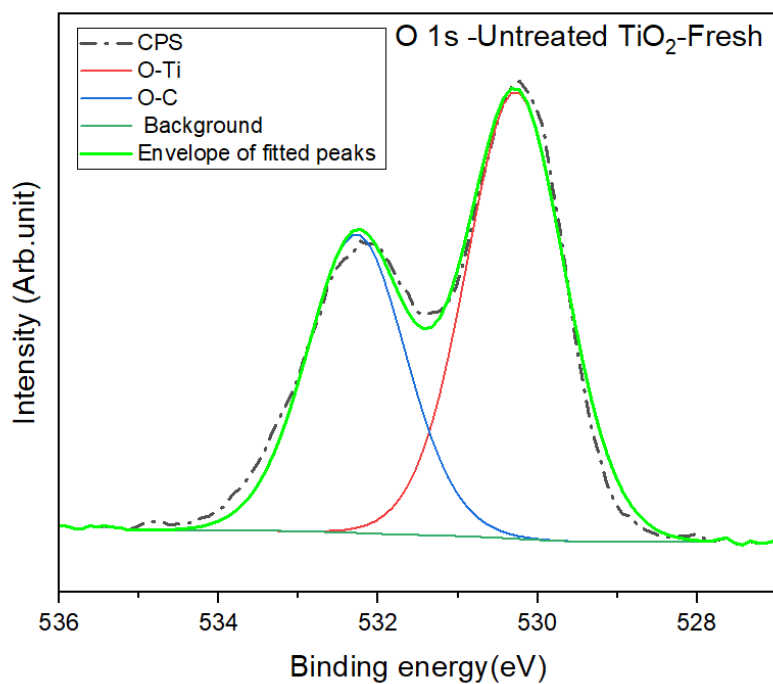


Fig (6-5): O 1s spectrum from fresh untreated TiO₂

To study the effectiveness of the fluoridation treatment on reducing the adsorption of adventitious hydrocarbon, we measured the samples with XPS after 35 and 50 days and compared the results. Fig (6-6 (a)) shows the Ti 2p, O 1s and C 1s spectra for the untreated TiO₂ “fresh”, after 35 days and after 50 days. In the Ti 2p spectra, for all samples (fresh and aged), there are two peaks at 458.8 and 464.5 eV, which correspond to the binding energies of the Ti 2p_{3/2} and 2p_{1/2} spin-orbit split states [139]. A slight decrease in the peak intensity of Ti

spectra of aged samples is observed, but this is thought to be simply due to the increase in the amount of contamination accumulating at the surface, as the Ti content of the sample is unlikely to be affected by ageing. In contrast, Figs (6-6 b and c) reveal that the intensity of organic oxygen and C 1s peaks increase slightly over time.

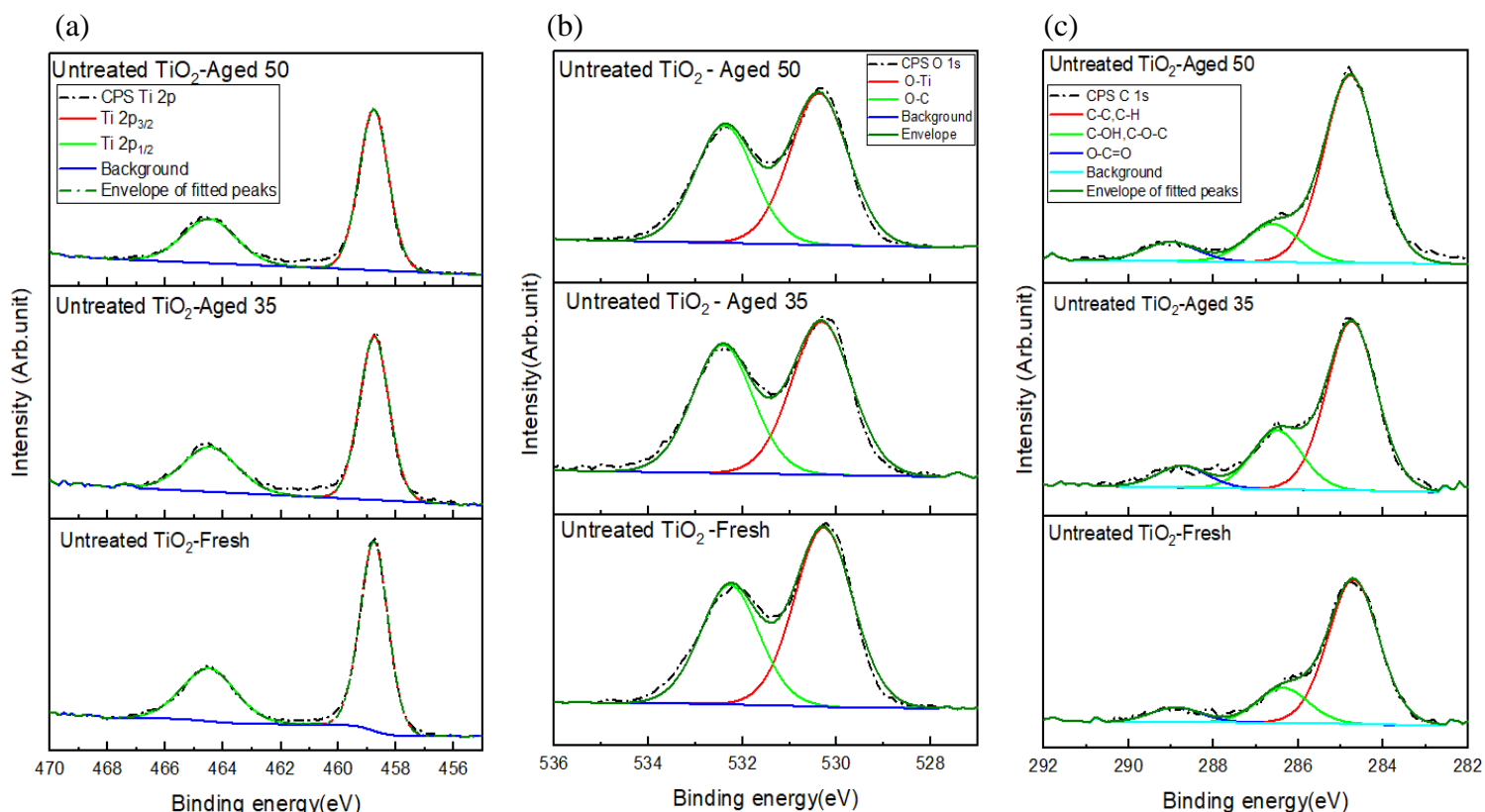


Fig (6-6): Ti 2p (a), O 1s (b) and C 1s(C) spectra from untreated TiO₂ – fresh, aged 35 days and aged 50 days.

The atomic ratio of the elements relative to Ti can be used as a benchmark for comparing the amount of material adsorbed on the samples studied. The atomic ratio is calculated from the peak areas for each chemical environment using empirically derived Kratos relative sensitivity factors[140]. Fig (6-7) shows the ratios of C1s and O1s (respectively) to Ti 2p for the fresh

untreated TiO₂ sample and for the two samples aged for 35 days and 50 days. According to the atomic ratio in Fig (6-7a), the aliphatic carbon signal increases clearly with ageing time on untreated TiO₂ thin films, whereas the increase in C-O functional groups is slight; so we will focus on the aliphatic carbon ratio. This is likely to be due to the fact that it is well established that O-containing hydrocarbons attach directly through the O-atoms, particularly in carboxylic acids resulting in a hydrophobic/oleophilic termination. This then is likely to result in the physisorption of aliphatic hydrocarbons. We therefore use the aliphatic carbon, C 1s peak for comparison between untreated and treated samples by the above methods to measure the F-treatment effect on the carbon contamination for the TiO₂ surface.

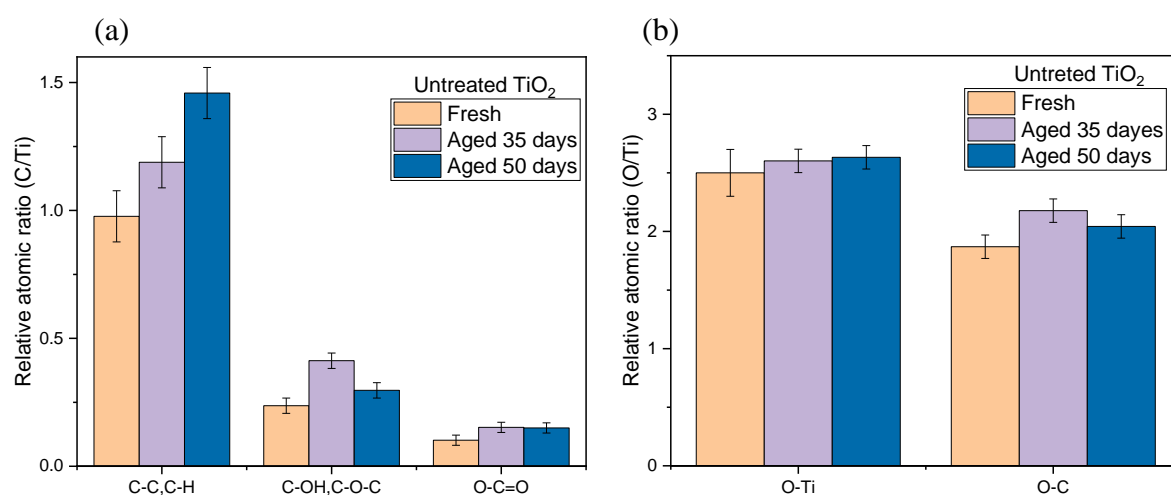


Fig (6-7): Relative atomic concentrations of C1s (a) and O1s (b) for Untreated TiO₂-Fresh, Aged 35 days and 50.

6.3.1.1 Treatment of TiO₂ thin films by immersing in 4-FA.

6.3.1.1.1 Using the cleaning by IPA (Isopropyl alcohol) to remove excess 4-FA.

Fig (6-8 a) shows F 1s spectra from samples treated by immersion in 4-FA, rinsing in IPA and subsequent UV exposure. The spectra show two peaks at binding energies of 684.4 eV and 687.2 eV. The peak at 684.4eV can be attributed to Ti-F bonding, in reasonable agreement with the work of Jackman' *et al.* for the Ti-F bond at binding energy 684.5-685eV [132]. This could indicate some of the 4-FA molecules interact with the surface resulting in the dissociation and loss of the aromatic component of the 4-FA, as observed in previous work [132].

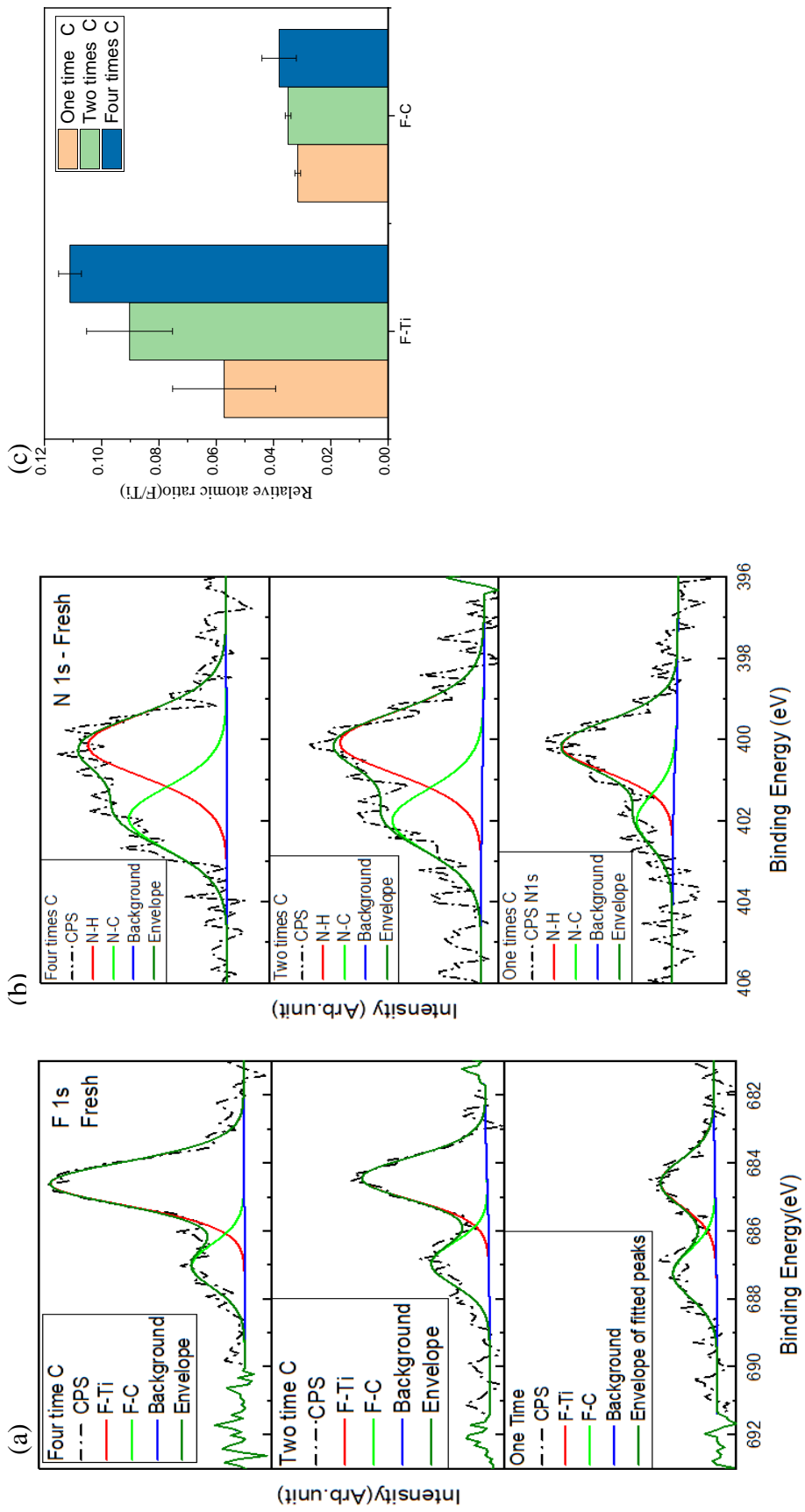


Fig (6-8): (a) and (b): F 1s and N 1s spectra, respectively, from fresh treated samples; once, twice and four times, (c): Relative atomic concentrations of F1s from fresh treated TiO₂; Once, Twice and Four times.

This results in fluoride atoms bonded directly to the surface Ti atoms. The ratio of fluorine atoms bonded to Ti increases with repeated treatment, as shown in Fig (6-8 c), which means repeated treatment increases the chance of interaction with the surface, thus increasing the F-Ti ratio. The second peak in the F 1s spectrum, at a binding energy of 687.2 eV, corresponds to the C-F in 4-FA showing that in all cases some intact molecules remain on the surface. By comparison, the binding energy of the 4-FA F 1s species adsorbed on a single crystal anatase surface was measured to be 687.5 eV [132]. The N 1s spectra from these samples (shown in Fig (6-8 b)) also indicates the presence of intact 4-FA on the surface. The N 1s spectra contain two peaks at binding energies of 400.0 eV and 402.0 eV. The peak at a binding energy of 400.0 eV is attributed to the C-NH₂ environment [141], in the 4-FA molecule, in agreement with previous work [132]. The higher binding energy peak most likely arises from protonation of the amine group to form NH₃⁺. Although this was not observed for the adsorption of 4-FA on single crystal surfaces, similar protonation and binding energy shifts have been observed for other amines including dopamine [14]. The reason for the difference is unclear but may arise from the presence of surface hydroxyls/protons on the more “realistic” samples studied here, which are prepared under atmospheric conditions, rather than in vacuum. In the single crystal work, the TiO₂ was prepared in vacuum by sputter anneal cycles to form an atomically clean surface. Further evidence for the assignment of the higher binding energy F 1s peak and the two N 1s peaks comes from the relative atomic ratios of (N-C)/(F-C) of 0.7, 1.1 and 1.05 for the samples treated one-time, two-times and four-times, respectively.

Fig (6-9) shows the C 1s spectra of fresh untreated and treated samples. All samples have the same three peaks at binding energies of 284.8 eV, 286.4 eV and 288.6 eV, that can be attributed to three different chemical states, i.e. aliphatic carbon C-C/C-C-OH/C-O-C and O-C=O, respectively, as in the case of the untreated sample [137]. The bar chart in Fig (6-10) shows the atomic ratio of carbon to Ti in order to compare the amount of C following the treatments. The amount of carbon in all chemical environments is found to increase in the samples treated once and twice, but in the sample treated four times the C content falls. The origin of the carbon signals in treated samples is unclear, i.e. whether it arises from hydrocarbon contamination or from undissociated 4-FA, since the functional groups C-C, C-N and C-F, have peaks at similar binding energies to those of the carbon contamination.

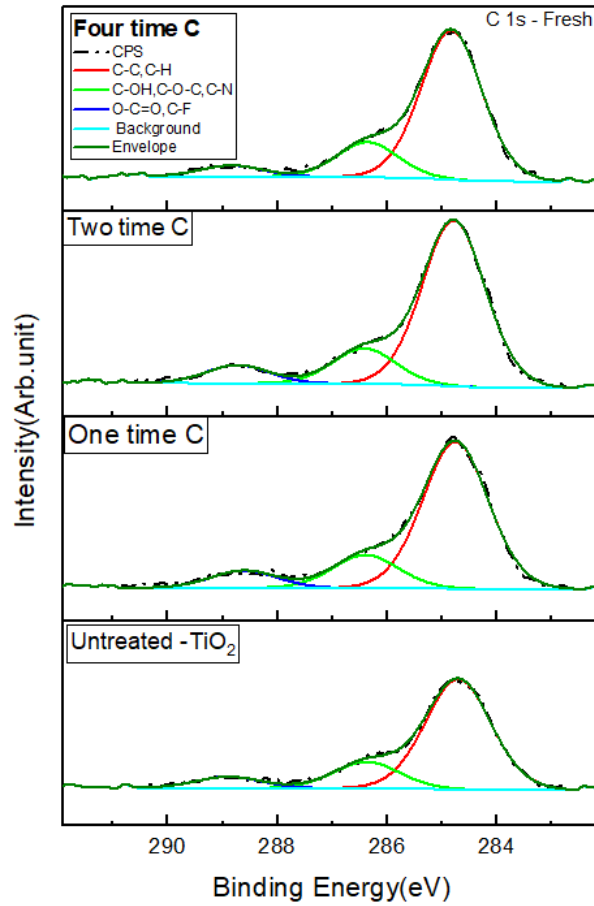


Fig (6-9): C 1s spectra from fresh untreated -TiO₂ and treated samples; once, twice and four times.

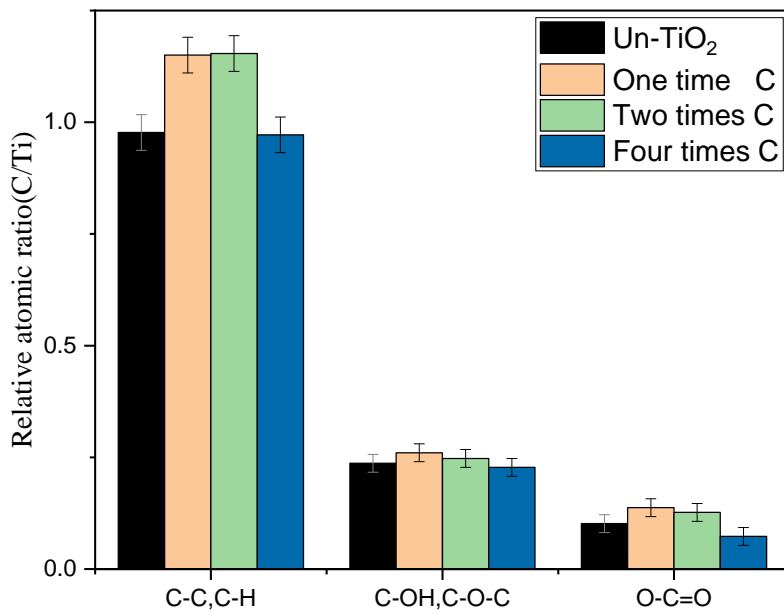


Fig (6-10): Relative atomic concentrations of C 1s from fresh treated TiO₂; Once, Twice and Four times.

The decreasing amount of O-C, in the O 1s spectra shown in Fig (6-11) and Fig (6-12) seems to suggest that repeating the treatment removes the organic contamination and that most of the carbon present in the C 1s spectrum belongs to 4-FA, indicating the molecule of 4-FA doesn't dissociate completely. However, the findings of the anatase-FA paper that used 3-FA suggested that the molecule completely degraded following exposure to broadband UV radiation from a Hg lamp, to leave only Ti-F [120]. Two possibilities could be used to interpret these different results for the two experiments. The first possibility is that the F in the ortho-position (or 4-position) is more stable than in the meta- (or 3- position). This may result in the higher BE observed for the C-F in 4-FA (288 eV) in this work, compared to that in 3-FA (287.3 eV). This increased stability would then explain why the molecule didn't decompose completely.

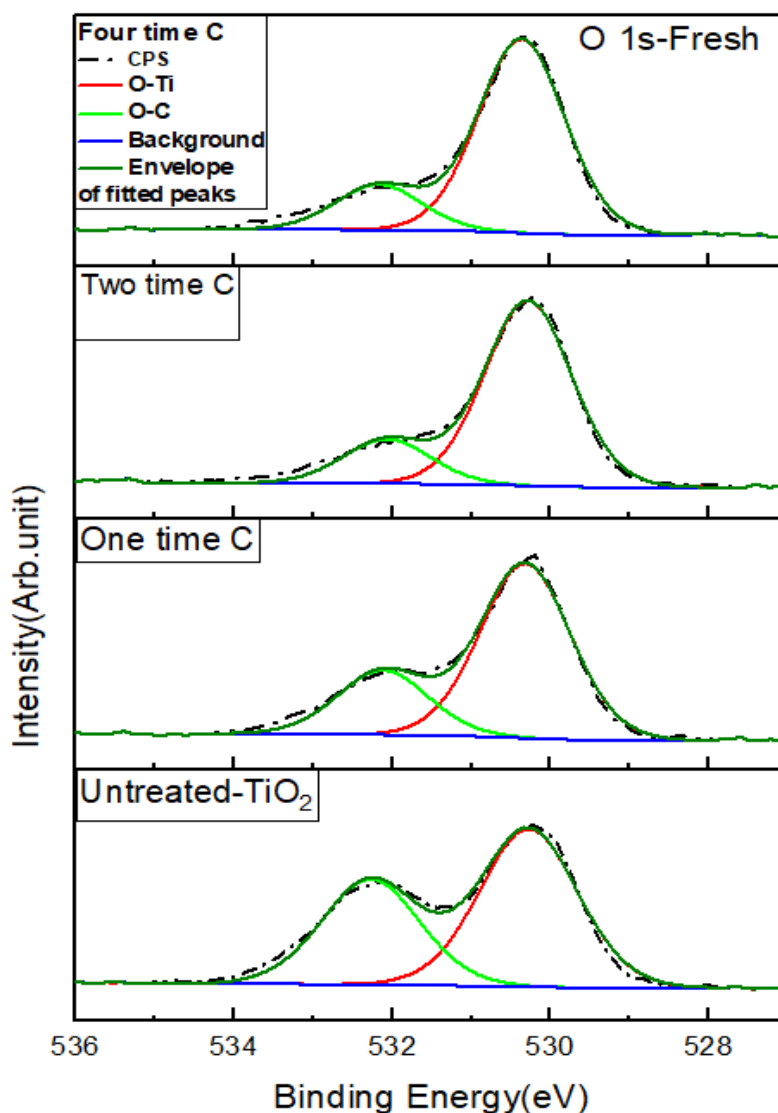


Fig (6-11): O 1s spectra from fresh untreated -TiO₂ and treated samples; once, twice and four times.

The other possibility is that in the anatase single crystal/3-FA experiment, the UV illumination was done in vacuum, and this may increase the rate at which the molecule leaves the surface. In addition, the measurement was done on an atomically clean, stoichiometric single crystal TiO_2 surface rather than the “dirty” surface that we measure in the current work. In the single crystal experiment, only 1 ML or less of 3-FA was deposited, whereas in the current work, we are likely to have a multilayer, therefore if the TiO_2 substrate is involved in the decomposition of the FA, then it would take much longer for this thick overlayer to decompose completely.

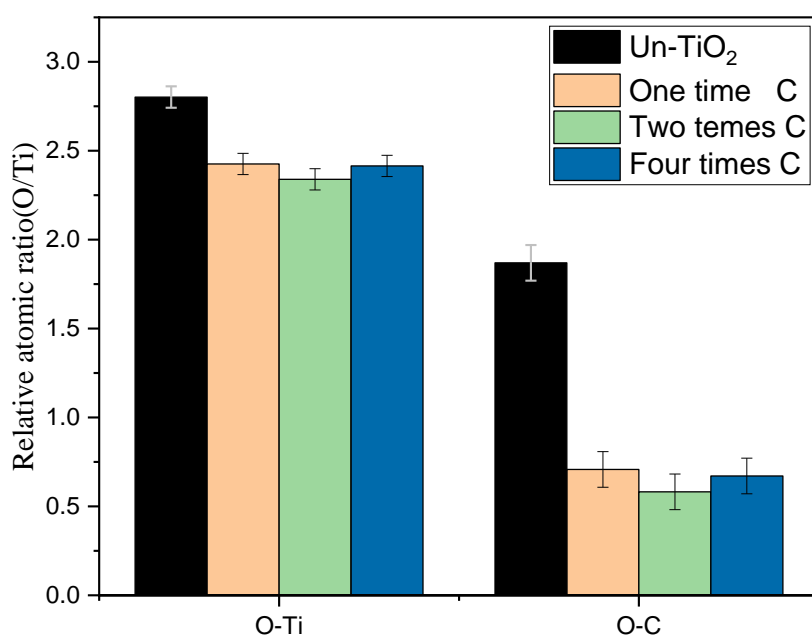


Fig (6-12): Relative atomic concentrations of O 1s from fresh treated TiO_2 ; Once, Twice and Four times.

Comparing the ratio of carbon after the samples' ageing could indicate the efficiency of this method in treating the TiO₂ surface to prevent further hydrocarbon adsorption. The samples were measured after 35 days and 50 days. Fig (6-13) shows the atomic ratio of aliphatic carbon for fresh samples and aged samples. The data measured from the sample 35 days after treatment shows that the ratio of carbon increased in the untreated sample by a higher rate than in samples that were treated once and twice. The ratio of carbon:titanium is seen to decrease in the sample treated four times compared to fresh samples. These results seem to confirm that the fluorinated sample exhibits some surface resistance to hydrocarbon absorption during this period. The data from the samples after 50 days, however, seem to show a decrease in the resistance to further C-contamination. It is clear that after 50 days the ratio of carbon in treated samples increases, suggesting a reduction in the efficacy of the 4-FA treatment. This may be attributed to the loss of fluorine atoms from the surface over time, as shown in Fig (6-14). The reason for observed loss of fluorine both from F-Ti and F-C is not clear from the data here, but one of the reasonable possibilities is the loss of the C-F species by evaporation of 4-FA from the surface. The loss of the TiF species is even less clear. One possibility is that F may diffuse into the bulk of the titanium dioxide film during aging. This could be confirmed using hard XPS (HAXPES), which can measure more deeply into the subsurface region.

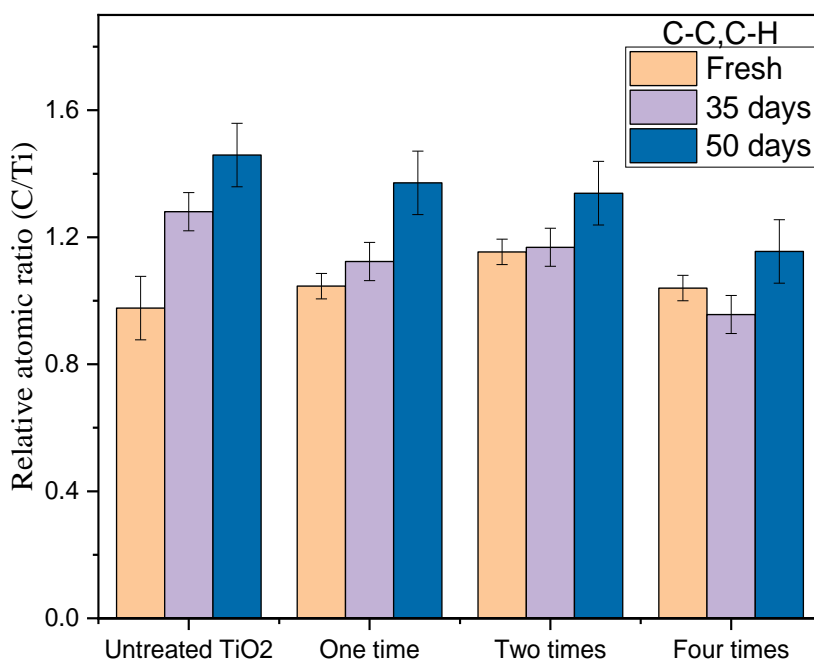


Fig (6-13): Relative atomic concentrations of C1s from fresh and aged untreated and treated TiO₂; Once, Twice and Four times.

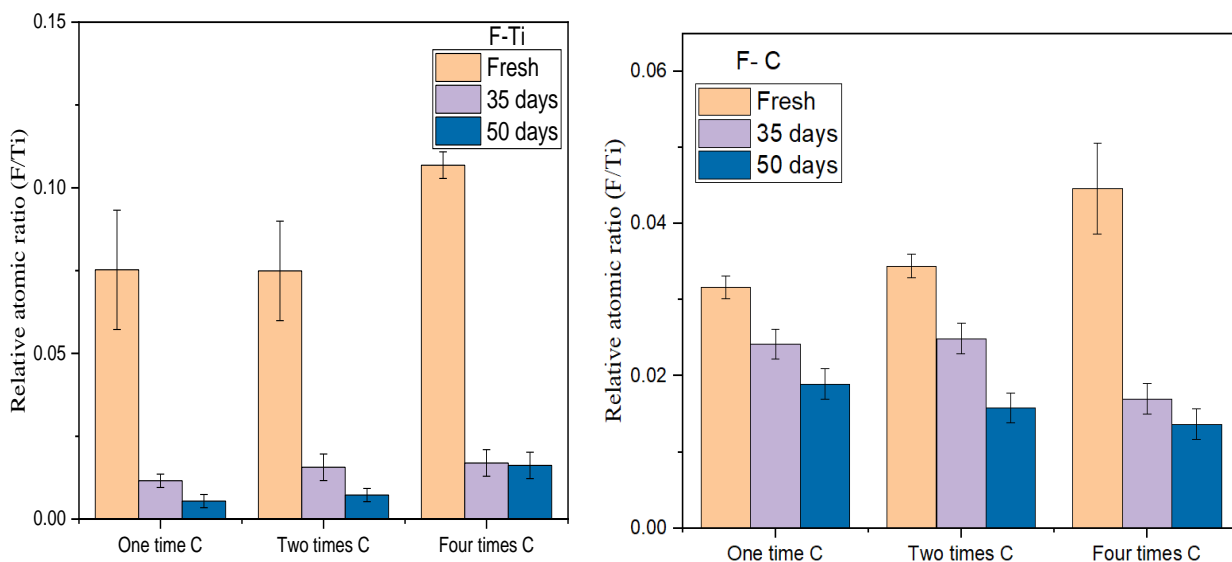


Fig (6-14): Relative atomic concentrations of F/Ti from fresh and aged untreated and treated TiO_2 ; Once, Twice and Four times. (Left for F-Ti and right for F-C)

6.3.1.1.2 Heating to remove the excess 4-FA

In this part, samples were treated in 4 steps:

- UV-ozone cleaning of the as prepared films,
- immersion in 4-FA,
- heating to a maximum of 187 °C, and
- UV-ozone cleaning.

The purpose of the heating is to dry the samples and remove any excess 4-FA, as well as to study the effect of heating in the treatment of TiO_2 because the heating could affect fluorination. According to Hines *et al* [75], F did not covalently bind to TiO_2 when immersed TiO_2 is immersed in HF for 10 min at room temperature. In contrast, others have fluorinated rutile (110) and TiO_2 nanocrystals by HF by heating at temperatures (200-500 °C). Hines fluorinated TiO_2 by exposing it to XeF_2 (g) at room temperature [75], suggesting that the requirement of heat in the fluorination of TiO_2 could depend on the fluorine source used, hence, we have investigated the effect of heating on fluorination using 4FA. The heating temperatures have been chosen randomly, up to the boiling point of 4-FA (187 °C). In addition, the duration of the heating was also varied to study its effect.

Fig (6-15) shows the F 1s spectra from treated and heated samples at different temperatures. The samples in (a) were heated at 120 °C and 150 °C for 15 min while those in (b) were heated at 150 °C and 180 °C for 10 min. Both spectra have two peaks at binding energies of 684.5 eV and 687.3 eV that are attributed to F-Ti and F-C bonds, as mentioned above. However, it is found that the F-Ti peak intensity decreases with an increase in the temperature, as confirmed by the atomic ratio of F to Ti shown in Fig (6-16). The sample treated without heating (marked as 'one time C' in Fig (6-16)) has a higher atomic ratio of fluoride than the heat-treated samples, confirming that the heating effect leads to a decrease in fluoride content that continues to decrease with higher temperatures. Also, by comparing samples heated at 150 °C for different times (green and light blue in Fig (6-16)), we found that the longer heating times causes a more significant loss of fluorine bonded to Ti, indicating that heating could break the F-Ti bond that was formed during immersion, which may have allowed the loss fluorine as gas or diffused into the bulk of TiO₂ during heating.

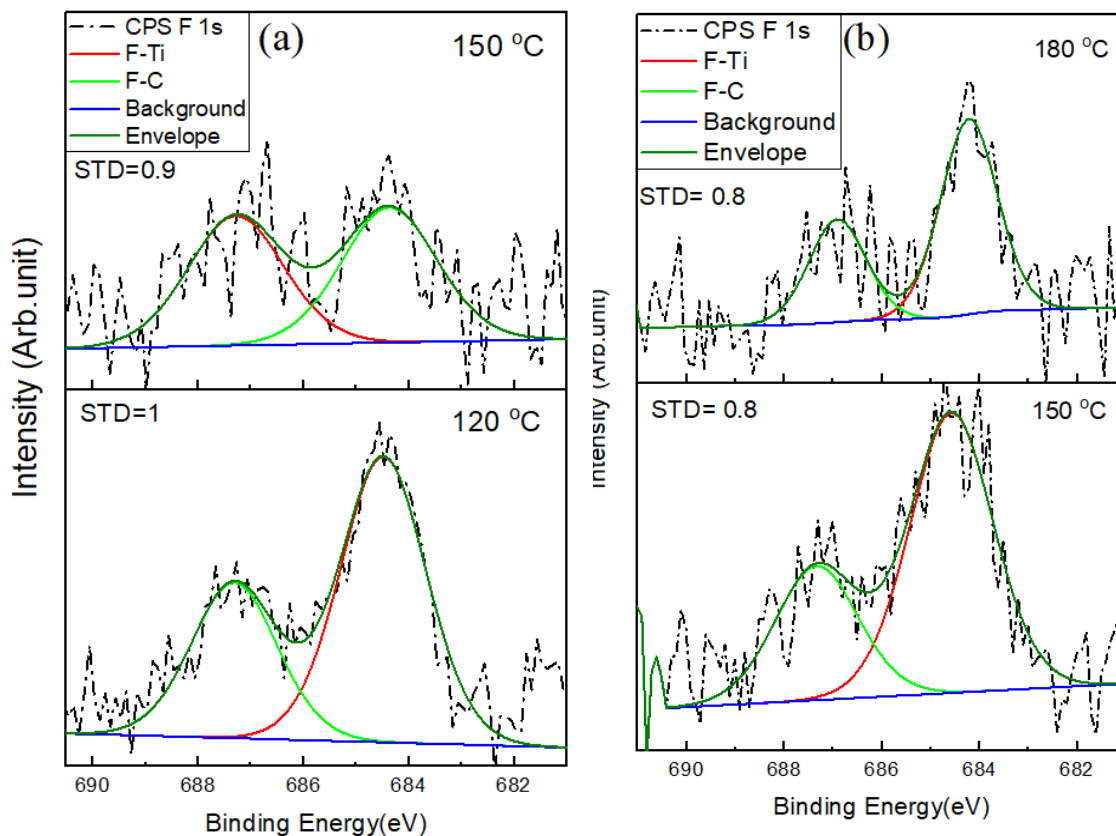


Fig (6-15): F 1s spectra from fresh treated and heated samples; (a) samples heated at 120 °C and 150 °C for 15 min (b) samples heated at 150 °C and 180 °C for 11 min.

In contrast, the fluorine ratio from the F-C bond is almost the same in the unheated sample and heated samples at 120 °C and 150 °C, as shown in Fig (6-18). But the sample heated at 180 °C loses a significant amount of fluorine. Also, the total nitrogen decreased by around 1.4 times of rate decrease of fluorine (F-C), as shown in Table (6-2). Based on the chemical formula of 4-FA (C_6H_6FN), the (N: F) is 1:1, indicating that this loss could be due to the evaporation of 4-FA molecules because the temperature was close to their boiling point.

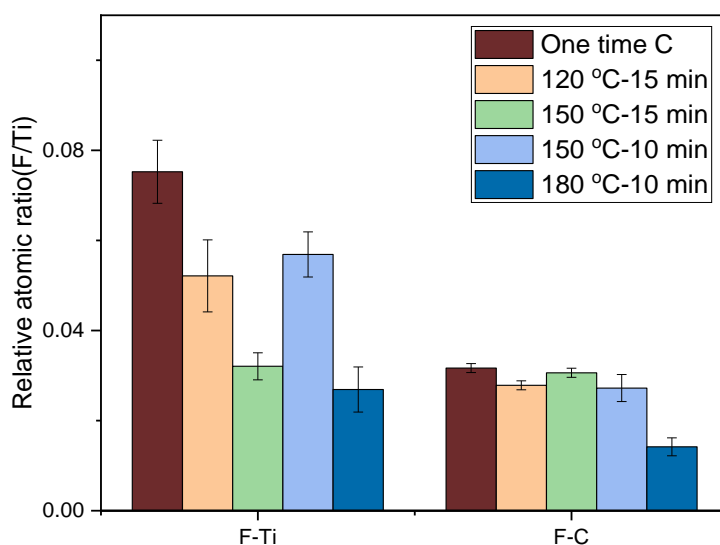


Fig (6-16): Relative atomic concentrations of F1s from fresh unheated and heated samples at different temperatures for different times.

Table (6-2): The atomic ratio of F 1s, C 1s and N 1s to Ti at the surface of fresh treated and heated samples at 150 °C and 180 °C for 10 min.

	150 °C 10 min	180 °C 10 min	The amount of decrease	Decrease of X / Decrease of F
F-C	0.036	0.016	0.02	
C-C	1.09	0.97	0.12	6
Total of N	0.095	0.067	0.028	1.4

Fig (6-17) (a and b) show the C 1s spectra from samples that were treated and heated at 120 °C and 150 °C for 15 min and the samples that were heated at 150 °C and 180 °C for 10 min. The C 1s spectra have the same three peaks present for all samples, with some differences in their intensities that can be compared clearly by the atomic ratio bar chart shown in Fig (6-18). The ratio of C from the C-C bond is almost the same for unheated sample and samples that were heated to less than 180 °C. This means the increase in carbon on the treated samples, as compared to the untreated samples, may have come from the immersion in 4FA, due to the to

the aromatic ring in 4FA. While this carbon in the heated sample at 180 °C decreased by around six times of rate decrease of fluorine (Table (6-2)) which gives a sign that part of the lost carbon may have been lost as a component of evaporated 4FA with fluorine and nitrogen above mentioned. The carbon peaks associated with C-OH/ C-O-C and O-C=O increased in relative intensity upon heating at 120 °C and 150 °C, especially for a longer heating time. This increase in carbon amount matches with the change in the amount of oxygen bonded to carbon as shown in Fig (6-19). This may indicate that heating at 120°C and 150°C could lead to an increase in the composition of organic compounds, whereas the sample heated at 180°C shows no change in carbon and oxygen compared to the unheated sample.

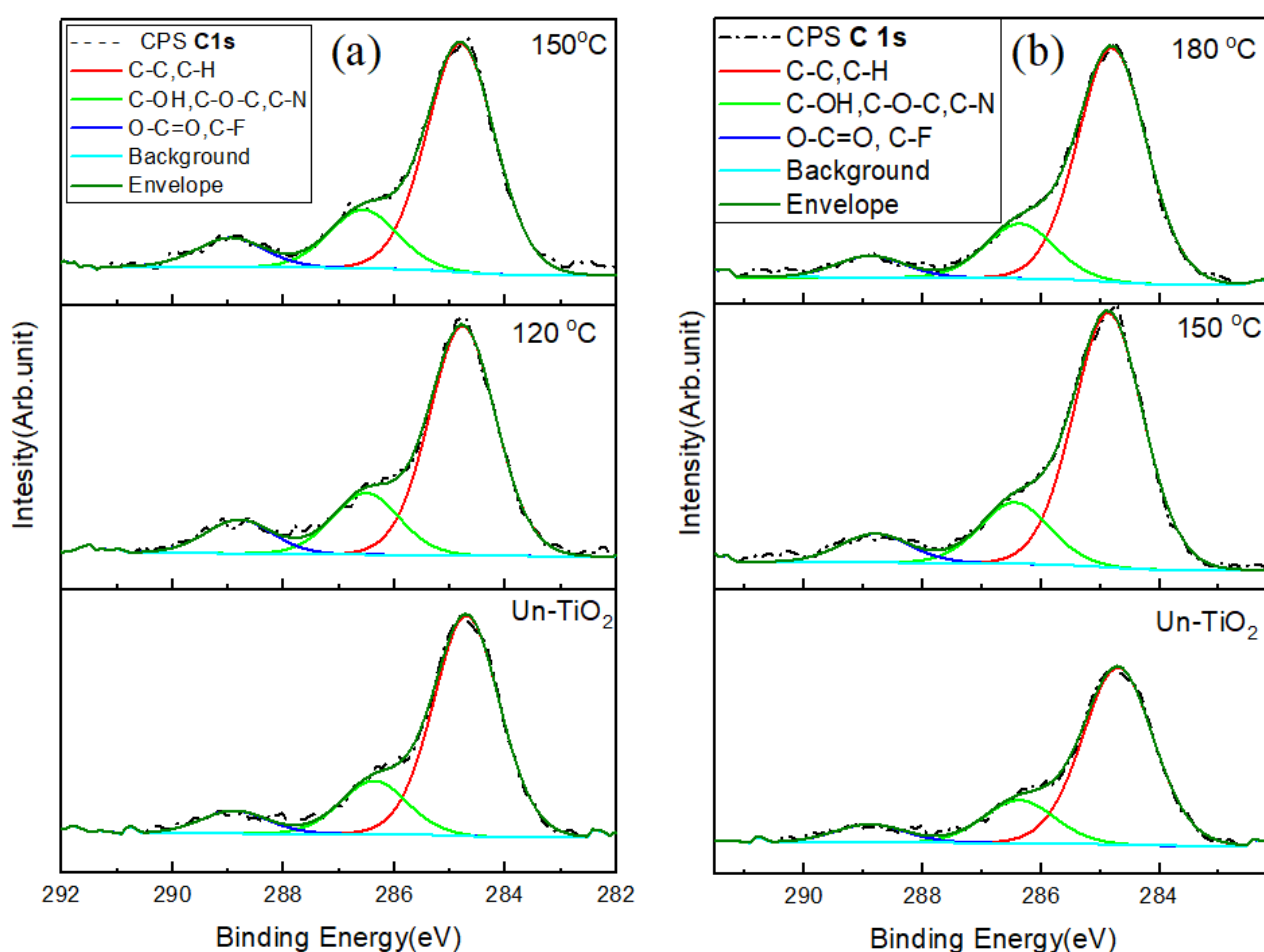


Fig (6-17): C 1s spectra from untreated samples and treated by heating; (a) samples heated at 120 and 150 for 15 min (b) samples heated at 150 and 180 for 11 min.

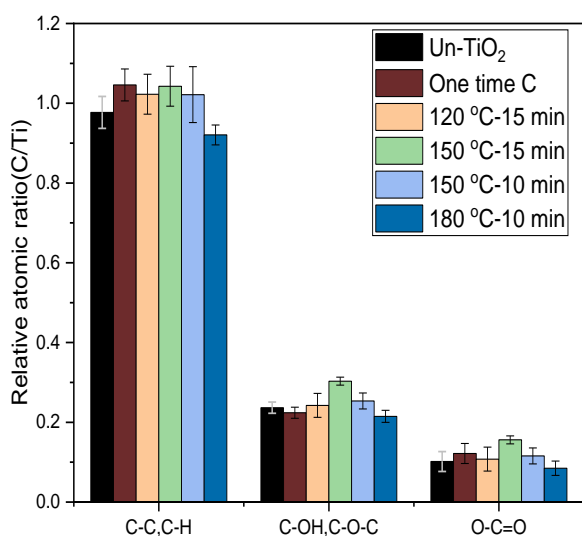


Fig (6-18): Relative atomic concentrations of C1s from fresh samples; untreated sample, unheated and heated treated samples (different temperatures)

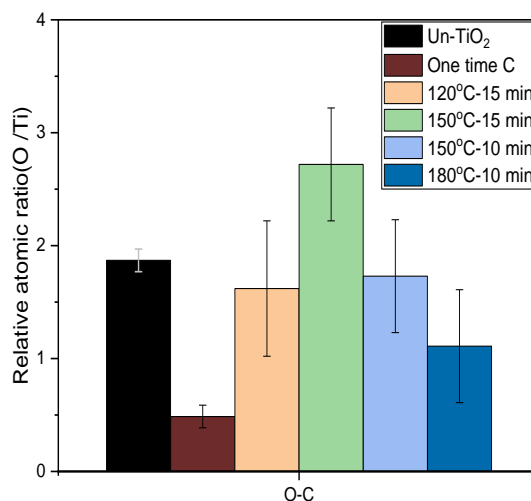


Fig (6-19): Relative atomic concentrations of O1s from fresh samples; untreated sample, unheated and heated treated samples (different temperatures)

In aged samples, the atomic ratio of aliphatic carbon for heated samples at 120 °C and 150 °C did not change for measured after 35 days, while it increased slightly after 50 days, as shown in Fig (6-20). This increase in carbon is proportional to the decrease in the fluorine (F-Ti) (Fig (6-21)), which means the fluorinated samples do seem to show some resistance to hydrocarbon adsorption. This resistance decreases as fluorine is lost from the surface with time, as in the samples measured after 50 days. Also, the significant increase in carbon content in the heated samples at 180 °C, which corresponds to the largest decrease in the fluorine content, especially the data recorded after 50 days, appears to confirm the association of surface fluorination with resistance to carbon adsorption. This is in reasonable agreement with the results of the immersion and washing method reported above, indicating fluorination by both methods appears to offer some resistance against adsorption of atmospheric hydrocarbon on the surface, but this efficiency also decreases with time in both cases.

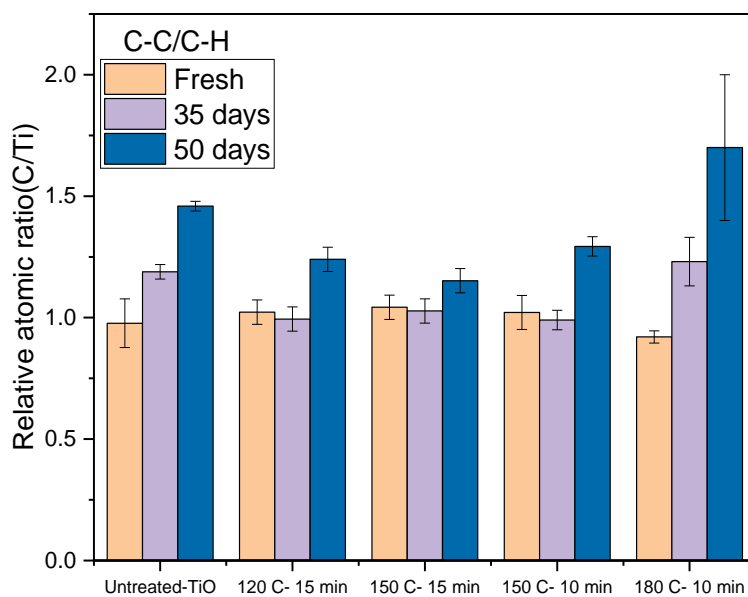


Fig (6-20): Relative atomic concentrations of C1s from fresh and aged untreated and treated TiO₂; different temperatures and heating times.

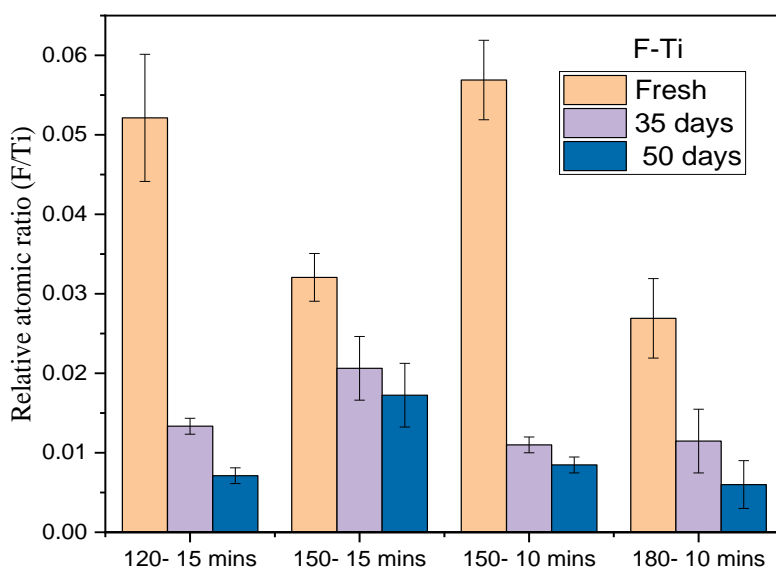


Fig (6-21): Relative atomic concentrations of F1s from fresh and aged untreated and treated TiO₂; different temperatures and heating times.

6.3.1.2 Treatment of TiO₂ thin films by using the evaporation of 4-fluoroaniline solution without direct contact between them.

Fig (6-22) shows the F 1s core-level XPS of samples treated by exposing them to 4-fluoroaniline for one hour (M1) and four hours (M4) in a vacuum desiccator at a pressure of $\sim 1 \times 10^{-2}$ mbar and then subjected to UV-O₃ cleaning. The spectra confirm that the 4FA is deposited upon the TiO₂ surface by evaporation and subsequent adsorption on the TiO₂. Two peaks are observed in the F 1s spectrum at binding energies of 684.6 eV and 687.5 eV that are attributed to the F-Ti bond and F-C in the 4-FA molecule, respectively. The atomic ratio of fluorine to Ti, as shown in Fig (6-23), reveals that a longer exposure time contributes to an increased fluorine to Ti ratio. In contrast, the F-C ratio shows a slight decrease that could be due to an increase in the reaction between 4FA and TiO₂ in the vacuum, because the ratio of total fluorine (*i.e.* F-Ti + F-C) to Ti on the surfaces of samples exposed for one and four hours are almost identical around (0.055). This appears to indicate that the duration of the exposure of the TiO₂ films to the 4FA, could affect the decomposition of 4-FA and incorporation of the fluorine atoms into TiO₂ film.

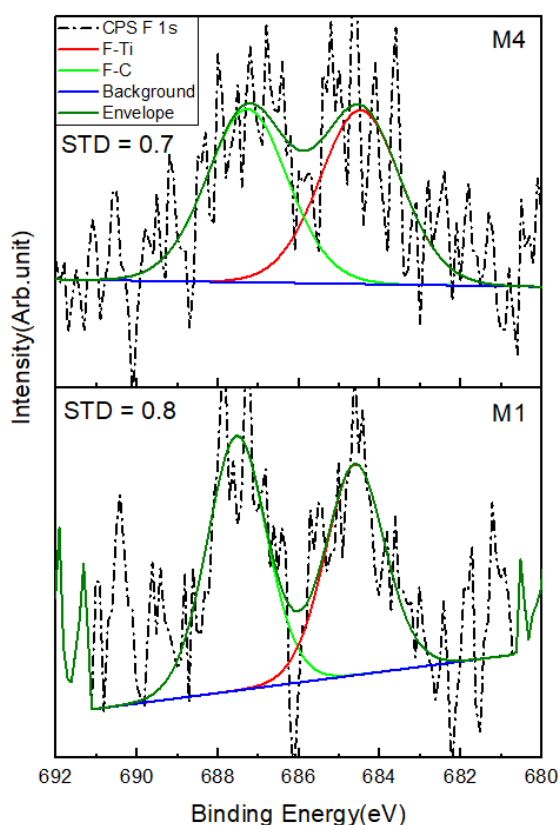


Fig (6-22): F 1s spectra from fresh treated samples treated by exposing them to 4FA for one hour (M1) and four hours (M4).

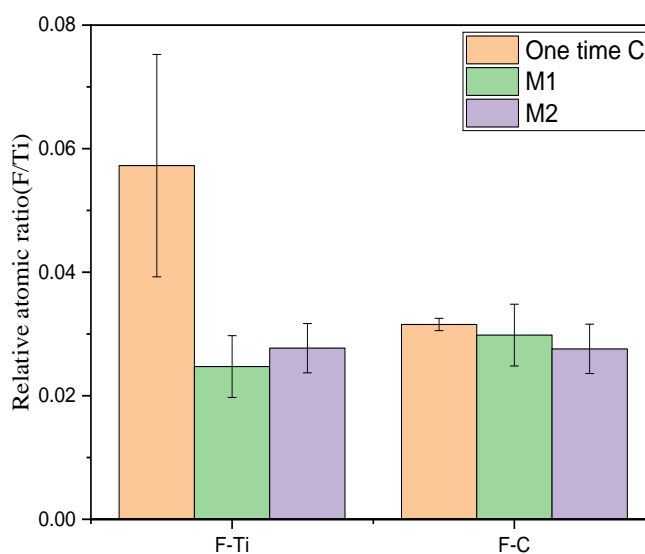


Fig (6-23): Relative atomic concentrations of F1s from fresh treated by immersing and cleaning by IPA (one time C) and exposing them to 4FA for one hour (M1) and four hours (M4).

The main finding, however, is that the amount of fluorine bonded to Ti by this treatment method is much lower than that obtained by the immersion and cleaning methods, discussed above. The effect of this low concentration of fluorine on the surface is mirrored by the ratio of carbon, and oxygen bonded to carbon, as shown in Fig (6-24). Samples M1 and M4 both have a higher ratio of hydrocarbon species and oxygen bonded to carbon, than the samples treated by immersing in 4-FA, suggesting a low treatment efficiency. Interestingly, the amount of hydrocarbon on the surface prepared by vacuum deposition, as shown in Fig (6-25), shows virtually no change within error. This is despite the loss of F over this time period (see Fig 6.26) as was seen for the surfaces produced by immersion in 4-FA. The reason for the difference in terms of the reduced reactivity of the surface with regards to adventitious carbon, is not clear. It is likely that the reduced uptake of 4-FA by the evaporation means that there is less C from the aromatic ring of the 4-FA on the surface initially and that it may simply be differences in the C content at different points on the sample that leads to the observed changes in the samples prepared by immersion.

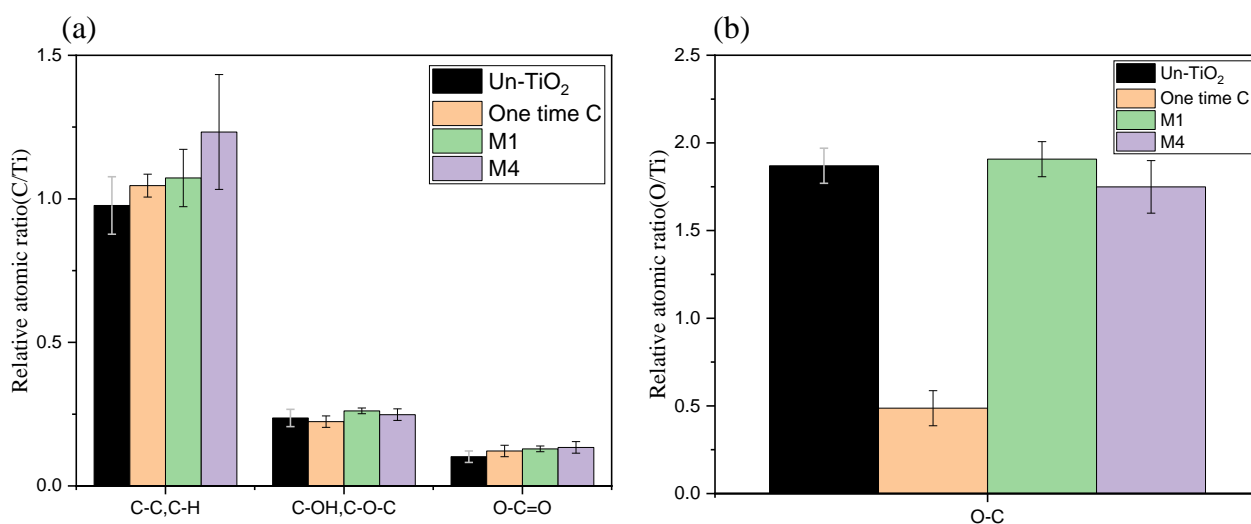


Fig (6-24): Relative atomic concentrations of C1s (a) and O1s (b) from fresh samples; untreated sample, treated by immersing and cleaning by IPA (one time C) and exposing them to 4FA for one hour (M1) and four hours (M4).

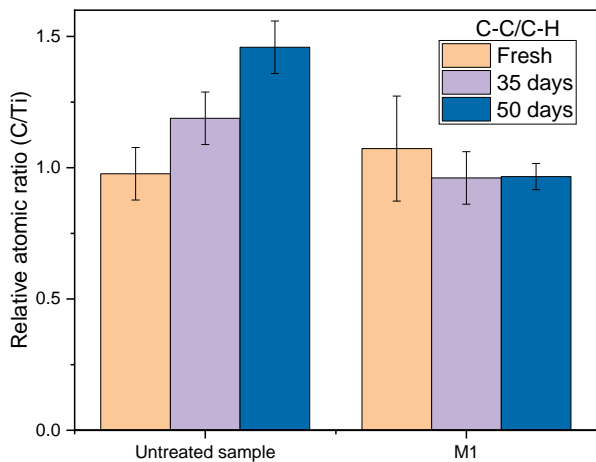


Fig (6-25): Relative atomic concentrations of C1s from fresh and aged untreated and treated TiO₂ by exposing it to 4FA for one hour (M1)

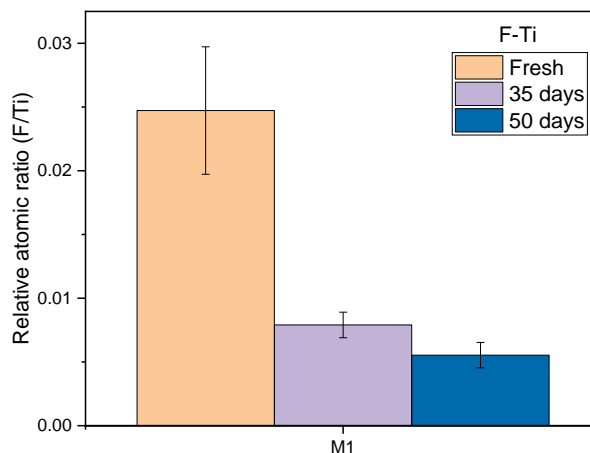


Fig (6-26): Relative atomic concentrations of F1s from fresh and aged untreated and treated TiO₂ by exposing it to 4FA for one hour (M1)

6.3.2 The UV–vis transmittance spectra

Optical transmittance is a critical factor in the photochemical properties of materials used as the ETL layer in perovskite solar cells. Fluorination of TiO_2 could affect optical transmittance of TiO_2 , which could affect the transmission of light to the active layer. Tang *et al.* reported that the fluorination process does not impact on the optical absorption of TiO_2 [142]. Yu *et al.*, on the other hand, found that F-doped TiO_2 has higher UV absorbance and a red shift of the band gap compared to pure TiO_2 . Fig (6-27) shows the UV–vis transmittance spectra of untreated TiO_2 and treated samples using the abovementioned methods. In all methods, fluorinated samples show an optical transmittance similar to that of untreated ones, which

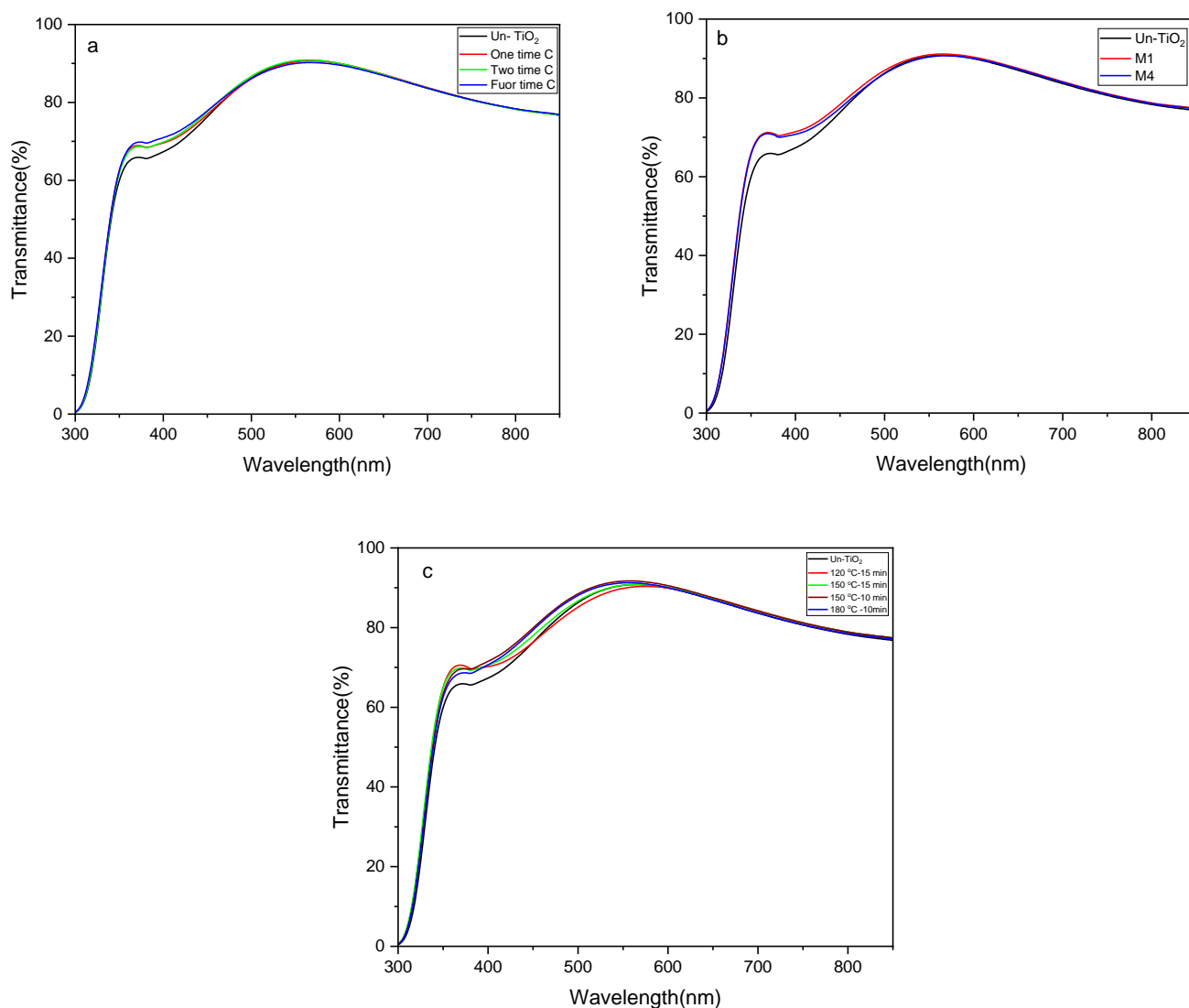


Fig (6-27): The UV–vis transmittance spectra of untreated TiO_2 and treated samples; (a) by immersing and cleaning (b) by exposing them to 4FA (c) by immersing and heating

agrees with the result of Tang *et al.*, indicating the treatment process used does not affect the optical properties of TiO₂. This is perhaps not surprising in the current work since only the topmost surface layers should be affected by the fluorination process.

6.4 CONCLUSIONS

The purpose of experiments in this chapter was to examine the treatment of the TiO₂ surface to prevent or reduce carbon contamination using 4FA to form a blocking layer of fluoride atoms bonded to Ti thus reducing the available surface Ti-sites thought to be the adsorption sites for organic acids present in the atmosphere. Films were characterised using XPS and UV-Vis.

The XPS results found from all methods of treatment confirmed the presence of fluorine atoms on the surface of TiO₂ in two chemical states, F-Ti and F-C in the 4-FA molecule, at different concentrations, depending on the method used to prepare the substrates. Assuming that an increase in the ratio of fluorine bonded to Ti in the sample surface is a benchmark for the efficiency of treatment, the immersing and washing method is the most efficient one where the samples treated by it have a high ratio of fluorine bonded to Ti, which increased with repeated treatment. Heating the substrate after immersing caused a decrease in the surface fluorine ratio, presumably due to evaporation of unbound 4-FA from the surface of the samples. The samples treated by evaporation of 4-FA and deposition under low vacuum conditions had the lowest amount of fluorine at the surface. All samples treated have carbon species that could be attributed to carbon contamination as well as C signal from the 4-FA molecule, but the low oxygen ratio could confirm that most of the present of carbon in treated samples belongs to 4-FA, especially in samples treated by immersing.

The effect of the F-treatment is apparent in aged samples where all data measured after 35 days show resistance of the treated surfaces to adsorb more carbon species. But the 50 days data show an increase in the ratio of carbon in their surfaces that could be attributed to the loss of fluorine that led to a decrease in the resistance of adsorbing of carbon. Overall it seems that F-doping of the TiO₂ surface may have some effect on preventing adsorption of adventitious hydrocarbon, and that formation of Ti-F by 4-FA is a viable technique. However, it would be interesting to determine how much influence the method of synthesis of the TiO₂ from Ti isopropoxide has on the C content, e.g. does the use of commercial TiO₂ show similar C content. In addition it would be useful to study the water contact angle of these treated films to determine the hydrophilicity. Finally, it would also be interesting to determine whether these treated surfaces show any improvement in the efficiency of photovoltaic cells using the F-doped TiO₂ as the ETL.

Chapter 7: Conclusions and future work

7.1. CONCLUSION

Since template techniques offer an opportunity to synthesise perovskite nanomaterials with well-controlled size, shape and stability. Two chapters of this study investigated the use of two peptide gels, F8 and F9, as templates for fabricating MAPI perovskite.

The results indicated that using both peptides (F8 and F9) contributed to a decrease in the size particles of MAPI with a change in its optoelectronic properties. Also, the stability of the templated MAPI by these peptides increased. The observed things are that the effect of templating increased with an increase in peptide concentration which could be attributed to an increase in fibre density that leads to decreased network mesh size, thus the effects on fabricated MAPI. The F9 showed higher solubility in the MAPI precursor that allowed the addition of higher concentrations and led to an increase in the blue shift in PL spectra that could be attributed to a further decrease in the size of MAPI particles due to the decrease of the network mesh size.

Regarding the solar cells, an optimal amount of F8 was found to improve the efficiency and stability of devices based on templated MAPI, where exceeding it led to decreased photocurrent that could be due to producing an insulating layer that affects the transfer of the charge carriers to transport layers. The F8 peptide seemed to offer improved stability compared to the F9 peptide and also produced a larger increase in PL, suggesting it was more effective in passivating Pb^{2+} defects at the surface of the perovskite. This in turn suggests that the additional basic/amine group on the F9 peptide in some way reduces the ability of the peptide to bind to the perovskite surface. Whether this is a steric issue, due to the slightly increased size, or due to the way the peptide forms the network – i.e. with the amine preferentially interacting with other peptides is not clear.

The thesis also investigated using 4-fluoroaniline (4FA) as a fluorination agent to treat TiO_2 surfaces to prevent or reduce carbon contamination. The results showed an increase in the resistance of fluorinated samples' surfaces to adsorb more carbon species compared to the reference sample that was kept in the same condition for the same periods. Noticeably, treatment efficiency decreases with increasing time, accompanied by fluorine loss from samples' surfaces that could not be interpreted clearly from our findings.

7.2. SUGGESTIONS FOR FUTURE WORK

The apparent effect on optoelectronic properties and stability of MAPI perovskite by using F8 and F9 peptides in the synthesis encourages repeating the measurements with other perovskite materials, such as MAPbBr₃ or CsPbI₃. Although it is not discussed in the thesis, attempts to template formamidinium (FA) lead iodide (FAPbI₃ or FAPI) were unsuccessful. It was found that the PbI₂ formed but FAPI did not. The reasons for this were unclear, but it would be interesting to investigate this further. One possibility is that the charge on the amine and the formamidinium (FA) ion prevented the FA being incorporated into the peptide.

It would also be useful to determine the effect of the F9 peptide in the synthesis of PV cells based on F9-perovskite composites, again to determine whether there is an optimum concentration to boost efficiency. For both peptides further investigations into what causes the limitations, i.e. is it due to the insulating nature of the peptide – does the peptide affect the charge transport between the perovskite and ETL or HTL, would also be of interest.

Also, the use of other types of peptides to study their effectiveness as templates for the fabrication of perovskite materials is a possible option for future work.

Using the HAXPES for treated TiO₂ samples by 4FA could be helpful to interpret losing fluorine from aged treated samples. Also, a study of the effect of fluorination TiO₂ on the efficiency of solar cells based on fluorinated TiO₂ could give some indicators of the effectiveness of using this treatment.

References

- [1] C. F. Baes, H. E. Goeller, J. S. Olson, and R. M. Rotty, "Carbon dioxide and climate: the uncontrolled experiment," *Am. Sci.*, vol. 65, no. 3, pp. 310–320, 1977.
- [2] H. Tyagi, A. Kumar, A. Prodyut, R. Chakraborty, and S. Powar, *Applications of Solar Energy, Environment, and Sustainability*. 2018.
- [3] Liang; Xinxing (University of Bath), "Synthesis of Perovskite Nanocrystals and Their Applications in Perovskite Solar Cells," 2018.
- [4] "<https://ourworldindata.org/cheap-renewables-growth>, accessed 26.04.2023."
- [5] (<https://www.nrel.gov/pv/cell-efficiency.html> accessed Dec 2022, "Best Research-Cell Efficiencies," p. 2020, 2022.
- [6] M. M. A. Moon, M. F. Rahman, J. Hossain, and A. B. M. Ismail, "Comparative Study of the Second Generation a-Si:H, CdTe, and CIGS Thin-Film Solar Cells," *Adv. Mater. Res.*, vol. 1154, pp. 102–111, 2019.
- [7] C. Li, X. Lu, W. Ding, L. Feng, Y. Gao, and Z. Guo, "Formability of ABX₃ (X = F, Cl, Br, I) halide perovskites," *Acta Crystallogr. Sect. B Struct. Sci.*, vol. 64, no. 6, pp. 702–707, 2008.
- [8] M. A. Green, A. Ho-Baillie, and H. J. Snaith, "The emergence of perovskite solar cells," *Nat. Photonics*, vol. 8, no. 7, pp. 506–514, 2014.
- [9] S. Ahmad, S. Kazim, and M. Grätzel, *Perovskite solar cells : materials, processes, and devices*. .
- [10] W. Travis, E. N. K. Glover, H. Bronstein, D. O. Scanlon, and R. G. Palgrave, "On the application of the tolerance factor to inorganic and hybrid halide perovskites: A revised system," *Chem. Sci.*, vol. 7, no. 7, pp. 4548–4556, 2016.
- [11] H. Tian, *Molecular Devices for Solar Energy Conversion and Storage*. 2018.
- [12] S. Tao *et al.*, "Absolute energy level positions in tin- and lead-based halide perovskites," *Nat. Commun.*, vol. 10, no. 1, pp. 1–10, 2019.
- [13] A. Kojima, K. Teshima, Y. Shirai, and T. Miyasaka, "Organometal halide perovskites as visible-light sensitizers for photovoltaic cells," *J. Am. Chem. Soc.*, vol. 131, no. 17, pp. 6050–6051, 2009.
- [14] J. H. Im, C. R. Lee, J. W. Lee, S. W. Park, and N. G. Park, "6.5% Efficient Perovskite Quantum-Dot-Sensitized Solar Cell," *Nanoscale*, vol. 3, no. 10, pp. 4088–4093, 2011.
- [15] H. S. Kim *et al.*, "Lead iodide perovskite sensitized all-solid-state submicron thin film mesoscopic solar cell with efficiency exceeding 9%," *Sci. Rep.*, vol. 2, pp. 1–7, 2012.
- [16] E. Tenuta, C. Zheng, and O. Rubel, "Thermodynamic origin of instability in hybrid halide perovskites," *Sci. Rep.*, vol. 6, no. July, pp. 1–8, 2016.
- [17] A. M. A. Leguy *et al.*, "Reversible hydration of CH₃NH₃PbI₃ in films, single crystals, and solar cells," *Chem. Mater.*, vol. 27, no. 9, pp. 3397–3407, 2015.
- [18] J. Chun-Ren Ke *et al.*, "In situ investigation of degradation at organometal halide perovskite surfaces by X-ray photoelectron spectroscopy at realistic water vapour pressure," *Chem. Commun.*, vol. 53, no. 37, pp. 5231–5234, 2017.

- [19] F. Tian, W. Feng, B. Xing, X. He, W. A. Saidi, and L. Zhang, "Grain Boundaries in Methylammonium Lead Halide Perovskites Facilitate Water Diffusion," *Adv. Energy Sustain. Res.*, vol. 2, no. 11, p. 2100087, 2021.
- [20] D. Bryant *et al.*, "Light and oxygen induced degradation limits the operational stability of methylammonium lead triiodide perovskite solar cells," *Energy Environ. Sci.*, vol. 9, no. 5, pp. 1655–1660, 2016.
- [21] C. C. Boyd, R. Cheacharoen, T. Leijtens, and M. D. McGehee, "Understanding Degradation Mechanisms and Improving Stability of Perovskite Photovoltaics," *Chem. Rev.*, vol. 119, no. 5, pp. 3418–3451, 2019.
- [22] B. Conings *et al.*, "Intrinsic Thermal Instability of Methylammonium Lead Trihalide Perovskite," *Adv. Energy Mater.*, vol. 5, no. 15, pp. 1–8, 2015.
- [23] J. Yang *et al.*, "Comprehensive understanding of heat-induced degradation of triple-cation mixed halide perovskite for a robust solar cell," *Nano Energy*, vol. 54, no. August, pp. 218–226, 2018.
- [24] N. Phung and A. Abate, *Stability of materials and complete devices*. Elsevier Inc., 2019.
- [25] S. S. Dipta and A. Uddin, "Stability Issues of Perovskite Solar Cells: A Critical Review," *Energy Technol.*, vol. 9, no. 11, pp. 1–20, 2021.
- [26] T. Zhu, Y. Yang, and X. Gong, "Recent Advancements and Challenges for Low-Toxicity Perovskite Materials," *ACS Appl. Mater. Interfaces*, vol. 12, no. 24, pp. 26776–26811, 2020.
- [27] C. Enriquez *et al.*, *Perovskite Solar Cells*. 2019.
- [28] N. Pellet *et al.*, "Mixed-Organic-Cation Perovskite Photovoltaics for Enhanced Solar-Light Harvesting," *Angew. Chemie*, vol. 126, no. 12, pp. 3215–3221, 2014.
- [29] Y. Zhang, G. Grancini, Y. Feng, A. M. Asiri, and M. K. Nazeeruddin, "Optimization of Stable Quasi-Cubic FAxMA1-xPbI3 Perovskite Structure for Solar Cells with Efficiency beyond 20%," *ACS Energy Lett.*, vol. 2, no. 4, pp. 802–806, 2017.
- [30] A. Binek, F. C. Hanusch, P. Docampo, and T. Bein, "Stabilization of the trigonal high-temperature phase of formamidinium lead iodide," *J. Phys. Chem. Lett.*, vol. 6, no. 7, pp. 1249–1253, 2015.
- [31] G. Niu, W. Li, J. Li, X. Liang, and L. Wang, "Enhancement of thermal stability for perovskite solar cells through cesium doping," *RSC Adv.*, vol. 7, no. 28, pp. 17473–17479, 2017.
- [32] Y. H. Park *et al.*, "Inorganic Rubidium Cation as an Enhancer for Photovoltaic Performance and Moisture Stability of HC(NH2)2PbI3 Perovskite Solar Cells," *Adv. Funct. Mater.*, vol. 27, no. 16, 2017.
- [33] M. Saliba *et al.*, "Cesium-containing triple cation perovskite solar cells: Improved stability, reproducibility and high efficiency," *Energy Environ. Sci.*, vol. 9, no. 6, pp. 1989–1997, 2016.
- [34] T. Niu *et al.*, "Stable High-Performance Perovskite Solar Cells via Grain Boundary Passivation," *Adv. Mater.*, vol. 30, no. 16, pp. 1–11, 2018.

- [35] R. Wang *et al.*, “Constructive molecular configurations for surface-defect passivation of perovskite photovoltaics,” *Science* (80-.), vol. 366, no. 6472, pp. 1509–1513, 2019.
- [36] B. Chaudhary *et al.*, “Poly(4-Vinylpyridine)-Based Interfacial Passivation to Enhance Voltage and Moisture Stability of Lead Halide Perovskite Solar Cells,” *ChemSusChem*, vol. 10, no. 11, pp. 2473–2479, 2017.
- [37] S. Ma, G. Yuan, Y. Zhang, N. Yang, Y. Li, and Q. Chen, “Development of encapsulation strategies towards the commercialization of perovskite solar cells,” *Energy Environ. Sci.*, vol. 15, no. 1, pp. 13–55, 2022.
- [38] Q. Dong *et al.*, “Encapsulation of Perovskite Solar Cells for High Humidity Conditions,” *ChemSusChem*, vol. 9, no. 18, pp. 2597–2603, 2016.
- [39] Y. Il Lee *et al.*, “A Low-Temperature Thin-Film Encapsulation for Enhanced Stability of a Highly Efficient Perovskite Solar Cell,” *Adv. Energy Mater.*, vol. 8, no. 9, pp. 1–8, 2018.
- [40] T. Liu *et al.*, “Stable Formamidinium-Based Perovskite Solar Cells via In Situ Grain Encapsulation,” *Adv. Energy Mater.*, vol. 8, no. 22, pp. 1–9, 2018.
- [41] Y. Lin *et al.*, “Enhanced Thermal Stability in Perovskite Solar Cells by Assembling 2D/3D Stacking Structures,” *J. Phys. Chem. Lett.*, vol. 9, no. 3, pp. 654–658, 2018.
- [42] Y. Liu, J. Goebel, and Y. Yin, “Templated synthesis of nanostructured materials,” *Chem. Soc. Rev.*, vol. 42, no. 7, pp. 2610–2653, 2013.
- [43] Y. Xie, D. Kocafe, C. Chen, and Y. Kocafe, “Review of Research on Template Methods in Preparation of Nanomaterials,” *J. Nanomater.*, vol. 2016, 2016.
- [44] W. Liu, H. Zhou, and G. Chen, “Patterned Lead Halide Perovskite Crystals Fabricated by Microstructured Templates,” *Cryst. Growth Des.*, vol. 20, no. 4, pp. 2803–2816, 2020.
- [45] H. Wang *et al.*, “Nanoimprinted Perovskite Nanograting Photodetector with Improved Efficiency,” *ACS Nano*, vol. 10, no. 12, pp. 10921–10928, 2016.
- [46] S. Paul, K. Ariga, D. D. Sarma, and S. Acharya, “Dimension-controlled halide perovskites using templates,” *Nano Today*, vol. 39, p. 101181, 2021.
- [47] V. Malgras, J. Henzie, T. Takei, and Y. Yamauchi, “Hybrid methylammonium lead halide perovskite nanocrystals confined in gyroidal silica templates,” *Chem. Commun.*, vol. 53, no. 15, pp. 2359–2362, 2017.
- [48] J. Ghosh, R. Ghosh, and P. K. Giri, “Mesoporous Si Nanowire Templated Controlled Fabrication of Organometal Halide Perovskite Nanoparticles with High Photoluminescence Quantum Yield for Light-Emitting Applications,” *ACS Appl. Nano Mater.*, vol. 1, no. 4, pp. 1551–1562, 2018.
- [49] Y. Q. Hu, L. J. Fan, H. Y. Hui, H. Q. Wen, D. S. Yang, and G. D. Feng, “Monodisperse bismuth-halide double perovskite nanocrystals confined in mesoporous silica templates,” *Inorg. Chem.*, vol. 58, no. 13, pp. 8500–8505, 2019.
- [50] Y. Chen, M. Yu, S. Ye, J. Song, and J. Qu, “All-inorganic CsPbBr₃ perovskite quantum dots embedded in dual-mesoporous silica with moisture resistance for two-photon-pumped plasmonic nanoLasers,” *Nanoscale*, vol. 10, no. 14, pp. 6704–6711, 2018.

- 2018.
- [51] M. M. Tavakoli *et al.*, “A non-catalytic vapor growth regime for organohalide perovskite nanowires using anodic aluminum oxide templates,” *Nanoscale*, vol. 9, no. 18, pp. 5828–5834, 2017.
- [52] D. Zhang *et al.*, “Increasing Photoluminescence Quantum Yield by Nanophotonic Design of Quantum-Confined Halide Perovskite Nanowire Arrays,” *Nano Lett.*, vol. 19, no. 5, pp. 2850–2857, 2019.
- [53] D. Rambabu, S. Bhattacharyya, T. Singh, C. M. L., and T. K. Maji, “Stabilization of MAPbBr₃ Perovskite Quantum Dots on Perovskite MOFs by a One-Step Mechanochemical Synthesis,” *Inorg. Chem.*, vol. 59, no. 2, pp. 1436–1443, 2020.
- [54] Z. Chen, Z. G. Gu, W. Q. Fu, F. Wang, and J. Zhang, “A Confined Fabrication of Perovskite Quantum Dots in Oriented MOF Thin Film,” *ACS Appl. Mater. Interfaces*, vol. 8, no. 42, pp. 28737–28742, 2016.
- [55] C. Dokkhan, M. Z. Mokhtar, Q. Chen, B. R. Saunders, N. W. Hodson, and B. Hamilton, “Using microgels to control the morphology and optoelectronic properties of hybrid organic-inorganic perovskite films,” *Phys. Chem. Chem. Phys.*, vol. 20, no. 44, pp. 27959–27969, 2018.
- [56] O. M. Alkudhari *et al.*, “High efficiency semitransparent perovskite solar cells containing 2D nanopore arrays deposited in a single step,” *J. Mater. Chem. A*, pp. 10227–10241, 2022.
- [57] C. Zhen, T. Wu, R. Chen, L. Wang, G. Liu, and H. M. Cheng, “Strategies for Modifying TiO₂ Based Electron Transport Layers to Boost Perovskite Solar Cells,” *ACS Sustain. Chem. Eng.*, vol. 7, no. 5, pp. 4586–4618, 2019.
- [58] N. J. Jeon, J. H. Noh, Y. C. Kim, W. S. Yang, S. Ryu, and S. Il Seok, “Solvent engineering for high-performance inorganic-organic hybrid perovskite solar cells,” *Nat. Mater.*, vol. 13, no. 9, pp. 897–903, 2014.
- [59] G. W. P. Adhyaksa *et al.*, “Understanding Detrimental and Beneficial Grain Boundary Effects in Halide Perovskites,” *Adv. Mater.*, vol. 30, no. 52, 2018.
- [60] S. A. McHugo, H. Hiesimair, and E. R. Weber, “Gettering of metallic impurities in photovoltaic silicon,” *Appl. Phys. A Mater. Sci. Process.*, vol. 64, no. 2, pp. 127–137, 1997.
- [61] L. Lin *et al.*, “Inorganic Electron Transport Materials in Perovskite Solar Cells,” *Adv. Funct. Mater.*, vol. 31, no. 5, 2021.
- [62] H. Zhang *et al.*, “New generation perovskite solar cells with solution-processed amino-substituted perylene diimide derivative as electron-transport layer,” *J. Mater. Chem. A*, vol. 4, no. 22, pp. 8724–8733, 2016.
- [63] S. Do Sung, D. P. Ojha, J. S. You, J. Lee, J. Kim, and W. I. Lee, “50 nm sized spherical TiO₂ nanocrystals for highly efficient mesoscopic perovskite solar cells,” *Nanoscale*, vol. 7, no. 19, pp. 8898–8906, 2015.
- [64] K. Wojciechowski *et al.*, “Heterojunction Modification for Highly Efficient Organic/Inorganic Perovskite solar cells,” *ACS Nano*, vol. 8, no. 12, pp. 12701–12709, 2014.

- [65] B. Li, Y. Chen, Z. Liang, D. Gao, and W. Huang, “Interfacial engineering by using self-assembled monolayer in mesoporous perovskite solar cell,” *RSC Adv.*, vol. 5, no. 114, pp. 94290–94295, 2015.
- [66] Z. Zhu *et al.*, “Efficiency enhancement of perovskite solar cells through fast electron extraction: The role of graphene quantum dots,” *J. Am. Chem. Soc.*, vol. 136, no. 10, pp. 3760–3763, 2014.
- [67] G. Kakavelakis, D. Konios, E. Stratakis, and E. Kymakis, “Enhancement of the efficiency and stability of organic photovoltaic devices via the addition of a lithium-neutralized graphene oxide electron-transporting layer,” *Chem. Mater.*, vol. 26, no. 20, pp. 5988–5993, 2014.
- [68] J. Balajka *et al.*, “High-affinity adsorption leads to molecularly ordered interfaces on TiO₂ in air and solution,” *Science (80-.)*, vol. 361, no. 6404, pp. 786–789, 2018.
- [69] A. Song, E. S. Skibinski, W. J. I. Debenedetti, A. G. Ortoll-Bloch, and M. A. Hines, “Nanoscale solvation leads to spontaneous formation of a bicarbonate monolayer on rutile (110) under ambient conditions: Implications for CO₂ photoreduction,” *J. Phys. Chem. C*, vol. 120, no. 17, pp. 9326–9333, 2016.
- [70] Y. Son, M. K. Lee, and Y. C. Park, “Contact Angle Relaxation on Amorphous, Mixed-Phase (Anatase + Rutile), and Anatase TiO₂ Films and Its Mechanism,” *Langmuir*, vol. 37, no. 5, pp. 1850–1860, 2021.
- [71] W. Wu, N. G. Combs, T. E. Mates, and S. Stemmer, “Carbon impurity concentrations in BaSnO₃ films grown by molecular beam epitaxy using a tin oxide source,” *J. Vac. Sci. Technol. A*, vol. 38, no. 4, p. 043405, 2020.
- [72] X. Sun, H. Guo, Y. Zhang, X. Li, and Z. Cao, “Effects of Carbon Impurity in Monocrystalline Silicon on Electrical Properties and the Mechanism Analysis of PIN Rectifier Diodes,” *IEEE Access*, vol. 9, pp. 22868–22875, 2021.
- [73] S. W. Cha, G. Y. Cho, Y. Lee, T. Park, Y. Kim, and J. moo Lee, “Effects of carbon contaminations on Y₂O₃-stabilized ZrO₂ thin film electrolyte prepared by atomic layer deposition for thin film solid oxide fuel cells,” *CIRP Ann. - Manuf. Technol.*, vol. 65, no. 1, pp. 515–518, 2016.
- [74] H. G. Yang *et al.*, “Anatase TiO₂ single crystals with a large percentage of reactive facets,” *Nature*, vol. 453, no. 7195, pp. 638–641, 2008.
- [75] W. J. I. Debenedetti and M. A. Hines, “Photochemical Fluorination of TiO₂(110) Produces an Atomically Thin Passivating Layer,” *J. Phys. Chem. C*, vol. 126, no. 10, pp. 4899–4906, 2022.
- [76] D. A. Neamen, *Semiconductor Physics and Devices Basic Principles*. New York: Ragu Srinivasan, 2012.
- [77] A. KITAI, *Principles of Solar Cells, LEDs and Related Devices The Role of the PN Junction*, Second. Wiley, 2019.
- [78] E. M. Anastassakis and J. D. Joannopoulos, *The Physics of Semiconductors*. 1990.
- [79] K. Novakova and A. Sandberg, “IV-measurements of InP NW solar cells,” pp. 1–9, 2019.

- [80] T. Kita, *Energy conversion efficiency of solar cells*. 2012.
- [81] O. J. Weber, “Structural Chemistry of Hybrid Halide Perovskites for Thin Film Photovoltaics Structural Chemistry of Hybrid Halide Perovskites for Thin Film Photovoltaics University of Bath,” University of Bath, 2018.
- [82] S. Hegedus, *Photovoltaic Science*. 2003.
- [83] I. Hussain, H. P. Tran, J. Jaksik, J. Moore, N. Islam, and M. J. Uddin, “Functional materials, device architecture, and flexibility of perovskite solar cell,” *Emergent Mater.*, vol. 1, no. 3–4, pp. 133–154, 2018.
- [84] N. Marinova, S. Valero, and J. L. Delgado, “Organic and perovskite solar cells: Working principles, materials and interfaces,” *J. Colloid Interface Sci.*, vol. 488, pp. 373–389, 2017.
- [85] J. K. Wychowaniec, A. M. Smith, C. Ligorio, O. O. Mykhaylyk, A. F. Miller, and A. Saiani, “Role of Sheet-Edge Interactions in β -sheet Self-Assembling Peptide Hydrogels,” *Biomacromolecules*, vol. 21, no. 6, pp. 2285–2297, 2020.
- [86] A. Mujeeb, “THESIS: Self-assembled octapeptide gels for cartilage repair,” [Thesis]. Manchester, UK Univ. Manchester; 2013., 2013.
- [87] P. Sciences, S. Boothroyd, and A. Science, “Peptide Self-assembly : Controlling Conformation and Mechanical Properties A thesis submitted to the University of Manchester for the degree of Doctor of Philosophy in the Faculty of Engineering and Physical Sciences Stephen Boothroyd,” 2011.
- [88] J. Banerjee, E. Radvar, and H. S. Azevedo, *Self-assembling peptides and their application in tissue engineering and regenerative medicine*. Elsevier Ltd., 2018.
- [89] A. Saiani *et al.*, “Self-assembly and gelation properties of α -helix versus β -sheet forming peptides,” *Soft Matter*, vol. 5, no. 1, pp. 193–202, 2009.
- [90] R. Li, A. Rodriguez, D. R. Nisbet, C. J. Barrow, and R. J. Williams, *Self-Assembled Peptide Nanostructures for the Fabrication of Cell Scaffolds*. Elsevier Inc., 2015.
- [91] M. A. Elsayy, A. M. Smith, N. Hodson, A. Squires, A. F. Miller, and A. Saiani, “Modification of β -Sheet Forming Peptide Hydrophobic Face: Effect on Self-Assembly and Gelation,” *Langmuir*, vol. 32, no. 19, pp. 4917–4923, 2016.
- [92] F. Parrino, F. R. Pomilla, G. Camera-Roda, V. Loddo, and L. Palmisano, *Properties of titanium dioxide*. INC, 2020.
- [93] M. Pelaez *et al.*, “A review on the visible light active titanium dioxide photocatalysts for environmental applications,” *Appl. Catal. B Environ.*, vol. 125, pp. 331–349, 2012.
- [94] Buddy D. Ranter and David G. Castner, “17 Electron Spectroscopy for Chemical Analysis,” *Surf. Anal. Princ. Tech.*, pp. 43–98, 2002.
- [95] C.S. Fadley, “X-ray photoelectron spectroscopy: Progress and perspectives,” *J. Electron Spectros. Relat. Phenomena*, vol. 178–179, pp. 2–32, 2010.
- [96] A. Pengpad, “Electron spectroscopy of surfaces and interfaces for novel solid state photovoltaic cells,” *PQDT - UK Irel.*, 2017.
- [97] J. Knudsen, J. N. Andersen, and J. Schnadt, “A versatile instrument for ambient

- pressure x-ray photoelectron spectroscopy: The Lund cell approach,” *Surf. Sci.*, vol. 646, pp. 160–169, 2016.
- [98] K. Laajalehto, I. Kartio, and E. Suoninen, “XPS and SR-XPS techniques applied to sulphide mineral surfaces,” *Int. J. Miner. Process.*, vol. 51, no. 1–4, pp. 163–170, 2002.
- [99] R. Lindsay and A. Thomas, *Introducing X-ray photoelectron spectroscopy for corrosion studies: A tool for elucidating interfacial composition and chemistry*. Elsevier Inc., 2022.
- [100] D. J. B. and P. W. G. Rosaleen J. Anderson, “Spectroscopy,” in *Organic Spectroscopic Analysis*, 2004, pp. 7–23.
- [101] L. Krückemeier, U. Rau, M. Stolterfoht, and T. Kirchartz, “How to Report Record Open-Circuit Voltages in Lead-Halide Perovskite Solar Cells,” *Adv. Energy Mater.*, vol. 10, no. 1, 2020.
- [102] Y. Li, J. Shi, Y. Mi, X. Sui, H. Xu, and X. Liu, “Ultrafast carrier dynamics in two-dimensional transition metal dichalcogenides,” *J. Mater. Chem. C*, vol. 7, no. 15, pp. 4304–4319, 2019.
- [103] R. L. Snyder, “1 X-Ray Diffraction,” 1999.
- [104] H. H. W. Stanjek, “3-Basics of X-Ray Diffraction,” pp. 107–119, 2004.
- [105] X. Diffraction, T. Dioxide, and D. Pattern, “materials Structural characterization of hybrid Scherrer Equation.”
- [106] Y. Liu, J. Goebel, and Y. Yin, “Templated synthesis of nanostructured materials,” *Chem. Soc. Rev.*, vol. 42, no. 7, pp. 2610–2653, 2013.
- [107] A. Jancik Prochazkova *et al.*, “Cyclic Peptide Stabilized Lead Halide Perovskite Nanoparticles,” *Sci. Rep.*, vol. 9, no. 1, pp. 3–8, 2019.
- [108] [Http://www.crystallography.net, “/cod/2107954.html,”](http://www.crystallography.net/cod/2107954.html) *Acta Crystallogr. Sect. B Struct. Sci. Cryst. Eng. Mater.*, vol. 72, no. 5, pp. 716–722, 2016.
- [109] L. Brus, “Electronic wave functions in semiconductor clusters: Experiment and theory,” *J. Phys. Chem.*, vol. 90, no. 12, pp. 2555–2560, 1986.
- [110] S. T. Harry and M. . Adekanmbi, “Confinement Energy of Quantum Dots and the Brus Equation,” *Int. J. Res. -GRANTHAALAYAH*, vol. 8, no. 11, pp. 318–323, 2020.
- [111] J. Peng *et al.*, “A Universal Double-Side Passivation for High Open-Circuit Voltage in Perovskite Solar Cells: Role of Carbonyl Groups in Poly(methyl methacrylate),” *Adv. Energy Mater.*, vol. 8, no. 30, pp. 1–9, 2018.
- [112] S. Singh *et al.*, “Investigation on Organic Molecule Additive for Moisture Stability and Defect Passivation via Physisorption in CH₃NH₃PbI₃ Based Perovskite,” *ACS Appl. Energy Mater.*, vol. 1, no. 5, pp. 1870–1877, 2018.
- [113] S. Lee *et al.*, “Amine-Based Passivating Materials for Enhanced Optical Properties and Performance of Organic-Inorganic Perovskites in Light-Emitting Diodes,” *J. Phys. Chem. Lett.*, vol. 8, no. 8, pp. 1784–1792, 2017.
- [114] B. P. Finkenauer, Akriti, K. Ma, and L. Dou, “Degradation and Self-Healing in

- Perovskite Solar Cells,” *ACS Appl. Mater. Interfaces*, vol. 14, no. 21, pp. 24073–24088, 2022.
- [115] R. A. Kerner *et al.*, “Amine additive reactions induced by the soft Lewis acidity of Pb²⁺ in halide perovskites. Part I: Evidence for Pb-alkylamide formation,” *J. Mater. Chem. C*, vol. 7, no. 18, pp. 5251–5259, 2019.
- [116] W. Becker, *Springer Series in Chemical Physics 111 Advanced Time- Correlated Single Photon Counting Applications*. 2015.
- [117] B. A. Koscher, J. K. Swabeck, N. D. Bronstein, and A. P. Alivisatos, “Essentially Trap-Free CsPbBr₃ Colloidal Nanocrystals by Postsynthetic Thiocyanate Surface Treatment,” *J. Am. Chem. Soc.*, vol. 139, no. 19, pp. 6566–6569, 2017.
- [118] J. A. Christians, P. A. Miranda Herrera, and P. V. Kamat, “Transformation of the excited state and photovoltaic efficiency of CH₃NH₃PbI₃ perovskite upon controlled exposure to humidified air,” *J. Am. Chem. Soc.*, vol. 137, no. 4, pp. 1530–1538, 2015.
- [119] Y. K. Ren *et al.*, “Controllable intermediates by molecular self-assembly for optimizing the fabrication of large-grain perovskite films via one-step spin-coating,” *J. Alloys Compd.*, vol. 705, pp. 205–210, 2017.
- [120] M. J. Jackman, K. L. Syres, D. J. H. Cant, S. J. O. Hardman, and A. G. Thomas, “Adsorption of dopamine on rutile TiO₂ (110): A photoemission and near-edge x-ray absorption fine structure study,” *Langmuir*, vol. 30, no. 29, pp. 8761–8769, 2014.
- [121] M. A. Elsayy, J. K. Wychowaniec, L. A. Castillo Díaz, A. M. Smith, A. F. Miller, and A. Saiani, “Controlling Doxorubicin Release from a Peptide Hydrogel through Fine-Tuning of Drug-Peptide Fiber Interactions,” *Biomacromolecules*, vol. 23, no. 6, pp. 2624–2634, 2022.
- [122] J. Gao, C. Tang, M. A. Elsayy, A. M. Smith, A. F. Miller, and A. Saiani, “Controlling Self-Assembling Peptide Hydrogel Properties through Network Topology,” *Biomacromolecules*, vol. 18, no. 3, pp. 826–834, 2017.
- [123] J. Wu, Y. Wang, C. Su, H. Zhou, H. Xu, and L. Jin, “Preparation and characterization of planar heterojunction perovskite solar cells based on c-TiO₂/CH₃NH₃PbI₃/HTM/Ag structure,” *J. Sol-Gel Sci. Technol.*, vol. 100, no. 3, pp. 440–450, 2021.
- [124] S. S. Mali, J. V. Patil, D. W. Park, Y. H. Jung, and C. K. Hong, “Intrinsic and extrinsic stability of triple-cation perovskite solar cells through synergistic influence of organic additive,” *Cell Reports Phys. Sci.*, vol. 3, no. 6, p. 100906, 2022.
- [125] H. Yang and X. Zhang, “Synthesis, characterization and computational simulation of visible-light irradiated fluorine-doped titanium oxide thin films,” *J. Mater. Chem.*, vol. 19, no. 37, pp. 6907–6914, 2009.
- [126] J. Balajka *et al.*, “High-affinity adsorption leads to molecularly ordered interfaces on TiO₂ in air and solution,” *Science (80-.)*, vol. 361, no. 6404, pp. 786–789, Aug. 2018.
- [127] K. L. Syres, A. G. Thomas, D. J. H. Cant, S. J. O. Hardman, and A. Preobrajenski, “Pyrocatechol as a surface capping molecule on rutile TiO₂ (110),” *Surf. Sci.*, vol. 606, no. 3–4, pp. 273–277, 2012.
- [128] L. C. Mayor *et al.*, “Photoemission, resonant photoemission, and x-ray absorption of a

- Ru(II) complex adsorbed on rutile TiO₂(110) prepared by in situ electrospray deposition,” *J. Chem. Phys.*, vol. 129, no. 11, 2008.
- [129] U. I. Gaya and A. H. Abdullah, “Heterogeneous photocatalytic degradation of organic contaminants over titanium dioxide: A review of fundamentals, progress and problems,” *J. Photochem. Photobiol. C Photochem. Rev.*, vol. 9, no. 1, pp. 1–12, 2008.
- [130] W. Wu, N. G. Combs, T. E. Mates, and S. Stemmer, “Carbon impurity concentrations in BaSnO₃ films grown by molecular beam epitaxy using a tin oxide source,” *J. Vac. Sci. Technol. A*, vol. 38, no. 4, p. 043405, Jul. 2020.
- [131] G. Li *et al.*, “Surface study of the reconstructed anatase TiO₂ (001) surface,” *Prog. Nat. Sci. Mater. Int.*, vol. 31, no. 1, pp. 1–13, 2021.
- [132] M. J. Jackman, K. L. Syres, D. J. H. Cant, S. J. O. Hardman, and A. G. Thomas, “Adsorption and Photocatalytic Degradation of 3-Fluoroaniline on Anatase TiO₂(101): A Photoemission and Near-Edge X-ray Absorption Fine Structure Study,” *Langmuir*, vol. 30, no. 29, pp. 8761–8769, 2014.
- [133] A. Zakrzewska, E. Kolehmainen, B. Osmialowski, and R. Gawinecki, “4-Fluoroanilines: Synthesis and decomposition,” *J. Fluor. Chem.*, vol. 111, no. 1, pp. 1–10, 2001.
- [134] C. Intermolecular and I. Involving, “In Situ Cryo-Crystallization of Fluorinated Amines: A Comparative Study of Cooperative Intermolecular Interactions Involving Ordered and Disordered Fluorine,” pp. 11–13, 2006.
- [135] K. Tanaka, “Photocatalytic Degradation of 1,1-Dechloroethane,” vol. 36, no. 9, pp. 1985–1992, 1998.
- [136] N. C. for B. I. (2023). P. Compound, T. diisopropoxide bis(acetylacetonate). R. Summary for CID 6010749, and 2023 from <https://pubchem.ncbi.nlm.nih.gov/compound/6010749> March 2, “National Center for Biotechnology Information,” pp. 1723–1723, 2023.
- [137] G. Greczynski and L. Hultman, “Reliable determination of chemical state in x-ray photoelectron spectroscopy based on sample-work-function referencing to adventitious carbon: Resolving the myth of apparent constant binding energy of the C 1s peak,” *Appl. Surf. Sci.*, vol. 451, pp. 99–103, 2018.
- [138] R. S. Devan *et al.*, “Nano-Heteroarchitectures of Two-Dimensional MoS₂@ One-Dimensional Brookite TiO₂ Nanorods: Prominent Electron Emitters for Displays,” *ACS Omega*, vol. 2, no. 6, pp. 2925–2934, 2017.
- [139] D. A. Armitage and D. M. Grant, “Characterisation of surface-modified nickel titanium alloys,” *Mater. Sci. Eng. A*, vol. 349, no. 1–2, pp. 89–97, 2003.
- [140] “N. Fairley, CasaXPS manual 2.3. 15, Acolyte Science, 2009,” *3 Acolyte Science*, vol. 15. 2009.
- [141] E. Farfan-Arribas and R. J. Madix, “Characterization of the acid-base properties of the TiO₂(110) surface by adsorption of amines,” *J. Phys. Chem. B*, vol. 107, no. 14, pp. 3225–3233, 2003.
- [142] J. Tang, H. Quan, and J. Ye, “Photocatalytic properties and photoinduced hydrophilicity of surface-fluorinated TiO₂,” *Chem. Mater.*, vol. 19, no. 1, pp. 116–

122, 2007.